Royal Holloway, University of London

Physics Department

Detector Development for Particle Physics and Applications to Environmental Monitoring

Author:

Adriana Dias

Supervisors:

Professor Jocelyn Monroe

Dr Alexander Deisting

February 27, 2024

A thesis submitted to the University of London for the degree of Doctor of Philosophy

Declaration

I, Adriana Mendes Filipe Dias, hereby declare that this thesis and the work presented in it is entirely my own. Where I have consulted the work of others, this is always clearly stated.

Signed:

Adriana Dias

Date: February 27, 2024

Acknowledgements

If I was like my 6 year old niece I would probably say "I did it all by myself!", but that just wouldn't be truthful.

Firstly, I would like to thank my primary supervisor, Professor Jocelyn Monroe, for giving me the opportunity to fulfil a childhood dream of becoming a physicist! I had a wonderful PhD experience and her guidance and encouragement have been invaluable. I would like to thank my secondary supervisor, Dr. Alexander Deisting, for having the patience of a saint and guiding me step by step through challenges I was too afraid to face.

The PlomBOX collaborators, *mis hermanos y hermanas*, have been truly wonderful and it was a pleasure to work with all of them, specially Dr. Yami Gándola, Maca Alvarez, Silvina Gutierrez, Melissa Tallis, Dr Francisco Favela and Dr. Jaime Guerra.

I had a great amount of support from the Physics Department at Royal Holloway. Thank you to Dr. Grégoire Ithier for giving me so much constructive criticism and invaluable advice during our annual reviews. In particular, thank you Ian Murray and Dr. Siobhan Alden for letting me hide in the back of your office like a hermit for my final year. Thank you for all the coffee (chai latte) runs, the chats and support I received from both of you. I am grateful to all my peers from the Dark Matter office and for all the bad tennis and badminton matches we had. Everyone at the mechanical (Richard's Team) and electrical (Tom Crane) workshop was so accommodating and kind every time I went there with my complicated requests. Thank you to Gill for being so dedicated to all of us and ensuring my PhD ran smoothly.

This project also gave me the opportunity to peek into the Biology Department at Royal Holloway. Thank you to Dr. Paul Devlin for his never ending kindness and for allowing me to use his lab to conduct my (not always successful) experiments. Thank you to Declan as well for giving me tips on how to be a better honorary biologist in the lab.

Thank you Mary, the massage therapist at Royal Holloway, for helping me stay healthy and for being such a good listener.

I also have to thank Glenn and Matt, for being so supportive and not considering me mad for leaving a stable job to pursue further education.

Beyond my professional support I also extend my thanks to my friends. To Josh, Rafa, Michael, Hannah, James (the cat), Ashe, Jack, Eleni, Mark, Teresa, Isabel, Carlos and Gaspar, all in different timezones, for keeping me sane and smiling through it all. To Claire and Chris for being so supportive and also highlighting all the unnecessary extra commas I had in my thesis.

I must thank my family, my parents Carlos and Odete, my brother Bruno, my sister-in-law Inês, my auntie Tia Bia and my cousin Quiqui for all the love and support through all these years and for letting me *study dolphins.* A super super special thank you to my gorgeous nieces, Maria and Beatriz, for being the best nieces in the world and giving me so much joy.

My final thanks (and the most important ones) go to my partner Rebecca, my universal constant, for being there for me everyday, good or bad, and for being the most supportive partner.

Abstract

This thesis reports on the development of a novel device, called PlomBOX, employing a CMOS sensor and lead-sensing bacteria to assay lead in drinking water, up to the World Health Organisation (WHO)'s upper limit of 10 ppb. As a first step, a scientific CMOS was used to demonstrate the capability of detecting gamma energies in an Si detector from a lead-210 (^{210}Pb) sample through calorimetry methods. While this technique is promising for dosimetry applications, it is not able to reach the WHO level in sensitivity. A second step was to explore how the sensitivity range of any device could be improved by increasing the concentration of the substance of interest in a sample. Lead doped water samples were boiled to explore if an increase in heavy metal concentration was observed. This technique was able to retain $99 \pm 9\,\%$ of ^{210}Pb, allowing for an increase of its concentration. The third step involved the development of the PlomBOX. The project followed three development paths: a) Certain bacteria can change colour when in the presence of lead. A genetically modified strain of *Escherichia coli* sensitive to lead concentrations up to 10 ppb was developed together with a team of biologists. This constitutes the biosensor that emits colour in proportion to the presence of lead. b) Bacteria response is imaged using a microprocessor (ESP32) with a camera module. This constitutes the optical metrology component of the PlomBOX. c) Data acquisition and control of the PlomBOX is achieved through a Bluetooth connection with the PlomApp, a custom-developed mobile phone application. Data are sent from the PlomApp to a database where a bespoke automated analysis software provides a result of the lead concentration in a sample of water. A full description of the experimental set up and analysis software is provided and results of the first *in situ* assay are discussed.

Contents

List of Figures

List of Tables

Acronyms

A mass number

ABS Acrylonitrile Butadiene Styrene

ADC analogue-to-digital converter

ADU Analogue-to-Digital

AEC automatic exposure control

APS active pixel sensors

AQC Analytical Quality Control

ATP adenosine triphosphate

B blue

BEGe Broad Energy Germanium

BLC Blood Lead Concentration

BLE Bluetooth Low Energy

BLL blood lead levels

BUGS Boulby Underground Germanium Suite

CDC Centers for Disease Control and Prevention

CdTe Cadmium Telluride

CI confidence interval

CL Confidence Level

CMOS Complementary Metal-Oxide-Semiconductor

SARS-CoV-2 severe acute respiratory syndrome Coronavirus 2

DAQ Data Acquisition

DEAP-3600 Dark matter Experiment using Argon Pulse-shape discrimination

DM Dark Matter

DNA Deoxyribonucleic acid

DWTS Drinking Water Testing Specification

E. coli *Escherichia coli*

FITS Flexible Image Transport System

FN false negative

FP false positive

FWHM Full Width at Half Maximum

G green

GPS Global Positioning System

HPGe High Purity Germanium Detectors

HSV Hue Saturation and Value

HTiO Hydrous Titanium Oxide

ICP-MS Inductively Coupled Plasma Mass Spectrometry

$I_{\mathbf{diff}}$ diffusion current

$I_{\mathbf{drift}}$ drift current

IF UNAM Institute of Physics of the National Autonomous University of Mexico

INA National Institute of Water

JPEG Joint Photographic Experts Group

JSON JavaScript Object Notation

JUNO Jiangmen Underground Neutrino Observatory

LB Luria-Bertani

LED light emitting diodes

LFA lateral flow assays

LL lower limits

LOD limit of detection

MC Monte Carlo

MQTT Message Queuing Telemetry Transport

NaI(TI) Sodium Iodide

Neo sCMOS Oxford Instruments Neo 5.5 CMOS

OS operating system

PCB Printed Circuit Board

PLA polylactic acid

PMT photomultiplier tubes

ppb parts per billion

PPS passive pixel sensors

QE Quantum Efficiency

R red

RF radio frequencies

RGB Red Green Blue

RHUL Royal Holloway University of London

RNA Ribonucleic acid

ROI region of interest

ROIs regions of interest

RS row selecting

% RSD relative standard deviation

sfGFP Superfolder Green Fluorescent Protein

SNO Sudbury Neutrino Observatory

SQL Structured Query Language

TEL tetraethylene lead

TLS Transport Layer Security

TN true negative

TP true positive

UK United Kingdom

UKAS United Kingdom Accreditation Service

UNAM	National Autonomous University of Mexico
UPW	ultrapure water
USA	United States of America
UUID	Universally Unique ID
UV	ultraviolet
WHO	World Health Organisation
WIMP	weakly interacting massive particles
YSI	Yellow Spring Instruments
Z	atomic number

Chapter 1

Introduction

Rare event searches in particle physics address some of the most fundamental open questions in science today, such as the search for Dark Matter (DM) particles. Due to the low probability of DM interactions, these detectors require high sensitivities and an understanding of the background signal is necessary. Lead-210, an unstable radioactive isotope of lead, is an example of an isotope whose presence can affect background measurements. Techniques have been developed to detect it at high sensitivities. These techniques could in principal be applied for lead detection in fields unrelated to particle physics. Lead is toxic for human consumption and the development of environmental detection techniques should be explored.

This chapter details the motivations and state of the art methods for lead monitoring and proposes a new innovative detector to measure quantities of lead in drinking water.

1.1 Motivation

Lead is a heavy metal that has been used by humans since at least 7000-6500 BCE [1]. Throughout history, lead has been utilised by many civilisations for different purposes: Ancient Egyptians used lead in fishing, by applying sinkers to fishing nets, enamels, glasses [2]; in the Fertile Crescent region, civilisations used lead as coins [3] and construction material [2]; and in Ancient China lead was used in royal courts as currency [4] and as a stimulant [2]. It was with the Roman Empire and its development of lead mining that lead usage increased, as it became the greatest producer of lead during this period, reaching an output peak of 80 000 t per year [5]. Lead was used in medicine, currency, warfare, roofing [6] and chiefly in water utility infrastructure [1], due to a low melting point of 600.71 K [7], ductility and inertness to oxidation [1].

The first time lead production rates exceeded those of the Roman Empire occurred during the Industrial Revolution, beginning in the second half on the 18th century [5]. During this period, lead was necessary for plumbing and lead paints [8].

With the increase of lead usage and mining came reports of the health hazards associated with lead. In the 2nd century BC, people who had acute effects associated with high-dose exposure were described as suffering from colic and paralysis by the Greek botanist Nicander of Colophon [8, 9]. During the Renaissance period, it is postulated that the greatest exposure to lead was experienced by painters, due to their use of lead-based colours [8]. In the 17th century, many physicians advised on the hazards of handling lead: "Transactions of the Royal Society of England" published several articles regarding the risks of the manufacturing of white lead and glass [8] and physician Bernardino Ramazzini inferred that all the lead processing techniques used by craftsmen were dangerous [10].

In this period, several outbreaks of saturnine colic appeared in some European areas. During this time, wine preservatives derived from the Ancient Rome's *sapa* (lead acetate used to sweeten wine [11]) were still in use. Doctor Eberhard Gockel deduced that the lead levels in wine were responsible for the saturnine colic outbreaks observed. This was the first instance in which exposure to lead was presumed to happen across the general population and not just craftsmen and manufacturers [12].

In the 19th century, the mechanisms of lead poisoning through dietary intake became understood [8]. During the Industrial Revolution, there was an increase of workers suffering from lead poisoning, due to its intensive use in manufacturing systems [8]. Several physicians took an interest in these workers' symptoms: Louis Tanquerel des Planches detailed the signs and symptoms of chronic lead intoxication [13] and Sir Alfred Baring Garrod postulated a direct link between lead poisoning and gout [14]. With this knowledge, attempts began to replace or remove harmful agents, like lead, from the manufacturing cycle [15].

In the beginning of the 20th century, some governments began to produce legislation to reduce the concentration of lead in paint [8]. This happened after it was identified that Australian children presented high blood lead levels (BLL) and lead poisoning and it was deduced that this was caused by lead paint present in their houses [16]. In the mid 20th century, the first preventative strategies were introduced in factories, which involved the use of personal protective equipment, ventilation, wetting of dusty processes and the abolition of the use of lead [8]. In late 20th century it was understood that the tetraethylene lead (TEL) that was added to gasoline, to create more powerful engines, caused environmental pollution and was hazardous to the general population [8]. In the last two decades of the 20th century TEL was replaced with benzene and a reduction of BLLs by half was reported in the general population [11].

To date, there is no confirmed biological role for lead [17]. Lead produces nefarious effects on the human body: it interferes with enzymes that help produce vitamin D and maintain the integrity of cell membranes [18] and it damages cells structures, including DNA [19]. Lead also interferes with the development of the brain and the nervous system in children, who are therefore considered to be more at risk of lead poisoning than adults [20].

The WHO has identified lead as one of ten chemicals of major public concern [17] and has set an upper limit of 0.01 mg/l (10 ppb - parts per billion) for lead in drinking water [21], although there is no level of exposure that does not cause harmful effects [17]. The WHO has determined that most occurrences of lead in drinking-water arise from lead service connections and plumbing [21], although it can occur in small rural water systems, which include private wells and hand pumps [22].

Despite all progress shown previously regarding awareness and understanding of the hazards of lead poisoning, in 2019, according to the institute for Health Metrics and Evaluation, 900 000 people died from lead exposure [17]. In the United States of America (USA), the Centers for Disease Control and Prevention (CDC) determined that in 2018, 87 144 children had confirmed BLL $\geq$ 5 µg/dl, or 50 ppb [23]. In the United Kingdom (UK), Public Health England estimated that 213 702 children aged between 0 and 19 years had a Blood Lead Concentration (BLC) $\geq$ 5 µg/dl [24]. Low and middle income countries are mostly at risk from lead exposure, with an estimated 26 million people being affected globally [25]. People in these countries are exposed to lead via recycling of used lead-acid batteries, lead mining, metal smelting and production [25].

In the UK, lead screening tests are carried out in both public and private water supplies [26]. In public water supplies samples are collected at water treatment facilities, service reservoirs, water supply points, etc. In private water supplies samples are collected at the point of use. These samples are analysed by laboratories which are accredited by the United Kingdom Accreditation Service (UKAS) and the Drinking Water Testing Specification (DWTS). Their analysis is done using ICP-MS [27] – this method is explained in Section 1.6.

In low and middle income countries access to accredited laboratories is more limited and possibly expensive - a new ICP-MS device can cost between 50 000 \$ and 500 000 \$ [28]. In sub-Saharan African countries, more than 400 million people rely on groundwater for their water supply, and 184 million use hand pumps in rural locations [29, 30]. These rural systems are monitored infrequently and laboratory capacity is limited [22].

Ergo, there is a demand to develop new and improved methods in environmental monitoring with sensitivities comparable to ICP-MS devices that are portable, low-cost and rapid. Biosensor technology has become more cost-effective and capable of delivering fast *in situ* results with increased sensitivities reaching 0.9 pM (picomolar), or 1.86×10^{-4} ppb [31]. Detecting such small levels of contamination is a challenge that is common in DM experiments, which must assay detector components for trace radioactivity at a level of 1×10^{-8} ppb of ^{210}Pb, in the presence of a background of natural radioactivity [32].

This thesis research combines these two approaches with the aim of developing a low-cost sensor for lead in drinking water.

In this chapter, Section 1.2 introduces the lead isotopes (stable and unstable) present on the Earth's crust; Section 1.3 and 1.4 describe different methods of radiation emission and how they interact with matter; Section 1.5 outlines how lead assays are done in DM experiments to characterise radioactive traces in backgrounds; Section 1.6 describes the current methodology used by water suppliers in the UK to assay lead in drinking water; Section 1.7 illustrates the historical developments of biosensor technology, highlights its main defining features and depicts the latest research on biosensor technology for the assay of lead in drinking water; Section 1.8 outlines how lead interacts with bacteria; and Section 1.9 describes the goals and innovative characteristics of this project compared with present research.

1.2 Isotopes of lead

On Earth, lead is found in the mineral galena, PbS, which is present in zinc ores [33], and combined with sulphur [34]. Lead is rarely found in its metallic form [33]. It has an abundance of 14 ppm on the Earth's crust, with 4 820 000 t having been extracted in 2016 [35].

Naturally occurring lead contains four stable isotopes,^{204}Pb, ^{206}Pb, ^{207}Pb and ^{208}Pb [36], and trace amounts of five radioisotopes: ^{209}Pb, ^{210}Pb, ^{211}Pb, ^{212}Pb, ^{214}Pb [37].

1.2.1 Stable lead isotopes

Lead-204 is a primordial nuclide - it has existed in its current form prior to Earth's formation and is present in the Earth's crust [38]. ^{206}Pb, ^{207}Pb and ^{208}Pb are radiogenic nuclides, produced in radioactive decays [39]. They are the end product of three decay chains: the uranium series (starting with ^{238}U – Figure 1.1a), the actinium series (starting with ^{235}U – Figure 1.1b) and the thorium series (starting with ^{232}Th – Figure 1.1c) respectively [40–42].

These exist on Earth with the abundances shown in Table 1.1.

Isotope	Abundance
^{204}Pb	1.4 %
^{206}Pb	24.1 %
^{207}Pb	22.1 %
^{208}Pb	52.4 %

Table 1.1: Abundances of stable lead isotopes [36]

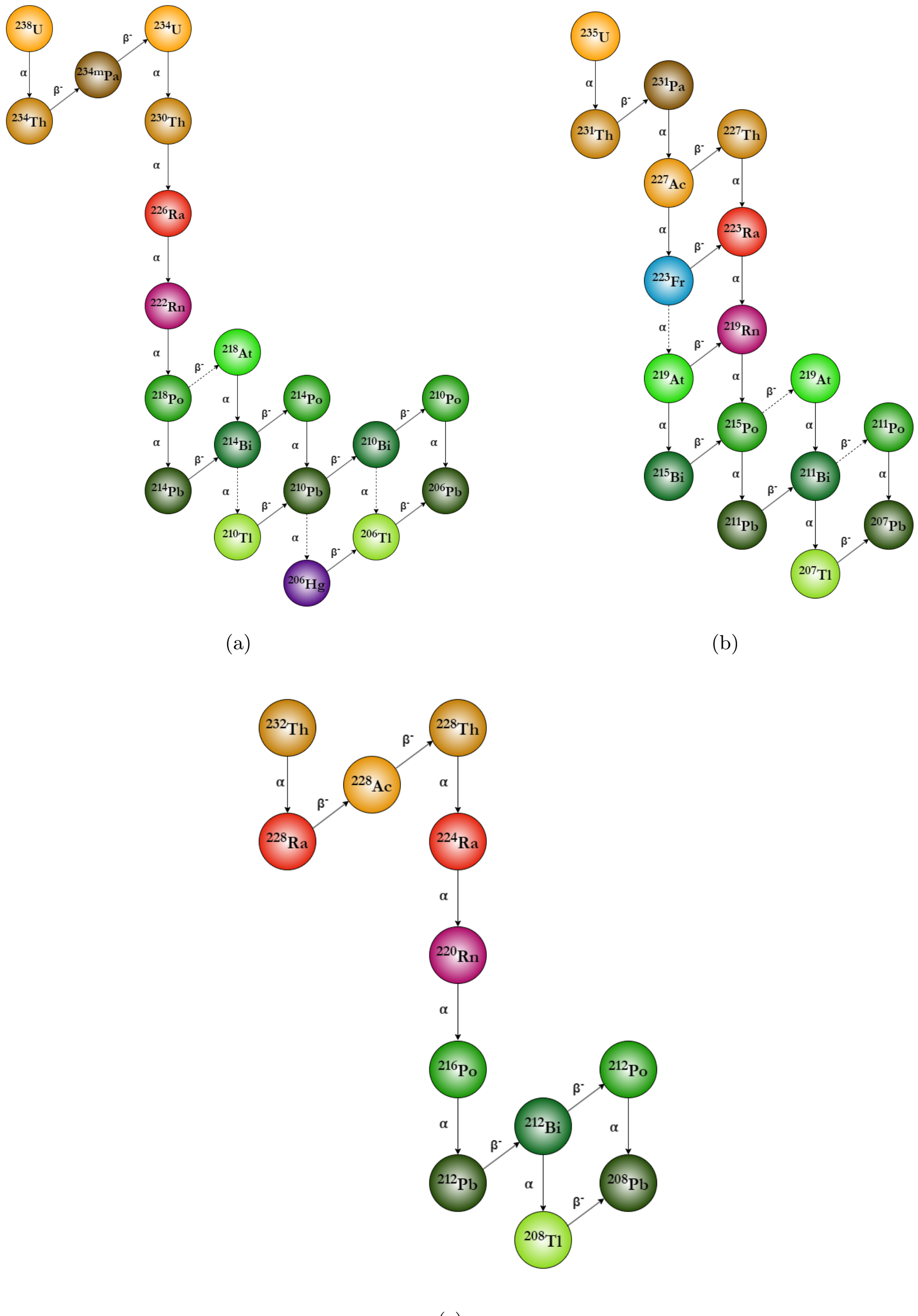

(a)

(b)

(c)

Figure 1.1: 1.1a Uranium series; 1.1b Actinium series; 1.1c Thorium series [40–42]. These series progress downwards with decreasing Z and A.

1.2.2 Unstable lead isotopes

All the unstable lead isotopes exist on Earth in trace amounts. ^{209}Pb is produced from the decay chain of ^{237}Np [43]. ^{211}Pb, ^{212}Pb are present in the actinium series and the thorium series, respectively. ^{210}Pb and ^{214}Pb are present in the uranium series, thus traces of these isotopes are found naturally. Table 1.2 shows the half-lives and decay modes of these unstable lead isotopes.

Lead-210 is of particular interest for the work in this thesis as it can occur in trace amounts with stable lead. Methods to assay this isotope are described in Section 1.5 and further in Chapter 3.

Lead-210 decays with 84 % probability via β^- decay resulting in an excited state of ^{210}Bi, whilst emitting an electron with an average decay energy of 4.16 keV. The nucleus de-excites by emitting a γ of 46.5 keV with a 4 % yield per decay. The de-excitation is accompanied by the emission of X-rays from approximately 9 keV to 16 keV with a yield of 22 % per decay. The second most probable decay (16 %) is a β^- decay with an electron mean energy of 16.2 keV to ^{210}Bi in the ground state [44].

This lead isotope can occur in trace amounts with stable lead, because it is a precursor of ^{206}Pb in the Uranium decay series - see Figure 1.1a. Measurements in [45] show a range of 3.9×10^{-8} ppb to 2.4×10^{-5} ppb for the fraction of ^{206}Pb in stable lead samples.

Assaying ^{210}Pb at trace levels is of particular interest to geologists, because it can be used to date sediment layers up to 100 yr [46]; in environmental science, to assess pollution levels [47]; and in rare event searches, since radioactivity in materials contributes backgrounds to, for example, DM searches [48].

Isotope	Isotope Half-Life	Decay Mode	Decay Product
^{209}Pb	3.253 ± 0.014 h	β^-	^{209}Bi
^{210}Pb	22.20 ± 0.22 y	β^-	^{210}Bi
^{211}Pb	36.1 ± 0.2 min	β^-	^{211}Bi
^{212}Pb	10.64 ± 0.01 h	β^-	^{212}Bi
^{214}Pb	26.8 ± 0.9 min	β^-	^{214}Bi

Table 1.2: Unstable isotopes of lead [36]

1.3 Radioactive decays and de-excitations

Before discussing how ^{210}Pb is assayed, it is important to understand how emissions from nuclear processes occur and how the resulting decay radiation interacts with matter (see Section 1.4).

Nuclear decays can be divided into three categories: α, β and γ decays [49].

1.3.1 Alpha decays

Heavy nuclei with an Z greater than 82 are energetically unstable and can spontaneously emit α particles, which are helium nuclei - ${}^{4}_{2}$He [49]. The decay process can be written as [50]:

$$ {}^{\mathrm{A}}_{\mathrm{Z}}X \rightarrow {}^{\mathrm{A-4}}_{\mathrm{Z-2}} Y + {}^{4}_{2}\,\alpha \tag{1.1}$$

Here, X and Y are the initial and final nuclear species, respectively and A is the species' mass number. Each decay between the initial and final nucleus has a fixed characteristic energy or Q-value. The decay energy is split between the alpha particle and the recoil nucleus, Y. The energy of the alpha particle is given by $\frac{Q(A-4)}{A}$ [50], with a range between 4 and 10 MeV [49].

1.3.2 Beta decays

Beta decays are the spontaneous emission or absorption of an electron or a positron by a nucleus [49]. β decays can occur via electron emission, positron emission or electron capture [49]. The β^- (electron) decay process can be written as [51]:

$$ {}^{\mathrm{A}}_{\mathrm{Z}}X \rightarrow {}^{\mathrm{A}}_{\mathrm{Z+1}} Y + \beta^- + \overline{\nu_e} \tag{1.2}$$

X and Y are again the initial and final nuclear species respectively, and $\overline{\nu_e}$ is an electron antineutrino. A neutron is converted into a proton, and emits an electron in the process.

The β^+ (positron) decay occurs as follows [52]:

$$ {}^{\mathrm{A}}_{\mathrm{Z}}X \rightarrow {}^{\mathrm{A}}_{\mathrm{Z-1}} Y + \beta^+ + \nu_e \tag{1.3}$$

Here, ν_e is an electron neutrino and a positron is emitted by the nucleus following the conversion of a proton into a neutron.

For electron capture, the nucleus absorbs an orbital electron, and a proton is converted into a neutron [52]:

$$ {}^{\mathrm{A}}_{\mathrm{Z}}X + e^- \rightarrow {}^{\mathrm{A}}_{\mathrm{Z-1}} Y + \nu_e \tag{1.4}$$

Y recoils with a small recoil energy, normally below the ionisation threshold, and thus cannot be detected by conventional means [51].

The majority of β decays populate an excited state of Y, resulting in the emission of de-excitation γ rays together with an electron and an antineutrino, for β^- emission, or a positron and a neutrino, for β^+ emission.

Analogous to α decays, β decays have a fixed decay energy or Q-value. As the recoil energy of Y is ~ 0, the decay energy is divided between the electron and the antineutrino for β^- decay, the positron and neutrino for β^+ decay and the neutrino only, for electron capture. The energy of the electron/positron/neutrino can vary between decays, with a range from 0 to the *beta endpoint energy*, which is equal to the Q-value. β decay energies are typically below 1 MeV [49].

1.3.3 Gamma decays

Gamma radiation is emitted when excited nuclei transition to lower energy levels. Due to nuclear excited states having energy differences greater than 10^{-3}MeV, γ ray energy will be greater than this value [49].

When γ radiation is emitted following a β decay, the γ ray has an energy equal to the difference between the initial and final nuclear states X and Y. The γ rays will have a half-life characteristic of the X electron decay, with an energy that reflects the energy level structure of Y [51].

The β decay of X can exhibit various probabilities for de-excitation transitions, called *branching ratios*. For each transition, the number of γ ray photons emitted can be deduced.

Gamma decays can occur via internal conversion. In this process, an excited nuclear state de-excites and interacts with an orbital electron, ejecting it [52]. The nuclear excitation energy E_{ex} transferred directly to the electron will have an energy E_{e^-}:

$$E_{e^-} = E_{\text{ex}} - E_{\text{b}} \tag{1.5}$$

where E_{b} is the original binding energy in the electron shell. γ decay energies are typically above 100 keV [53].

1.3.3.1 X-rays

Atoms can exist in an excited state for a short period of time if their orbital atoms are disrupted from their normal configuration by some excitation process. Electrons tend to rearrange themselves and return the atom to a ground state in a nanosecond or less, for solid materials [51]. When the atom transitions from an excited state to a lower energy state, the energy is released in the form of a characteristic X-ray photon, with its energy being equal to the difference between X and Y. For example, if a space is created in the K shell of an atom (the closest electron shell to the nucleus), then a characteristic K Shell X-ray is emitted when the space is subsequently filled.

In the electron capture process mentioned in Section 1.3.2, the capture of an orbital electron from the K-shell will leave a vacancy. When the vacancy is filled, X-rays are emitted with an energy characteristic of the daughter element Y. This decay may populate the ground state or an excited state, in the daughter nucleus, and the characteristic X-rays can be accompanied by γ rays from subsequent nuclear de-excitation.

In internal conversion, K Shell X-rays are emitted along with the ejected electron. Radioactive sources of this type emit γ rays in addition to the characteristic X-rays, because γ ray de-excitation of the nuclear state is always a competing process to internal conversion.

Electron capture and internal conversion describe methods of excitation of an atom by radioactive decay. Additionally, atoms can be excited by external radiation. In this process, an external source of radiation (X-rays, γ rays, electrons, α particles) strikes a target, creating excited or ionised atoms in the target. When the excited atoms or ions de-excite to a ground state, they emit characteristic X-rays and the target is a localised source of X-rays. X-rays decay with energies between 100 eV to 100 keV [53].

1.3.3.2 ***Auger-Meitner*** electrons

This process is analogous to internal conversion when the excitation energy originates in the electron cloud of the atom rather than in the nucleus. A preceding process may leave the atom with a vacancy in an electron shell that would otherwise be complete. The vacancy can be filled with an electron from the outer shells with the emission of a characteristic X-ray photon. Alternatively, the excitation energy of the atom can be transferred to one or more of the outer electrons, which are ejected from the atom.

1.4 Particle interactions with matter

1.4.1 Interaction of alpha particles with matter

When an α particle interacts with a medium, the interaction leads to the particle's energy loss via ionisation or excitation of the atoms in the medium [54].

This interaction happens simultaneously with many electrons and the α particle's energy transfer can be sufficient to raise the electrons to a higher-lying energy level in the atoms, causing excitation, or high enough to remove the electron from the atom, causing ionisation. The momentum of the α particle will be reduced due to the energy that is transferred to the electrons. The maximum energy that can be transferred by an α particle of mass m, with kinetic energy E, to an electron of mass m_e in a single collision is $\frac{4Em_e}{m}$ [51]. This is a small fraction of the α particle's total energy and the particle will lose energy in similar interactions as it passes through the interacting medium. Its momentum will become zero after interacting with many electrons.

The linear stopping power S of an α particle is given by the differential energy loss within the material, divided by the corresponding differential path length [51, 54]:

$$S = -\frac{\mathrm{d}E}{\mathrm{d}x} = \frac{4\pi e^4 z^2}{m_0 \nu^2} NZ \left[\ln \frac{2 m_0 \nu^2}{I} - \ln\left(1 - \frac{\nu^2}{c^2}\right) - \frac{\nu^2}{c^2} \right] \tag{1.6}$$

Here, ν and z are the velocity and charge of the α particle, N is the number density of the atoms in the interacting medium, e is the electronic charge, m_0 is the electron rest mass, E is the energy of the α particle, I is the average excitation and ionisation potential of the atoms and c is the speed of light.

Table 1.3 shows the range of α particles for different elements and H_2O, assuming the particle has an energy of 4 MeV.

Element	Range (cm)	Stopping Power ($\mathrm{MeV} \cdot \mathrm{cm}^2/\mathrm{g}$)
Silicon	1.781×10^{-3}	7.137×10^2
Germanium	1.37×10^{-3}	4.533×10^2
Lead	0.11×10^{-2}	2.586×10^2
H_2O	2.72×10^{-3}	1.035×10^3

Table 1.3: Table showing the ranges of an α particle with an energy of 4 MeV for different elements and H_2O [55].

1.4.2 Interaction of beta particles with matter

Upon interaction with matter, β particles (electrons and positrons) lose their energy in two processes: ionisation at low energies and via Bremsstrahlung processes at energies above the critical energy E_c, when the two types of energy loss are equal [54, 56].

Bremsstrahlung radiation refers to the phenomena when β particles (or other charged particles) interact with matter and part of their energy is converted into electromagnetic radiation, resulting in photon emission in the X-ray energy range [49]. The amount of electron energy that is converted into Bremsstrahlung rises with increasing electron energy and is greatest for absorbing materials of high Z.

Unlike α particles, the β particle's path shows large deviations because its mass is equal to the mass of orbital electrons and a larger fraction of its energy can be lost in a single interaction. Additionally, electron-nucleus interactions can occur which change the electron direction [51].

The stopping power from ionisation processes is given by [51]:

$$\left(\frac{\mathrm{d}E}{\mathrm{d}x}\right)_\mathrm{c} = \frac{2\pi e^4 NZ}{m_e \nu^2} \left(\ln \frac{m_e \nu^2 E}{2I^2 (1 - \frac{\nu}{c}^2)} - (\ln 2)\left(2\sqrt{1 - \frac{\nu}{c}^2} - 1 + \frac{\nu}{c}^2 \right) + \left(1 - \frac{\nu}{c}^2\right) + \frac{1}{8}\left(1 - \sqrt{1 - \frac{\nu}{c}^2}\right)^2 \right) \tag{1.7}$$

Here, ν is the velocity of the β particle, N is the number density of the atoms in the interacting medium, e is the electronic charge, E is the energy of the β particle, I is the average excitation and ionisation potential of the atoms and c is the speed of light.

For Bremsstrahlung processes the stopping power is given by [51]:

$$\left(\frac{\mathrm{d}E}{\mathrm{d}x}\right)_{\mathrm{r}} = \frac{NEZ(Z+1)e^4}{137m_e^2c^4}\left(4\ln\frac{2E}{m_ec^2}-\frac{4}{3}\right) \tag{1.8}$$

The total linear stopping power $\frac{\mathrm{d}E}{\mathrm{d}x}$ will be a combination of energy loss via the Bremsstrahlung process and the ionisation and excitation of the interacting medium:

$$\frac{\mathrm{d}E}{\mathrm{d}x} = \left(\frac{\mathrm{d}E}{\mathrm{d}x}\right)_{\mathrm{c}} + \left(\frac{\mathrm{d}E}{\mathrm{d}x}\right)_{\mathrm{r}} \tag{1.9}$$

The ratio of the specific energy losses is given by:

$$\frac{\left(\frac{\mathrm{d}E}{\mathrm{d}x}\right)_{\mathrm{c}}}{\left(\frac{\mathrm{d}E}{\mathrm{d}x}\right)_{\mathrm{r}}} \cong \frac{E\cdot Z}{700} \tag{1.10}$$

where E is shown in units of MeV. The energies of the electrons are less than a few MeV, therefore the contribution of radiative losses is a small fraction of the contribution of losses from ionisation and excitation, and they only become significant in interacting media with large Z [51].

Table 1.4 shows the range of β particles for different elements and H_2O, assuming the particle has an energy of 1 MeV.

Element	Range (cm)	Stopping Power ($\mathrm{MeV}\cdot\mathrm{cm}^2/\mathrm{g}$)
Silicon	0.23	1.531
Germanium	0.12	1.283
Lead	0.07	1.123
H_2O	0.44	1.862

Table 1.4: Table showing the ranges of electrons with an energy of 1 MeV for different elements and H_2O [55].

1.4.3 Interaction of gamma rays with matter

There are three interaction mechanisms of photons (X-rays and γ rays) with matter that are important in radiation measurements: photoelectric absorption, Compton/Rayleigh scattering and pair production. These processes lead to partial or complete transfer of photon energy to electron energy. Contrary to α and β decays addressed earlier, photons are absorbed or scattered.

Figure 1.2 summarises the dominance of each process for different photon energies, for lead. It shows the cross section σ i.e. the probability of a photon interacting with the atom, for the Compton and Rayleigh scattering (σ_{s}), the photoelectric effect (σ_{PE}) and pair production (σ_{PR}). For lead, the photoelectric effect will be dominant for energies $< 5\times10^5$ eV, Compton and Rayleigh scattering will be present for energies between 5×10^5 eV and 5×10^6 eV and pair production for energies above 5×10^6 eV [49].

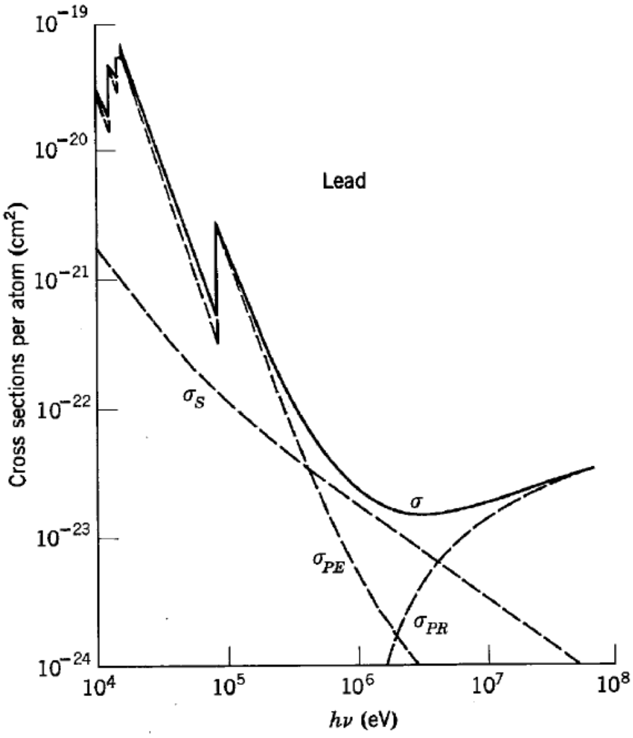

Figure 1.2: Cross sections for Compton and Rayleigh scattering (σ_S), photoelectric effect (σ_PE) and pair production (σ_PR), with respect to energy $h\nu$ in eV, for a lead atom. σ is the total cross section [49].

1.4.3.1 Photo electric absorption

This process dominates at low energies [54]. A photon undergoes an interaction with an atom in the interacting medium and is absorbed. In its place there will be an energetic photo-electron that is ejected from one of the atom's shells. If the photon has sufficient energy, the photo-electron will be ejected from the K-Shell. The photo-electron will have the following energy E_{e^-}:

$$\mathrm{E}_{e^-} = h\nu - \mathrm{E_b} \tag{1.11}$$

where E_b is the binding energy of the photo-electron to its original shell and $h\nu$ is the energy of the photon.

1.4.3.2 Compton and Rayleigh scattering

This interaction takes place between the incident γ ray photon and an electron in the interacting medium. It occurs more often for γ ray energies typical of radioisotope sources [51].

The photon is deflected by an angle θ with respect to its original direction and it transfers some of its energy to a recoil electron, changing the photon's frequency and wavelength [49]. The energy transferred to the electron can vary from zero to a large fraction of the photon's original energy.

The relation between the transferred energy and the scattering angle is given by:

$$h\nu' = \frac{h\nu}{1 + \frac{h\nu}{m_e c^2}(1 - \cos\theta)} \tag{1.12}$$

where $m_e c^2$ is the rest-mass energy of the electron (0.510 MeV) [57]. Low amounts of energy are transferred for small scattering angles θ. Some of the original energy is always retained by the incident photon.

In the event that the recoil electron remains bound to the atom after the collision, the photon's wavelength will not change, and this is the Rayleigh scattering process [49]. Rayleigh scattering will be the dominant process for photon energies below X-ray values. For X-ray and γ ray energies, Compton scattering will be the dominant process [49].

1.4.3.3 Pair production

Pair production occurs when the γ ray energy exceeds twice the rest mass of an electron, 1.02 MeV [51]. The probability of this interaction is very low until the γ ray energy approaches several MeV i.e. this interaction happens with high-energy γ rays.

The photon is absorbed, producing an electron-positron pair. All the photon energy, excluding the 1.02 MeV necessary to create the pair, will be kinetic energy shared by the electron and the positron. The positron will annihilate after slowing down in the interacting medium and two annihilation photons are produced as secondary products of the interaction.

1.5 Lead assay procedures in particle physics

In the Uranium series (Figure 1.1a) ^{226}Ra decays into the noble gas ^{222}Rn, which has a half life of 3.8 d [32]. ^{226}Ra can diffuse out of the Earth's crust, where it is formed, and contaminate surfaces through diffusion and deposition [32]. ^{226}Ra can be deposited in acrylic during its casting process, which is used in Neutrino and DM experiments, and can therefore contribute to background events [32]. As these experiments operate with rare events, background events can be mistaken with the detector's signal; therefore, all sources of background need to be studied and measured [58]. ^{226}Ra decays to ^{210}Pb, which has a half life of 22.20 ± 0.22 y, as seen in Table 1.1.

In Particle Physics experiments, the detection of ^{210}Pb is done with radiometric methods such as β counting, α and γ spectroscopy [59].

- β Counting - this method measures the electrons emitted during the decay from ^{210}Bi to ^{210}Po. Gas-based detectors can measure the endpoint energy of the emitted electron (1.1 MeV) [32]. Detection limits of 6 mBq have been observed for this method [32]. Another method is the detection of the low energy electrons emitted during the ^{210}Pb decay with a liquid scintillator [32]. In [59] it is stated a detection limit of 33 mBq for liquid scintillation counting.

- α Spectrometry - an indirect measurement of the activity of ^{210}Pb is done by determining the activity of ^{210}Po. Semiconductor surface barriers or PIN diodes are used to detect the 5.4 MeV α emission of ^{210}Po [32]. This method provides a detection limit of 1 mBq [60].

- γ Spectroscopy - uses low-energy sensitive semiconductor detectors, such as HPGe, to directly detect the 46.5 keV γ [32]. A description of how HPGe detectors work is given in Chapter 4. This method has provided a detection limit of 172 mBq for ^{210}Pb. [61]

DEAP-3600 and SNO+ are two particle physics experiments that have limits on the concentrations of ^{210}Pb that can be found in their acrylic vessels. DEAP-3600 allows for up to 1.1×10^{-8} ppt (parts per trillion) of ^{210}Pb [58] and SNO+ allows for up to 4.5×10^{-13} g^{238}U/gH$_2$O (0.45 ppt of ^{238}U), which is the predecessor of ^{210}Pb in the uranium decay chain, as seen in Section 1.2.2 [62]. It is necessary to measure the radiopurity of the acrylic at such low concentrations and the next two sections describe ^{210}Pb measurement techniques that are capable of achieving this.

1.5.1 Radiopurity measurement of acrylic for DEAP-3600 experiment

DEAP-3600 is a DM experiment based in the SNOLAB, Canada. This detector is located 2 km underground at SNOLAB, to shield against cosmic muons. It comprises a liquid argon detector which is searching for weakly interacting massive particles (WIMP). The detector contains 3600 kg of liquid argon inside a 2 in thick acrylic vessel with an inner radius of 85 cm.

Reference [63] addresses surface backgrounds on the detector i.e. α decays from the surface of the vessel. All other potential sources of background have been studied. The acrylic contains trace levels of ^{238}U and ^{232}Th, although the collaboration was involved in the manufacturing process to ensure that the acrylic material was clean.

Monte Carlo simulations were developed to infer the maximum allowed concentrations of ^{238}U, ^{232}Th and ^{210}Pb, ensuring they do not affect WIMP detection and remain within the background budget. To detect the concentrations of these elements in the acrylic, an assay was made using a vaporisation technique that had been used by the Sudbury Neutrino Observatory (SNO). This technique was able to achieve 0.5 ppt sensitivity for ^{238}U and ^{232}Th [64]. 10 kg of the acrylic material was vaporised and its residue was collected by rinsing with heating acids. The ^{214}Pb and

^{212}Pb γ rays resulting from the ^{238}U and ^{232}Th decay chains were measured with an ultra low background HPGe detector. ^{210}Pb was measured by a well detector and by its ^{210}Po daughter, using an α counter.

The well detector showed a result of $(2 \pm 7) \times 10^{-19}$ g/g ^{210}Pb; ICP-MS returned a value of $(0.6 \pm 2.2) \times 10^{-19}$ g/g ^{210}Pb [58]; The α counter presented a value of $(0.8 \pm 2.1) \times 10^{-19}$ g/g ^{210}Pb [58]. All the results obtained were consistent with a level of 1×10^{-19} g/g ^{210}Pb, or 1×10^{-7} ppt [58].

1.5.2 Sensitive assay technique for ^{210}Pb in water for SNO+ experiment

The SNO+ experiment aims to search for neutrinoless double electron decay [65].

The detector consists of a 12 m diameter acrylic vessel containing the detector media. This vessel is surrounded by a steel structure with a 17 m diameter containing $\sim$ 9500 photomultiplier tubes (PMT).

The volume between the acrylic vessel and the steel structure is filled with 1700 t of ultrapure water (UPW) and the region between the steel structure and the cavity is filled with 5300 t of UPW. The UPW is used to shield the detector from radioactivity coming from the rock, PMTs, ropes and the steel structure [65]. Analogous to what was mentioned in Section 1.5.1, the main source of background for SNO+ is the radioactivity resulting from ^{238}U and ^{232}Th decay chains. The experiment requires very low radioactivity levels in the water. The SNO experiment developed a water assay technique, called Hydrous Titanium Oxide (HTiO) technique, to measure the amount of radium and thorium radioisotopes in the water regions [66]. This is an inorganic ion exchanger that can remove heavy metal ions, such as lead, thorium and radium, from water. HTiO adsorbent is deposited onto a pair of 1 m long filters. The loaded filters are connected to the water systems of the detector and radium is extracted. The radium in the filters is removed through elution (process in which the filters are washed with HNO_3). The HNO_3 eluate is further concentrated to a small sample volume and the radium present in it is counted with a liquid scintillation counter [66]. With this assay technique the following sensitivities were achieved: 4×10^{-16} gTh/gD2O for ^{232}Th and 3×10^{-16} gU/gD2O for ^{238}U for a 275 t heavy water assay in SNO [66].

When SNO was being constructed and during the transition from SNO to SNO+, ^{222}Ra daughter isotopes, such as ^{210}Pb, were embedded on the surface of detector materials. ^{210}Pb could contaminate the detector and increase its radioactivity levels, which would affect background measurements. Therefore, the SNO+ collaboration extended the HTiO technique to allow for measurements of ^{210}Pb to be made in the water [65]. The modified HTiO technique was able to increase its sensitivity to ^{210}Pb to $0.4 \pm 0.13\,\mathrm{mBq/m^3}$.

1.6 Assay methodology used by water suppliers in the UK

This section discusses the assay methodology used by Affinity Water Ltd, which is typical for UK suppliers. Affinity Water Ltd is the drinking water supplier to Royal Holloway University of London (RHUL).

Affinity Water Ltd has sampling teams located in Staines, Stevenage, Rickmansworth, Manningtree and Folkestone [67]. The analysis of the samples is carried out in the laboratory at Staines. This lab contains four departments: microbiology, cryptosporidium, organic chemistry and inorganic chemistry. Tests can be done for *cryptosporidium*, *E. coli*, cyanides, pesticides, algae and metals [68].

In 2018, Affinity Water Ltd carried out $\sim$ 180,000 tests on water leaving treatment works. Table 1.5 shows the lead values detected in 2021 in the water supply zone containing RHUL [69]. < 1.00 ppb was detected in the area.

Parameter	Units	Number of Samples	PCV	Minimum	Mean	Maximum
Lead	µgPb/l (ppb)	8	10	< 1.00	< 1.00	< 1.00

Table 1.5: Lead values detected in 2021 by Affinity Water Ltd in the Bagshot/Sunninghill water supply zone [69]. PCV stands for Prescribed Concentration or Value or Specification Concentration or Value.

To carry out assays of lead in surface, drinking and groundwater, Affinity Water uses ICP-MS devices. The methodology used references the Blue Book Method produced by the Standing Committee of Analysts [70]. The equipment has a limit of detection (LOD) of 31.25 µg/l and a relative standard deviation (% RSD) of 5.1 %, assuming the analysed water is hard [27, 71].

Prior to the ICP-MS analysis, the water samples are acidified with nitric acid to 1% v/v (1% of nitric acid in total sample volume) and oven digested at 80 ± 5 °C for a minimum of 6 h [27].

Figure 1.3 shows a diagram of an ICP-MS which illustrates how the device works and how samples are analysed by Affinity Water Ltd.

The liquid sample is pumped into a nebuliser where it is converted into an aerosol with argon gas - this is seen in Figure 1.3, labelled "spray chamber and nebuliser". The Blue Book Method recommends an Argon gas supply of high purity grade (minimum 99.996 %) [27]. The smaller droplets of the sample are separated from the larger ones and are transported into the plasma torch via a sample injector, seen in Figure 1.3 in the inductively coupled plasma section.

In the loaded coil segment, argon gas is contained within electric and magnetic fields at radio frequencies (RF). When an electron is introduced into this region, argon plasma is created. The electrons collide, with high energy, with argon atoms, producing an electron avalanche. This process continues with the electrons colliding with more argon atoms, resulting in a plasma containing argon

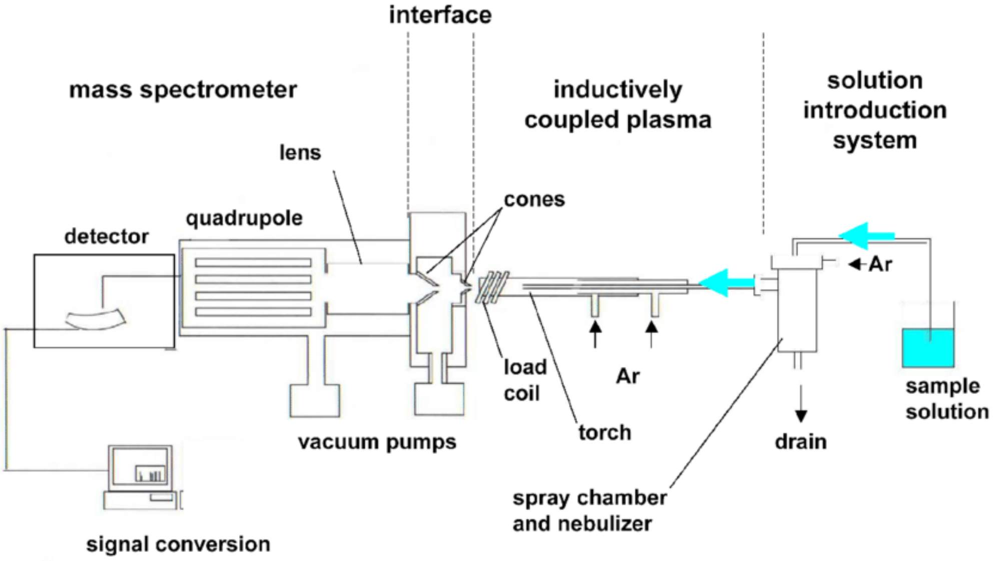

Figure 1.3: Diagram of an ICP-MS [72]. An explanation of how the detector works is shown in the text.

atoms, ions and electrons. The plasma has a high temperature >6000 K [27].

The ions that are produced in the plasma are directed to the mass spectrometer via the interface region, which is maintained in a vacuum. The ions are focused towards the mass separation device by an electrostatic lens system, which also eliminates photons and other particulates from reaching the detector [27].

The ion beam passes into the mass separation device, which is also kept at vacuum - seen in Figure 1.3 labelled as quadrupole. This mass separation device allows ions of a specific mass-to-charge ratio to pass through to the detection. All other ions are removed, ensuring that only one element is being measured.

The detectors used are electron multiplier detectors. The impact of ions releases an avalanche of electrons, which are amplified and turned into a measurable electrical signal.

The water samples are compared with blanks of deionised water and Analytical Quality Control (AQC) solutions, which are solutions that may include reference materials, certified reference materials, spiked samples, duplicates and blanks [27]. The blanks and AQC solutions undergo the same filtration and acidification procedures as the water samples of unknown lead concentrations. This ensures that any contamination that occurs during sampling or preparation is detected [27].

This assay method is reviewed by several individuals and organisations to ensure the procedure is reliable and robust [27].

1.7 Biosensor technology

This thesis develops a new method for lead assay in drinking water based on using biosensors in the detection process. Biosensor technology is used in food control, forensics, biomedical research and diagnosis, monitoring of progression and treatment of diseases, and environmental monitoring [73]. This section presents a brief historical overview and a general introduction to biosensors.

1.7.1 Characteristics of a biosensor

A biosensor is a device which measures chemical or biological reactions by generating a signal proportional to the concentration of the substance of interest in the reaction [73]. Biosensors contain several components [73], seen in Figure 1.4:

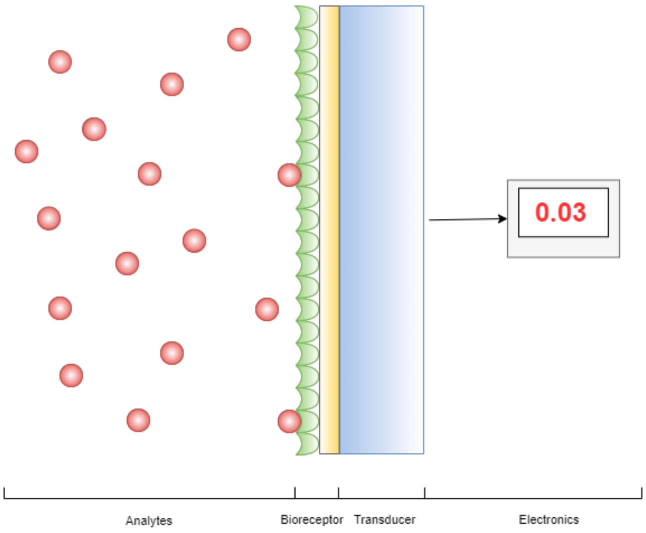

Figure 1.4: Diagram of a biosensor, showing its main components: analytes, bioreceptors, transducers and electronics.

- **Analytes** - the substance of interest in the reaction that needs to be detected. In the case of this project, the analyte will be lead.
- **Bioreceptors** - the molecule designed to recognise the analyte. These can be enzymes, nanoparticles, DNA, etc.
- **Transducers** - an element that converts one form of energy into another. In biosensors this entails converting one bio-recognition event (light or heat emission, pH or mass change) into a measurable signal, also referred to as signalisation. The most common measurable signals are optical or electrical, like photo diodes, thermistors, quartz electrodes, etc.
- **Electronics** - this element comprises signal amplifiers, processors and displays [74]. When the transducer signal is produced, the electronics process it by amplifying and converting

the signal from analogue to digital. The processed signals are quantified and shown in the display unit of the biosensor.

The key characteristics and the optimisation criteria for biosensors are the following: selectivity, reproducibility, stability, sensitivity and linearity [73]. Selectivity is the ability of a biosensor to detect a specific analyte when in the presence of contaminants and other substances. Reproducibility is the ability of a biosensor to produce identical responses to an analyte in several experimental set-ups. A biosensor exhibiting reproducible signals is considered reliable and robust. Stability is related to how susceptible the biosensor is to ambient disturbances surrounding it. Disturbances can affect the output signal of a biosensor and cause an error on the measured analyte concentration. Several factors can affect the stability of a biosensor: the transducer and electronics can be temperature sensitive, the degree to which the analyte can bind with the bioreceptor (i.e. the affinity of the bioreceptor) and the degradation of the bioreceptor over time. Sensitivity is the minimum amount of analyte that can be detected by a biosensor, referred to as LOD. In medical and environmental monitoring, concentrations of ng/ml or fg/ml are required. Linearity relates the measurements to a linear polynomial ($\mathrm{y} = \mathrm{mc}$). Here, y is the output signal, m is the sensitivity of the biosensor and c is the concentration of the analyte. The resolution of a biosensor relates the change in the response of a biosensor resultant from the change in concentration of an analyte.

1.7.2 Historical background

In 1906, M. Cremer laid the groundwork for biosensors, by demonstrating that the concentration of an acid placed in a liquid separated by a glass membrane was proportional to the electric potential between the liquid located in opposite sides of the membrane [75].

In 1956 Clark developed the Clark electrode for oxygen detection in blood during cardiopulmonary bypass surgery [76]. This lead to the development of the first biosensor in 1962, to measure glucose levels. To calibrate the Clark electrode, he deoxygenated test solutions by adding small amounts of the glucose oxidase enzyme and its substrate, glucose, which converted oxygen into hydrogen peroxide. Thus, the oxygen levels would decrease proportionally to the concentration of glucose in a solution [76].

In 1969, Guilbault and Montalvo developed the first potentiometric biosensor, which measures the potential difference between a working electrode and a reference electrode, to detect urea [77]. The potential of the working electrode is dependent on the concentration of the substance to be detected.

The first commercial biosensor was developed in 1975 by Yellow Spring Instruments (YSI), for glucose detection [78]. From 1975 to 1992, important developments occurred in biosensor technology, with the first microbe-based immunosensor being developed in 1975 [79], a fibre-optic biosensor for glucose detection developed in 1982 [80] and a handheld blood biosensor developed in 1992 [81].

Today, biosensors are used to monitor air, water and soil pollutants such as pesticides and toxins [82] and to detect pathogenic organisms [83]. Recently, biosensors have been embedded in face masks to detect severe acute respiratory syndrome Coronavirus 2 (SARS-CoV-2) [84]. Biosensor technology can be applied to applications in food analysis, such as the detection of gluten in beer and soy sauce [85]. Oncological biosensors have been developed to detect breast [86] and lung cancers [87].

Bioassays suffer limitations from high costs, long assay times, specialised hardware, high data variability, low specificity for distinct metals and ethical considerations [88]. However, new biosensors are becoming more cost effective, and are capable of delivering fast *in situ* results [88].

1.7.3 Biosensors to assay lead in drinking water

The following sections summarise two of the latest biosensor research for heavy metal and lead detection.

1.7.3.1 Paper-based microfluidic platform for detection of Pb^{+2} ions in a solution

Some molecules can undergo changes in their shape in the presence of heavy metal ions, such as the lead ion Pb^{+2} [89]. Molecules with modified shape can enhance the light emission of the iridium ion Ir^{+3}. This research, [90], tests the detection of Pb^{+2} based on Ir^{+3} light emission, using a self-contained paper-based system [89].

Microfluidic paper-based analytical devices are capable of transporting fluid from an inlet to an outlet via capillary action [91]. In the design of the biosensor, the paper contains reservoirs where the liquid is suspended. The paper is tilted and the liquid moves to other reservoirs, following specific channels. This motion is driven by gravity rather than capillary force. The device was named suspending-droplet mode paper-based microfluidic device.

The paper is placed inside a portable detection device and a smartphone is used to acquire images of the optical signal from Ir^{+3}, from a filter window. The paper contains two reservoirs referred to as reaction zones and detection zones. On the first one, the modified shape molecules are formed under heat. On the later one, the molecules and Ir^{+3} complex are mixed. The paper contains three channels which are set for positive control, negative control and the sample. A Pb^{+2} ion standard solution with a concentration of 50 nM ($\sim$ 10 ppb) was used as the positive control while deionised water was used as the negative control. This allows for the sample results to be compared with the controls, and to be disqualified when the sample's concentration is greater than the one for the positive control.

The device contains a heater to form the molecules in the reaction zone – Figure 1.5 A. After heating, the paper is tilted 90° and the liquid sample flows to the detection zone, and reacts with the Ir^{+3} complex. The Ir^{+3} complex has an excitation wavelength at $\sim 365\,\text{nm}$ and a maximum emission wavelength at $\sim 650\,\text{nm}$, thus optical filters and a LED light source, for excitation, were used – Figure 1.5 B. The optical signal can be captured by a low-cost portable device i.e. a mobile phone [90] – Figure 1.5 D.

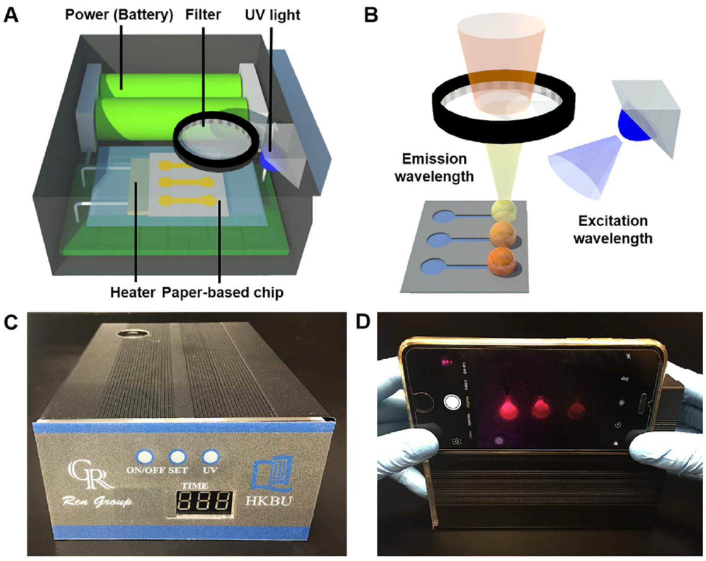

Figure 1.5: A – Layout structure of the portable detection device; B – detection principle; C – detection device; D – lead detection using a mobile phone [90].

The system was tested with other common metal ions, such as K^{+}, Na^{+}, Li^{+}, Zn^{+2}, Cu^{+2}, Mg^{+2}, Ca^{+2}, Hg^{+2}, Al^{+3}, and Fe^{+3} ions. Only Pb^{+2} ions could enhance the light emission of the system.

Assays were performed to the system and the results indicated good linearity in the correlation between Pb^{+2} ion concentration and emission intensity, in the range of 10 nM (2.072 ppb) and 100 nM (20.72 ppb).

1.7.3.2 Detection of lead ions in drinking water based on a strip immunosensor

This research, [92], used lateral flow assay technology, similar to the one used in COVID tests, to detect lead ions in drinking water. Lateral flow assay is a paper-based platform for the detection and quantification of analytes in mixtures, in a low-cost manner [93].

A strip immunosensor was constructed capable of achieving a visual LOD of 2 ng/ml (2 ppb), as seen in Figure 1.6. When a lead solution is applied to the sample pad, it spreads through the paper via capillary action. The paper contains a red control zone at the top (C) and a red test zone at the bottom (T) - highlighted with arrows in Figure 1.6. The colour intensity of the test zone will decrease as the concentration of lead increases.

Figure 1.6: Detection results of the lateral flow assay method, with lead concentrations between 0 ng (0 ppb) and 2 ng, per ml (2 ppb) of water [92].

To determine the sensitivity of the method, the visual detection limit was defined as the minimum target lead concentration making the colour on the test line disappear. The visual LOD was 2 ppb and the LOD for semi-quantitative detection could reach 0.19 ppb, using a scanning reader. Interference from other metals, namely Hg^{+2}, Cd^{+2}, Cu^{+2}, Cr^{+3}, Mn^{+2}, Co^{+2}, Fe^{+2}, Zn^{+2}, Al^{+3}, Mg^{+2} and Ca^{+2} were tested. No cross-reactivity was observed, even when the concentrations of these metals were 1 ppb.

This research proposes this method can be used as a preliminary tool for monitoring lead contamination in drinking water as the process is simple and provides results in 15 min.

1.8 Lead interaction with bacteria

The biosensor developed in this project uses bacteria, therefore it is important to highlight the different methods through which lead can interact with bacteria [94].

Lead can be bioabsorbed on cell surfaces. An example of this is on Gram-positive and Gram-negative bacteria. The Gram term comes from the Gram's method, which is a process of staining (technique used to enhance contrast in samples) used to classify bacterial species into two large groups, gram-positive and gram-negative bacteria. The differentiation comes from the chemical and physical properties of their cells walls. If a bacteria is gram-positive, its cell walls contain a thick layer of peptidoglycan, a carbohydrate that retains the stain inside the cells walls. If the bacteria are gram-negative the walls have a thinner layer of peptidoglycan and the stain can propagate outside the cell's walls [95]. Gram-positive and negative bacteria naturally carry a negative charge in their cell walls [94]. This charge binds with positively charged metal ions and regulates the movement of metals across the membrane [94].

Bacteria can also interact with lead by absorbing metals by secreting extracellular polymeric substances (EPS), which are organic polymers of microbial origin [96]. EPS can be involved in the flocculation process (precipitation of particles in the shape of a floc, i.e. bacteria aggregate) and binding of metal ions from solutions [97]. After binding, the metal becomes immobilised, preventing toxic metals from entering the cell. EPS has enzymatic activities which can detoxify metals by transforming and precipitating them [94].

Lead can be bio-accumulated. This is an active metabolic process that requires energy [98]. Bio-accumulation binds metals inside the cell walls [99].

Precipitation is another mechanism used by several bacteria to lower the concentration of free metals to insoluble complexes, therefore reducing their bio-availability and toxicity. The precipitation process can occur outside or inside the cell [100].

1.9 Innovation of lead detection with the PlomBOX project

Section 1.7.3 showed that advancements have been made in biosensor technology to assay lead in drinking water with low-cost devices that can provide fast results with sensitivities comparable to WHO's limit of 10 ppb. However, this research did not cross-calibrate their results with external lead assay from chemical water analysis such as ICP-MS detectors. Section 1.5 described how detecting small indicators of contamination is a challenge that is common in particle physics experiments. Often, detector components must be assayed for trace radioactivity levels at or below 1 ppb of lead.

Chapter 2 outlines how CMOS sensors and Biosensors work.

Chapter 3 explores if CMOS sensors built for optical light detection can perform as decay radiation detectors. Detecting the decay radiation of radioisotopes occurring in trace amounts with lead, e.g. ^{210}Pb, can potentially enable its detection in food and drinking water. This chapter showcases the research featured in [101], in which I served as the second author and played a role in drafting the initial manuscript, alongside contributing to its review and editing process. I made substantial contributions encompassing the methodology, software development, validation processes, formal analysis, data curation and visualisation techniques for the research presented in this chapter.

Chapter 4 examines the principles of reducing samples in volume, introduced in Section 1.5, to increase the concentration of heavy metals for measurement. Lead retention through volume reduction can be investigated by boiling water samples, spiked with a known amount of ^{210}Pb. This chapter presents the research featured in [102], for which I was the first author. I made substantial contributions towards the data acquisition, data curation, visualisation techniques and validation processes of the work presented.

Finally, the project will combine biology and particle physics assay approaches with the aim of developing a sensor for lead in drinking water called PlomBOX. Such a sensor would expedite access to on-demand assay methods and help mitigate lead intake through contaminated drinking water. Sensors are widely available, such as CMOS sensors in mobile phone cameras. Furthermore, low-cost microprocessors with CMOS cameras are available off-the shelf (COTS) and can be used by non-experts in the field. The principles of biosensor and CMOS detectors are described in Chapter 2. The operational concept of PlomBOX is based on the ability of specially engineered bacteria to change colour when exposed to a water sample, reflecting its lead level. This can be measured precisely via colour spectroscopy using a CMOS sensor. The project follows three development paths: the design of a genetically modified strain of *E. coli* sensitive to lead concentrations up to 10 ppb (Section 5.1), the development of the imaging platform that will record the bacteria response (Section 5.2) and the design of a custom-developed mobile phone application, the PlomApp, that will control data acquisition with the PlomBOX and will send the data to a server, where bespoke automated analysis software provides a result of the lead concentration in a water sample (Section 5.3). I designed and developed the PlomApp and its communication protocols with the imaging platform. The progress of research and development concerning the biosensor detailed in Section 5.1.2 was significantly hindered by the COVID-19 pandemic, requiring a shift in focus. The project proceeded with an established biosensor, as described in Section 5.1.3. The analysis and results presented in Chapter 6 are performed by myself in their entirety.

Following design and development, the project aims to undertake a field test, to optimize user experience and utility by obtaining a field evaluation and survey on user experience. Furthermore, the field test results will be cross-calibrated with Germanium and ICP-MS detectors.

In addition to the scientific significance of the project, there is a notable emphasis on its social implications, particularly regarding the potential impact on small local communities through the analysis of contaminated samples from people's homes. Outreach activities were conducted with local schools to educate pupils on the risks of drinking water contaminated with lead.

Chapter 2

Detection of small signals in biological and CMOS sensors

This chapter examines two detection devices used in the project: biosensors and CMOS image sensors.

In Section 2.1, the operation of biosensors, introduced in Chapter 1, is explored. The working components of analytes, bioreceptors, and biotransducers used in biosensor construction are explained in Sections 2.1.1, 2.1.2 and 2.1.3.

To understand CMOS sensors, knowledge of semiconductor devices and photodiodes is necessary. Section 2.2 details the properties of semiconductors, effects of ionising radiation, use as a radiation detector, and photodiode integration. Section 2.3 explains the working principle and applications of CMOS sensors.

2.1 Biosensors

This section describes the components of the biosensor used in our project. The bioreceptors use transcription-factor based methods while the biotransducer employs colourimetry. The subsequent sections provide an explanation of the functioning of these types of bioreceptors and biotransducers, with a brief overview of the analyte and electronic components.

2.1.1 Analytes - samples under test

The biosensor used in this project detects lead in water. Both deionised and tap water are tested, with doped and naturally occurring concentrations of lead.

2.1.2 Bioreceptors

A transcription-factor based biosensor, associated with the process of controlling protein synthesis in a cell, is referred to as a transcription biosensor. This process involves copying DNA segments into RNA [103].

Cells are fundamental units of life that are defined by their membrane boundary and contain various specialised subunits known as organelles. One organelle, the nucleus, serves as the central repository of genetic information necessary for cell growth and reproduction [104]. Cytoplasm is a semifluid substance contained inside the cell walls, but external to the nucleus [105]. Cells can contain or lack a nucleus and thus be classified as eukaryotic and prokaryotic, respectively [106, 107]. Bacteria are microscopic single-celled organisms with no nucleus [108].

In cells with a nucleus the copying of target genes can be stimulated or inhibited when there are molecules, called transcriptional factors, which move from the cytoplasm into the nucleus, initiating or inhibiting transcription [109]. The transcriptional factors will bind to certain sequences of DNA, and thus control the gene's possibility to create a protein [110]. A transcription control is present to determine whether a copy of DNA can occur or not.

To initiate transcription, transcription factors, referred to as activators, bind to the target DNA to which they are complementary in shape – Figure 2.1a. A copy of that gene is created, and it moves into the cytoplasm to create a protein [110].

In the case of inhibiting transcription, transcription factors, referred to as repressors, bind to the target DNA, preventing any copies of this gene from occurring – Figure 2.1b [110].

The action of transcription factors can be affected by interactions with molecules, ions, physical parameters like temperature, protein to protein interactions or protein modifications [103].

Transcription can also occur in cells with no nucleus, thus occurring in the cytoplasm.

When this mechanism is applied to transcription factor based biosensors, the analytes combine with the transcription factors [112]. The transcription system is modified to express a gene that will report a signal [113]. This reporter gene will constitute the biotransducer of the biosensor and will be described in the next section.

2.1.3 Biotransducers

As mentioned in Section 1.7.1, transducers are the ADC of assay with biosensors.

The level of expression of a reporter gene, which is the signal, is directly related to the transcriptional activity resultant from the introduction of transgenic factors i.e. the analyte that binds with the receptor transcriptional factor [114].

When reporter genes are expressed they produce a protein which can have visual responses, such as bioluminescence and fluorescence [114]. Bioluminescence occurs when oxidative chemical

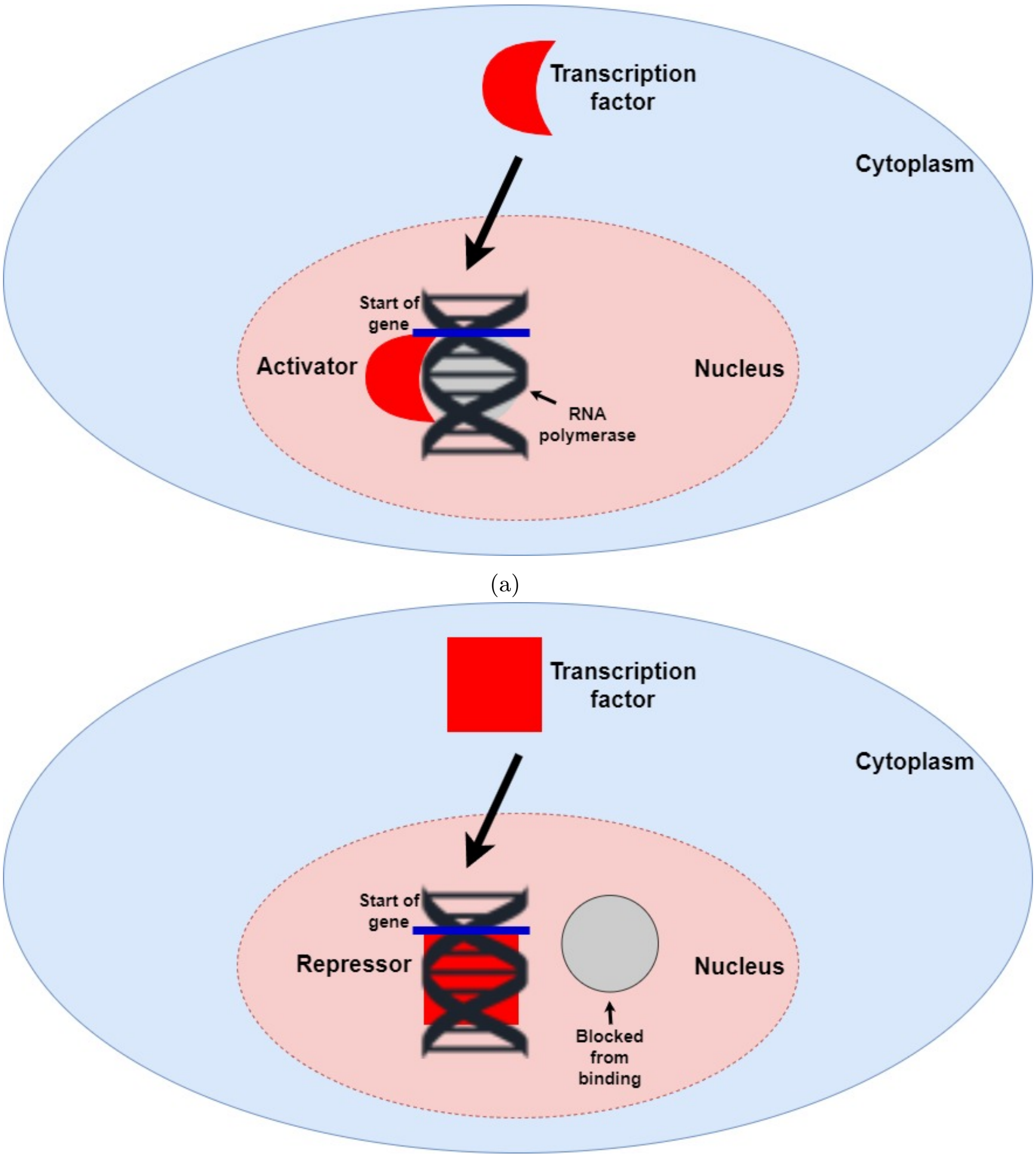

(a)

(b)

Figure 2.1: Diagram describing the transcription process inside the nucleus. Transcription factors move from the cytoplasm to the nucleus and bind to target DNA. 2.1a In the case of activator transcription factors, RNA polymerase is able to bind to the target sequence and begin transcription. RNA polymerase is an enzyme responsible for copying a DNA sequence into an RNA sequence [111]; 2.1b For repressor transcription factors, RNA polymerase is unable to bind to the target gene and transcription is inhibited [110].

reactions in organisms emit light [115]. Fluorescence occurs when an atom absorbs a photon and is excited to a higher energy state. The de-excitation that follows is quantised, and the emitted de-excitation photons will have lower energies, individually, than the absorbed photon – Figure 2.2. If the absorbed photon is in the ultraviolet (UV) region of the electromagnetic spectrum and the emitted photon is in the visible region of the spectrum, fluorescence will be observed [52].

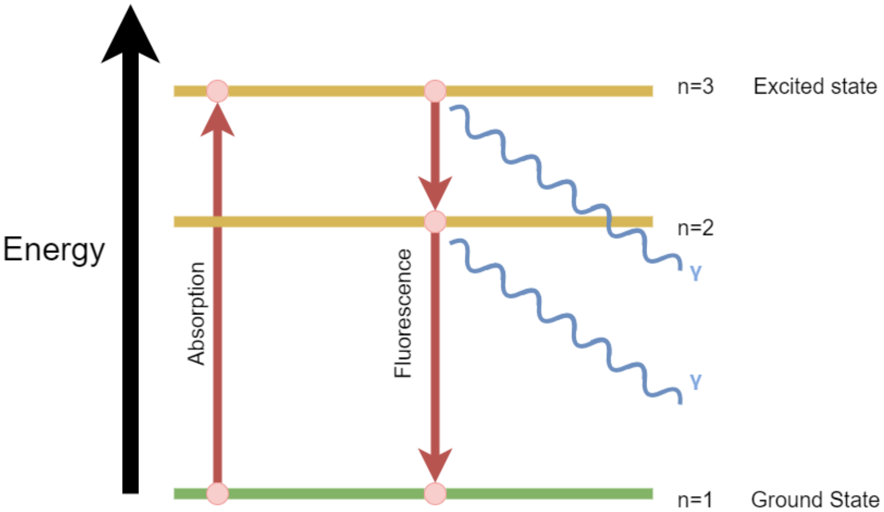

Figure 2.2: Energy level diagram detailing fluorescence process. An atom can absorb a photon and be excited to a higher energy state. When de-excitation occurs, several photons can be emitted which have lower energies than the original absorbed photon.

Three commonly used proteins in reporter gene assays will be discussed in the next sections. *Luciferase* produces a bioluminescence response, sfGFP produces a fluorescent response and β-Galactosidase produces a chromogenic response.

2.1.3.1 *Luciferase* enzyme

Fireflies exhibit the bioluminescence response of the *luciferase* enzyme. The *luciferase* reaction occurs in the peroxisomes of the firefly's light organs [114]. Peroxisomes are organelles that facilitate oxidative reactions within cells and serve important functions in metabolism, detoxification of reactive oxygen species and signaling pathways [116]. The reaction requires adenosine triphosphate (ATP), a compound that provides energy to cells, Mg^{2+}, O^2 and the substrate luciferin. Luciferin is a compound that oxidises and produces light in the presence of *luciferase* [117]. Light with a wavelength of 560 nm is emitted from this reaction – Figure 2.3.

Figure 2.3: The Brazilian *Amydetes vivianii* firefly on the left and its *luciferase* bioluminescence *in vitro* on the right [118]

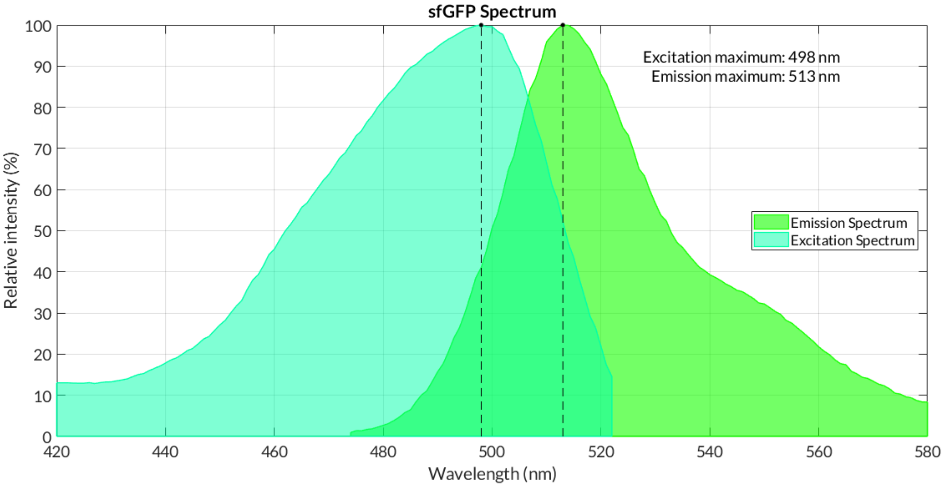

Figure 2.4: sfGFP spectrum showing the maximum emission and excitation wavelengths for this protein [120].

2.1.3.2 sfGFP

The sfGFP, a type of protein, emits green fluorescent light when exposed to light ranging from blue to the UV spectrum [119]. This protein can be found in *Aequorea victoria* jellyfish and, unlike luciferin, it does not require other enzymes or compounds [114]. This protein has a maximum excitation wavelength of 498 nm and the emission wavelength peaks at 513 nm – Figure 2.4 [120]. Figure 5.3 presents initial tests done in the project to explore different reporter genes such as the sfGFP. A petri dish is shown with several *E. coli* bacteria colonies expressing sfGFP.

2.1.3.3 β-Galactosidase

β-Galactosidase, referred to as β-Gal, is an enzyme that can be used with the compound 5-bromo-4-chloro-3-indolyl-β-D-galactopyranoside, known as X-Gal, to reflect light in the visible band at wavelengths between 450 and 495 nm (blue) – Figure 2.5. The X-Gal is hydrolised by β-Gal, splitting its glycosidic bond [121]. Hydrolysis is a chemical decomposition reaction in which water is a component, resulting in the chemical species breaking into smaller parts [122]. Glycosidic bonds are a type of covalent bond that joins a carbohydrate molecule to another group of molecules [123]. When the glycosidic bond is split in X-Gal, a sugar and a chromogenic compound are formed, which are galactose and 5-bromo-4-chloro-3-hydroxyindole, respectively [124, 125]. The chromogenic compound is dimerised (combines with a similar molecule to form a dimer) and oxidised to an organic compound with blue colour with strong optical absorption, 5,5'-dibromo-4,4'-dichloro-indigo [121, 126, 127].

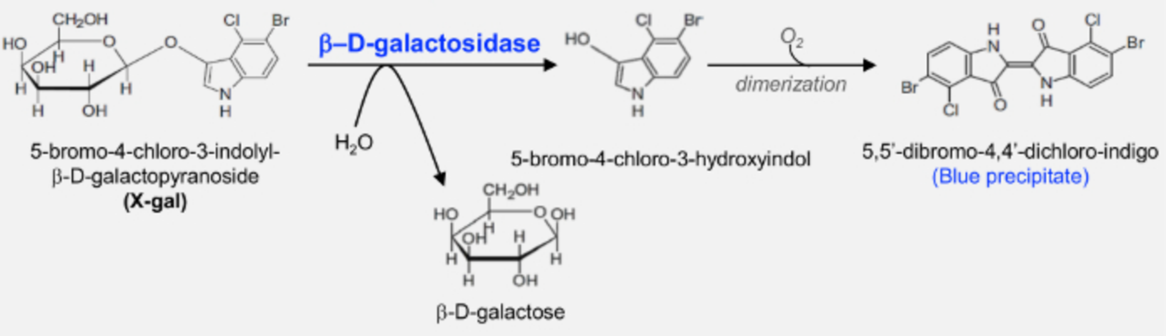

Figure 2.5: Diagram describing the hydrolysis process of X-Gal by β-Gal. Following hydrolysis, galactose and 5-bromo-4-chloro-3-hydroxyindole are formed. The 5-bromo-4-chloro-3-hydroxyindole is dimerised and oxidised to 5,5'-dibromo-4,4'-dichloro-indigo. This component reflects blue colour [128]

This project explored the uses of sfGFP and β-Gal as reporter genes for the biosensor. β-Gal was the preferred reporter gene and the design of the biosensor is described in Chapter 5.

2.1.4 Electronics

Section 1.7.3 described applications of biosensors to assay lead in drinking water, which used different methods to display results. Section 1.7.3.1 showed how a mobile phone camera acquired images of the biosensor response and Section 1.7.3.2 described how a lateral flow assays (LFA) test displayed the results of the assay.

In our project, CMOS sensors are employed, as described in Section 2.2, to acquire images of the biosensor response. These images are subjected to processing and analysis. The biosensor response exhibits a proportional relationship with the concentration of lead in the water sample. Therefore, as the concentration of lead increases, the biosensor will emit a greater amount of blue light upon interaction with more analytes. This light is captured by the CMOS sensor. The property of the image that is analysed is saturation, which refers to the colorfulness of a stimulus in relation to its own brightness [129]. These methods are described in detail in Chapter 5 and Chapter 6.

2.2 Semiconductor detectors

When atoms combine to form a solid, each of the individual atom's energy levels become continuous energy bands [49, 52]. An electron in this material is confined to these bands, which can be separated by forbidden regions, where there are no electron energy levels [49, 51]. The band containing the outer-shell electrons is the valence band. The band above it is the conduction band, where electrons can move freely between atoms, resulting in an increase of the electrical conductivity of the material [51].

Materials can be classified as conductors, insulators and semiconductors depending on the size of energy bandgap between the valence band and the conduction band – Figure 2.6. In conductors, the valence band is partially filled and it overlaps with the conduction band, thus electrons can move freely between these bands – Figure 2.6 a) [49]. Magnesium, sodium, iron and copper are examples of conductor materials [52, 130]. In insulators, the valence band is completely full and there is a bandgap between the valence and conduction bands with an energy of 5 eV – Figure 2.6 b) [51, 52, 131]. At room temperature conditions (300 K), few electrons can obtain an energy equal or greater than 5 eV to reach the conduction band [52]. In semiconductors, the valence band is full but the bandgap between the valence and conduction bands has an energy of 1 eV – Figure 2.6 c) [51, 52, 131]. Thermally excited electrons are capable of crossing the bandgap to the conduction band, thus the conductivity of a semiconductor is proportional to temperature [49, 51].

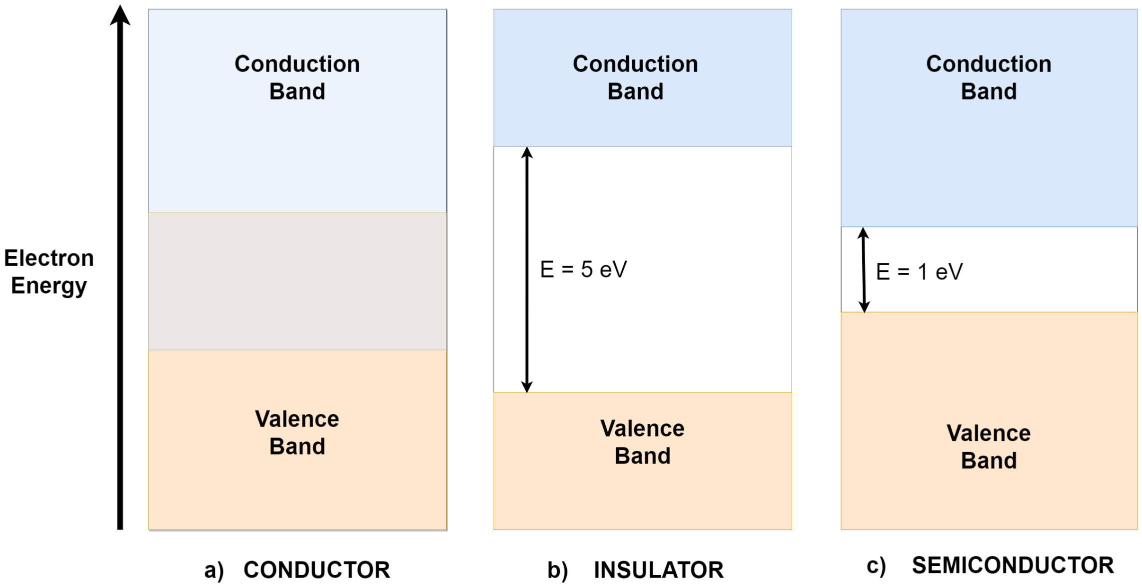

Figure 2.6: Band structure for conductor, insulator and semiconductor materials.

2.2.1 Semiconductor properties

When an electron transitions from the valence band to fill a vacancy in the conduction band, it leaves behind a hole [51]. The electron-hole pairs in semiconductors constitute the charge carriers and are analogous to electron-ion pairs in gaseous detectors. The electron will have a negative charge and the hole will have a positive effective charge therefore, if an electric field is applied to the system, the charge carriers will move in opposite directions [51].

Semiconductors exhibiting electric conductivity solely from thermal excitation, without ionising radiation, are referred to as *intrinsic semiconductors* [49, 51]. In this system the number of electrons is equal to the number of holes. In practice it is impossible to achieve this system, as residual impurities can be present in the material [51]. These impurities are atoms of another element, called dopants, and their presence can increase the conductivity, *extrinsic conductivity*, of the semiconductor [49].

The doping of materials, such as silicon, can result in the creation of N-type or P-type semiconductors.

Silicon is a tetravalent material which forms covalent bonds with the four nearest silicon atoms in the lattice. A pentavalent impurity, such as a phosphorous atom, can be introduced, replacing a silicon atom – Figure 2.7a. Four of its electrons are involved in covalent binding with neighbouring silicon atoms but the fifth electron moves in the material lattice and forms a donor level below the conduction band – Figure 2.7b [131]. Electrons from this level can be thermally excited into the conduction band, increasing the electrical conductivity of the material [49]. Materials that contain excess free electrons (majority charge carriers) due to the introduction of donor impurities are called n-type (negative) semiconductors [49]. In this material, electrons and holes represent majority and minority charge carriers, respectively [132].

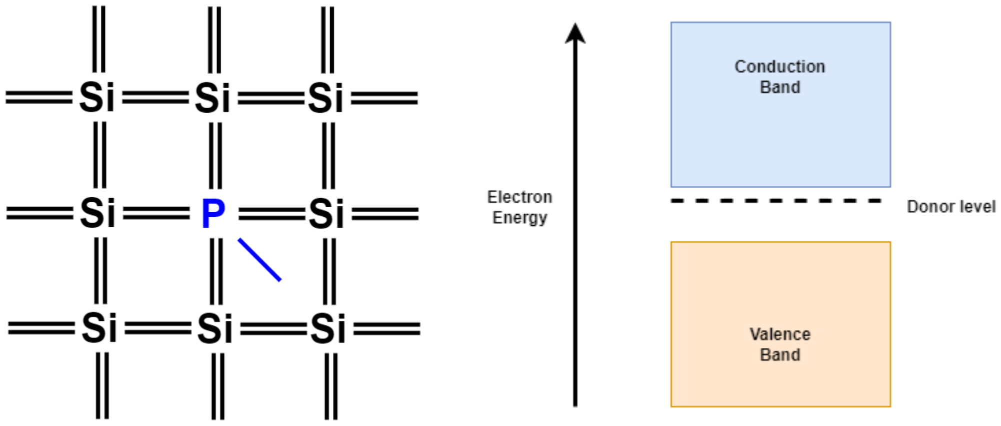

(a) (b)

Figure 2.7: 2.7a Diagram of a silicon crystal showing a phosphorus donor impurity substituting a silicon atom; 2.7b Donor levels created in the silicon by the introduction of a donor impurity [51].

Conversely, a trivalent impurity, such as a boron atom, can be introduced to replace a silicon atom – Figure 2.8a. This atom will have one fewer valence electron compared to the silicon atoms in the material. This vacancy results in a hole that can move through the material, as electrons will create holes when filling the vacancy caused by the impurity [49]. The impurity introduces an acceptor energy level above the valence band which is filled by thermally excited electrons, increasing electrical conductivity – Figure 2.8b [51]. Materials that contain a deficiency in free electrons (minority charge carriers) due to the introduction of acceptor impurities are called p-type (positive) semiconductors [49]. In this material, electrons and holes represent minority and majority charge carriers, respectively [132].

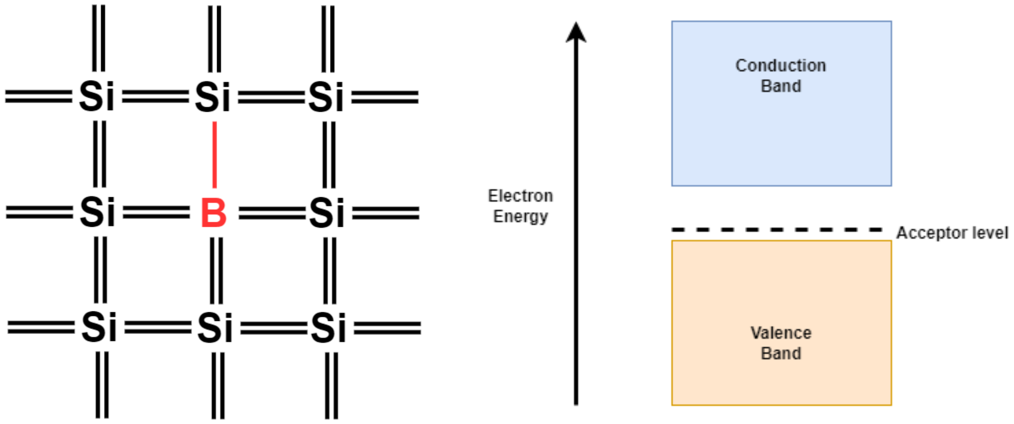

(a) (b)

Figure 2.8: 2.8a Diagram of a silicon crystal showing a boron acceptor impurity substituting a silicon atom; 2.8b Acceptor levels created in the silicon by the introduction of an acceptor impurity [51].

2.2.2 Ionising radiation in semiconductors

A charged particle traversing a semiconductor will undergo ionisation energy loss, as described in Sections 1.4.1 and 1.4.2, which creates electron-hole pairs along its path. For uncharged radiation such as X-rays, the photons interact with target electrons, as seen in Section 1.4.3, which consequently create electron-hole pairs [133]. The ionising energy w represents the amount of energy lost by the interacting particle to produce one electron-hole pair and is specific to the absorbing material [51, 133]. Table 2.1 compares the average energy required for electron-hole pair creation for different semiconductor materials. The number of electron-hole pairs N can be obtained by dividing the absorbed energy E by w [133]:

$$N = \frac{E}{w} \tag{2.1}$$

An advantage of the use of semiconductors as radiation detectors is their high energy resolu-

Material	w (eV)
Si	3.65
Ge	2.96
GaAs	4.2
CdTe	4.43
Diamond	13.1

Table 2.1: Energy required for electron-hole pair creation for silicon, germanium, gallium arsenide, cadmium telluride and diamond [134]

tion. In silicon and germanium semiconductors an energy of $\sim 3\,\mathrm{eV}$ will create an electron-hole pair compared with $\sim 30\,\mathrm{eV}$ necessary to create an electron-ion pair in gas detectors [51]. Thus, semiconductor detectors will have ten times more charge carriers than gas detectors, for the same deposited energy E. Semiconductor detectors present compact sizes, an effective thickness that can be built to suit the experiments needs and fast timing characteristics [51].

2.2.3 Semiconductors as radiation detectors

If an electric field is applied across a semiconductor, the electrons and holes created by ionising radiation will move in opposite directions [51]. The displacement of the carriers will create a current that will be present in the system until they are collected at the edges of the detector, where electrodes connect to a detection circuit [51].

Semiconductors become useful radiation detectors when n and p-type semiconductors are brought into contact, creating a diode junction [133]. Diode junctions constitute the basic component of a solid state device [132].

This is achieved by diffusing acceptor impurities into an n-type material or diffusing donor impurities into a p-type material. In the junction there will be a migration of majority charge carriers in opposite directions, i.e. motion of electrons from the n-type material into the p-type material and the migration of holes from the p-type material into the n-type material [132]. This will create a diffusion current (I_{diff}). At the junction, holes and electrons recombine, resulting in the region becoming depleted of mobile charge carriers. This depleted region of the system contains static uncompensated ions, constituting a space charge [132]. An electric field is created by these ions, which will decrease the tendency for further electron-hole migration [132]. This field causes a current in the opposite direction of I_{diff}, referred to as drift current (I_{drift}). At equilibrium between I_{diff} and I_{drift}, no further migration will occur and a "steady-state" is established, with the junction exhibiting high resistivity and the other parts of the semiconductor presenting low resistivity [51, 132]. The depleted region represents the active volume of a semiconductor detector and any electron-hole pairs created within it by ionising radiation will migrate to the boundaries of the detector, contributing to the I_{diff} and creating an electric signal [133].

This junction is referred to as an *unbiased junction* – Figure 2.9a. It is an inefficient detector because the depletion region is small, the capacitance in the junction is high and the electric field is low, thus being unable to collect charge carriers that are lost due to recombination with vacancies in the material [51, 133].

When an external voltage is applied, with a higher potential applied to the p-side and a lower potential applied to the n-side, a *forward bias junction* is created [132] – Figure 2.9b. The entire system remains electrically neutral and the potential difference is only relative to both sides of the junction. The presence of this external field will enhance I_{drift} relative to I_{diff} and thus enable the motion of the majority charge carriers into the depleted region, reducing its size. The potential barrier between the n-side and p-side of the junction will be reduced, allowing the motion of minority carriers across the junction, thus creating a current across it [132].

If an external voltage is applied, with a more negative potential applied to the p-side and a more positive potential applied to the n-side, the bias of the junction is reversed, improving the performance of the detector [131, 133]. A *reversed bias junction* will be created – Figure 2.9c. The external voltage increases the electric field in the depleted region and the majority carriers will move away from the depleted region, increasing its size [132, 133]. The energy of the electrons in the p-side will increase and the energy of the electrons in the n-side will decrease, thus increasing the potential difference between the two regions and making I_{drift} small [49, 51, 132]. If the external voltage increases, the width of the depletion region increases, the junction capacitance decreases and the detection performance improves, as a larger depletion zone corresponds to a larger sensitive volume for radiation detection [135]. However, if the external voltage is increased continuously, a point of breakdown in the junction will be reached in which minority carriers can move freely across the junction, increasing I_{drift} and making the junction conductive [51, 132]. This voltage is referred to as breakdown voltage and should be avoided as it damages the semiconductor material and damages the detector performance, thus decreasing the energy resolution [51, 132].

Semiconductor diodes are used in many devices, such as zener diodes, light emitting diodes (LED), solar cells, etc [132]. They can be built with different materials mentioned in Table 2.1. Silicon is the material best suited for particle or radiation detection [136]. Silicon has a bandgap energy of 1.12 eV between the valence and conduction bands, which is greater than the energy resultant from thermal oscillations at room temperature of 25.9 meV [137]. Therefore, silicon does not require cooling, unless being operated in ultra-low noise conditions or to mitigate radiation damage. Silicon has a low density $2.33\,\text{g/cm}^3$, and a large radiation length, as seen in Tables 1.3 and 1.4 [136]. Other materials, such as GaAs, are preferred over silicon when a large quantum efficiency, introduced in Section 2.3.3.1, is required for high energetic photons in the keV region [136]. Germanium is preferred over silicon in experiments which require a high energy resolution

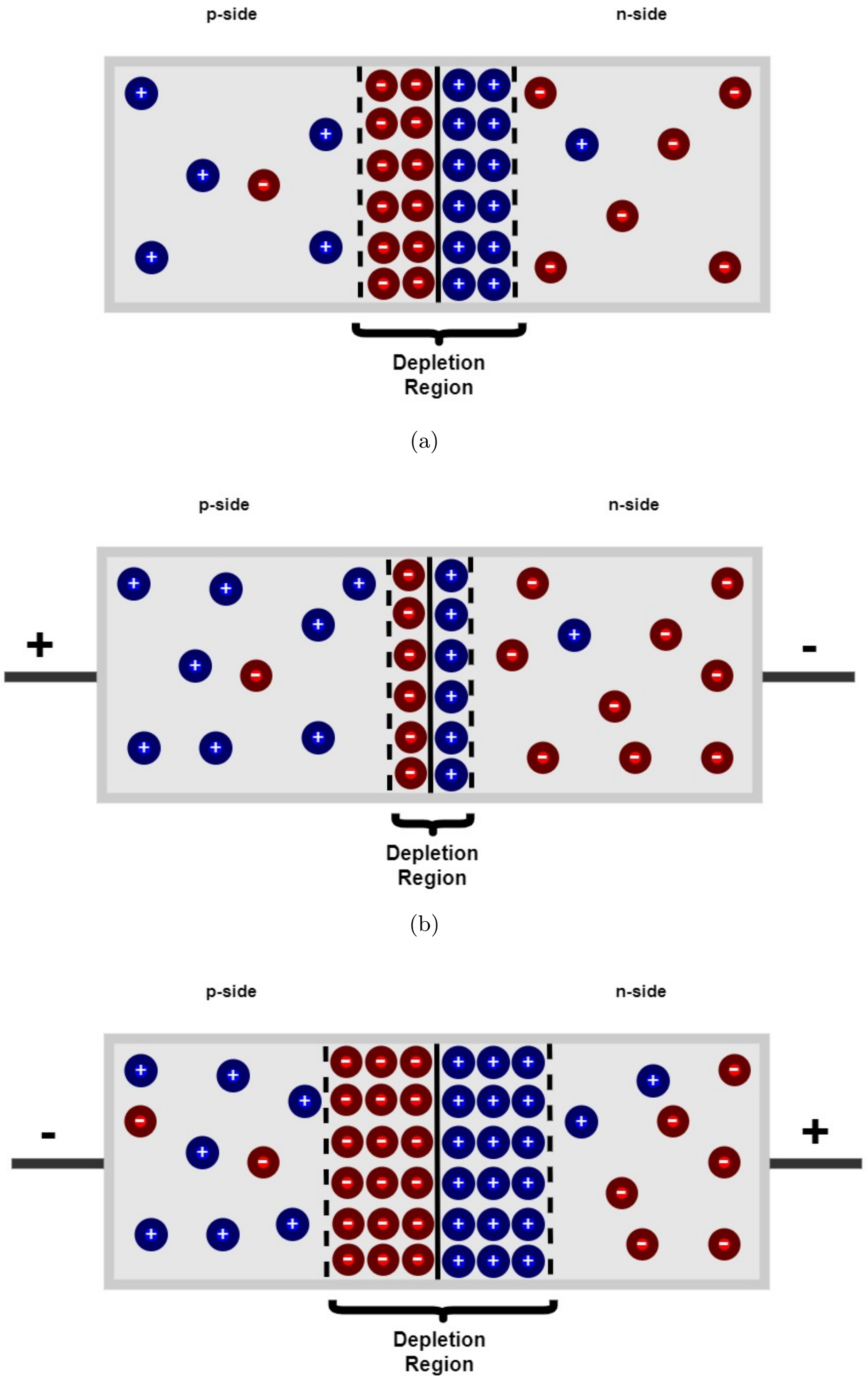

(a)

(b)

(c)

Figure 2.9: Diagram of a diode junction showing the n-side, p-side and depleted region in 2.9a unbiased conditions; 2.9b forward biased conditions and 2.9c reverse biased conditions

as it presents a smaller band gap energy of 0.7 eV [136]. However, it requires cooling to reduce thermal oscillations. For the purposes of this thesis, I will focus on silicon photodiodes used in CMOS image sensors. A description of how semiconductor germanium detectors work will be shown in Chapter 4.

2.2.4 Photodiodes

Photodiodes are reversed bias diode junctions that absorb light and convert it to electrical energy [132] – Figure 2.10a. When photons hit the surface of a semiconductor, electrons are excited from the valence band to the conduction band if the energy of the photon is greater than the bandgap energy. The excited electrons will create holes in the valence band, therefore the incidence of photons will increase the number of mobile electron-hole pair charge carriers in the material [132]. As an electric field is present in the semiconductor, the mobile charge carriers will move through the material towards their majority sides, creating a reverse-bias current. An increase of optical excitation leads to an increase in the reverse-bias current, thus photodiodes can be used as photodetectors [132].

Even when there are no photons present, there is some diffusion current flowing through the semiconductor, derived from the motion of minority carriers. This reverse leakage current is referred to as dark current, in the context of photon detectors [132]. Dark current is dependent on the reverse supplied voltage, the resistance of the junction and the ambient temperature [132].

PIN photodiodes and avalanche photodiodes constitute semiconductor devices with structure variations of the photodiode described in this section [132].

2.2.4.1 PIN photodiodes

This device contains p and n regions separated by a lightly doped intrinsic region [132] – Figure 2.10b. The depletion region extends into the intrinsic region therefore increasing the active volume of the semiconductor available to capture photons and, by extension, the detector's sensitivity, when compared to the diode junction described in Section 2.2.4.

2.2.4.2 Avalanche photodiodes

Avalanche photodiodes (APD) present a similar structure to PIN photodiodes, with an added internal gain mechanism that amplifies the reverse-bias current. The diode has a p^+ π p n^+ configuration [132] – Figure 2.10c. The p^+ and n^+ regions are heavily doped with low resistance. The π region is lightly doped and considered to be intrinsic.

Photons pass through the p^+ region, hitting the π region, creating electron-hole pairs. In the p-n^+ region, the depletion region increases with the reverse bias voltage increase. With further

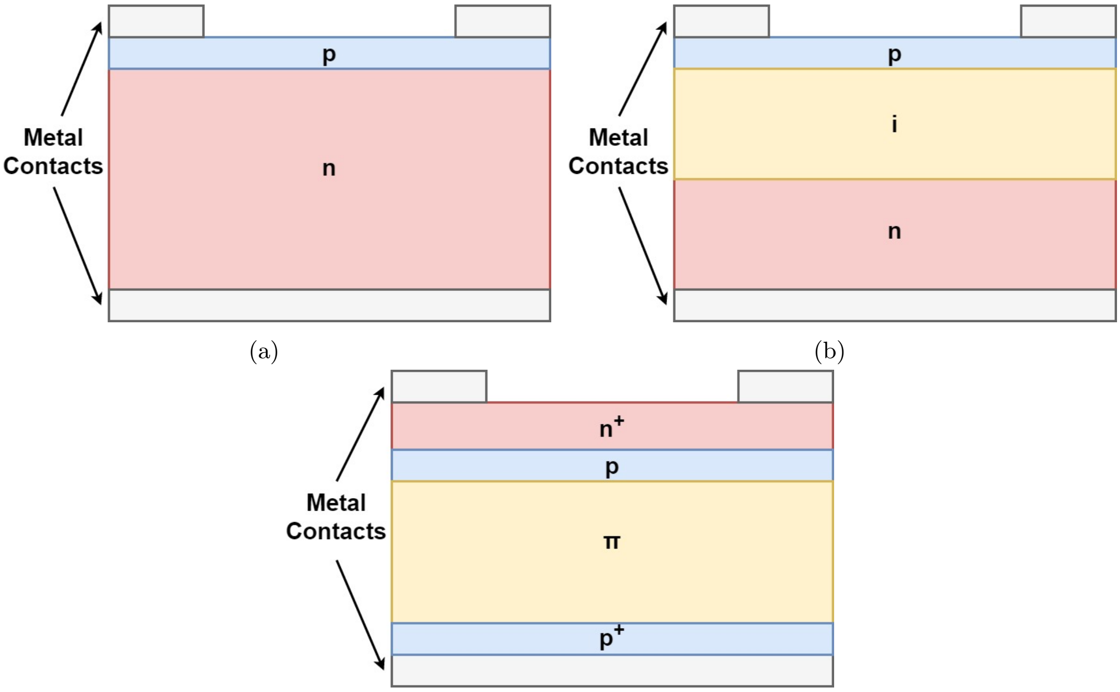

(a) (b) (c)

Figure 2.10: Side view schematic of a 2.10a photodiode; 2.10b PIN photodiode; 2.10c APD photodiode

reverse bias voltage increase, the depletion region is wide enough to reach the π region. The electric field becomes very high and the electron-hole pairs generated by the photons have enough energy to create further electron-hole pairs in an avalanche effect. This ensures high current gain due to charge carrier multiplication.

2.3 CMOS image sensors

The scope of this project includes the utilisation of two distinct types of CMOS imaging devices: the Neo sCMOS, designed for low-noise imaging of electromagnetic radiation within the visible band and the OV2640 device, which images the visible band under standard noise conditions. The Neo sCMOS will be described in detail in Chapter 3 and the OV2640 will be covered in Chapter 5. The latter works in tandem with a biosensor, the workings of which where explained in Section 2.1.

CMOS devices are composed of an array of pixels, with each pixel containing one photodiode and a row selecting (RS) transistor, which acts as a switch. The pixel arrays are enclosed by vertical (Y) and horizontal (X) scan circuits that can access the sensor line-by-line. The sensor also contains an output amplifier [138] – Figure 2.11.

Silicon is used to manufacture CMOS devices, although sensors which use Germanium based substrates have been reported in literature [139].

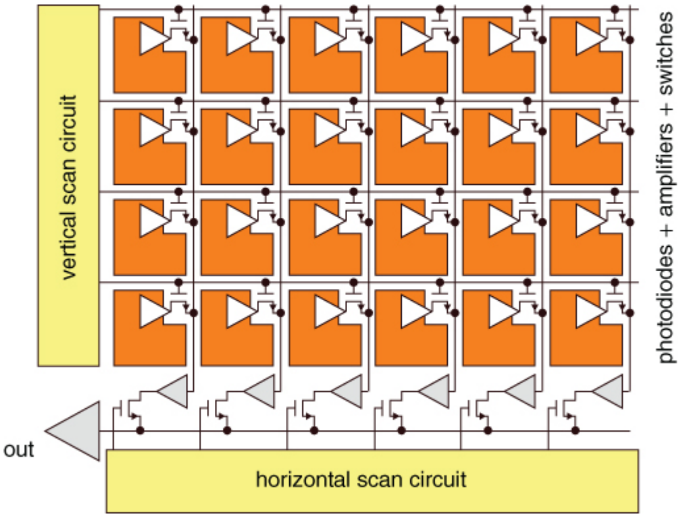

Figure 2.11: 2D CMOS image sensor schematic architecture [138]

2.3.1 Working principle

A CMOS sensor operates in the following manner, and as seen in Figure 2.12 [140, 141]:

- Before exposure starts, the photodiodes are reverse biased to a high voltage ∼3 V. The pixels are reset, and exposure can begin.
- During exposure, photons travel through the sensor and are absorbed by the silicon, generating electron-hole pairs. The electric field present in the junction will separate the two charged carriers. Electrons will move to the n-side and holes will move to the p-side of the diode. This will result in the decrease of the reverse voltage across the photodiode.
- When the exposure ends on the photodiode, the remaining reverse voltage is measured, and the difference between this final value and the original reverse voltage value is a measure of the number of photons that were absorbed during exposure. Following this process, this value, which represents the signal voltage, is amplified.
- The pixel array is accessed one row at a time via the RS transistors and, at the bottom of the array, the signal voltage of each individual pixel is read one by one. This type of readout process is known as rolling shutter.
- The signal voltages for all pixels are supplied to an analogue output amplifier and an ADC. The ADC works as follows: the signal that needs to be converted, V_{IN}, is compared to an analogue ramp signal, V_{ramp}, which is generated by a digital counter. When V_{IN} and V_{ramp} have the same value, the counter stores the value into the device's memory. Data stored in memory is therefore the digital value corresponding to V_{IN} and is referred to as grey level. The ADC rate is known as gain [142]. For example, if 100 electrons are converted to 200 grey levels, the sensor has a gain of 2.

- The grey levels can be mapped and displayed on a computer monitor as an image [142].
- Before a new exposure begins, the photodiodes are reset again i.e. discharged.

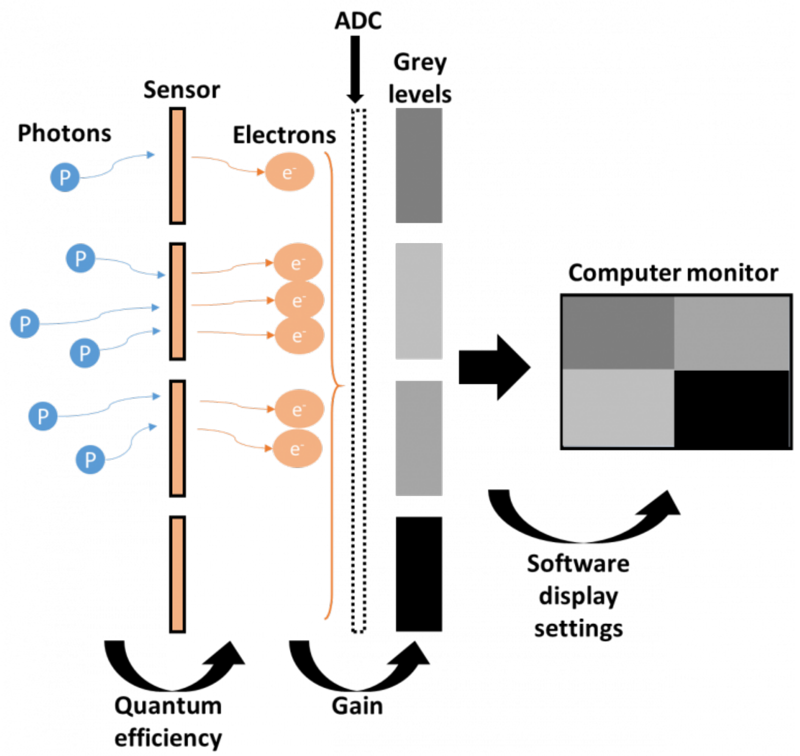

Figure 2.12: Diagram of CMOS sensor operation. Photons travel through the sensor and create electron-hole pairs. Quantum efficiency is the percentage of photons that create electron-hole pairs and is described in detail in Section 2.3.3.1. The electrons are converted into a digital signal via an ADC. The digital signal can be displayed in a computer monitor. [142]

A drawback of CMOS sensors using rolling shutter as the readout process of the pixel arrays is that exposures for each pixel row begin and end at different times. This creates motion artefacts in the resulting image which are difficult to compensate for [138]. Global shutter has been developed for CMOS sensors, which allows for all pixels to start and end the exposure at the same time.

2.3.2 Photon shot noise

CMOS sensors experience different sources of noise, with dark current being a source of noise addressed earlier in Section 2.2.4. The Neo sCMOS exhibits capabilities in cooling the chip to $-30\,°\mathrm{C}$, resulting in a low value of dark current – $0.015\,\mathrm{e}^-/\mathrm{pixel/sec}$, at $-30\,°\mathrm{C}$. In contrast, the OV2640 lacks cooling capabilities, leading to a comparatively higher dark current value – $4.88\,\mathrm{e}^-/\mathrm{pixel/sec}$, at $60\,°\mathrm{C}$.

Another important component of noise that should be considered is the photon shot noise. This type of noise relates to the statistical variation in the amount of photons hitting the sensor during exposure [138]. This process can be described by a Poisson distribution. Pixels receive an average amount of photons μ_γ during exposure which have a noise component σ_γ. The average amount of photons and the noise are related by $\sigma_\gamma = \sqrt{\mu_\gamma}$ [138]. This relation holds when photons are converted to electrons, as the average amount of electrons μ_e in the pixel will contain a noise component σ_e, related by $\sigma_e = \sqrt{\mu_e}$ [138]. This source of noise is constantly present and influences the maximum signal-to-noise ratio $\frac{S}{N}$ possible for the sensor [138]:

$$\frac{S}{N} = \frac{\mu_e}{\sigma_e} = \frac{\mu_e}{\sqrt{\mu_e}} = \sqrt{\mu_e} \tag{2.2}$$

A minimum $\frac{S}{N}$ of 40 dB is required for CMOS sensors used for consumer applications [138] and is the value specified for the OV2640. A $\frac{S}{N}$ value for the Neo sCMOS could not be found.

As the Neo sCMOS will be used as a radiation detector, maintaining low noise conditions is of utmost importance. The OV2640 will be used for optical light detection without a cooling system, therefore higher noise is expected.

2.3.3 Light sensitivity

Another consideration with CMOS sensors is their light sensitivity. Not all the photons that hit the pixels are converted to signal voltage due to several aspects: some of the sections of the pixel surface aren't sensitive to incoming photons, as they house the readout electronics, some of the photons hitting the pixel surface will not generate electron-hole pairs, as they can be reflected on the pixel surface, and not every generated electron-hole pair will be collected at the edges of the sensor, as they can recombine with other electrons and holes in the junction [138]. Several techniques have been developed to overcome the challenges mentioned above: microlenses can be placed on top of the pixels [143], inner-lenses can be built into the pixel during the fabrication process [144], light guides can be placed on top of pixels [145] and CMOS sensors can be back-side illuminated [146].

2.3.3.1 Quantum efficiency

The light sensitivity of a CMOS sensor can be quantified by its QE. QE is the percentage of incident photons that a CMOS sensor can convert to signal voltage [147]. It is dependent on the wavelength of the incident light and on the sensor's semiconductor material. The absorption depth of the material is related to the incident photon wavelength i.e. the penetration depth will be shorter for shorter wavelengths [147]. Photons need an energy greater than the material's band gap energy to create an electron-hole pair. Silicon, with a bandgap energy of 1.12 eV, has a QE of 95 % for incident photon wavelengths between 500 and 600 nm but lower QE for larger wavelengths [147]. To illustrate this, Figure 2.13 compares the QE of two epitaxial silicon materials (EPI - silicon in crystal structure), with thicknesses of 12 µm and 5 µm [148]. The material with greater thickness and thus greater absorption depth presents a higher QE, specially at longer wavelengths.

Figure 2.14 shows the QE with respect to wavelength for the Neo sCMOS and it is briefly discussed in Section 3.1. A similar plot could not be found for the OV2640 device.

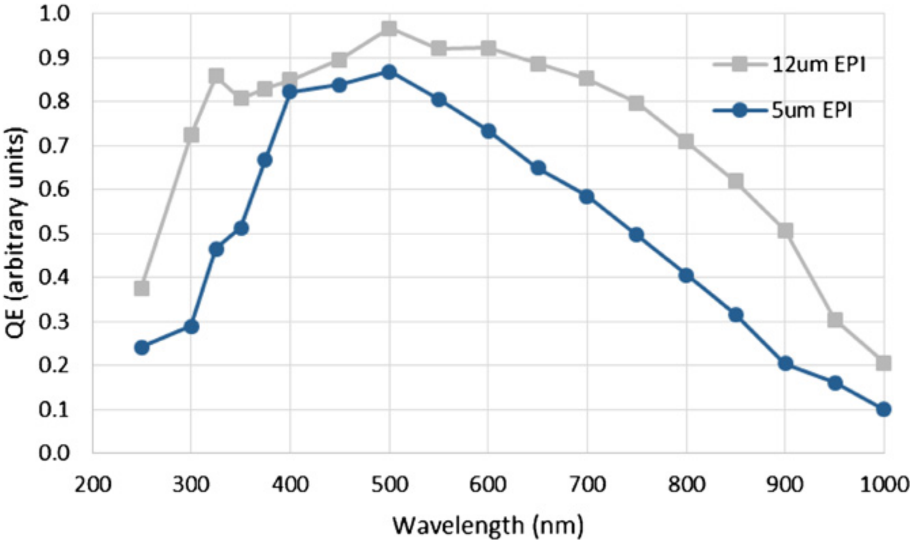

Figure 2.13: QE vs wavelength for two epitaxial silicon materials, with thicknesses of 12 µm and 5 µm. The material with greater thickness and therefore absorption depth presents a higher QE [148]

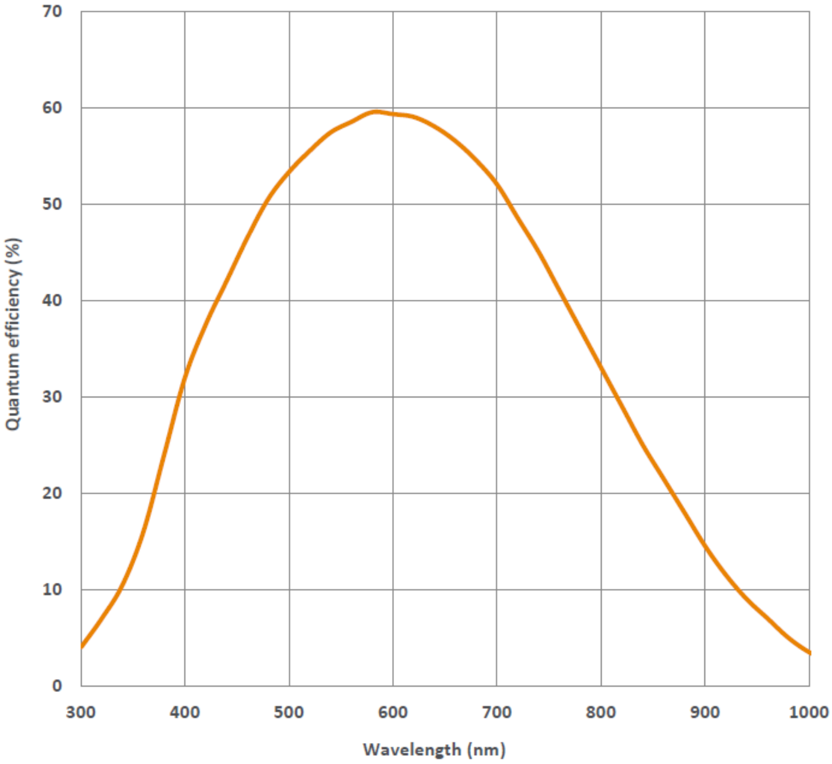

Figure 2.14: QE vs wavelength for the Neo sCMOS device [149]

2.3.4 Active pixel and passive pixel sensors

There are two different types of CMOS image sensors: active pixel sensors (APS) and passive pixel sensors (PPS).

APS are the most common type of CMOS image sensors. They use a transistor for each pixel in the sensor that amplify the signal voltage and reduce noise [150]. PPS are the precursors to APS and are readout without any amplification. As each pixel only contains a photodiode and a switch transistor, the cost of the circuit is low [150].

Chapter 3

Dosimetry and calorimetry performance of a scientific CMOS

This chapter examines the performance of a scientific CMOS sensor, built for optical light detection, as a radiation detector. Previous studies have shown that it is possible to use CMOS sensors to distinguish between α-decays and other types of radiation, as well as counting events from different radiation dosages [151]. Additionally, these sensors can provide good spatial resolution, since they allow for a geometrical confinement of the received signal, for either X-rays or for charged particles [152]. Gaseous detectors, used in high energy physics research, have been reported to have conducted measurements with a hybrid use of charge and optical readout (CMOS sensors) [153].

This chapter, which presents work published in [101], is structured as follows: in Section 3.1 technical details of the scientific CMOS sensor – Neo sCMOS [149] are provided; in Section 3.2 the experimental set-up and measurement procedures are outlined; Section 3.3 describes the analysis procedure – the steps taken to go from camera exposure frames to the reconstruction of the energy deposited in the CMOS chip. Results from measurements with radioactive sources and a X-ray tube are presented in Section 3.4. The general performance of the Neo sCMOS when exposed to X-rays and γ rays is examined. As the camera has a glass lens before the sensor, α particles emitted by the sources tested in Section 3.4 cannot be measured. The performance analysis includes a study of the calorimetric capabilities of the camera, *i.e.* its capabilities to measure the energy of incident photons and its energy resolution as function of the incident energy, as seen in Section 3.4.1. Furthermore, this chapter describes the measurements of the background rate without any source present, the minimal detectable rate with an ^{241}Am source and the camera's detection efficiency for X-rays and γ rays, in Section 3.4.2. The measured efficiencies were used to make an estimate on the sensor thickness in Section 3.4.2.4. The chapter concludes with a discussion of the results in

Section 3.5 in which the sensitivity of the CMOS approach to measure lead concentration in water down to the WHO limit of 10 ppb is addressed, based on potential trace radioisotopes present in lead.

3.1 CMOS camera specifications

The Neo sCMOS camera [149] features a chip with 2560 × 2160 active pixels, each with a height and width of 6.5 µm. The active size of the sensor is 16.6 × 14.0 mm^2 (height × width). Each pixel in the Neo sCMOS's chip has a typical well depth of $30 \times 10^3\,\mathrm{e}^-$ (electron) and is equipped with its own micro lens. The micro lens array ensures that light arriving at the chip's surface is focused into the active region of the pixels. As addressed in Section 2.2.3, silicon can be cooled to operate in ultra-low noise conditions to improve energy resolution. The Neo sCMOS's cooling system allows cooling of the chip to −30 °C in a room temperature environment. Connecting an external water cooling system allows a minimal temperature of −40 °C to be reached. The dark current is $0.015\,\mathrm{e}^-$/pixel/sec at −30 °C and $0.01\,\mathrm{e}^-$/pixel/sec at −40 °C. Groups of hardware pixels (2 × 2, 3 × 3, 4 × 4, 8 × 8) can be binned together, prior to readout, to reduce the overall contribution of readout noise and increase readout speed. These are read together as one readout pixel. Table 3.1 lists the operating parameters for the CMOS during the measurements presented in this chapter. They were chosen for several reasons: a readout binning of 4 × 4 was preferred over 1 × 1 due to limitations of the data transfer rate and to optimise data processing; the number of exposures and exposure time were chosen to ensure enough γ ray and X-ray events were recorded to result in a clear peak in the energy spectra.

No information on the cross section of the camera chip, *i.e.* its different layers and the thickness of the active silicon, is provided by the supplier. Information on the QE is only available for radiation in the wavelength range from 300 nm to 1000 nm and not for short wavelengths (X-ray and γ ray energies). It is not known how layers on top of the silicon (*i.e.* the micro lenses) affect a measurement of X-rays / γ rays. The thickness of the sensor was assessed by comparing the measurements to toy Monte Carlo simulations treating the camera as only one silicon layer, as described in Section 3.4.2.4.

3.2 Experimental description

CMOS data for radioactive source measurements were acquired inside a dark box, with dimensions of 244 cm × 122 cm × 122 cm (L × W × H). The large size of the box allows the distance between the radioactive source and the camera to be increased up to ∼2.5 m. This permits a measurement of the minimal detectable source activity to be made, as described in Section 3.4.2.2. The camera was

Setting	Value
Temperature	$-30\,^{\circ}\mathrm{C}$
Readout binning	4×4
Exposure time	$10\,\mathrm{s}$
Camera to source distance	$1.75 \pm 0.04\,\mathrm{cm}$
Number of exposures / data taking run	100

Table 3.1: Default settings of Neo sCMOS camera during all measurement runs. Runs with different settings are explicitly noted.

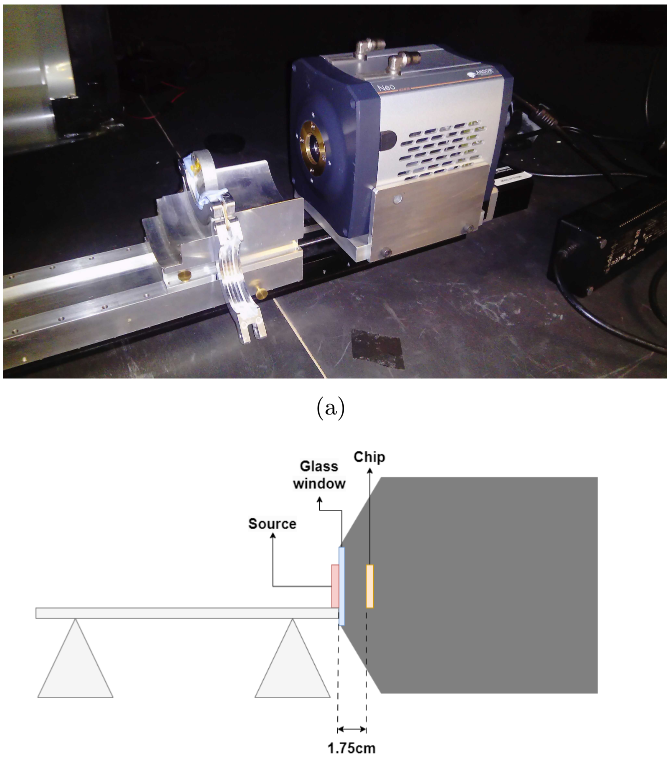

(a)

(b)

Figure 3.1: 3.1a Photograph and 3.1b diagram of the source holder and the Neo sCMOS camera in the dark-box.

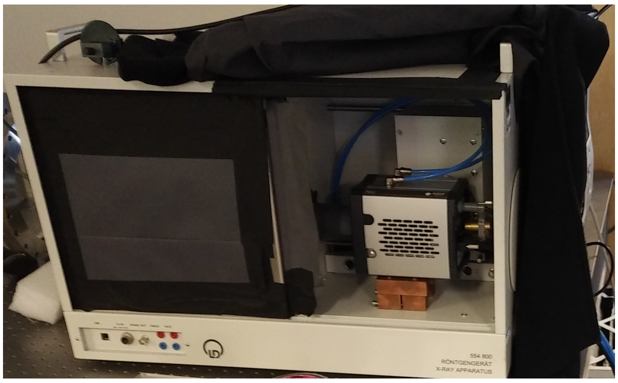

Figure 3.2: The Neo sCMOS in the LD Didactic X-ray apparatus (554 800) – the blue lines are for the water cooling circuit, which is not necessary for operation in the dark box.

positioned inside the box as shown in Figure 3.1 and all data was taken whilst the box is closed. Several calibration sources were used to understand the camera's behaviour and to obtain different spectra for calorimetry. Background data was taken without any sources and ^{241}Am, ^{55}Fe, ^{210}Pb, ^{133}Ba and ^{137}Cs sources were also used. Data taking with the X-ray tube was performed under dark-box conditions, in a different enclosure, shown in Figure 3.2 and described in Section 3.2.1. Prior to a data acquisition run the camera was cooled to $-30\,^{\circ}$C and the respective source was positioned in front of the camera, with the source aligned with the chip centre, as seen in Figure 3.1a. The NEO sCMOS was controlled via a cable, which was fanned out of the dark-box and connected to a custom PCIe card hosted in the data acquisition computer. The *Andor SOLIS for Imaging* software package was used for the data acquisition and to set the camera's parameters [154].

3.2.1 X-ray data taking

A LD Didactic X-ray apparatus (554 800) [155] was used for the X-ray data taking. Figure 3.2 shows the camera inside the apparatus. The door to the compartment containing the camera was closed before data taking and the compartment was sealed light-tight. The X-ray tube and camera developed substantial heat, therefore the camera's water cooling was used to ensure stable operation at $-30\,^{\circ}$C. The rate of X-rays of the apparatus was larger than the rate of any of the other radioactive sources used, allowing shorter exposure times than stated in Table 3.1: 0.004 s and 0.025 s.

The anode in the X-ray tube was made of Mo, with its characteristic K_α and K_β lines at 17.41 keV and 19.61 keV, respectively. Data was acquired with Cu and Zr filters between the X-ray tube and the camera. The observation of absorption edges adds more energy measurements in addition to the two X-ray lines, which makes these tests valuable for the energy calibration of the sensor. In Section 3.4.1.1 the results with the X-ray source are discussed.

3.3 Data analysis

The camera control software produced files in the Flexible Image Transport System (FITS) format [156]. Each FITS file can contain several frames, i.e. 2D arrays with one ADU measurement for each camera pixel – shown in Figure 3.3. After data taking, frames were processed by PYTHON code and CERN ROOT [157] routines. During normal data acquisition conditions several *runs* of $N_\mathrm{f} = 100$ frames were taken, as seen in Table 3.1.

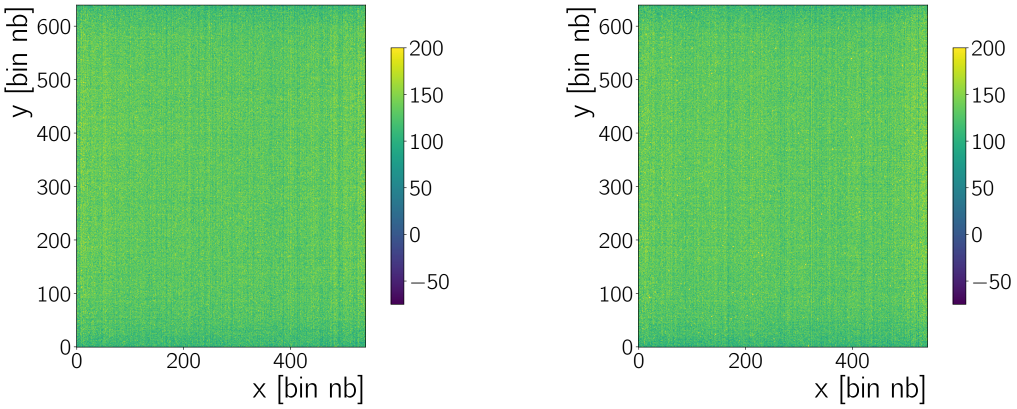

(a) BKG

(b) ^{241}Am

Figure 3.3: Raw frames (without any correction) recorded when no source of radiation is present, *i.e* background (Figure 3.3a), and when the camera is irradiated with an ^{241}Am source (Figure 3.3b). A zoom in x and y of Figure 3.3b is shown in Figure 3.6a. All images are zoomed on the intensity scale, visible in the colour-bar to the right of each image. (Which means values larger than 200 are displayed as 200.)

3.3.1 Frame background calculation

The image processing analysis corrected for the pixel pedestal in two steps, described in Section 3.3.1.1 and Section 3.3.1.2, found clusters of signal pixels, described in Section 3.3.2, and measured the energy within each cluster. These clusters were identified by their difference to the remaining pedestal value, after the corrections.

3.3.1.1 Column correction

The first step of the analysis was to correct for the raw image pedestal, which is defined as the background ADU measurement in each pixel in the absence of a source. The ADU values of each pixel in a given column are correlated with each other, giving rise to the distinct columns in Figure 3.3. This is due to the rolling shutter readout introduced in Section 2.3.1. The mean column value $\langle C \rangle_{\mathrm{col}}(x, n_{\mathrm{f}})$ and its standard deviation $\sigma_{C_{\mathrm{col}}}(x, n_{\mathrm{f}})$ for each column were calculated:

$$\langle C \rangle_{\mathrm{col}}(x, n_{\mathrm{f}}) = \frac{1}{N_{\mathrm{y}}} \sum_{y=0}^{N_{\mathrm{y}}} C(x, y, n_{\mathrm{f}}) \tag{3.1}$$

$$\sigma_{C_{\mathrm{col}}}(x, n_{\mathrm{f}}) = \sqrt{\frac{1}{N_{\mathrm{y}}-1} \sum_{y=0}^{N_{\mathrm{y}}} (C(x, y, n_{\mathrm{f}}) - \langle C \rangle_{\mathrm{col}}(x, n_{\mathrm{f}}))^2} \quad , \quad n_{\mathrm{f}} = j, \quad x = \mathrm{k} \tag{3.2}$$

where $C(x, y, n_{\mathrm{f}})$ is the charge, in ADU, measured by a pixel at a given x, y position in frame n_{f}. The column coordinate and the frame number were fixed ($x = k$, $n_{\mathrm{f}} = j$) while the sum runs over the row coordinate ($y = 0 \ldots N_{\mathrm{y}}$). After a first calculation of the column mean and standard deviation using Equation (3.1) and Equation (3.2), all pixel values $C(k, y, j) \notin \langle C \rangle_{\mathrm{col}}(k, j) \pm 5 \cdot \sigma_{C_{\mathrm{col}}}(k, j)$ were excluded and $\langle C \rangle_{\mathrm{col}}(k, j)$ and $\sigma_{C_{\mathrm{col}}}(k, j)$ were calculated again until $\sigma_{C_{\mathrm{col}}}(k, j)$ changes less

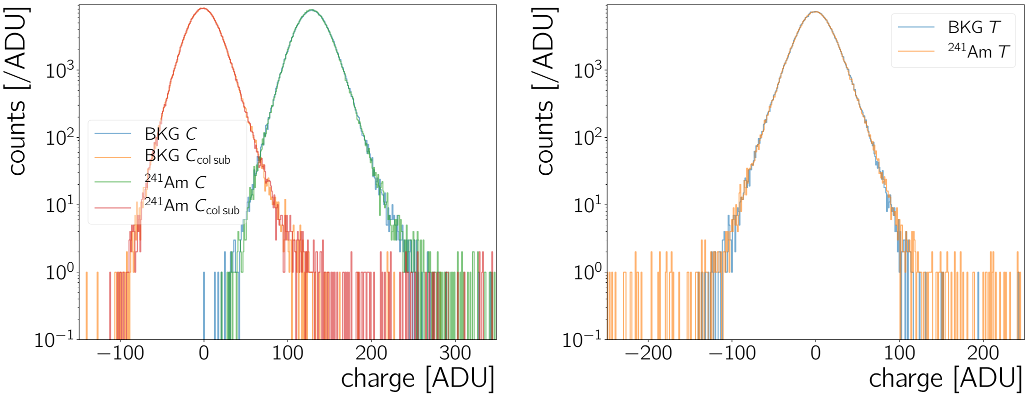

(a) (b)

Figure 3.4: 3.4a Histograms of the raw pixel values C of all pixels in the frame in Figure 3.3a (BKG C), Figure 3.3b (^{241}Am C), and of the $C_{\mathrm{col\,sub}}$ values calculated for the data in these frames using Equation (3.3). 3.4b Histogram of the $C_{\mathrm{col\,sub}}$ values after time-series subtraction (T, form Equation (3.4)).

than 0.5 % between two iterations. This iterative approach is necessary to exclude pixels with a high charge value as *e.g.* hot pixels – transient high values in a certain x, y position – or pixels with a higher charge value due to a signal induced by incident radiation. In the zoomed image in Figure 3.6a some pixels with a high charge value are visible with $C \geq 200$. After the final mean and standard deviation were found, that mean was subtracted from each pixel value:

$$C_{\mathrm{col\,sub}}(x, y, n_{\mathrm{f}}) = C(x, y, n_{\mathrm{f}}) - \langle C \rangle_{\mathrm{col}} (x_{\mathrm{k}}, n_{\mathrm{f}}) \tag{3.3}$$

x_k in $\langle C \rangle$ indicates that the column mean is the same for all the $C(x, y, n_{\mathrm{f}})$ along a column with $x = k$, i.e. in y direction.

The result of this column-pedestal correction procedure is shown in Figure 3.4a, for the raw data of Figure 3.3. A raw frame recorded during data taking with no source and with ^{241}Am has a mean of 129 ± 20 ADU and 130 ± 73 ADU, respectively, where the uncertainty is chosen to be one standard deviation. After the column correction the mean moves to 0 ± 18 ADU and 0 ± 73 ADU, respectively.

3.3.1.2 Time-series analysis

At this stage it is possible that there were still substructures in the recorded frames, *e.g.* pixels which have, in every frame, a C value elevated over the neighbouring pixel's values. These pixels may be hot pixels or pixels with charge values of a few 100 ADU. To correct for these a *time-series* approach was adopted: all charge values $C_{\mathrm{col\,sub}}(x, y, j)$ in the $n_{\mathrm{f}} = j$ frame in a run, with N_{f} frames in total, were subtracted from their corresponding values in the $n_{\mathrm{f}} = j + 1$ frame,

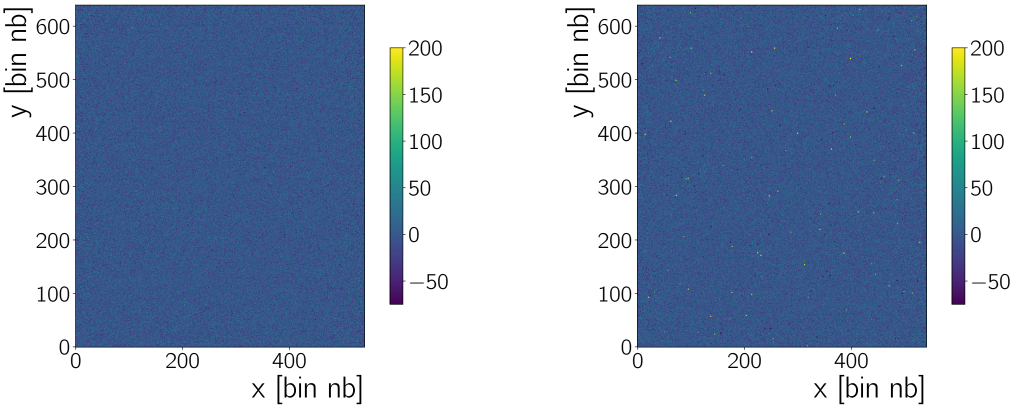

(a) BKG (b) ^{241}Am

Figure 3.5: Pair wise subtracted frames (*cf.* Section 3.3.1.2). The same frames as in Figure 3.3 are shown to illustrate this next step in the background rejection procedure. More high intensity points in the ^{241}Am frame than in the BKG frame are visble, when comparing the two plots.

$C_{\mathrm{col\,sub}}(x, y, j+1)$. The result were $N_\mathrm{f} - 1$ frames with pixel intensities $T(x, y, n_\mathrm{f})$ given by

$$T(x, y, n_\mathrm{f}) = C_{\mathrm{col\,sub}}(x, y, n_\mathrm{f}) - C_{\mathrm{col\,sub}}(x, y, n_\mathrm{f}+1) \qquad n_\mathrm{f} = 0 \ldots N_\mathrm{f} - 1 \quad . \tag{3.4}$$

The time series pair-wise subtraction removed effects that are persistent in time. Transient features, *e.g.* radiation from a source, may create negative entries during this procedure, *cf* Figure 3.6b. This can be tolerated as long as the source rate is not too high such that transient features occur at the same x, y coordinate in two subsequent frames. Figure 3.4b shows the effect on the 1D charge distributions. The tails of the distributions change due to the subtraction of transient pixels with a high charge value. This leads to a mean of 0 ± 21 ADU and 0 ± 112 ADU for the time-series corrected frame with no source and ^{241}Am, respectively. The standard deviation increases, as there are more negative pixel values in the distribution from the pairwise subtraction of transient features.

3.3.2 Clustering

The data, corrected for column and time-series subtraction following Equation (3.3) and Equation (3.4), were searched for clusters. A cluster is defined as one or more spatially adjacent pixels which have a charge value larger than the remaining pedestal value.

3.3.2.1 Threshold calculation

The threshold value was constructed by a data driven method: All $N_\mathrm{f} - 1$ individual values a pixel at coordinates $x = m, y = i$ measures over the course of a run were checked. In the notation introduced before, these values correspond to all $T(x, y, n_\mathrm{f})$, where x and y are held constant and

n_f runs from 0 to $N_\mathrm{f}-1$. From these charge values a run-averaged pixel pedestal value $p(x,y)$ and its standard deviation $\sigma_\mathrm{p}(x,y)$ were calculated for all pixels at coordinates x, y.

$$p\,(x,y) = \langle\, T\,\rangle\,(x,y) = \frac{1}{N_\mathrm{f}-1}\sum_{n_\mathrm{f}=0}^{N_\mathrm{f}-1} T(x,y,n_\mathrm{f}) \tag{3.5}$$

$$\sigma_\mathrm{p}\,(x,y) = \sqrt{\frac{1}{N_\mathrm{f}-2}\sum_{n_\mathrm{f}=0}^{N_\mathrm{f}-1}\left(T(x,y,n_\mathrm{f}) - p\,(x,y)\right)^2}\quad , \qquad x = m, y = i \tag{3.6}$$

This is an iterative procedure, similar to what is done to calculate the column mean. From subsequent iterations all pixel values $T(x,y,n_\mathrm{f}) \notin p\,(x,y) \pm 5\cdot\sigma_\mathrm{p}\,(x,y)$ are rejected when using Equation (3.5) and Equation (3.6) to (re)calculate $p(x,y)$ and $\sigma_\mathrm{p}\,(x,y)$. Both values are regarded as final when $\sigma_\mathrm{p}\,(x,y)$ changes less than 0.5 % between two iterations. While $p(x,y)$ is by construction close to zero for column subtracted and time-series subtracted data, $\sigma_\mathrm{p}\,(x,y)$ has a minimal value slightly above 6 ADU and most probable value between 14 ADU and 15 ADU, skewed towards higher values. Without time-series subtraction and column correction, the pedestal values and their standard deviation for every pixel should allow discrimination between background and a charge signal, provided the fluctuations of the background are randomly distributed. However, the column mean of a specific column changes from exposure to exposure, motivating the approach described here. The camera's manual states a read noise RMS value of $1.5\,\mathrm{e}^-$. Converting to ADU, ~2.24 ADU is obtained, using the conversion factor of $0.67\,\mathrm{e}^-/\mathrm{ADU}$ as specified by the supplier. The modification of this RMS value by the column correction and the pair-wise subtraction have to be taken into account before comparing the RMS to $\sigma_\mathrm{p}\,(x,y)$. While the corrections described in Section 3.3.1.1 lead to a negligible reduction of the RMS, the pairwise subtraction described in Section 3.3.1.2 increases the resulting RMS by a factor of $\sqrt{2}$. The smallest measured $\sigma_\mathrm{p}\,(x,y)$ value of $\gtrsim$ 6 ADU is larger than this expectation of 3.17 ADU, indicating that the corrections applied here do not remove all noise contributions other than the read-noise.

3.3.2.2 Cluster finding

The cluster finding algorithm employed two values, a *seed* and a *skirt* pixel threshold intensity. The *seed* is a higher threshold value designed to quickly find the cluster's largest charge values. The *skirt* is a lower threshold value designed to find potentially dimmer adjacent pixels to the *seed* pixel associated with the cluster. The following threshold condition was used to discriminate whether a pixel value $T(x,y,n_\mathrm{f})$ was part of the background or part of the charge deposit of a signal *e.g.* by radiation incident on the chip:

$$T(x,y,n_\mathrm{f}) > p\,(x,y) + k\cdot\sigma_\mathrm{p}\,(x,y) \qquad k = k_\mathrm{seed} \vee k_\mathrm{skirt} \tag{3.7}$$

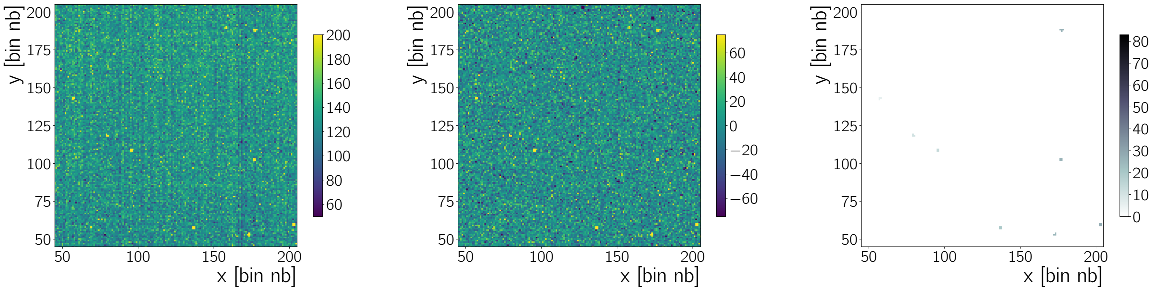

(a) raw (b) corrections applied (c) found clusters

Figure 3.6: Detail view 3.6a of the frame in Figure 3.3b – raw frame without corrections applied – and 3.6b of the frame in Figure 3.5b, pair wise subtracted frame. 3.6c Identified clusters in the zoomed image shown in 3.6b using $k_{\text{seed}} = 10$ and $k_{\text{skirt}} = 3$ as parameters for the cluster finding thresholds, *cf.* Section 3.3.2, Equation (3.7). The scale to the right of the image shows the cluster number.

Two cases (k_{seed} or k_{skirt}) are distinguished for the multiplier k. First, the factor to find the seed pixel for a cluster (k_{seed}). After the seed pixel has been found its vicinity is checked for pixels fulfilling Equation (3.7) with k_{skirt}, where $k_{\text{skirt}} \leq k_{\text{seed}}$. All contiguous pixels with charge values larger than the skirt threshold, as well as the seed pixel, constitute one cluster. For each cluster its defining properties are stored, such as size, charge, x, y position, frame number, pedestal value and an identification number (*cf.* Section 3.4). Figure 3.6c shows the clusters identified in the previously shown zoomed image of a frame taken with the ^{241}Am source.

The parameter k_{seed} and k_{skirt} were optimised using background data, while aiming for a low cluster count per recorded frame and a small cluster size. Clusters in the background data are due to cosmic radiation passing through the chip, noise fluctuations and radiation from natural radio-isotopes. For these sources a cluster with a small size is expected – especially since 4×4 readout binning is used – since γ- and X-ray photons should deposit their energy localised and it is not likely that cosmic muons or β particles pass exactly parallel through the chip [158]. With $k_{\text{seed}} = 10$ less than 0.5 clusters per frame are found while a further increase to *e.g.* $k_{\text{seed}} = 20$ does not result in a further reduction. The cluster size decreases exponentially with k_{skirt} and approaches a mean of ∼3 clusters for all tested k_{seed} values. The change is no longer significant for $k_{\text{skirt}} \geq 3$. Therefore, $k_{\text{seed}} = 10$ and $k_{\text{skirt}} = 3$ were used during analysis. Using $k_{\text{seed}} = 10$ and $k_{\text{skirt}} = 3$ reduces the amount of background clusters found as stated before. When combined with additional cuts on cluster properties, as discussed in Section 3.4, these cluster finding settings allow to create almost background free samples.

3.3.2.3 Cluster parameters

For each cluster, the following properties were stored:

- the frame number

Energy	Source	Intensity
13.8 keV	Np: $L_{\alpha 1}$, X-ray	
17.8 keV	Np: $L_{\beta 1}$, X-ray	
20.8 keV	Np: $L_{\gamma 1}$, X-ray	
26.3 keV	^{241}Am: γ	2.3 %
59.5 keV	^{241}Am: γ	35.9 %

Table 3.2: Expected lines in the decay spectrum of ^{241}Am based on data from [44, 159]. Np X-rays in the energy region from 11.87 keV to 22.4 keV are expected to make up for another 37 % of intensity [44]. The X-ray energies are approximate and are composed of several overlapping lines. Therefore no intensities are given, since these require assumptions on the detector's energy resolution.

- the cluster number, which is a counter for all clusters in one frame
- the x/y position, *i.e* the coordinates of the seed pixel
- the cluster *size*, *i.e* how many pixels make up a cluster
- the *cluster charge*, *i.e* the integral over all $T(x, y, n_\mathrm{f})$ in a cluster subtracted by the cluster pedestal. In case of the time-series approach $p\,(x, y) \sim 0$. Without the time-series approach subtracting the cluster pedestal is essential since it is different from zero.
- the *cluster pedestal*, *i.e* the integral over all the clusters pixels' $p\,(x, y)$
- the charge of the pixel with the highest charge in the cluster (*maximal charge*).

Figure 3.7a and Figure 3.7b show the cluster charge and the maximal charge without additional cuts on cluster properties. In some data taking runs the camera took a short time to reach a stable state. Therefore, as a precaution, clusters of the first five frames of each run were not used. Occasional runs with no-stable camera conditions have in general been rejected.

Cluster charge and maximal charge spectra of the background data peak at a few 100 ADU, seen in Figure 3.7b, and have a tail towards higher values. Their most probable cluster size is ∼2 pixel – Figure 3.7d. The shape of the spectra and the cluster size are compatible with the expectations that the background counts are created by noise fluctuations and cosmic radiation (muons) passing through the chip.

A clear peak-structure is observed in the case of the ^{241}Am data in Figure 3.7a. The charge of a cluster should be proportional to the energy deposited by the incident radiation. From ^{241}Am-decay energy spectra in the literature there should be five prominent lines [159, 160] at energies stated in Table 3.2. The spectra presented here show five prominent peaks, which will be discussed in detail in Section 3.4.1 – Figure 3.7, first column.

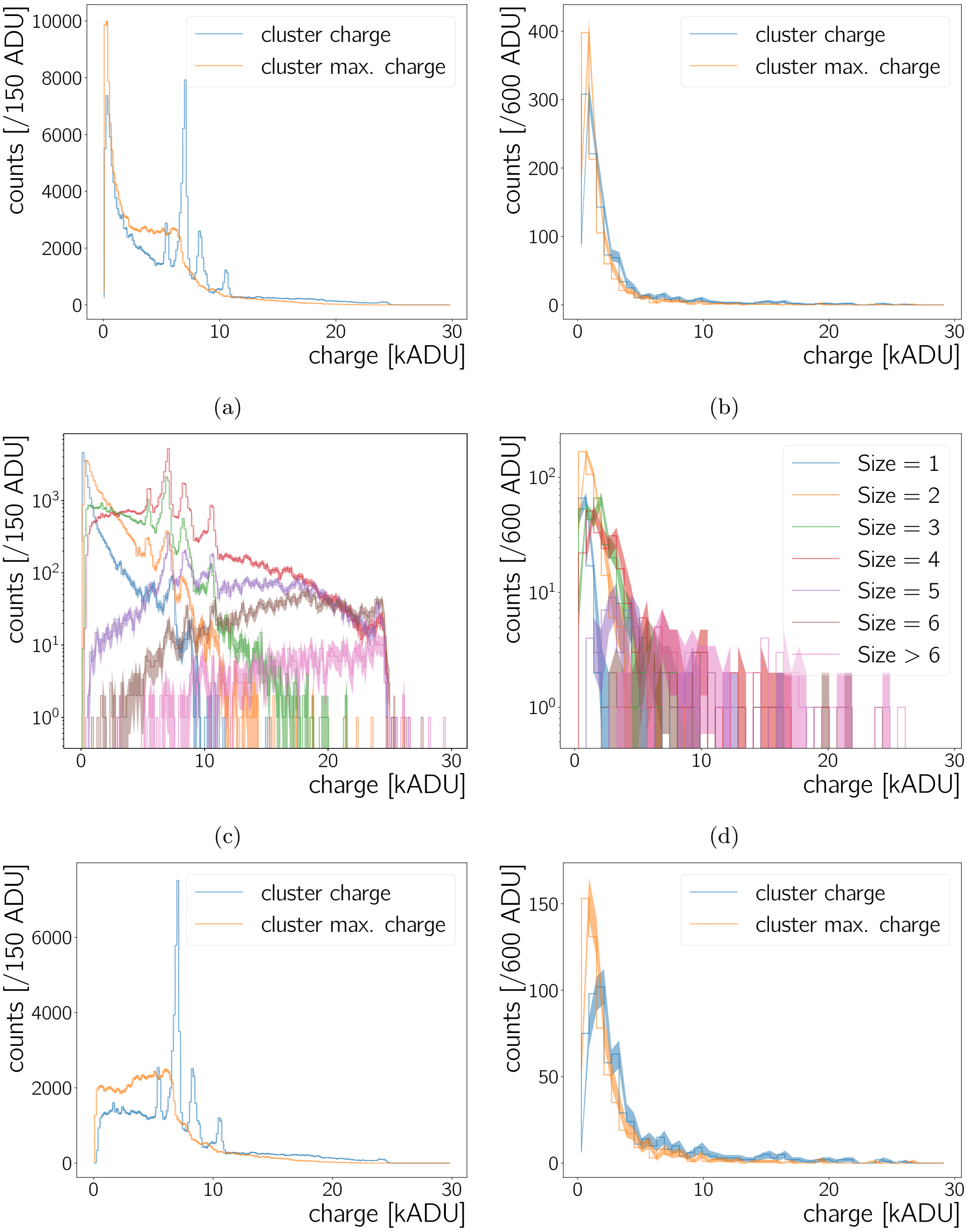

(a) (b)

(c) (d)

(e) (f)

Figure 3.7: The plots show cluster charge and maximal charge spectra for ^{241}Am data in the left column (3.7a, 3.7c, and 3.7e), and for background data in the right column (3.7b, 3.7d and 3.7f). As energy unit kilo ADU, *i.e* kADU, is used. The live-time of the camera during the ^{241}Am data taking is 2470 s where the camera is radiated with the corresponding source, while the live-time for the background data taking as 2945 s. The first row shows spectra containing all clusters, the second row shows cluster charge spectra grouped by cluster size in logarithmic scale while third row shows all data displayed in the first column, which passed a size $>$ 2 cut. Note the larger binning in the second column. The labels in Figure 3.7c have been omitted to enhance visibility, but they match those in Figure 3.7d.

3.3.2.4 Sizes of identified clusters

The peaks visible in Figures 3.7a and 3.7e sit on a floor which is itself related to the decay radiation of the source. Examining the cluster charge spectrum as a function of the cluster size (Figure 3.7c) shows that this floor is mainly due to clusters with a size of 1 and 2 pixels. For cluster sizes larger than four pixels the peak heights decrease again. There is a correlation between cluster size and cluster charge, i.e. energy deposited in the sensor. For increasing cluster size the ratio of clusters with a large charge value to ones with a low charge value increases. Gamma radiation and X-rays are expected to interact in the CMOS sensor and to release their energy locally. Therefore, the observed cluster sizes are larger than expected, even more so, given the readout binning of 4×4, resulting side length per readout pixel of $4 \times 6.5\,\mu\mathrm{m} = 26\,\mu\mathrm{m}$ each. As stated in Section 3.2 the exact layout of the actual CMOS is not known – its different layers may lead to a spread of the charge which reaches a few 10 µm. Incident radiation can *e.g.* be absorbed in a non-active layer of the chip and then diffuse towards the collection zones. Another possible explanation is that a substantial fraction of the incoming γ energy gets transferred to a few δ-electrons which can then travel more than a pixel length in the sensor, while they produce further ionisation. It can be excluded that the cluster size gets inflated by pixels accidentally assigned to the respective cluster. Comparing the spectrum where only the most energetic pixel per cluster is shown (maximal charge) with the cluster charge spectrum shows that the information from the lower energy pixels in a cluster is needed to measure a spectrum with distinguishable peaks (Figure 3.7a and Figure 3.7e).

For the analysis of the Neo sCMOS' calorimetric response the cluster size needs to be larger than 2 pixels to improve the quality of the peak spectrum and reduce noise contributions. Figure 3.7e shows the data displayed in Figure 3.7a but with a size > 2 pixels cut. Approximately half of the entries in the background spectrum are removed when this cut is applied to the background data – Figure 3.7f vs Figure 3.7b.

3.4 Performance of the CMOS as radiation detector

3.4.1 Calorimetric capabilities of the Neo sCMOS

The camera response to ^{55}Fe, ^{210}Pb,^{241}Am, ^{133}Ba and ^{137}Cs source radiation was examined to determine the Neo sCMOS' calorimetric measurement capabilities. Figure 3.8 and Figure 3.9 show cluster charge spectra measured for these sources. To create these, the analysis procedures detailed in Section 3.3 were applied to the raw frames and a cluster size larger than two pixels was required for all entries in the plots.

The contribution of the source radiation to the spectra has to be disentangled from the contribution of the ambient background radiation. To this end, spectra obtained with radioactive sources

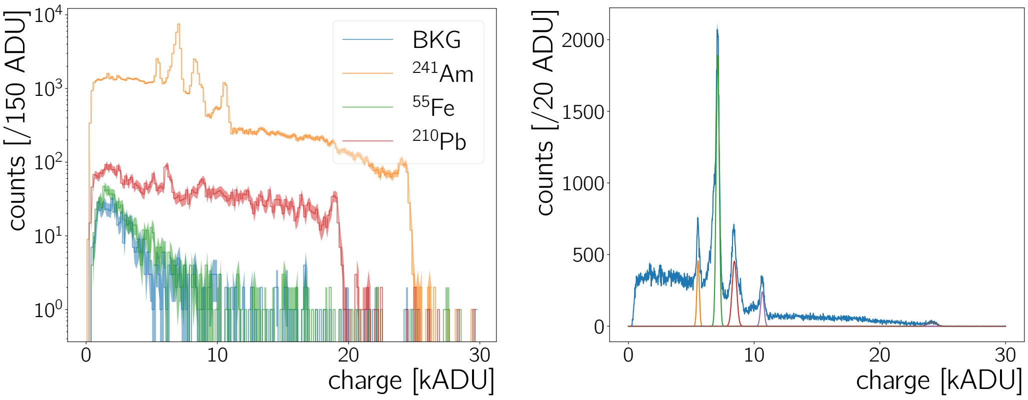

(a) Combined plot of ^{55}Fe, ^{210}Pb,^{241}Am and background

(b) ^{241}Am spectrum, counts scaled

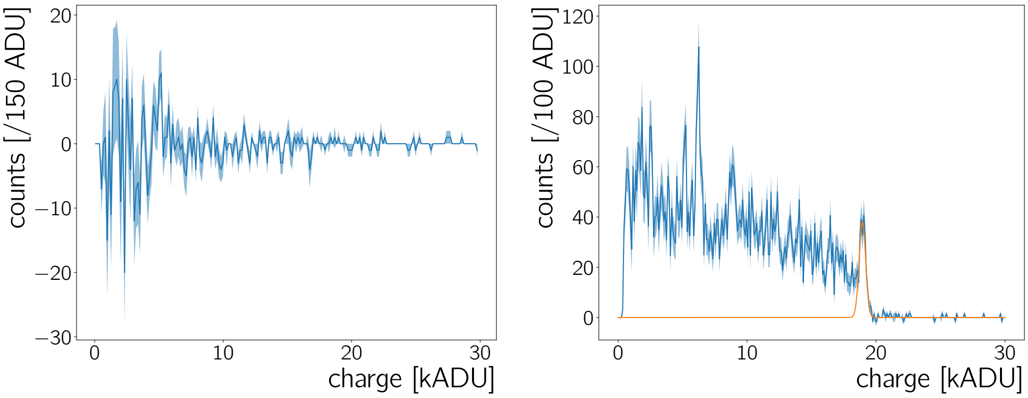

(c) ^{55}Fe spectrum, counts scaled

(d) ^{210}Pb spectrum, counts scaled

Figure 3.8: 3.8a Combined plot showing an overview of different data sets acquired with the Neo sCMOS. The live-time of the background (^{241}Am, ^{55}Fe and ^{210}Pb, respectively) measurement is 29 450 s (24 700 s, 41 800 s and 30 400 s, respectively). The spectra are shown on a log scale for better visibility since the rates of the sources vary as does the observed event rate. 3.8b, 3.8c, 3.8d shows spectra for the respective sources. These spectra have been scaled to a live-time of 47 500 s and are subtracted with the background spectrum scaled to the same live-time. Shaded regions represent the statistical error. For all plots a cluster size > 2 pixels is required. The spectra in 3.8b and 3.8d illustrate furthermore the peaks fitted with Gaussian functions, *cf.* Section 3.4.1.1. (Note that only the Gaussians are plotted, and not the additionally fitted backgrounds.)

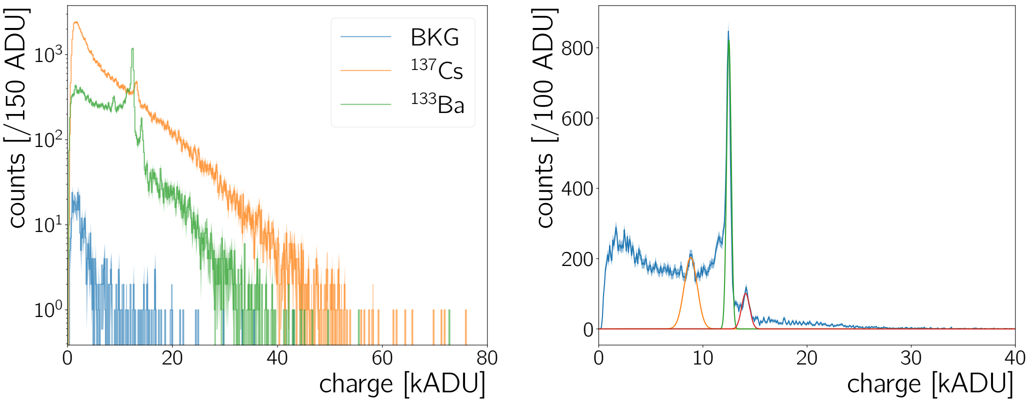

(a) Combined plot of ^{133}Ba and ^{137}Cs

(b) ^{133}Ba spectrum

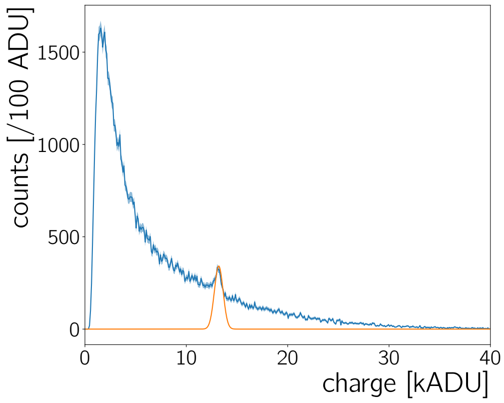

(c) ^{137}Cs spectrum

Figure 3.9: 3.9a Combined plot showing an overview of the different data sets acquired with the Neo sCMOS. The live-time of the background, ^{133}Ba and ^{137}Cs measurements is 15 200 s. The spectra are shown on a log scale for better visibility since the rates of the sources vary as does the observed event rate. 3.9b and 3.9c shows spectra for the respective sources. These spectra are subtracted with the background spectrum scaled to the same live-time. For all plots a cluster size > 2 pixels is required. The spectra in 3.9b and 3.9c illustrate the peaks fitted with Gaussian functions, *cf.* Section 3.4.1.1. (Note that only the Gaussians are plotted, and not the additionally fitted backgrounds.)

Source	Activity (kBq)
^{241}Am	344 ± 17
^{55}Fe	98.6 ± 29.6
^{210}Pb	185 ± 9
^{133}Ba	83 ± 4
^{137}Cs	161 ± 8

Table 3.3: List of sources used to assess the calorimetric capabilities of the Neo sCMOS, with their activities shown at the time of measurement. Where the uncertainty on the initial source activity is not known, a 5 % error is assumed.

and the background spectrum were normalised to the same live-time and then the background spectrum was subtracted from the source spectra. The results are shown in Figure 3.8b to Figure 3.8d and in Figure 3.9b to Figure 3.9c. The activities of the radioactive sources are shown in Table 3.3.

^{241}Am: The clearest spectrum was obtained with the ^{241}Am source. Americium-241 decays via an α-decay to ^{237}Np. There are many possible α-decays with different Q values from 5000 keV to 5500 keV [44], where the most probable (85 %) decay has an energy of 5485 keV. These α-decays occur together with γ ray emission and X-ray emission by the ^{237}Np atom [44]. Table 3.2 lists the two γ energies with the largest yield per decay as well as X-ray lines measured in ^{241}Am spectra elsewhere. The CMOS chip of the Neo sCMOS camera is housed behind a glass window, with an assumed thickness of 1 mm – therefore the α-particles will not reach the sensor, as the range of αs of this energy is less than 100 µm [161]. The energy deposits measured with the ^{241}Am source are thus due to γ- and X-rays. Attenuation lengths for different γ- and X-ray energies are given in Table 3.4.

^{55}Fe: Iron-55 decays via electron capture to ^{55}Mn [44]. After the decay, the electron shell rearranges to match the levels of ^{55}Mn and to fill the hole from the electron capture. Auger-Meitner electrons with an energy of up to 6 keV and X-rays of 5.9 keV and 6.5 keV are released. For these X-ray energies the yield per decay is 16.6 % and 7 %, respectively. The background subtracted spectrum in Figure 3.8c is compatible with zero. For low charge values, *i.e* low energy deposits, the spectrum is more erratic – however, no clear peak can be identified. The photon absorption in glass for energies $\leq$ 10 keV is estimated with the data from [162]. For a window of 1 mm and 2 mm, almost 97 % and 99.04 % of the X-rays are absorbed in the glass before they reach the chip, respectively. Therefore, the non observation of any clear peak is most likely due to the X-ray absorption in the Neo sCMOS window.

^{210}Pb: Lead-210 decays via β^- decay to ^{210}Bi as mentioned in Section 1.2.2. The ^{210}Pb source holds the lead diluted in nitric acid in a small glass vial. It is not likely that any of the low energy

Energy [keV]	Attenuation length/ Range in Silicon	
	γ-/X-ray	β^-
10	111 µm	1.2 µm
15	365 µm	2.5 µm
45	7 mm	16 µm
60	12 mm	28 µm
100	20 mm	66 µm
1000	59 mm	2 mm

Table 3.4: Approximate ranges of γ rays and β^-s (electrons) for typical decay energies in Silicon. For the γ rays the attenuation length is calculated from the attenuation cross section given in [163] using the density of silicon-dioxide. The same density is used to calculate the electron range from the CSDA range for electrons given in [164].

β-radiation is detected by the Neo sCMOS, given that the decay electrons have to traverse the liquid, the glass of the vial and the window of the Neo sCMOS before it can be detected by the CMOS chip. Therefore, similarly to the ^{241}Am source, only the X-rays and γ rays are measured. The ^{210}Pb spectrum in Figure 3.8d contains fewer counts than the ^{241}Am spectrum (Figure 3.8b). There are several factors contributing to this: First, the activity of the ^{210}Pb source is a factor of 1.85 lower than the activity of the ^{241}Am source. The latter source also has a significantly smaller extent – compared to the CMOS sensor it can be considered as a point source, while the lead source extends over a vial of more than 1 cm length and 0.5 cm diameter. Additionally, the γ yield for the two sources differs greatly – comparing ∼4 % to ∼36 % for the ^{210}Pb 46.5 keV γ ray and the ^{241}Am 59.5 keV γ ray. To establish whether the ^{241}Am and ^{210}Pb spectra are consistent with each other, we first need to establish the overall energy scale and compare peaks at a known energy directly. This is done in Section 3.4.1.1.

^{133}Ba: Barium-133 decays via electron capture to ^{133}Cs, with γ and X-ray emission. 356 keV is the γ energy with the largest yield per decay, $62.05 \pm 0.19\,\%$. X-rays decay with energies between $30.5 - 35.8$ keV [44]. Two peaks consistent with the X-ray energies of 30.5 keV and 34.9 keV are seen in Figure 3.9b. A third peak is also visible, at an energy of ∼ 21 keV. Literature returned no X-ray or γ-Ray emission consistent with this value. A planar high purity germanium low energy radiation detector was used to assess if this unknown peak was the result of a higher energy γ-Ray emission being attenuated by the CMOS glass window. The unknown peak is visible, ruling out any attenuation by the CMOS glass window or other artifacts. This unknown peak is observed in [165], but there is no mention of its energy or origin, therefore it will not be considered when calculating the energy response calibration in Section 3.4.1.1.

^{137}Cs: The source decays via β^- decay to ^{137}Ba, with γ and X-ray emission. Its main γ decay has an energy of 661 keV, with an yield per decay equal to 85.1 %. The X-rays decays have energies between $31 - 37$ keV. As seen in Figure 3.9c, the CMOS chip is capable of detecting the X-ray energy of 31.8 keV and the β decay spectrum energy, up to the Q value of 174.32 keV, which has

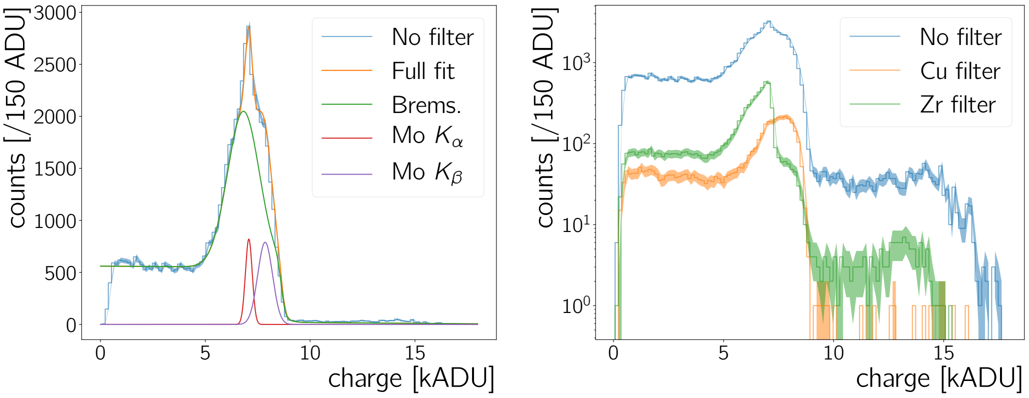

(a) (b)

Figure 3.10: 3.10a Spectrum recorded with the molybdenum X-ray tube (*cf.* Section 3.2.1) as well as fitted curves to establish the position of the K_α and K_β peak. 3.10b The same data as in 3.10a is shown together with data recorded when a Zr or a Cu filter is placed between the X-ray tube with Mo target and the Neo sCMOS. For this plot all data has been normalised to a live-time of 50 ms and a cluster size > 2 pixels is required. Shaded regions indicate the statistical error.

a decay probability of 94.7 % [44]. This demonstrates that the CMOS is sensitive to energies of at least 180 keV. It would be of interest to repeat these measurements with more energetic sources, to understand if the CMOS can measure energies beyond 180 keV.

3.4.1.1 Energy response calibration

All the spectra presented so far are shown with *analogue-to-digital* units as unit of the deposited energy in the detector. The Neo sCMOS's manuals consulted during this work do not state a conversion factor from ADU to energy in eV. However, the report [166] specifies a gain of either $0.59\,\mathrm{e}^-/\mathrm{ADU}$ or $0.67\,\mathrm{e}^-/\mathrm{ADU}$ according to the supplier. These gain values translate to a conversion factor of either 2.154 eV/ADU or 2.446 eV/ADU, respectively, accounting for the W factor in Si of 3.65 eV to create an electron-hole-pair [167]. To establish the exact energy scale, the known energies of radioactive sources from literature were matched to the ADU values at which peaks are observed. All discernible peaks in the cluster charge spectra were fitted with a Gaussian curve and their mean energy, $\varepsilon_{\mathrm{peak}}$, and σ was extracted. Table 3.5 lists all peaks used for this analysis and the result of the fits. The Gaussians are plotted in Figure 3.8b, Figure 3.8d, Figure 3.9b, Figure 3.9c and Figure 3.10a. The fits were done locally – in the ranges from $\varepsilon_{\mathrm{min}}$ to $\varepsilon_{\mathrm{max}}$ as specified in Table 3.5 – and where necessary a polynomial of order one was added to the Gaussian curve to account for the floor due to other radiation. For the peaks at the high energy end of the ^{241}Am and ^{210}Pb spectrum an error-function was used instead of a polynomial – Figure 3.11.

The second, independent, dataset to obtain the energy scale calibration used measurements where the CMOS was irradiated by an X-ray tube, described in Section 3.2. For the spectra

Source		^{241}Am					^{210}Pb	Mo X-ray tube			^{133}Ba			^{137}Cs
Radiation		γ		X-ray (Np)			γ	X-ray		Zr edge		X-ray		X-ray
Expected energy [keV]		26.3	59.5	13.8	17.8	20.8	46.5	17.4	19.6	18.0	-	30.5	34.9	32.1
Fit range	ε_{min} [kADU]	9.87	23.49	4.99	6.01	7.78	18.37	1		n.a.	8.4	12.1	13.7	12.7
	ε_{max} [kADU]	11.45	24.5	6.12	7.9	9.99	19.64	15		n.a.	9.3	13.0	14.5	13.6
Fit result	$\varepsilon_{\text{peak}}$ [kADU]	10.65	24.13	5.54	7.1	8.37	18.94	7.08	7.85	7.3	8.8	12.4	14.1	13.2
	σ_{peak} [ADU]	133	276	95	124	199	239	163	353	n.a.	622	217	388	427
	χ^2/N_{dof}	1.22	1.05	1.61	2.2	1.32	0.77	4.62		n.a.	5.42	7.22	6.97	0.41

Table 3.5: The table lists the fit results (peak position $\varepsilon_{\text{peak}}$ and standard deviation σ) of Gaussian peak fits in Figures 3.8b, 3.8d, 3.9b, 3.9c and 3.10a as well as the absorption edge estimated from 3.10b. (Since the properties of the absorption edge are not determined by a fit, the corresponding values in the "Zr edge" column are labelled *n.a.* for non applicable.). The *expected energies* have been extracted from [44] and the Zr absorption edge form [163].

obtained with the X-ray tube using only Gaussian fits with a local background was not sufficient – Figure 3.10a: the two characteristic peaks of the molybdenum X-ray tube are expected to be located on top of the *bremsstrahlung* spectrum of the tube. For low X-ray energies the camera has negligible calorimetric capabilities as seen in the measurements with the ^{55}Fe source – previous section, Figure 3.8c. Hence, the Neo sCMOS should become efficient for X-rays of the molybdenum X-ray tube somewhere after ~6 keV – from that point onwards there should be an increasing number of counts due to *bremsstrahlung* and eventually the molybdenum K_α and K_β peaks at 17.4 keV and 19.6 keV, respectively. Figure 3.10a shows the spectrum, the fit to the spectrum, and the fit's components. An onset of counts is observed at ~5 kADU however, no clear double peak structure is observed. As there is no clear expected functional shape for the bremsstrahlung contribution, it is modelled as the minimal functional addition ($Brems(\varepsilon)$) needed so $Brems(\varepsilon) + Gau\beta(\varepsilon)_{\mathrm{K}_\alpha} + Gau\beta(\varepsilon)_{\mathrm{K}_\beta}$ fits the data well.

$$Brems\,(\varepsilon) = p_0 \cdot \exp\left(-\frac{1}{2}\left(\frac{\varepsilon - p_1}{\sigma}\right)^2\right) + p_2 \cdot \Big(1 - \mathrm{erf}\big(p_3 \cdot (\varepsilon - p_4)\big)\Big) + p_5 \cdot \varepsilon + p_6 \tag{3.8}$$

$$Gau\beta(\varepsilon)_{\mathrm{K}_j} = p_0^j \cdot \exp\left(-\frac{1}{2}\left(\frac{\varepsilon - \varepsilon^j_{\mathrm{peak}}}{\sigma^j}\right)^2\right) \qquad j = \alpha \vee \beta \tag{3.9}$$

In these equations ε is the cluster charge, or energy deposited in the chip, in ADU. The parametrisation (3.8) for the bremsstrahlung contribution yields the lowest χ^2/N_{dof} of 4.62 for the total fit of $Brems(\varepsilon) + Gau\beta(\varepsilon)_{K_\alpha} + Gau\beta(\varepsilon)_{K_\beta}$ to the data, whilst all fit parameters are free. The extracted parameters of the two K lines ($\varepsilon_{\mathrm{peak}}$, σ_{peak}) are listed in Table 3.5.

Using a Cu or a Zr foil to filter the molybdenum X-rays results in the spectra shown in Figure 3.10b. The absorption edges of those two elements for energies higher than ~6 keV are at 8.98 keV (Cu) and at 18 keV (Zr). The shape of the spectrum recorded with the Cu filter does not feature a drop which can be identified with an absorption edge – the edge is thus placed in the energy range where the Neo sCMOS is not sensitive to allow X-ray calorimetry. There is a larger reduction of counts for energies $\lesssim 7$ kADU, relative to the not filtered spectrum and the one with the Zr filter. After, the number of counts increases again. Starting from low energies, the shape of spectrum with the zirconium filter matches the un-filtered spectrum, until the edge at ~7.5 kADU. This drop is identified with the Zr absorption edge. The ADU value at which the amplitude reaches the 50 % value between maximal peak height and the floor in the spectrum is taken as its energy position –Table 3.5. The uncertainty on the edge's position is taken to be half of the ADU range between the edge's 10 % and 90 % value.

Figure 3.11a displays the measured charge values plotted against their expected energies for all peaks and edges in Table 3.5. Fitting a linear function without an axis intercept to these

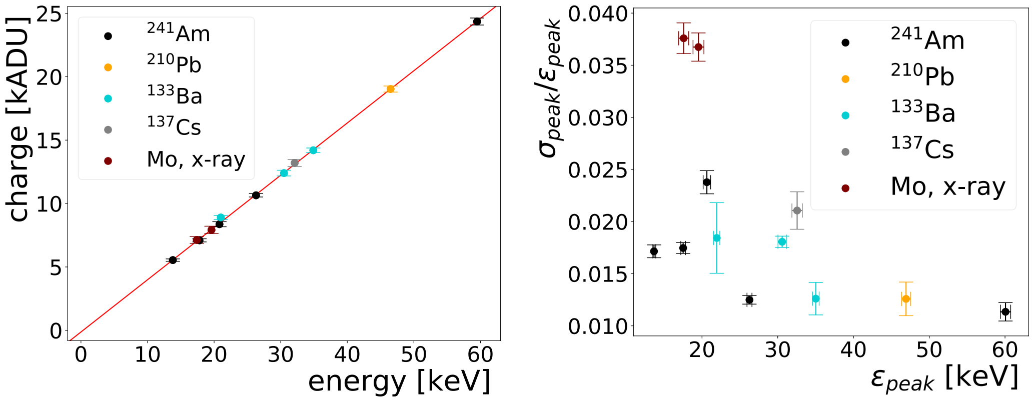

(a) (b)

Figure 3.11: 3.11a Comparison between the expected and the measured peak and edge energies ($\varepsilon_{\text{peak}}$) in Table 3.5. One σ_{peak} of the peak is used as uncertainty for $\varepsilon_{\text{peak}}$ and the red line through the points is a fit without an additional axis intercept. 3.11b Measured energy resolution ($\sigma_{\text{peak}}/\varepsilon_{\text{peak}}$) as function of the measured peak position. The boxes indicate to what spectrum a given peak belongs to.

points yields the conversion factor from eV to ADU (and vice versa) to be 0.406 ± 0.001 ADU/eV (2.463 ± 0.007 eV/ADU). For this fit χ^2/N_{dof} is 1.71 while using a function with an intercept results in a χ^2/N_{dof} of 0.54, an intercept of 0.42 ± 0.09 keV, and a slope of 2.426 ± 0.008 eV/ADU (0.41 ± 0.01 ADU/eV). These values are compatible with the conversion factor mentioned before, although slightly different from an intercept of zero. In the next sections the conversion factor without an intercept is favoured over the conversion with an intercept, since the low χ^2/N_{dof} in the latter case indicates over-fitting.

The measured conversion factors matches well with the higher of the two gain values discussed before, i.e. 2.446 eV/ADU which is located between the two different fit values. This agreement is taken as another reason to use the conversion factor determined without an intercept, given the supplier does not specify an offset.

3.4.1.2 Energy resolution

In Figure 3.11b the energy resolution is shown as σ_{peak} divided by their positions $\varepsilon_{\text{peak}}$ – Table 3.5. The uncertainty of the fit represents the uncertainty on σ while σ_{peak} itself is used as the uncertainty of the peak position $\varepsilon_{\text{peak}}$. The uncertainty on the energy resolution, $\Delta\left(\sigma_{\text{peak}}/\varepsilon_{\text{peak}}\right)$ includes both of these contributions. For the most part the resolution is better than 2 %. Outliers from this trend are the two molybdenum X-ray lines and the Np, $L_{\gamma 1}$ line (at ~20 keV). The two X-ray lines are extracted from a more complicated fit with the worst χ^2/N_{dof} and the uncertainty on their σ_{peak} values is likely to be underestimated.

3.4.2 Radiation detection efficiency

In this section the minimum detectable decay rate is quantified using the Neo sCMOS, and the efficiency of the sensor as a detector for γ- and X-rays is measured. Both are done using the ^{241}Am source, as this source has a well suited activity and an energy spectrum with clear peaks.

3.4.2.1 Geometric acceptance of the experimental set-up

The fraction of the ^{241}Am activity detected by the sensor depends on the source-detector distance. The geometric acceptance (ϵ_{G}) is calculated assuming the ^{241}Am emits radiation as a point source, as

$$\begin{aligned} \epsilon_{\mathrm{G}} &= \frac{A_{\text{spherical cap}}}{A_{\text{sphere}}} \frac{A_{\text{camera}}}{A_{\bigcirc\ \text{camera plane}}} \\ &= \frac{0.0889\,\mathrm{cm}^2}{r^2} \qquad (r \text{ in cm}) \end{aligned} \tag{3.10}$$

The calculation of this expression exploits the sphere into which the source emits radiation and its intersection with the plane of the camera chip. Therefore, A_{sphere} is the surface area of that sphere, $A_{\text{spherical cap}}$ is the surface area of the base of the spherical cone covering the camera chip, $A_{\bigcirc\ \text{camera plane}}$ is the corresponding surface area of an otherwise similar cone with a flat base and A_{camera} is the surface area of the camera and r is the camera to source distance - Figure 3.12.

Figure 3.13 compares the analytical estimate of Equation (3.10) with a toy Monte Carlo simulation, showing good consistency. The simulation assumed a source with a radius of $6.2 \pm 0.1\,\mathrm{mm}$ that decays 1200 times. It calculated the geometric acceptance for decays between distances of $1.75 \pm 0.04\,\mathrm{cm}$ and $258.55 \pm 0.04\,\mathrm{cm}$.

3.4.2.2 Minimum detectable decay rate

Data is acquired for 3800 s each at distances from 1.8 cm up to 258.6 cm between source and sensor. The detected spectra, the inferred incident activity using the geometric acceptance from Equation (3.10) and the known source activity are shown in Figure 3.14. At a distance of $258.6 \pm 0.1\,\mathrm{cm}$ this activity is as low as $0.42 \pm 0.24\,\mathrm{Bq}$. Given the background spectrum dominates at lower energies, it is of interest to look at the CMOS' sensitivity at higher energies. Thus, the incident activity was determined considering only certain γ ray energies emitted by the ^{241}Am source, as opposed to the full source activity. These are obtained by multiplying the incident activity for all ^{241}Am decays by the respective peak yields which are $2.40 \pm 0.04\,\%$ and $35.9 \pm 0.4\,\%$ for the 26.3 keV and 59.5 keV energy peaks, respectively [44]. These incident activities can be seen in Figure 3.14a.

To obtain the uncertainty on the incident activities in this figure the distance uncertainty is propagated through the calculations in Equation (3.10), as well as the uncertainty of the initial

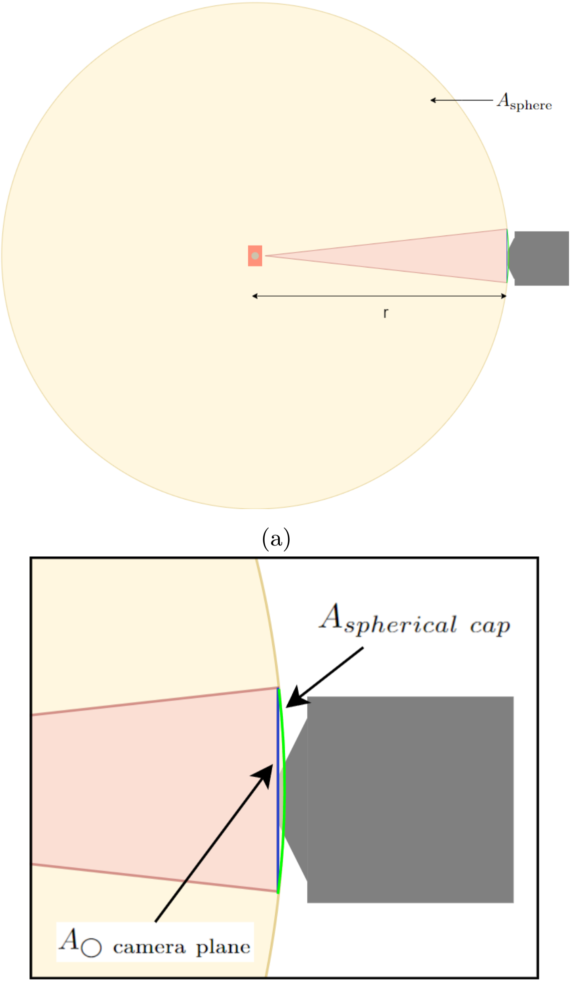

(a)

(b)

Figure 3.12: Diagram describing geometric acceptance calculation. 3.12a The circle in yellow represents the sphere, A_{sphere}, resultant from the emission of radiation from the source, in red in the middle, with the CMOS positioned on the right, in black. 3.12b shows Figure 3.12a zoomed into the CMOS region, showing the $A_{spherical\ cap}$ in green and the $A_{\bigcirc\ \text{camera plane}}$ in blue.

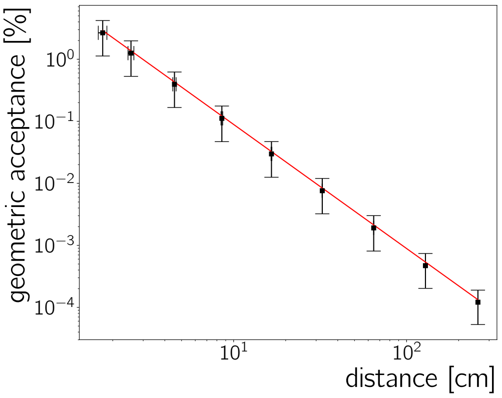

Figure 3.13: Geometric acceptance of the experimental set-up with the Neo sCMOS: Shown is the analytical function for a point source in Equation (3.10) and values from a toy Monte Carlo resembling the actual source geometry.

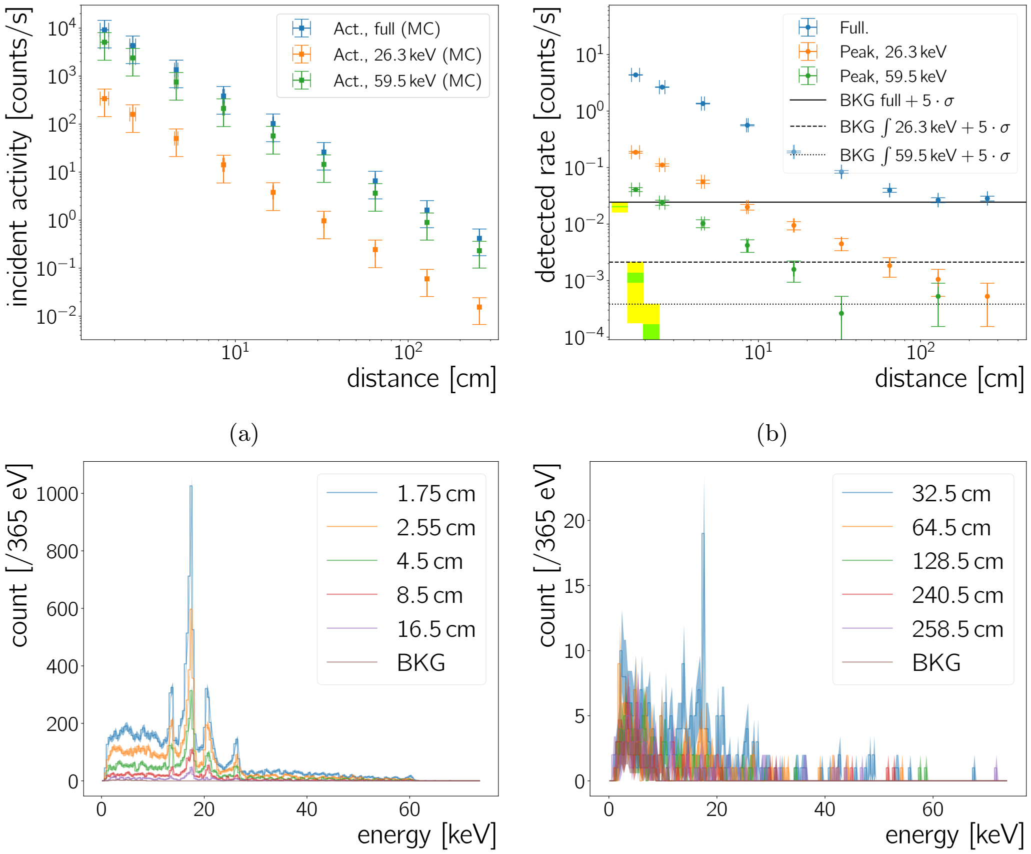

(a) (b)

(c) (d)

Figure 3.14: 3.14a Simulated incident activity on the camera chip for different camera-to-source distances for the full source activity, and for the fractional activities corresponding to the 26.3 keV and 59.5 keV γ-lines. 3.14b The measured rates are calculated using Equation (3.11) and integrating over the full ^{241}Am spectra in Figures 3.14c and 3.14d, or integrating only over the energy region of the 26.3 keV and 59.5 keV peaks in the same spectra. The measured background rate is established by integrating over the full spectrum recorded in absence of any source and in $\pm 5\sigma_{\text{peak}}$ windows around the mentioned peak energies. The shaded areas in the left half of the plot below the lines of the respective background rates show the 5 and 1.28 standard deviation (σ) regions around the background rate in yellow and green, respectively. 3.14c and 3.14d Measured ^{241}Am spectra at different distances with a live time of 3800 s. The data has to pass the cluster size > 2 pixels cut and is not background subtracted. The background data sample in both plots is the same as it has been shown previously (*e.g.* Figure 3.7f) and is normalised to the same live-time.

	^{241}Am				Background
	incident activity		measured rate		measured rate
	5σ	90 % CL	5σ	90 % CL	5σ
full spectrum	7 ± 4 Bq	2 ± 1 Bq	40 ± 3 mHz	27 ± 3 mHz	20.4 ± 0.8 mHz
26.3 keV-peak	1.0 ± 0.6 Bq	1.0 ± 0.6 Bq	4 ± 1 mHz	4 ± 1 mHz	1.1 ± 0.2 mHz
59.5 keV-peak	57 ± 33 Bq	57 ± 33 Bq	1.5 ± 0.1 mHz	1.5 ± 0.1 mHz	0.10 ± 0.06 mHz

Table 3.6: The lowest incident activities and the corresponding measured rates obtained with the Neo sCMOS, for ^{241}Am and background data. See Section 3.4.2.2 and Figure 3.14b. Values for two cases – either a 5σ or a 90 % CL condition – are quoted.

activity of the ^{241}Am source and the uncertainty of the emission probabilities. In the case of the toy Monte Carlo simulation, the statistical uncertainty on the counts obtained is used.

To estimate the minimum detectable decay rate and eventually the Neo sCMOS' detection efficiency, the detected rates in Figure 3.14b are determined as, where t represents time:

$$R^{\text{decay}} = \frac{\int \text{spectrum}\ \text{d}t}{t} \left[\frac{\text{counts}}{\text{s}}\right] \tag{3.11}$$

The measured rate without any source present is calculated using the background spectrum in Figure 3.7f. During 30 400 s of data taking 619 clusters with a size > 2 pixels are recorded, yielding a background rate of 20.4 ± 0.8 mHz. In energy windows corresponding to 5σ of the integration limits around the 26.3 keV and the 59.5 keV γ-peak energies, as seen in Table 3.5, the background rate measured with no source present is 1.1 ± 0.2 mHz (0.10 ± 0.06 mHz) for the 26.3 keV (59.5 keV) peak region. The exposure time per frame and the number of considered frames are known with great certainty, hence the statistical uncertainty on the cluster count is the only contribution to the uncertainty of the quoted rates. Figure 3.14b shows the background rates added with five times their uncertainty, i.e. 5σ, as yellow shaded regions and as horizontal lines. The green shaded regions correspond to 90 % CL, i.e. 1.28σ, around the measured background rate, where the background uncertainty is the standard deviation, i.e. σ. Count rates higher than 21.41 mHz, 1.4 mHz and 0.17 mHz for the full background rate, the background rate in the 26.3 keV peak window, and the background rate in the 59.5 keV peak window, respectively, are larger than the background at 90 % CL. Table 3.6 shows the source peak measured rates, compared with background, and the inferred incident activity at 90 % CL and 5σ. The detected rate measured for a distance of 128.5 cm is the first to be compatible with the background rate added with five standard deviations (27 ± 3 mHz), while the rate measured at 64.5 cm distance (40 ± 3 mHz) is significantly larger than the background rate. The incident source activity at 64.5 cm and 128.5 cm distance is 7 ± 4 Bq and 2 ± 1 Bq, respectively.

Performing the same analysis for the two most intense ^{241}Am γ-lines establishes whether this limit can be improved taking calorimetric information into account. For the 26.3 keV line a falling trend for the detected rate is observed over the full distance range – Figure 3.14b. Comparing to

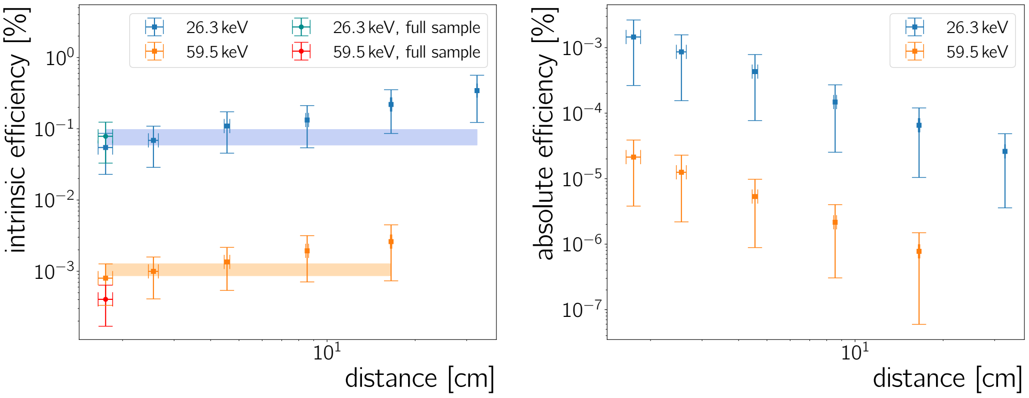

(a)

(b)

Figure 3.15: 3.15a Intrinsic and 3.15b absolute efficiency for the 26.3 keV and the 59.5 keV peaks. The bands in 3.15a correspond to the result of fitting a constant to the data as discussed in Section 3.4.2.3 with its error bars. The two *full sample* points are extracted from data in Figure 3.8b in the same manner as all the other points are extracted from the data in Figure 3.14.

the rate measured when no source is present the point at 64.5 cm is already compatible within five standard deviations. For 32.5 cm distance the detected activity is 4 ± 1 mHz, corresponding to an incident activity of 1.0 ± 0.6 Bq. In the case of the 59.5 keV γ line, the 32.5 cm point is already compatible with the background rate for this energy window within five standard deviations. The detected rate at 16.5 cm of 1.5 ± 0.1 mHz, corresponding to an incident activity of 57 ± 33 Bq, is thus the minimal detected rate, different from the background rate in this energy window.

3.4.2.3 Detection efficiency of the Neo sCMOS

A comparison between Figure 3.14a and Figure 3.14b permits calculation both the intrinsic and absolute efficiency of the detector. These are defined as

$$\epsilon_{\text{intrinsic}} = \frac{\text{number of particles recorded}}{\text{number of particles incident on the detector}} \tag{3.12}$$

$$\epsilon_{\text{absolute}} = \frac{\text{number of particles recorded}}{\text{number of particles emitted by source}} = \epsilon_{\text{intrinsic}} \cdot \epsilon_{\text{G}} \tag{3.13}$$

where ϵ_{G} is the geometric acceptance, which is given by Equation (3.10). The ratio of the recorded rate, seen in Figure 3.14b, and the incident activity, seen in Figure 3.14a, yield the intrinsic efficiency of the Neo sCMOS camera for γ rays of an ^{241}Am source. This is shown in Figure 3.15a for the 26.3 keV and 59.5 keV peaks as a function of the camera-to-source distance. For completeness, the absolute efficiencies for these two γ rays are shown in Figure 3.15b. By definition $\epsilon_{\text{intrinsic}}$ is independent of the distance.

The results of a constant fit to the data are shown in Figure 3.15a. However, a weak distance dependence of $\epsilon_{\text{intrinsic}}$ is observed; this is likely caused by a slight discrepancy between the calculated geometric acceptance and the actual source geometry. However, all points are within error-bars compatible with a constant as expected from Equation (3.12). The absolute efficiency's dependence on the distance in Figure 3.15b is expected, due its dependence on the geometric efficiency – Equation (3.13). The corresponding intrinsic efficiencies for the 26.3 keV and the 59.5 keV peaks are $0.08 \pm 0.02\,\%$ and $0.0011 \pm 0.0002\,\%$, respectively. Thus, the efficiency to detect a 26.3 keV γ ray is a factor of 80 higher than the efficiency to detect a γ ray with an energy of 59.5 keV. To check this ratio for consistency the material composition and thickness of the sensor would need to be known, which is not the case. Figure 3.16b in the next section shows photon absorption efficiencies calculated from the attenuation coefficients in [168]. Depending on the CMOS silicon thickness, the difference in photo-absorption for 59.5 keV and 26.3 keV can easily reach a factor 80. However, the efficiency at the 59.5 keV γ-line appears lower than expected from photo-absorption cross sections in Si.

3.4.2.4 CMOS sensor thickness

As a validation study, a toy Monte Carlo (MC) simulation was developed to enable a comparison of the observed data for different thicknesses of the CMOS chip used in the Neo sCMOS camera. The findings validate that the obtained efficiencies are reasonable for a plausible CMOS chip dimension.

The toy MC simulation of the ^{241}Am spectrum is used together with the photon attenuation coefficient from [168] to calculate, for each photon, the energy-dependent photon absorption probability in silicon. This step is repeated for different silicon thicknesses. For each thickness a spectrum of the photons absorbed in Si was created – these photons are the ones which would be measured by a chip as in the Neo sCMOS. The ratio of the unattenuated ^{241}Am toy MC spectrum divided by the spectra of absorbed photons is constructed. Finally, these ratios are compared to the ratio of the measured count rate at the γ peak energies divided by the incident activity for the respective γ line.

For the toy MC, all possible γ rays and X-rays of ^{241}Am decays as listed in [169] are taken into account. These are used to create a probability density function for photons emitted during ^{241}Am decays. Each γ- and X-ray line is represented by a Gaussian peak where the amplitude is proportional to the yield per decay. The $\varepsilon_{\text{peak}}$ is set to the respective X-ray or γ ray energy and the σ_{peak} is set to 2 % of the peak energy to approximate the measurement for the Neo sCMOS in Section 3.4.1.2. Creating 1 M decays from this probability density function results in the **No att.** cluster charge spectrum in Figure 3.16a. This unattenuated spectrum does not take material effects into account.

Figure 3.16a shows spectra of photons absorbed in silicon layers with a thickness from 1 µm to 5 µm. Toy MC spectra for absorbed photons and the measured spectrum (*e.g.* Figure 3.8b) are

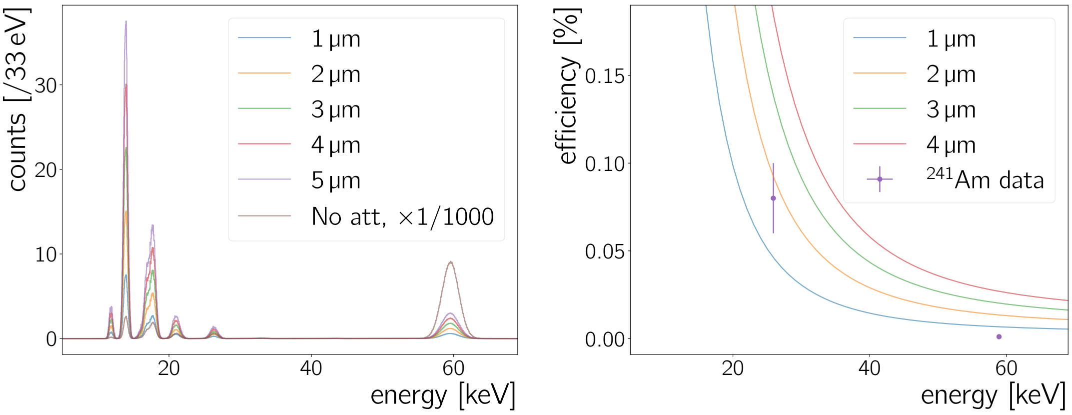

(a) (b)

Figure 3.16: 3.16a ^{241}Am γ ray and X-ray simulation for 1 M decays. The spectrum with no material effects taken into account (No att.) is scaled by a factor of 1/1000 to improve the readability of the plot. The other spectra show the photons which are absorbed by a silicon layer of given thickness. 3.16b Photon absorption efficiencies in silicon for different silicon layer thickness as well as the measured intrinsic efficiency of the Neo sCMOS at the two ^{241}Am γ ray energies.

similar. The ordering of the different peaks' height is the same except for the fact that the largest measured peak is at 18 keV, while the peak with the most counts in the simulation is the peak at 14 keV. In Section 3.4.1.1 the detection efficiency is observed to drop at lower energies – most notably making it impossible to detect a peak below ∼10 keV, *cf.* Figure 3.8c and Figure 3.10. The efficiency turn-on responsible for this behaviour may affect the peak height of the 14 keV peak and lead to the non-observation of the small peak visible at ∼11 keV in Figure 3.16a.

Figure 3.16b shows photon absorption efficiency curves calculated from the coefficients in [168] for 1 µm, 2 µm and 4 µm silicon layer thickness. Furthermore, the intrinsic efficiency values calculated in Section 3.4.2.3 are shown –Figure 3.15a. The two points follow roughly the trend expected by photon absorption in silicon, although the efficiency measured for the 59.5 keV peak is lower than expected from any absorption efficiency curve. The actual peak height of any γ-line is given by the absorption probability and by the capability of the active material to contain the full energy deposit. The latter is not contained in the toy MC simulation and this may explain that the 59.5 keV does not fit with the displayed curves. The 26.3 keV favours a silicon layer thickness of 2 µm. This scale of a few µm is on the same order of magnitude as the pixel dimension and seems reasonable for commercial CMOS chips, with a typical silicon-dioxide layer thickness of less than 10 µm [151, 152]. Since the silicon thickness is not the only contribution to the Neo sCMOS intrinsic efficiency, the estimate in this section can only be seen as a lower limit to the actual sensor thickness.

3.5 Lead detection capabilities assuming Lead-210 as a trace isotope

This section investigates the concept of placing a water sample in front of the Neo sCMOS and obtaining a ^{210}Pb spectrum similar to the one obtained in Figure 3.8d. From it the ^{210}Pb concentration could be inferred and by using a ratio of ^{210}Pb to stable lead the total lead concentration in the water sample could be determined.

The ratio of the *radioactive isotopes in Pb* to *stable Pb isotopes* is required to estimate the capability of the Neo sCMOS to detect lead in drinking water, assuming ^{210}Pb as a trace isotope to be measured by the Neo sCMOS. In [47] the ^{210}Pb to stable lead ratio is used to monitor the lead intake of plants. It measures $96 \pm 9\,\mathrm{Bq\,mg^{-1}}$ for $^{210}\mathrm{Pb/Pb}$ in rainwater in London, corresponding to a ratio of 34 ppb of $^{210}\mathrm{Pb/Pb}$ (molar mass of lead: 207.2 g/mol, half-life of lead: 22.3 yr). However, the origin of stable lead and ^{210}Pb are not necessarily the same. In [45] several Pb samples of different age – from ancient lead to recently produced lead – are analysed for their ^{210}Pb, ^{232}Th and ^{238}U contents. $^{210}\mathrm{Pb/Pb}$ ratios are found ranging from $0.09\,\mathrm{Bq\,kg^{-1}}$ to $68.7\,\mathrm{Bq\,kg^{-1}}$ (3.9×10^{-8} ppb to 2.4×10^{-5} ppb) in their lead samples.

In the next paragraph the incident activity on the Neo sCMOS is estimated, produced by 10 ppb lead in water. The use of the $^{210}\mathrm{Pb/Pb}$ ratio from [47] is justified, as it stems from a water-based measurement of Pb, while taking into consideration the findings presented in [45].

With the $^{210}\mathrm{Pb/Pb}$ ratio of 34 ppb, the WHO limit of 10 ppb [21] of lead in drinking water translates to a fraction of 3.4×10^{-16} parts ^{210}Pb to one part of water. One gram of water contains at this ratio 9.9×10^5 ^{210}Pb atoms, which initially decay at a rate of 0.96 mBq ($R^{\mathrm{decay}}_{^{210}\mathrm{Pb}}$). A sample of water containing lead could be placed on the camera's window – in 1.75 cm distance from the silicon chip. Considering 1 g of water as point source, the incident rate ($R^{\mathrm{incident}}_{^{210}\mathrm{Pb}}$) is 0.001 mHz after taking the geometric acceptance in Equation (3.10) into account and the fact that the γ-yield for the 45 keV γ is only 4 %:

$$\begin{aligned} R^{\mathrm{incident}}_{^{210}\mathrm{Pb}} &= R^{\mathrm{decay}}_{^{210}\mathrm{Pb}} \cdot \epsilon_{\mathrm{G}}\,(1.8\,\mathrm{cm}) \cdot \left\{^{210}\mathrm{Pb}\ \gamma\ \mathrm{yield}\right\} \\ &= 0.96 \times 10^{-3}\,\mathrm{Bq} \cdot (3 \pm 1\,\%) \cdot 4\,\% \\ &= (1.1 \pm 0.4) \times 10^{-6}\ \mathrm{Bq} \end{aligned} \tag{3.14}$$

$R^{\mathrm{incident}}_{^{210}\mathrm{Pb}}$ has to be compared to the measured value of the incident ^{241}Am source activity of 1.0 ± 0.6 Bq and 57 ± 33 Bq at the 26.3 keV and 59.5 keV lines, respectively (Section 3.4.2.3). With ∼46 keV the ^{210}Pb γ-line is located between these two energies. Thus, the sensitivity of the Neo sCMOS is a factor of 10^6 to 10^7 too low to detect the decay radiation of trace amounts of ^{210}Pb occurring with 10 ppb lead in 1 g of water. The fraction is even lower, given that the above calculations assume a point source and 1 g of water measures 1 cm^3.

Independently from the actual ^{210}Pb/Pb ratio for commercial lead or lead in the water one can estimate the fraction of ^{210}Pb per mass (*e.g.* ^{210}Pb/Pb or ^{210}Pb per gram of water) which corresponds to a $R^{\text{incident}}_{^{210}\text{Pb}}$ as the measured, minimal incident rate. Considering the same parameters in Equation (3.14) and using the two ^{241}Am γ-line energies the sensitivity is estimated to be between 0.3 ± 0.2 ppb and 166 ± 11 ppb ^{210}Pb per mass. This sensitivity makes the Neo sCMOS a competitive radiation detector, although it would not be able to measure lead at the WHO limit. To approach this, water can be concentrated by boiling it, potentially leaving heavy metals behind. This is addressed in Chapter 4. In case of ashing of plants and acrylic [47, 170], it has been found that heavy metals stay behind after the process.

Based on the results shown in Section 3.5 above, methodology was developed to assess how well ^{210}Pb is retained when water is concentrated by volume reducing it through boiling off. This is shown in Chapter 4. The PlomBOX was another alternative explored by detecting stable lead, as opposed to ^{210}Pb, in water. This is addressed in Chapters 5 and 6. Furthermore, while these results do not allow to conclude that ^{210}Pb can be measured in low enough concentrations as needed to detect 10 ppb of lead, this study has shown that a CMOS sensor optimised for optical wavelengths is well suited as γ- and X-ray detector for low energies in the range from ~10 keV to ~60 keV.

Chapter 4

Volatility of lead in water - reduction methods

Chapter 3 explored the potential of leveraging the calorimetry techniques of silicon (Si) detectors in assaying lead in drinking water. This work demonstrated the capability of detecting gamma energies in an Si detector from a 100 ppb Lead-210 (^{210}Pb) sample through calorimetry methods [101]. While this technique is promising for dosimetry applications, it is not able to reach the WHO level (10 ppb [21]) in sensitivity. One way to increase the sensitivity range of any device is to increase the concentration of a substance of interest (here: lead) in the sample. This chapter explores increase in heavy metal concentration by boiling doped water samples.

Volume concentration, by vaporization of acrylic, is a strategy developed to increase a sensor's sensitivity to ultra-low concentrations of radio-isotopes, for material screening for astroparticle physics experiments, and has been applied to measure the ^{210}Pb content of acrylic [171]. Astroparticle physics experiments have used volume reduction techniques on solid samples. For the construction of the SNO experiment it was of importance to measure the detector acrylic's Uranium and Thorium chain radionuclide content to characterise and minimise the detector backgrounds [172]. To achieve this, large samples of acrylic needed to be measured within a BEGe detector. To improve the efficiency of the assay campaign the acrylic was vapourised, reducing the sample to a char with a mass down to 15 % [173] of the original sample mass. Heavy metals associated with the ^{238}U and ^{232}Th decay chains remained in the char. The efficiency for this process to retain U and Th isotopes in the acrylic vaporisation system of the SNO experiment was found to be >93 % [174]. A vaporisation approach using ICP-MS for the Jiangmen Underground Neutrino Observatory (JUNO) experiment achieved 75 % efficiency for U and Th [175]. The SNO vaporisation system was adapted and applied to measurements of ^{210}Pb for the DEAP-3600 experiment, where the efficiency for retention of lead in the char was measured in samples with independently-assayed ^{210}Pb content to be 90-95 % [58].

In this chapter, which presents work published in [102], the principle of reducing measurement samples in volume is applied to increase the concentration of heavy metals for measurement. However, instead of vapourising solid samples, water samples are boiled to reduce their volume by evaporation. The goal was to develop a method suitable for use in the field, without specialised equipment. This experiment used water spiked with a known amount of ^{210}Pb. Lead-210's decay energy can be detected by HPGe detectors, as described in Section 4.1, and its molecular weight is similar to lead, thus the isotope can serve as a test bench for lead retention. Afterwards, the volume-reduced water samples are assayed with HPGe detectors to determine their radioisotope contents to assess the level at which these isotopes are retained. This chapter introduces HPGe detectors and their key characteristics in Section 4.1. It reports the procedure for volume reduction in Section 4.2.1 and the efficiency for retaining lead in Section 4.3.1.1. In a second experiment, using London tap-water, the method developed with ^{210}Pb was employed. Tap water samples were reduced and assayed with a BEGe detector to determine the radioisotope content of the tap-water and to assess the isotopic retention efficiency reported in Section 4.3.2.

4.1 High purity germanium detectors

As mentioned in Section 2.2.3, germanium is used as a semiconductor material for experiments which require high energy resolution. Germanium semiconductor detectors have a PIN structure [176]. Unlike silicon, germanium detectors require cooling below 120 K. Liquid nitrogen, with a temperature of 77 K, is commonly used for this [176, 177]. The detector is placed inside a vacuum chamber attached or inserted into a liquid nitrogen dewar.

Chapter 2 presented silicon detectors that are effective in detecting short-range radiation such as alpha particles. However, they are difficult to adapt for applications that need to detect more penetrating radiations such as X-rays and gamma rays. The thickness of a semiconductor detector can be given by:

$$d = \left(\frac{2\kappa V}{eN}\right)^{\frac{1}{2}} \tag{4.1}$$

Where V is the reverse bias voltage, N is the net concentration of impurities in the material, κ is the dielectric constant and e is the charge of an electron. For a given bias voltage, a greater depletion region can be achieved by lowering the concentration of impurities. By reducing impurities to a level of 10^{10} atoms/cm^3, a depleted region with a depth of 10 mm can be achieved for a voltage of 1000 V. Germanium detectors with these levels of purity are called High-Purity Germanium detectors, and can have depletion depths of several centimeters [51].

4.1.1 Configurations of HPGe detectors

HPGe detectors can have two configurations: planar or coaxial geometry [177].

In planar configuration, a germanium disk has the electrical contacts, n^+ and p^+, on its two flat surfaces – Figure 4.1a. The p^+ contact is usually less than 1 µm thick and the n^+ can have a thickness of 1 mm [177]. HPGe detectors are limited to a bias voltage of 5 kV to prevent induced breakdown of the material due to leakage currents [177]. Due to this, planar configuration detectors are limited to depleted region thicknesses of approximately 2 cm and an active volume between 10 and 30 cm^3.

To achieve depleted regions greater than 2 cm, hollow cylindrical or coaxial geometry configurations are preferred [51]. One electrode is fabricated on the outer surface of the cylinder and the other cylinder is fabricated on the inner cylindrical surface – Figure 4.1b. This configuration permits active volumes of up to 750 cm^3 [51].

This project used a planar HPGe detector, as detailed in Section 4.3.1.

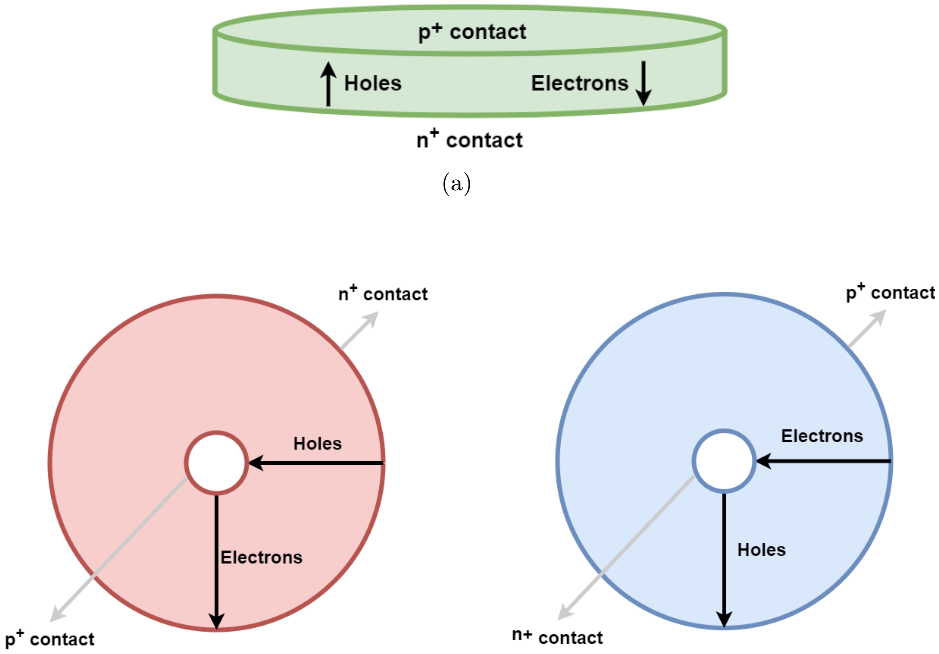

(a)

(b)

Figure 4.1: Diagram showing the two types of Germanium detector configurations. 4.1a planar, with a germanium disk with the electrical contacts on its two flat surfaces; and 4.1b coaxial, with the electrical contacts on the outer and inner surfaces of a hollow cylinder. This figure shows a cross section of the cylinder for a p-type and an n-type detector configuration, on the left and right respectively. [51]

4.1.2 Gamma ray spectroscopy with HPGe detectors

HPGe detectors are characterised by their high energy resolution, which can be observed in γ ray spectroscopy. Figure 4.2 compares the energy spectra obtained for ^{241}Am with a CdTe semiconductor detector, a HPGe detector and a NaI(TI) scintillation detector. The Full Width at Half Maximum (FWHM) is a measure of the energy resolution for a single peak, as it describes the level at which a detector can separate two adjacent energy peaks [178, 179]. A lower FWHM corresponds to a higher energy resolution. Figure 4.3 shows the energy resolution for the detectors aforementioned. The FWHM of CdTe and NaI(TI) is 5 times and 30 to 50 times larger, respectively, than the FWHM of the HPGe detector. Table 2.1, compares the average energy required for electron-hole pair creation in various semiconductor materials. It reveals that germanium requires an energy of 2.96 eV for this process, which is lower than the energy of 4.43 eV needed by CdTe to achieve the same outcome [136]. This property is responsible for the excellent resolution of HPGe detectors, making them optimal for γ energy identification [179].

Section 4.3.1 details the HPGe detectors used in the study addressed in this chapter.

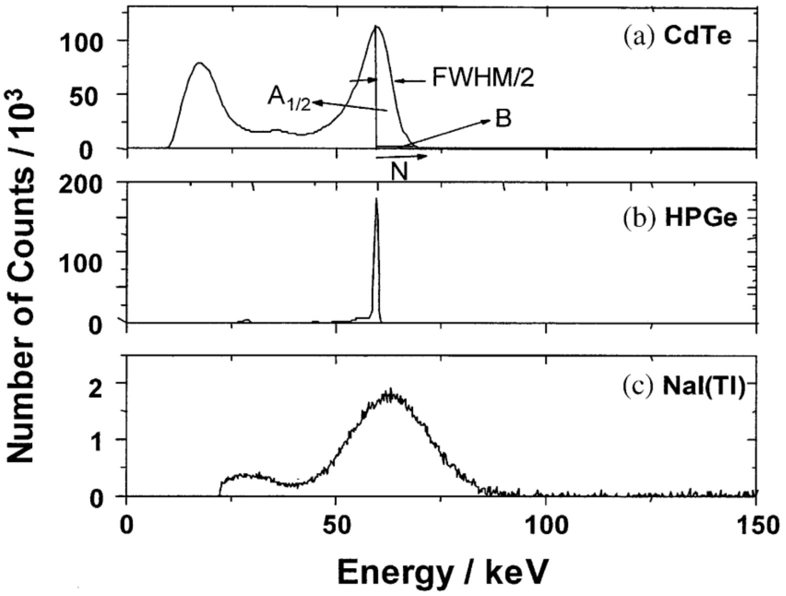

Figure 4.2: Comparison of ^{241}Am energy spectra obtained with CdTe, HPGe and NaI(TI) detectors [179]

4.2 Water reduction procedures

Two different methods were employed to reduce the volume of water samples. The first method uses an enclosed system, which allows for full control of the exposure of the sample to the atmosphere throughout the volume reduction process. This is suitable for a laboratory environment. The second uses an open system in which the evaporation escapes into the atmosphere, similarly to how such a volume reduction method could be employed in the field without specialist equipment.

Using volume-reduction as a means to enhance assay sensitivity requires knowledge of the retention of the isotopes of interest throughout the volume-reduction procedure. This was measured

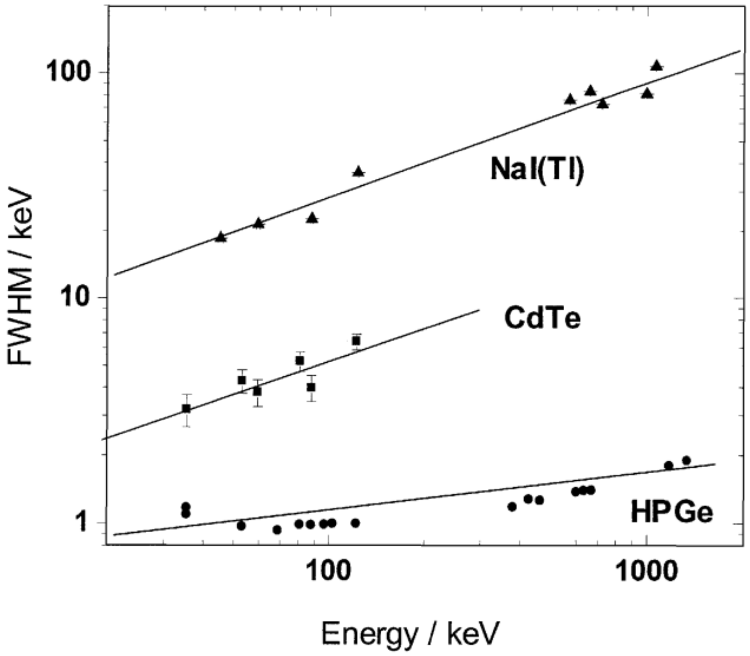

Figure 4.3: Energy resolution for the three detectors mentioned in Figure 4.2 as a function of γ ray energy [179]

for both enclosed and open volume reduction procedures. The enclosed volume reduction used a source of known ^{210}Pb activity and the open volume reduction procedure uses naturally occurring ^{40}K to assess retention efficiency.

Both enclosed and open methods were studied inside an ESCO Laboratory fume hood, with an airflow speed between 1.2 and 1.5 m s^{-1}, to control the exhaust path of ^{210}Pb-spiked samples.

4.2.1 Enclosed system procedure

A ^{210}Pb calibration source, prepared from a standard liquid source (activity 518 ± 58 Bq) dissolved in 1 mol of nitric acid, was purchased from Eckert & Ziegler Isotope Products [180]. The mass of this standard source was 5.121 ± 0.002 g. A sample of 1.66 ± 0.01 g was removed from the source vial, and diluted in 4236 ± 1 g of UPW. This produced a diluted ^{210}Pb calibration source for the measurements reported here, with activity of 167.9 ± 18.8 Bq (calculated as $518\,\mathrm{Bq} \times \frac{1.66\,\mathrm{g}}{5.121\,\mathrm{g}}$).

To produce volume-reduced samples, a UPW sample, spiked with the calibration source, was boiled in an enclosed system. A diagram and photo of the enclosed system are shown in Figure 4.4a and Figure 4.4b respectively.

In the enclosed system volume reduction apparatus, two DURAN 5000 ml round bottom flasks were connected on both sides of a coil condenser. The flask containing the UPW sample to be volume-reduced (flask A) was placed on top of a small electric hob and was connected to the inlet of the condenser. The outlet of the condenser was connected to the inlet of the flask for

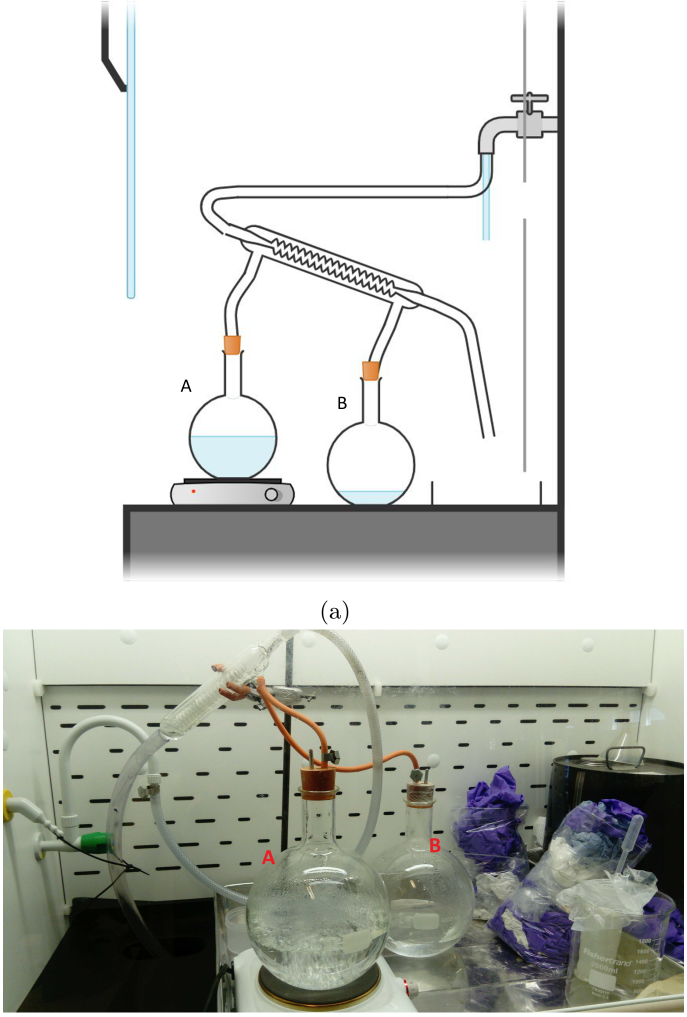

(a)

(b)

Figure 4.4: 4.4a Diagram of enclosed system set up detailing connections between the condenser and the two flasks; 4.4b Photograph of the enclosed system during a boil showing the flask undergoing volume-reduction, flask A, and the flask with the condensed liquid, flask B.

collection of the condensed solution (flask B). These connections were made using rubber tubing pipes with 6.74 mm inner diameter and the flasks were sealed with rubber bung stoppers to ensure no evaporated or liquid solution would leave the enclosed system. Additional UPW to be used in the reduction was stored in 1000 ml Pyrex® flasks. Prior to reduction, the flasks and the condenser were cleaned with decon® 90 and ethanol. Throughout the reduction, samples were taken from flask A and flask B. These samples were contained in identical pots made of Polypropylene and with dimensions of 8.9 cm outer diameter and 6.4 cm height. They were also cleaned, prior to reduction, with UPW and isopropanol.

To begin the reduction, the cold water tap connected to the coil condenser was turned on and adjusted until flow was steady and did not overflow the sink. The electric hob was turned on and the set up was monitored until it started boiling vigorously. When this point was reached, the hob was turned down until the UPW was observed to be simmering. The system was monitored every

30 minutes. When the volume of UPW in flask A was less than 1 l, the hob and the cold water tap were turned off and the flasks were left to cool. Once cool, the bung from flask A was removed and more UPW was added. In the instance when the volume of flask B reached 5 l, the hob and the cold water tap were also turned off, and the flasks were allowed to cool off. Following this, the bung was removed and the contents of flask B were deposited into a 20 l polyethylene container. This procedure was repeated until all the desired samples had been obtained.

With the enclosed system reduction, samples with volume reduction ratios of 1:1, 1:10, 1:25 and 1:100 were prepared. The enclosed system reduction samples are listed in Table 4.1. The first sample was prepared from the input UPW (Blue I). Then, the non-reduced UPW was spiked with 1.66 g ^{210}Pb solution, and a sample was extracted (Red II). The first reduction 1:10 (Green III) followed. After this reduction, Black IV was taken from the condensate flask. A sample was taken from Flask A after the second reduction reached 1:25 (Green V), and a final sample when the third reduction reached 1:100 (Blue VI). After this final reduction, Sample X was taken from the condensate flask. The remaining mass of the Eckert & Ziegler source solution, 3.33 g, was diluted into the remaining UPW, from which Sample IX was taken.

Sample Name	Description	Reduction	M_S	M_O
Blue I	UPW	-	201	n/a
Red II	UPW + ^{210}Pb	1:1	200	4236
Green III	1st reduction	1:10	20	700
Black IV	Condensate 1	-	200	n/a
Green V	2nd reduction	1:25	20	233
Blue VI	3rd reduction	1:100	191	26193
Sample IX	Final Source sample	-	200	n/a
Sample X	Condensate 2	-	205	n/a

Table 4.1: Corresponding sample (M_S) and original mass (M_O) values for different reductions. Samples related to reductions were prepared from the boiling flask (A). Samples referred to as "Condensate" in the Description column were prepared from the condensate flask (B). Sample Mass values are contained in the Original Mass values, with the latter being the mass prior to reduction. Both are quoted in (g). Sample and Original masses were measured with a set of scales with an uncertainty of ±1 g.

4.2.2 Open system

For the open system reduction, 5 tap water samples of the following volume reduction ratios were prepared: 1:1, 1:10, 1:100, 1:1000 and 1:5000. A sample of limescale extracted from the condensate was also prepared. Two Pyrex® trays were positioned inside the fume hood on top of two electric hobs and tap water was deposited inside the trays (Figure 4.5). The trays had dimensions of 0.27 m × 0.4 m × 0.055 m ($L \times W \times H$).

Two electric hobs were turned on and their temperatures were maintained between 55 and 70 °C. With a temperature of 55 °C, the reduction of 100 l of tap water to 1 l took place over 88

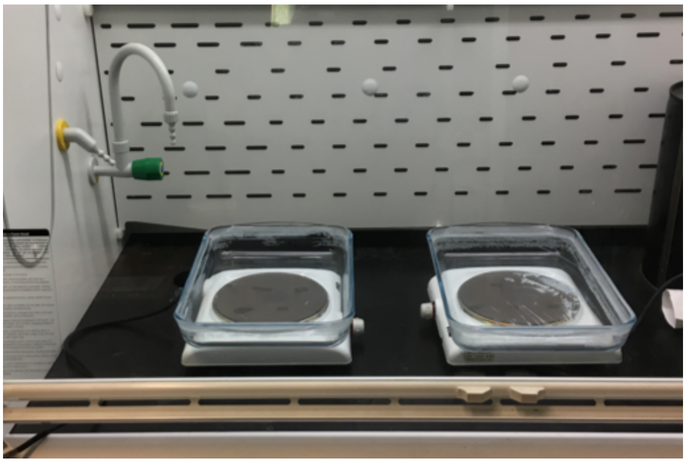

Figure 4.5: Photo of two Pyrex® trays positioned on top of two electric hobs to achieve the open system reduction.

hours. Tap water was added once per hour to maintain the water level in the trays.

The samples prepared using the open volume reduction technique are listed in Table 4.2. The uncertainty on the reduction factor R and $\frac{1}{R}$ values results from standard error propagation. Ex: $\frac{s_{\mathrm{R}}}{R} = \sqrt{\left(\frac{s_{\mathrm{M_O}}}{M_O}\right)^2 + \left(\frac{s_{\mathrm{M_S}}}{M_S}\right)^2}$, where s_{R}, $s_{\mathrm{M_O}}$ and $s_{\mathrm{M_S}}$ are the uncertainties of the separate quantities R, $Original\ Mass$ and $Sample\ Mass$. Sample E was taken after Sample D's reduction had been prepared.

Sample name	M_{O} (g)	M_{S} (g)	Reduction (R)	$\frac{1}{R}$
Tap water sample	n/a	270	1	1
Started reduction	100,685	n/a	n/a	n/a
A	9,926	103	0.099 ± 0.001	10.144 ± 0.001
B	903	102	0.0090 ± 0.0001	111.5 ± 0.1
C	159	10	0.0016 ± 0.0002	633.2 ± 3.9
D	28	28	0.00028 ± 0.00001	3595.9 ± 128.4
E (limescale)	-	46	0.00028 ± 0.00001	3595.9 ± 128.4

Table 4.2: London tap water samples. R in the table denotes the reduction factor calculated as the ratio of the volume after- to the volume before reduction. Original (M_{O}) and Sample (M_{S}) masses were measured with a set of scales with an uncertainty of 1 g.

4.3 Evaluation

4.3.1 Assay of closed system water samples

The γ emission of 46.5 keV resultant from a ^{210}Pb decay, shown in Section 1.2.2, constitutes the low energy γ band for which HPGe detectors are optimised, therefore justifying the use of these detectors for the radioassay of the water samples.

The Boulby Underground Germanium Suite (BUGS) contains a number of high purity germanium detectors that are discussed in depth in [181]. For the assay of the samples in this paper, Dr. Paul Scovell used the Roseberry detector. Roseberry is a Mirion© specialty ultra-low background (S-ULB) BE6530 broad energy germanium detector. The planar BEGe detector is constructed to have almost zero dead layer thickness on the front face and is optimised for the detection of low-energy gamma-rays. The BE6530 detector has a front face with a surface area of 65 cm^2 and a thickness of 30 mm. The Roseberry detector is housed in a shield comprising 9 cm of lead on the outside, followed by 9 cm of copper. The detector cryostat has a j-shaped neck to reduce any line-of-sight background that may come along the aperture where the detector neck passes through the shielding. This allows samples to sit on the face of the detector without the need for any additional support.

The sample pots had identical volumes to within manufacturing tolerance, meaning that a single simulation of geometric efficiency could be used. The simulated sample is shown sitting on the head of the Roseberry detector in Figure 4.6a. A flat spectrum of 0 to 3 MeV γ-rays are fired from the sample and any of them which deposit their full energy in the germanium crystal are used to determine the sample efficiency. Figure 4.6b shows the simulated efficiency with 46.5 keV (corresponding to the ^{210}Pb γ-ray) highlighted. For the assayed samples, a total efficiency of 10.2 % was calculated at 46.5 keV.

Samples for the measurements reported here were assayed between August 2019 and January 2020 with runs lasting between several days for samples that were more radioactive and 2 weeks for samples with little or no ^{210}Pb above background observed.

4.3.1.1 HPGe analysis

Dr. Paul Scovell conducted a lengthy background run using the detector without a sample pot. Although it was expected that the majority of water samples would be substantially above the detector background, this was of particular importance for comparison with the condensate samples from flask B (see Table 4.2) where little, if any, ^{210}Pb was expected. A background of 20.4 days was used – Figure 4.7.

For each sample, a simple and consistent method for determining the number of counts in the ^{210}Pb peak was used, as shown in Figure 4.8: the spectral region above and below the peak was fitted using a 0^{th} order polynomial and a simple interpolation between the two fits used to represent the underlying Compton continuum resulting from very small angle scatters of the ^{210}Pb's 46.5 keV γ-rays [182]. The peak region is defined as shown in Figure 4.8 and simple subtraction from the net counts of the Compton background and the measured detector background was performed to give a final number of counts in the peak. Results of this assay programme are shown in Table 4.3 in comparison with the expected results if the distillation process had 100% efficiency for retaining ^{210}Pb. Expected Activity A_{E} is calculated using the mass of the sample and the ratio of activity by

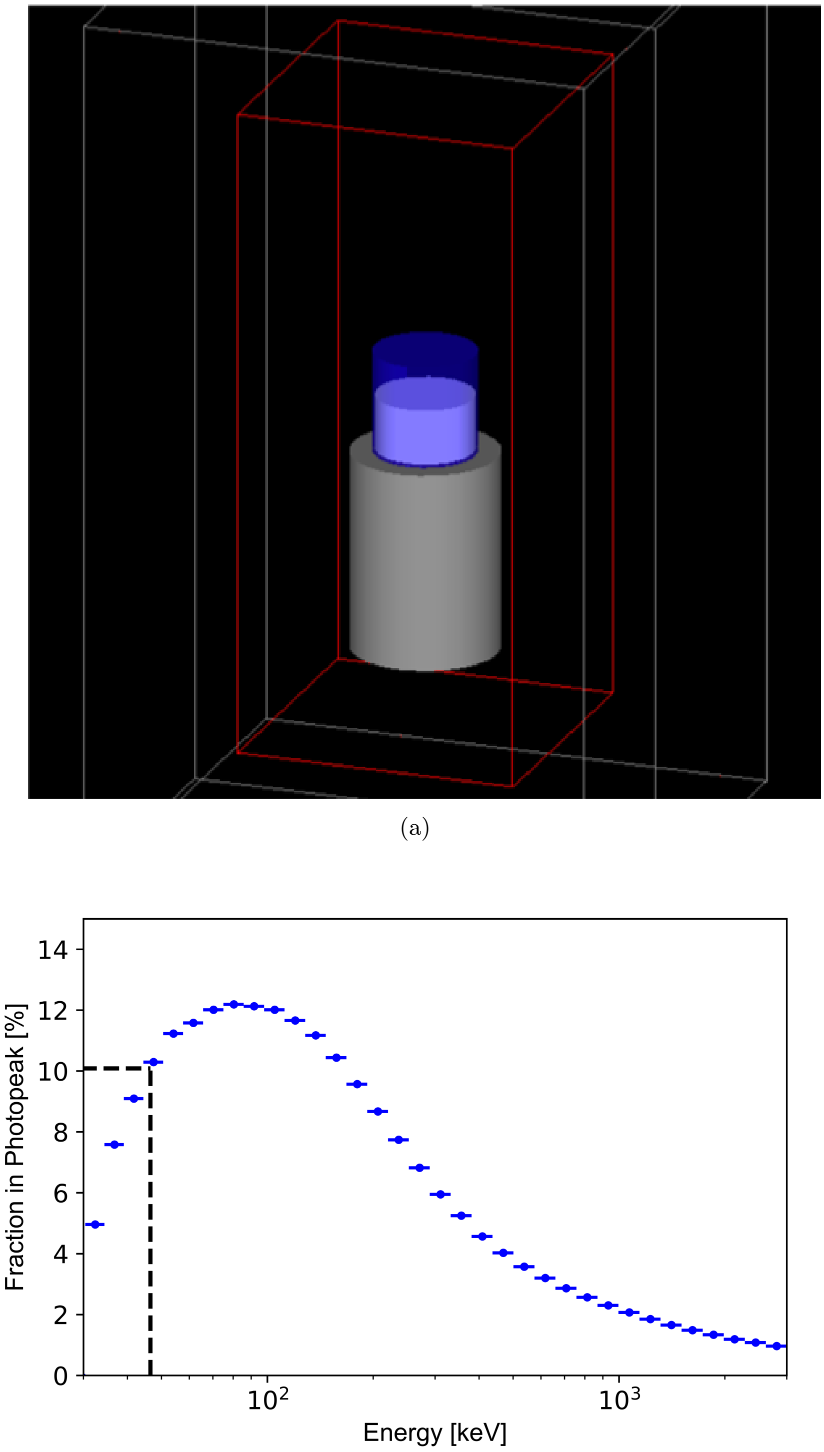

(a)

(b)

Figure 4.6: 4.6a Simulation showing sample placed on top of the Roseberry detector; 4.6b Spectrum showing simulated efficiency of Roseberry detector. For an energy of 46.5 keV it describes a geometric efficiency of 10.2 %, highlighted in the black dotted lines.

the total mass. For sample Red II, for example, A_E is $200\,\mathrm{g} \times \frac{167.9\,\mathrm{Bq}}{4236\,\mathrm{g}} = 7.9\,\mathrm{Bq}$, as per the activity and mass values provided in Section 4.2.1. Errors on Activity A combine statistical and systematic effects, the latter being estimated by running two simulations using Geant4 and Mirion© In Situ Object Counting System (ISOCS) software. The differences in the two efficiency values define the systematic error. Errors on the A_{E} result from the initial error of the calibration source and the scales used to measure the water samples' masses. Results show that the reduction retains $99 \pm 9\,\%$ of ^{210}Pb's activity - the Total Activity A $507 \pm 28\,\mathrm{Bq}$ compared to an A_{E} of $504 \pm 45\,\mathrm{Bq}$.

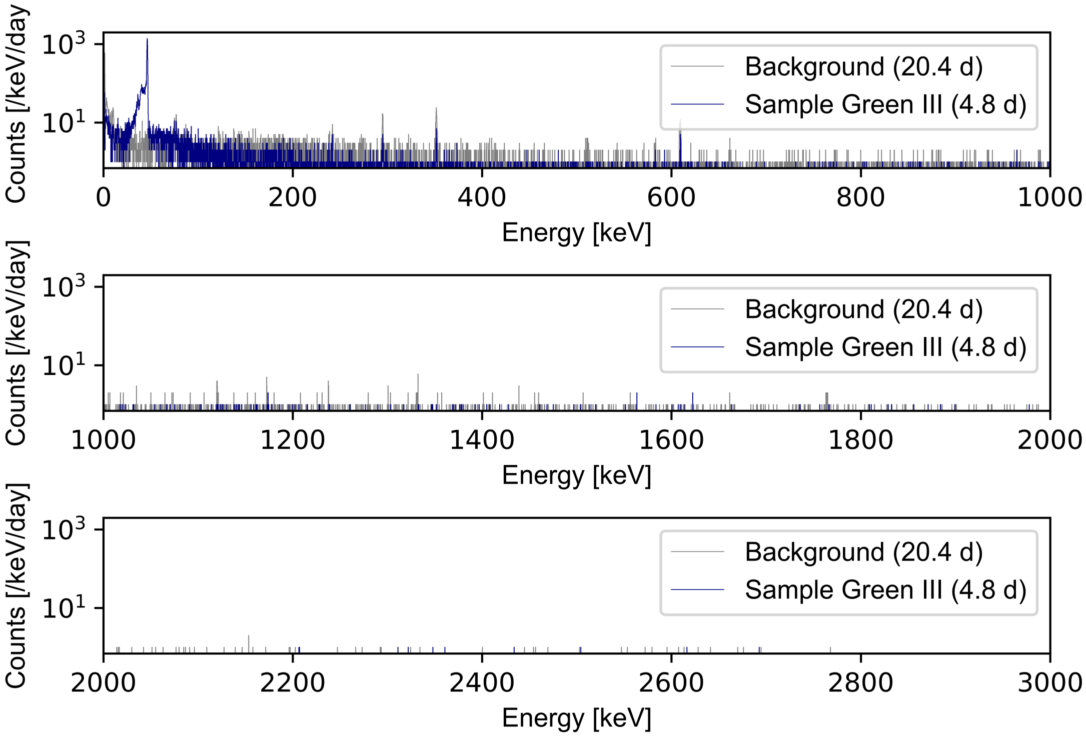

Figure 4.7: Sample Green III - full spectrum for this sample in blue, and the background spectrum in grey.

Sample Name	A (Bq)	A_{E} (Bq)	$\frac{(A-A_{\mathrm{E}})}{A_{\mathrm{E}}}$
Blue I	0	0	0
Red II	5.4 ± 0.4	7.9 ± 0.9	-0.32 ± 0.11
Green III	4.7 ± 0.3	4.6 ± 0.6	0.02 ± 0.13
Black IV	0.006 ± 0.002	0	-
Green V	15.5 ± 1.1	13.3 ± 1.8	0.16 ± 0.13
Blue VI	151 ± 8	142.1 ± 17.6	0.01 ± 0.12
Sample IX	331 ± 18	336 ± 41.6	0.01 ± 0.12
Sample X	0	0	-
Total	507 ± 28	503.9 ± 45.2	0.01 ± 0.09

Table 4.3: Comparison between measured activity, A, and calculated expected activity, A_{E}, in Bq, assuming >99 % efficiency for ^{210}Pb throughout the volume reduction process.

In addition to the assay conducted at Boulby using the ROSEBERRY BEGe detector, the ^{210}Pb water samples were characterised by the team at the IF UNAM using the BEGe detector described in [183]. The measurements and calibration with both IF UNAM and Boulby Germanium detectors were consistent as described in [183] and shown in Table 4.4. For the Boulby measurements, the statistical and systematic effects described for Table 4.3 also apply here. For the National Autonomous University of Mexico (UNAM) measurements, a 14% systematic error is included, to

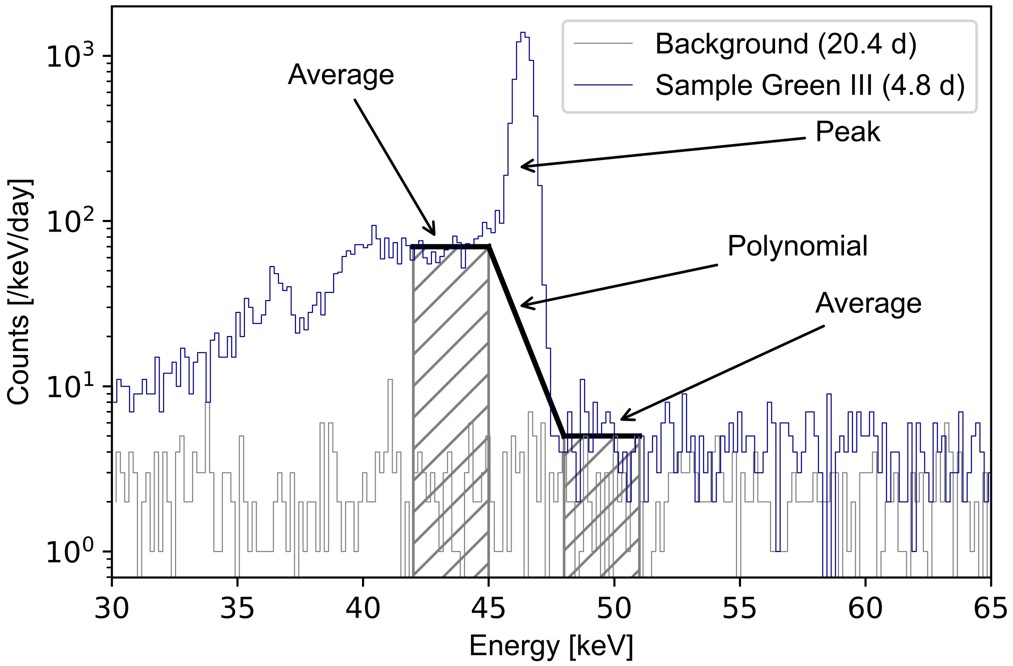

Figure 4.8: Figure 4.7 zoomed into the region of interest for ^{210}Pb peak extraction - 30 to 60 keV. The black line represents the 0th order polynomial fits made above and below the peak. The region between 45 keV and 48 keV represents the peak region.

account for differences between the real position of the sample and the Monte Carlo simulation. It is calculated by moving the position of the Marinelli Beaker ±4 mm on the axis of the germanium material. The water samples contained no isotopes above background, except for ^{210}Pb. Trace amounts of ^{40}K were observed for the Blue VI, Green V and Green III reductions, but these were consistent with background.

Sample Name	Boulby (stat [182] +sys)	UNAM (stat [182] +sys)
Blue I	-	3.4
Red II	26.9 ± 2.0	26 ± 4
Green III	23.3 ± 1.5	17 ± 2
Black IV	0.029 ± 0.009	2.5 ± 0.4
Green V	77 ± 5	71 ± 10
Blue VI	790 ± 44	837 ± 124
Sample IX	1613 ± 85	-
Sample X	-	-

Table 4.4: Cross calibration of sample's activities using BEGe detectors at Boulby and IF UNAM. All values shown correspond to Specific Activities (Bq/kg). The samples underwent an initial measurement at Boulby before being sent to UNAM after a period of time had passed. The subsequent measurements from UNAM indicate lower Specific Activities for certain samples, suggesting the occurrence of radioactive decay of ^{210}Pb. There is a discrepancy in the results reported by Boulby for the Black IV sample. The detector experienced a malfunction in its liquid nitrogen cooling system during this measurement, impacting its ability to accurately measure the Specific Activity.

4.3.2 Assay of open system water samples

To characterise the efficiency of the open system procedure, samples were assayed between March and April 2019 using the Chaloner BEGe detector at the Boulby Underground Laboratory. Chaloner is a Mirion© BE5030 BEGe detector with the same geometry as Roseberry and housed in identical shielding. The intrinsic background of the Chaloner detector is around 10× higher than that of the Roseberry detector but, for the samples assayed, this level of background was acceptable. An efficiency simulation was also preformed for Chaloner identical to that which was undertaken for Roseberry.

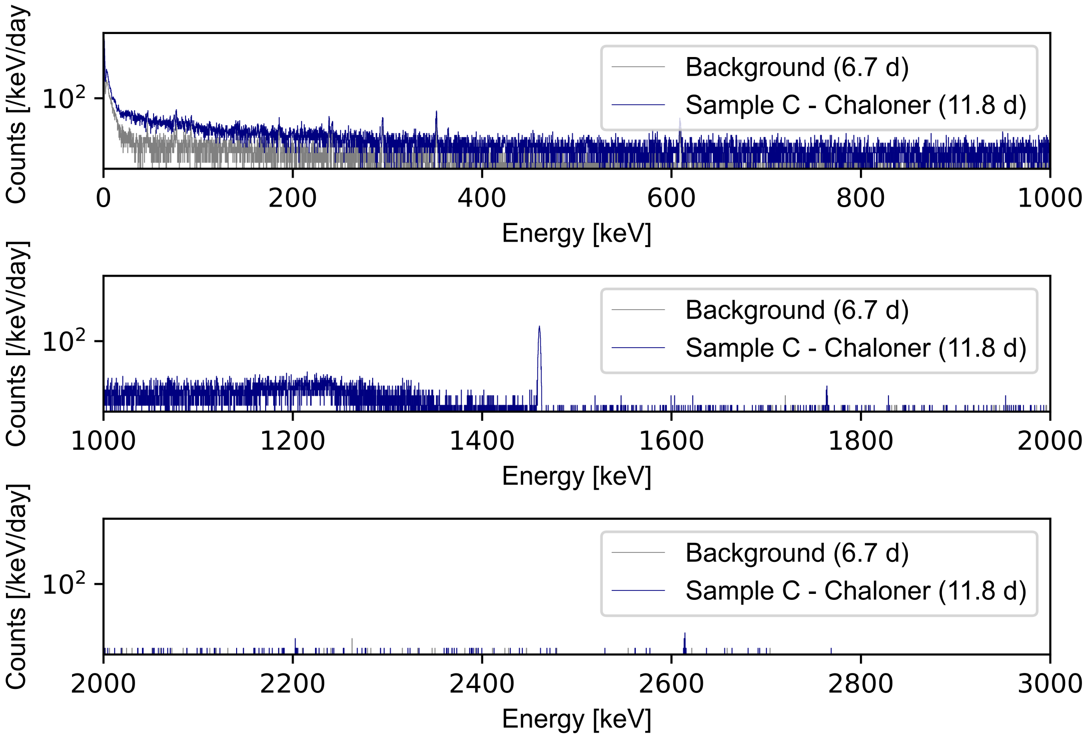

Figure 4.9: Spectra of open water system sample C.

In all samples, ^{40}K was observed, with an energy peak of 1.46 MeV. The measured gamma energy spectra from this assay are shown in Figure 4.9 and Figure 4.10. As a cross-calibration, the specific activities of ^{40}K in sample D measured on Roseberry and Chaloner were compared. These activities were $255 \pm 6\,\mathrm{Bq\,kg^{-1}}$ (2.83×10^3 ppb) and $259 \pm 2\,\mathrm{Bq\,kg^{-1}}$ respectively. The results of this measurement can be seen in Table 4.5. Even though Samples A through C show reasonable consistency in activity values, sample D is substantially lower. This is due to the amount of limescale present in this reduction that was removed prior to acquiring the sample – see Table 4.2. Given that the limescale sample presents an activity equal to 100 Bq/kg, it is reasonable to assume that potassium is lost as limescale is removed and, therefore, the reduction in measured activity of ^{40}K for sample D is reasonable, as the combined activity of samples D and

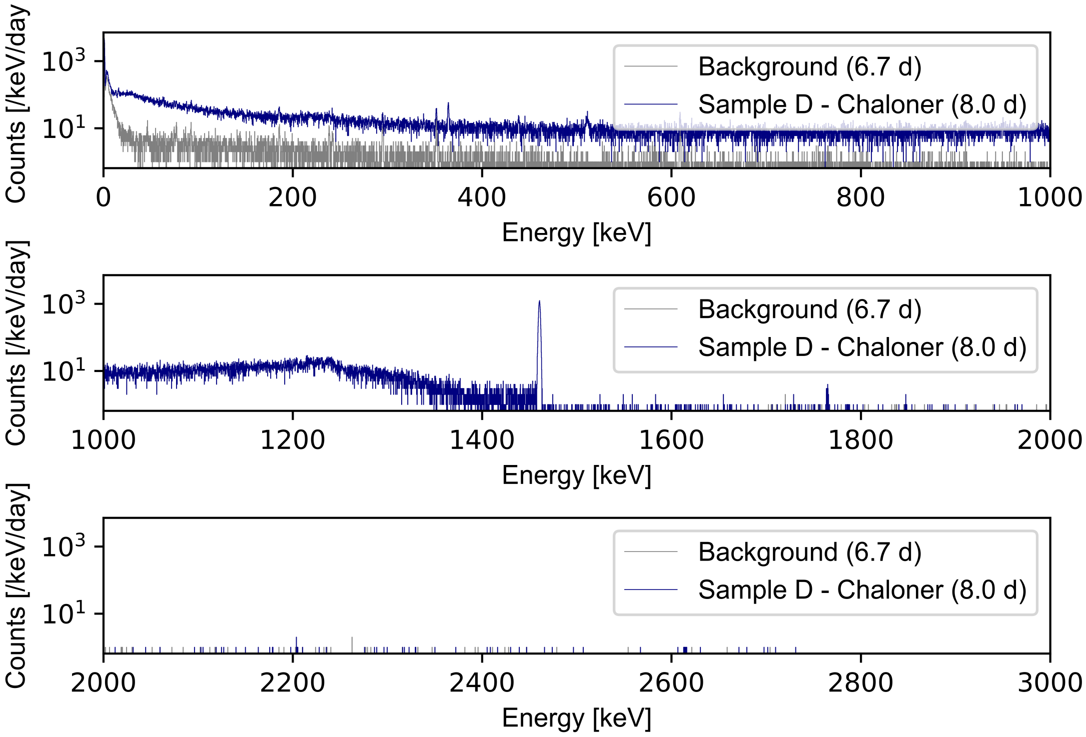

Figure 4.10: Spectra of open system water sample D. It is evident it presents the highest concentration factor out of all assayed samples.

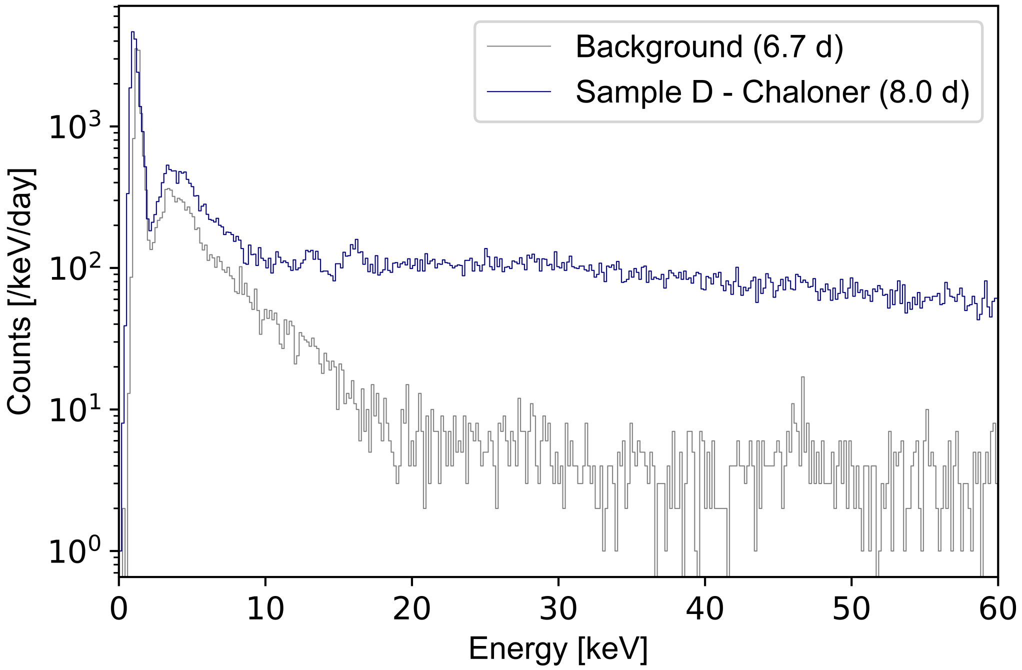

Figure 4.11: Spectra of open system water sample D, zoomed to region of ^{210}Pb peak.

E is 172 ± 20 Bq/kg. This value is confirmed using the initial measurement of sample D performed on Roseberry. This qualitatively indicates that this method retains at least 90 ± 50 % of ^{40}K by comparing the average of activity measured in CHALONER from samples A through E, with the initial activity of 167 ± 26 Bq kg^{-1} (measured in ROSEBERRY).

Sample name	A (CHALONER)	A (ROSEBERRY)
Tap water sample	-8 ± 106	167 ± 26
A	153 ± 21	-
B	124 ± 7	-
C	150 ± 13	-
D	72 ± 2	71 ± 3
E (limescale)	100 ± 20	-

Table 4.5: Measured ^{40}K concentrated specific activities A in all open water samples, in Bq/kg. For samples A-D, values are corrected based on the reduction factors described in Table 4.2. If all ^{40}K remained in the sample under concentration, all values should be identical. For the tap water sample, the CHALONER run was very short, hence why a high uncertainty is documented. As the intrinsic background of the CHALONER detector is around 10× higher than that of the ROSEBERRY detector, a negative A value for the tap water sample shows it is consistent with the background.

For the runs on CHALONER, ^{210}Pb was observed in sample C with a calculated specific activity of 786 ± 369 mBq kg^{-1}, which scales to a non-concentrated specific activity of 1.24 ± 0.58 mBq kg^{-1}. Although sample D has a concentration factor 5.6× higher than sample C, the Compton continuum of the ^{40}K peak in this sample was so dominant that the count rate in the expected peak from ^{210}Pb (at 289 ± 271 mBq kg^{-1}) is consistent with fluctuations in the background and could easily be lost within it – Figure 4.11. This suggests that over-concentration can actually impede the ability to measure ^{210}Pb in water using a germanium detector.

From the ROSEBERRY run on sample D, performed on 26th March 2019, a surprising result was observed: peaks in the energy spectrum consistent with the presence of ^{131}I were observed with a specific activity of 2.4 ± 0.3 Bq kg^{-1} (5.06×10^{-10} ppb). During the analysis of the sample D assay using CHALONER (a run starting on the 18th April 2019 and ending on the 1st May 2019) these peaks were re-analysed and were found to have reduced to an average of 0.28 ± 0.05 Bq kg^{-1}. To verify this result, the decay law $A = A_0 e^{-\lambda t}$ was used, where A is the activity of a radioactive sample, A_0 is the activity at $t = 0$ and λ is the decay constant, $= \frac{ln(2)}{t_{1/2}}$, where $t_{1/2}$ is the half life. Assuming an A_0 of 2.4 ± 0.3 Bq kg^{-1} and an ^{131}I $t_{1/2}$ of 8.0252 ± 0.0006 d, an estimated reduced activity of 0.20 ± 0.02 Bq kg^{-1} was found. This calculation confirms that the measured peaks were consistent with ^{131}I. Its activity would have been higher at the point the water was extracted from the tap on the 14th March 2019 – 5.5 Bq kg^{-1}.

In addition to ^{131}I, ^{177}Lu was also found in sample D. In the ROSEBERRY run of 26th March 2019, ^{177}Lu was observed with a specific activity of 3.3 ± 0.5 Bq kg^{-1} (5.84×10^{-10} ppb). In the CHALONER run, the activity was shown to have reduced to 0.22 ± 0.10 Bq kg^{-1}. To verify this result, the decay law was used again. Assuming an A_0 of 3.3 ± 0.5 Bq kg^{-1} and a ^{177}Lu $t_{1/2}$ of 6.73 ± 0.01 d, an estimated reduced activity of 0.17 ± 0.03 Bq kg^{-1} was found.

Whilst ^{40}K occurs naturally and ^{210}Pb can be found in water in trace amounts, ^{131}I and ^{177}Lu are used for medical and industrial purposes. In medicine, ^{131}I is used in radiotherapy for the treatment of thyrotoxicosis and thyroid cancer [184, 185]. In industry, ^{131}I is used in the oil industry [186]. ^{177}Lu is a component in Lutetium chloride, a radioactive compound used for radio labelling other medicines such as anti-cancer therapy [187]. In [69], more than fifty "parameters", including lead, are measured in tap water, but ^{177}Lu and ^{131}I do not constitute those parameters. A literature review regarding the presence of these isotopes in London tap water returned only one result [188], dated back to 1986, which reports on ^{125}I and ^{131}I being measured in environmental samples from the Thames Valley. It is therefore of note that these isotopes can be found in London tap-water.

Chapter 5

PlomBOX - device development

This chapter will describe the development pathways employed to design the components of the PlomBOX, as addressed in Chapter 1. Figure 5.1 highlights how all the components are combined into a single device. The PlomBOX encapsulates the biosensor and the imaging device. The biosensor is contained on a tray and mixed with the water that is to be analysed. The imaging device, which constitutes the Data Acquisition (DAQ) system of the PlomBOX, captures images of the biosensor's response to the presence of lead in the water. When the assay finishes, the images are sent to the PlomApp via Bluetooth. The PlomApp, which constitutes the user slow control of the DAQ system, sends these images to the server via Wi-Fi, where they are processed and analysed. A final lead result is returned to the user via the PlomApp.

Section 5.1 will focus on the design of the lead sensitive bacterium. This includes a discussion on the biosensor used as a reference for this project, seen in Section 5.1.1, sharing preliminary biosensor developments utilising a fluorescent biotransducer, seen in Section 5.1.2, and describing the colourimetric biosensor ultimately developed for the PlomBOX, seen in Section 5.1.3. Section 5.2 will address the design of the hardware, encompassing a discussion of the electronic components utilised, as well as elaborating on the design of the PlomBOX casing, presented in Section 5.2.1. Section 5.3 will elaborate on the design of the PlomApp. This includes a justification of the application architecture choices made, in Section 5.3.1, a description of all the user interface components, in Section 5.3.2, a description of the communication protocols between the PlomApp and the PlomBOX, in Section 5.3.3, and the communication between the PlomApp and the server, in Section 5.3.4.

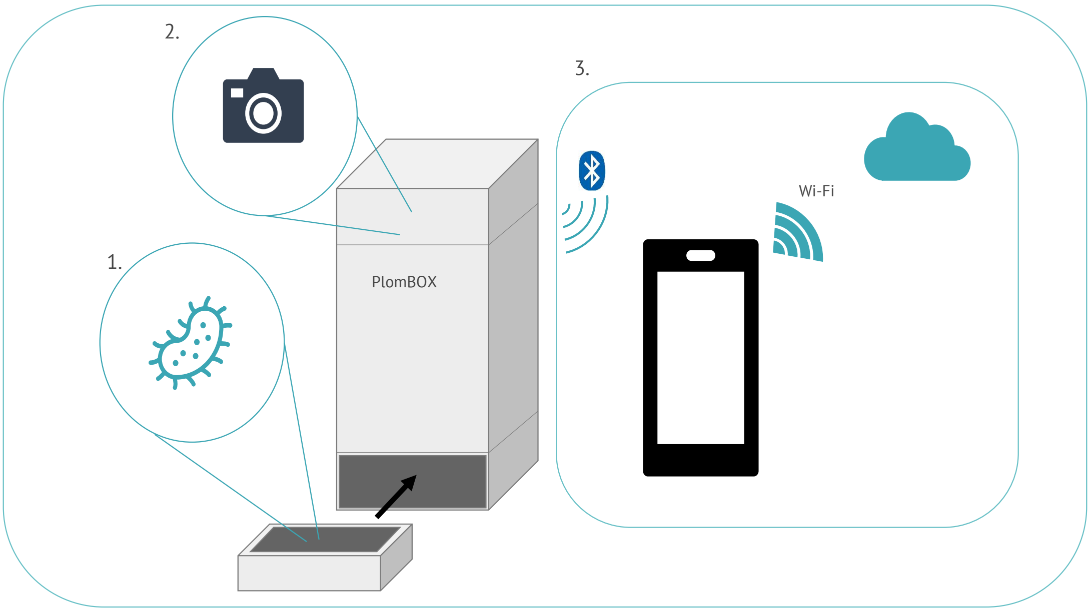

Figure 5.1: Diagram of the PlomBOX with all its working components. Point 1 represents the biosensor, located in a tray, mixed with the water that is to be analysed. This biosensor is imaged by the Data Acquisition device seen in point 2. The obtained images are sent to the PlomApp, seen in point 3, via Bluetooth and consequently sent from the PlomApp to the server via Wi-Fi. The server processes and analyses the images and returns a final lead result to the PlomApp.

5.1 Design of a lead sensitive bacterium

5.1.1 Reference biosensor - sensAr

The biosensor developed for this project uses another sensing device as a reference. This biosensor is called SensAr and its goal is to detect concentrations of arsenic in water samples as part of an inexpensive device [189].

SensAr uses genetically modified *E. coli*. It contains genes to measure the level of arsenic and to produce a colourimetric response based on the level of arsenic in the sample.

SensAr is contained in a box and the user does not handle any bacteria, but can infer the concentration of arsenic in a given water sample.

To make a measurement, the user needs to deposit a water sample into the well of the box. This box contains a sample of clean water, with no arsenic content, to be used as a control sample. After a few hours of assay, the user can compare the colour of SensAr's response to the water sample to the colour of the control sample – Figure 5.2. A yellow result represents an arsenic concentration lower than the WHO's limit of 50 µg/l, or 50 ppb [189]. A concentration equal to the WHO's arsenic limit returns an orange result and any samples with a concentration greater than 50 ppb present a red result. Samples of water that returned a red colourimetric response should not be consumed.

Figure 5.2: SensAr prototype, showing the casing and the biosensor colour results based on arsenic concentration [189]. If the biosensor presents a yellow colour, the water has an arsenic concentration below the WHO's limit. If the colour is orange then the sample has an arsenic concentration equal to WHO's limit, and if the colour is red then the concentration is greater than WHO's limit and the water should not be consumed, as shown in the Figure.

5.1.2 Fluorescent biosensor design

The fluorescent biosensor for lead detection in the PlomBOX uses an *E. coli* DH5α strain. This construction possesses a regulator protein (pbrR), which binds to lead, and a regulatory zone attached to the sfGFP gene, which is the reporter gene. For this biosensor the pbrR constitutes the bioreceptor and sfGFP constitutes the biotransducer, as introduced in Section 2.1.3.2.

To test the biosensor's lead sensitivity, the bacteria were grown overnight in a Luria-Bertani (LB) medium. LB medium is a nutrient-rich medium used for fast and good cultivation of bacteria [190]. An inoculum of 20 µl of this culture was diluted in 800 µl of final volume with solutions containing culture medium and lead until reaching a concentration of 0, 10 and 100 ppb for induction. The measurement was carried out at 37 °C in triplicate, in a 96-well plate and a Tecan Infinite® 200 PRO plate reader. For the fluorogenic method, the fluorescence intensity of the sfGFP was measured – Figure 5.3. Measurements using this reporter return high variability between data sets and the obtained response to lead is very small. This had previously been observed in [191] and is typical of biological systems.

5.1.3 Colourimetric biosensor design

As the fluorescent biosensor shown in the previous section presented variability in the results, the team of biologists explored the design of a colourimetric biosensor and chose it as the one to be used in the PlomBOX.

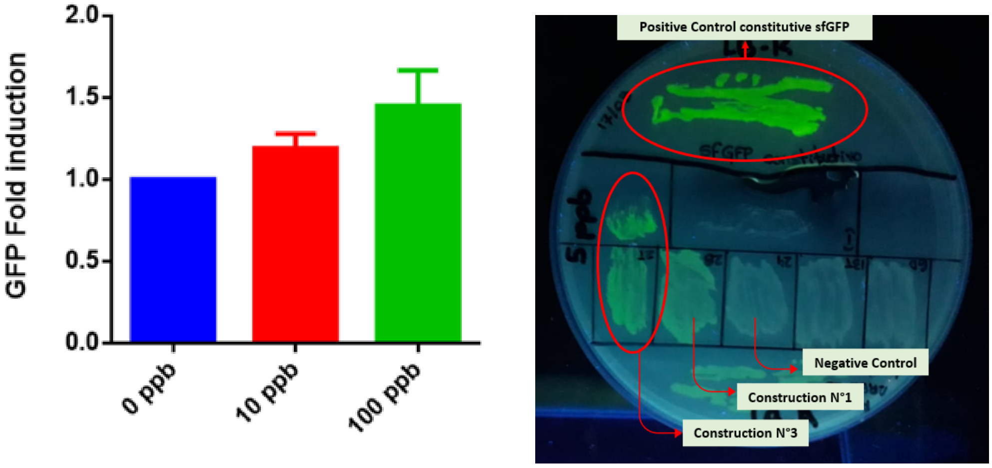

(a) (b)

Figure 5.3: Measurement of GFP protein lead dose response. 5.3a GFP Fold Induction (bacteria concentration increase %) vs Lead concentration in ppb for Construction n3; 5.3b Petri dish with several *E. coli* colonies expressing GFP. Negative Control and Positive control correspond to an untransformed *E. coli* strain and a GFP over-expressing strain, respectively.

As with sensAr, it uses an *E. coli* DH5α strain but, in this instance, it has a regulator protein (pbrR) binding to lead and a regulatory zone attached to the β-Gal gene as the reporter gene, introduced in Section 2.1. For this strain, a lead transporter protein (pbrT) was included to increase lead intracellular concentration, thereby enhancing the device's sensitivity. β-Gal expression is regulated by a lead sensitive promoter/operator that activates transcription when lead bound-pbrR binds to it. Therefore, when lead and X-Gal are present, the reporter protein is produced and the β-Gal enzyme can cleave the glycosidic bond in the X-gal to produce galactose and a blue product, as described in Section 2.1.3.3.

To perform a lead assay, bacteria was cultured in LB buffer supplemented with glucose [192] and ampicillin ($100\,\mu\text{g}\cdot\text{ml}^{-1}$) and placed in an incubator overnight at 37 °C and at 220 rpm. Ampicillin, an antibiotic, is added to the solution to prevent the growth of other bacterial species. A LB/X-gal solution was also prepared in which X-gal was diluted 1/10 in LB medium (1 part of X-gal per 10 parts of LB medium) prepared as described in [193]. 12 µl of the overnight culture was placed over a 10 × 7 mm Whatman Chromatography paper, together with 12 µl of LB/X-gal solution. Whatman paper is widely used in biology laboratory settings for general chromatography [194]. The paper was placed in the PlomBOX's sample holder and 750 µl of lead solution, with different lead concentrations, was added – Figure 5.4a. Before the assay, a lead solution was prepared by mixing 5000 ppb of lead nitrate [195] with distilled water. This solution was then diluted serially to produce lead concentrations ranging from 0 to 100 ppb, as indicated in Table 5.1. This operation used a MyPIPETMAN® P1000 pipette which has the following systematic errors: ±3 µl for volumes $<$ 100 µl, ±4 µl for volumes $>$ 100 µl and $<$ 500 µl and ±8 µl for volumes $>$

500 µl and < 1000 µl volumes. This suggests that there will be inherent uncertainty in the volume of the prepared lead solutions. Pipettes are devices capable of measuring precise quantities of liquid with reduced contamination of samples [196].

Lead concentration (ppb)	Solute Volume (ml)	Solvent Volume (ml)
500	0.5 of 5000 ppb	499.5
200	80 of 500 ppb	120
100	100 of 200 ppb	100
50	100 of 100 ppb	100
10	40 of 50 ppb	160

Table 5.1: Table showing dilution concentrations for the different lead solutions of the lead curve. This is done via a serial dilution, where the solute is the volume of the previous lead concentration solution and the solvent is deionised water.

The incubation period took 7 h at 37 °C, although this could also be achieved at room temperature (∼ 24 °C) for a longer period of time (> 12 h). During this period lead uptake took place and bound to the pbrR protein, β-Gal was expressed and blue colour was produced according to the lead concentration in the water sample – Figure 5.4b.

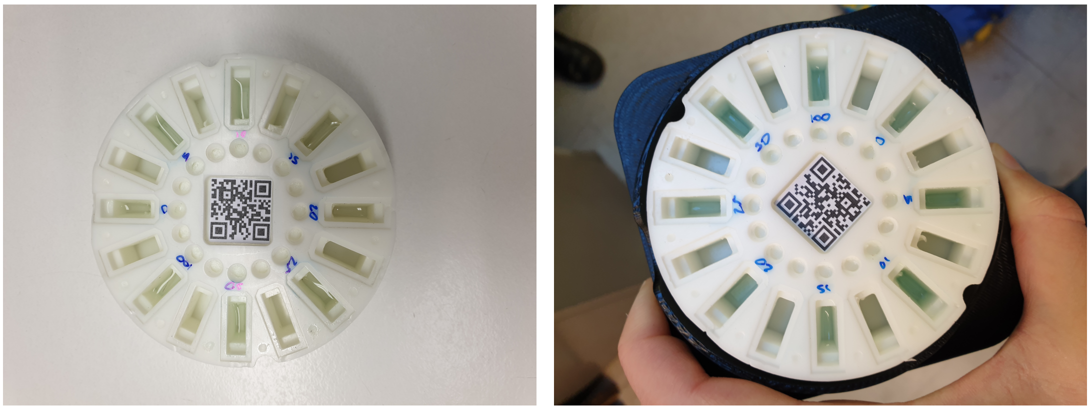
(a) (b)

Figure 5.4: PlomBOX sample holder containing biosensor and water doped with lead concentrations of 0-5-10-15-20-25-50-100 ppb. 5.4a shows the sample holder before assay started, and 5.4b shows the sample holder after overnight incubation, showing the blue colour resultant from β-Gal expression.

5.2 Design of hardware

The electronic hardware of PlomBOX system comprises a low-cost ESP32-CAM development board [197] and a bespoke PCB, designed by the team of electrical engineers, which drives a DS18B20 device for temperature sensing and PL9823 colour LEDs, used for illuminating the biosensor – Figure 5.5. The ESP32-CAM evaluation board has a dual-core 32-bit CPU operating at a maximum frequency of 240 MHz, with a built in 520kB SRAM and an external 8MB PSRAM, supports Wi-Fi and Bluetooth protocols (only Bluetooth is used in this project), and supports the OminiVision

OV2640 CMOS colour camera, which is used in the device to obtain colourimetric information from the biosensor. The OV2640 [198] image sensor has 1600×1200 active pixels each with a height and width of 2.2 µm. It contains a RGB colour filter array which provides colour information. Its dark current value is 15 mV/ sec at 60 °C. The sensor has on-chip image processing capabilities to improve the perceived visual image quality as automatic gain control, automatic exposure control, automatic white balance, automatic band filter, and automatic black level calibration which have been disabled to avoid systematic errors in the quantification of the incoming light. The sensor allows sub-sampling which was used to reduce the amount of transmitted information. The ESP32-CAM contains a MicroSD Card Module. An SD card is used to store all the data acquired by the ESP32-CAM.

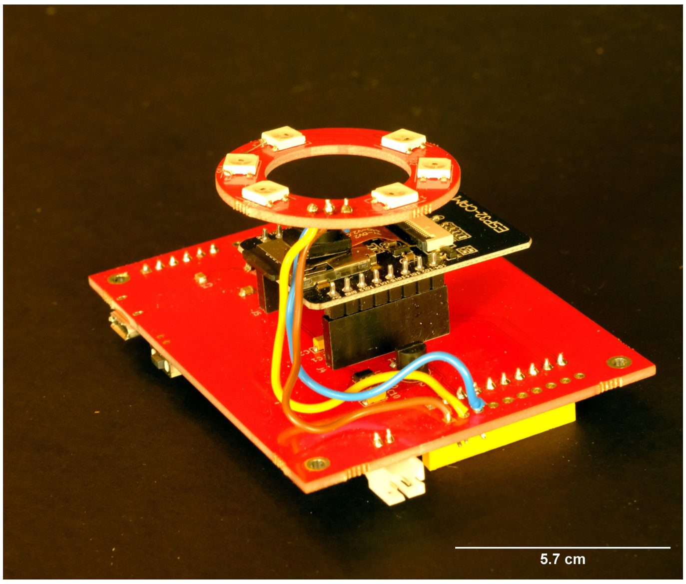

Figure 5.5: ESP32 with OV2640 camera module connected to the PCB. The ring with LEDs can be seen above the ESP32-CAM. [199]

5.2.1 PlomBOX casing

In adherence to the goal of ensuring affordability and accessibility of the PlomBOX device, it was determined that the casing would be 3D printed, with its design drawings made available to the public as open source material.

Figure 5.6 shows different casing designs developed for the PlomBOX. The black model on the left was the first and the one on the right is the most recent, final model. The final design was the result of addressing several challenges found in previous versions. For example, its height was adjusted to permit a focal length of 99.99 mm between the ESP32-CAM and the sample holder, as previous versions' heights resulted in images of the sample holder being out of focus - as seen in Figure 5.7. The sample holder design was changed to ensure that the Whatman paper with

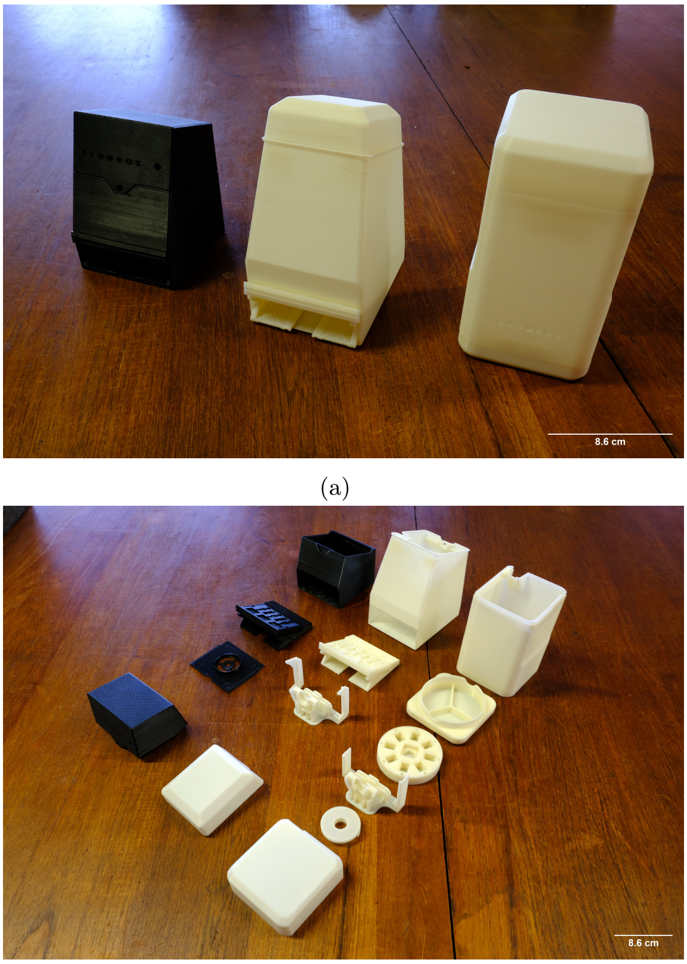

(a)

(b)

Figure 5.6: PlomBOX casing designs. 5.6a shows the difference in shape and size of the different versions, with the model on the left being the oldest and the model on the right being the most recent, final model; 5.6b shows all the components that fit inside the PlomBOX: the PlomBOX lid, at the top of the image, the body of the box, the sample holders and the PCB holders, at the bottom of the image. [199]

the biosensor could be placed in the wells, with the water sample, to be regularly imaged during the incubation period. In the previous versions this process occurred outside the PlomBOX and, after the incubation period, the Whatman papers were placed on the sample holder for imaging. The colour of the PlomBOX was changed from black to white to maximise light diffusion inside the box, to improve illumination of the samples. The design of the PCB holder was changed to include a diffuser to be placed on top of the LED ring, also to improve illumination of the samples and reduce glare on the liquids in the wells – Figure 5.8. Studies were performed on these last two points and are shown in Chapter 6, in Section 6.2.

All the designs were printed in a Stratasys uPrint SE plus 3D printer which uses ABS plastic. Liquid leaks were observed between sample holder wells that were printed with ABS – Figure 5.9, middle. Thus, resin was chosen as the optimal material to print the sample holders. The resin sample holder shown in Figure 5.9 was printed using an ELEGOO Mars 3 Resin 3D Printer [200].

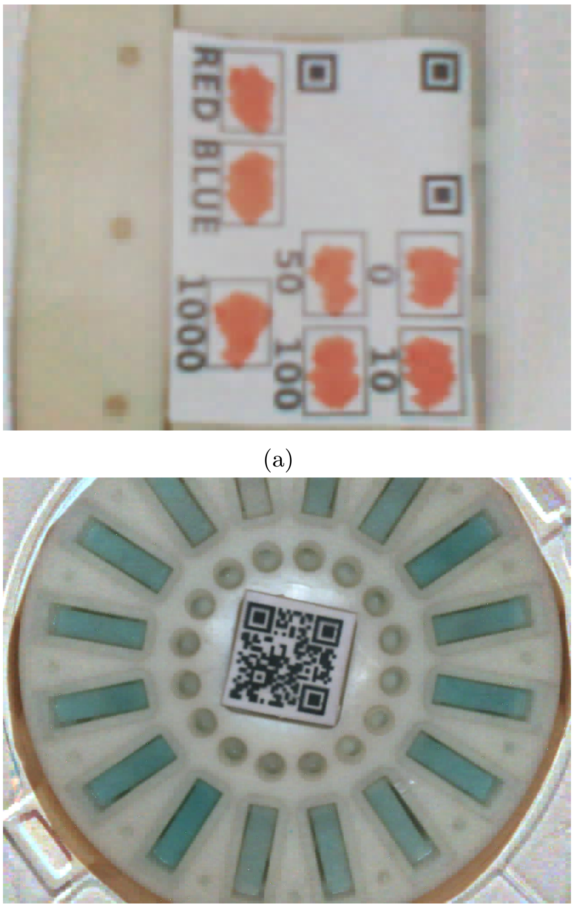

(a)

(b)

Figure 5.7: Comparison of sample holder imaging before and after focal distance adjustment between the ESP32-CAM and the sample holder. 5.7a shows the imaging of a test piece of paper placed on the sample holder of the second version of the PlomBOX, out of focus; 5.7b shows the imaging of the biosensor mixed with water samples in the sample holder wells of the third version of the PlomBOX, in focus. The corners of the QR code in both images provide a good comparison of the outcome of the focal distance adjustment.

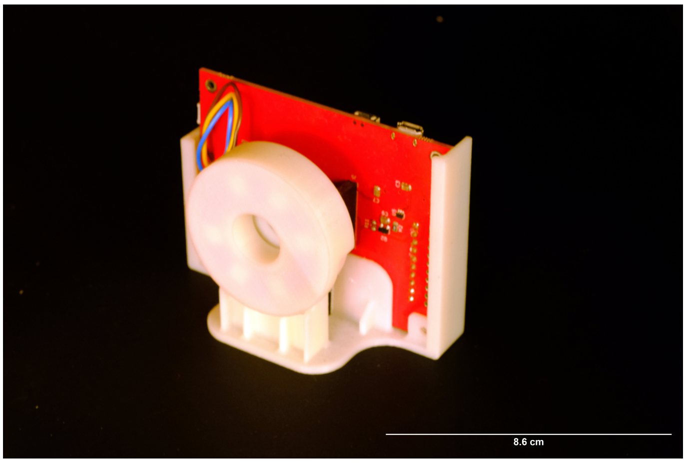

Figure 5.8: PCB slotted on the PCB holder, with diffuser covering the LED ring. [199]

In ABS 3D printing, the build line thickness is 0.2 mm whereas in resin 3D printing is 0.01 mm [200]. Thus, the resin printers have higher printing resolution, which helps to stop leaks between sample holder wells.

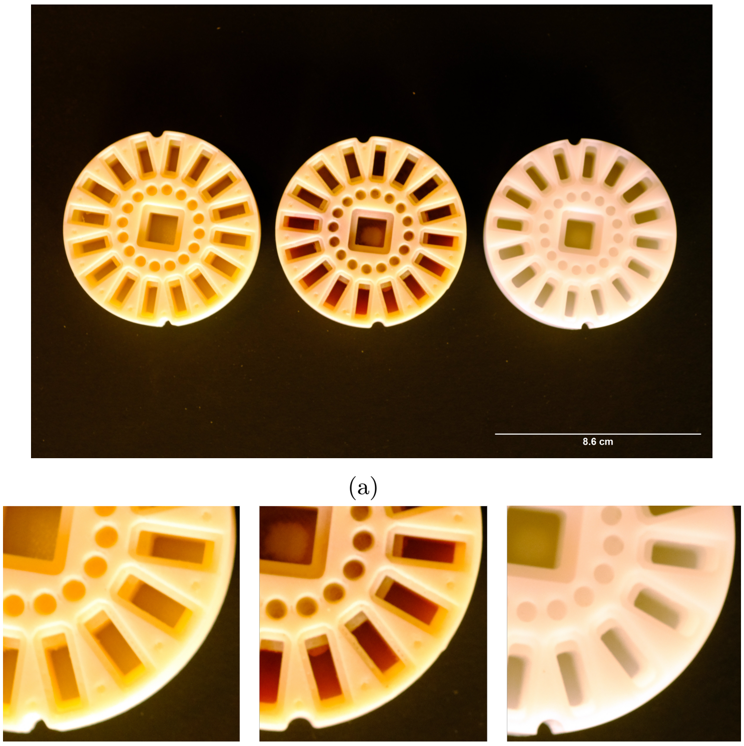

(a)

(b)

Figure 5.9: 5.9a Photo of sample holders printed with different materials. The left and centre sample holders were printed with ABS plastic and the right sample holder was printed with resin. To test leaking between wells, water died with red ink was placed on alternating wells in the middle sample holder. 5.9b Cross section of the different sample holders. The left is the ABS plastic sample holder, centre is the ABS plastic sample holder showing the staining and the right is the resin sample holder. [199]

Figure 5.10 shows the final design of the PlomBOX, with all the considerations mentioned above addressed.

5.3 Design of PlomApp

To be consistent with the objective of enhancing user-friendliness, accessibility and keeping cost down, it was determined that the utilisation of a mobile phone application as a slow control, as mentioned at the beginning of this chapter, was preferred over specialised equipment. The PlomApp was designed to require minimum user input with automation of the majority of the operations. Thus, the user only needs to control the connection from the mobile phone to the PlomBOX, dictate when and how much data is to be taken, and to send the data to the server at the end of an assay. The PlomApp architecture choices are discussed in Section 5.3.1. Section 5.3.2 will describe the user interface architecture of the PlomApp. The communication between the PlomApp and the PlomBOX is explained in Section 5.3.3, while the communication between the PlomApp and the server are explained in Section 5.3.4.

Figure 5.10: Photo of the PlomBOX's final design, with PCB visible at the top. [199]

5.3.1 App architecture choices

The application was developed for mobile phones with an Android operating system (OS) rather than an iPhone OS because Android is the leading mobile operating system worldwide, having had a market share of 71.64 % in the third quarter of 2022 [201]. Android Studio was chosen as the development environment for the application and Java was chosen as the programming language. Java was chosen as, until recently, it was the official programming language of Android application development [202].

The mobile phone communicates with the PlomBOX via Bluetooth and communicates with the server via Wi-Fi. Bluetooth is a type of wireless technology for transmitting data between devices over short distances [203]. The ESP32 uses Bluetooth Low Energy (BLE), which is designed for low power operation. Wi-Fi is also a type of wireless technology for transmitting data between devices over short distances and, for the purposes of the PlomApp, is used to connect to the Internet [204].

Using Wi-Fi, the PlomApp transfers data to the server. The server is run on `Linux` and encompasses several Docker containers. Docker is a software platform with the capability to build, test and deploy applications. In Docker, software is packaged into standardised units called containers [205]. The five containers in the server are: Message Queuing Telemetry Transport (MQTT) broker, database, dispatch, query and grafana. Figure 5.11 shows a diagram which explains the relationship between these containers. All the server software is written in `Python`.

Communication between the PlomApp and the server occurs via MQTT protocols which comprise three entities: publishers, a message broker and subscribers. Publishers, like the PlomApp,

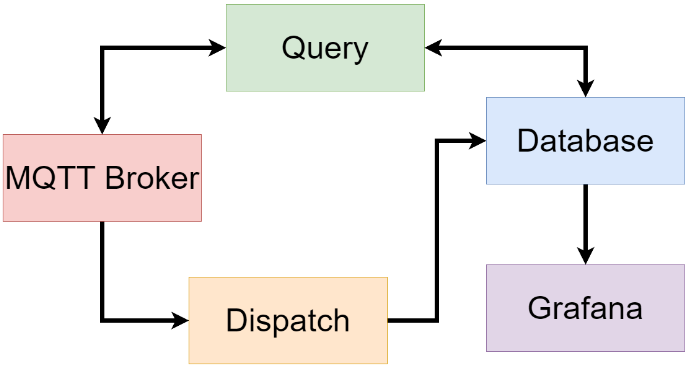

Figure 5.11: Layout of the server's containers

are entities which publish data on the MQTT broker. Subscribers receive information published on the MQTT broker. The PlomApp is also a subscriber as it receives analysis results from the server. The message broker is an intermediary that receives messages and then routes them to the appropriate subscribers based on "topics" [206]. Publishers and subscribers need to have the same "topic" for information to be shared between them. Additionally, in the implementation they need to authenticate themselves with Transport Layer Security (TLS) certificates to send or receive messages published on the MQTT broker. TLS certificates use encryption to secure and safeguard data that is exchanged between two systems [207].

The server uses an InfluxDB database, which is designed to handle, manage, and store large time series data [208]. It is filled by dispatch as well as the query containers, detailed below. The data on the InfluxDB is accessed using a Structured Query Language (SQL)-like query language. The dispatch container subscribes to the MQTT broker and processes incoming messages. The messages are processed and stored in the InfluxDB. The query container has read and write access on the MQTT broker and the InfluxDB database, allowing an user to send a command to query the database, with the result of the query being returned to the user via MQTT. Grafana is a tool to query, monitor and visualise data that is received on the server [209].

All the data that is exchanged between the PlomApp, the server and the PlomBOX is done in JavaScript Object Notation (JSON) string format. This is a lightweight data-interchange format that is language independent and presents itself as a collection of name/value pairs, or objects [210]. All images acquired by the PlomBOX, and their metadata, are consolidated in a single JSON string, per image. The images are stored inside the JSON strings in Base64 format, which is a binary-to-text encoding, used to represent binary data [211].

A JSON string created by the PlomBOX can be seen in the Appendix A.1.

With the exception of the image object, all the other objects in the JSON string store specific metadata components:

- `"version"` - version of the PlomApp that this data was acquired with, representing its development stage
- `"esp32"`
  - `"ID"` - ID of the physical PlomBOX being used, is necessary for user authentication, explained in Section 5.3.2.1
  - `"firmware"` - version of the ESP32 firmware code this data was acquired with, representing its development stage
- `"telemetry"` - all the elements within this object pertain to date, epoch time and temperature, in celsius and fahrenheit, of the PlomBOX, when the image was acquired
- `"measurement"` - contains all the identifying information for the measurement
  - `"ID"` - ID of the image and it increments by 1, starting from 1, for each RGB image set. The Red, Green and Blue sub images of one image will all have the same ID
  - `"run"` - run number of this data set, unique to each user, is obtained from the server at the start of data taking
  - `"fname"` - JSON filename of the image
  - `"image"` - object which stores the image. For brevity, in the example above it is shown as `...`
  - `"led"` - all the information in this object is related to the LED set up. We can control the brightness of the LED of the ESP32 (`"brightness"`), and set up its colours (`"R"`, `"G"` and `"B"`)
  - `"cam"` - settings for the ESP32's camera
  - `"type"` - type of data taken for a single image. It can be a `"calibration"` or `"calibrated"` data type. This aids the server on its LED calibration calculations, described in Section 6.1.2
  - `"dataSetname"` - the user can give a name to the data set, such as "Kitchen Tap Water", as shown in Section 5.3.2.6
  - `"extra"` - this object stores the JSON string command that the PlomApp sent to the PlomBOX to take the data
  - `"user"` - Universally Unique ID (UUID), used to identify the user
  - `"date"` - date the data was taken (`"plomapp date"`). It also contains another object to store the date in which the water sample was collected (`"water sample date"`) as shown in Section 5.3.2.6

  - `"location"` - Global Positioning System (GPS) coordinates (`"latitude"` and `"longitude"`) of the mobile phone.

5.3.2 User interface architecture

Android applications can contain four components through which the phone system or a user can use the application: **activities**, **services**, **broadcast receivers** and **content providers** [212]. Activities are single screens that operate as a user interface. Services allow the application to continue running in the background of the mobile phone device. Broadcast receivers allow the mobile phone system to deliver events to the application even if the user is not interacting with it. Content providers manage shared data from the application.

For the PlomApp, the key components are activities. To each activity there were associated pieces of software created for different purposes, as seen in the next sections. These are described in the order in which a user would come across them when they open the PlomApp.

5.3.2.1 User registration

User registration was developed to ensure application security. If users are not registered with an email, a password and they do not have a unique PlomBOX ID, they cannot use the PlomApp.

All user information and authentication is handled by Google's Firebase. Firebase is a Google-backed application development software that can provide services for analytics, authentication, cloud messaging, databases, etc [213].

To register a user, they input their email address and a chosen password on the PlomApp – Figure 5.12. An email is sent to that email address to authenticate the account. On completion of this process, Firebase creates a UUID for this user and they can log into the PlomApp with their email and password. The UUID is not visible to the user but allows for an individual "topic" to be created. Thus, the user will only receive data intended for them, as the MQTT broker selects information for their topic.

A database of PlomBOX IDs is stored in Firebase and, every time a user logs in and inputs the ID, this is checked against the database. Thus, two layers of security were implemented, with the creation of UUID for each user and unique PlomBOX IDs that are checked on Firebase every time they log into the PlomApp. On failure of these two steps, the user cannot enter the PlomApp and use the PlomBOX.

5.3.2.2 User instructions

An activity was set up to show instructions to the user on how they can navigate the PlomApp and set up the PlomBOX for a measurement of a water sample – Figure 5.13. This ensures that

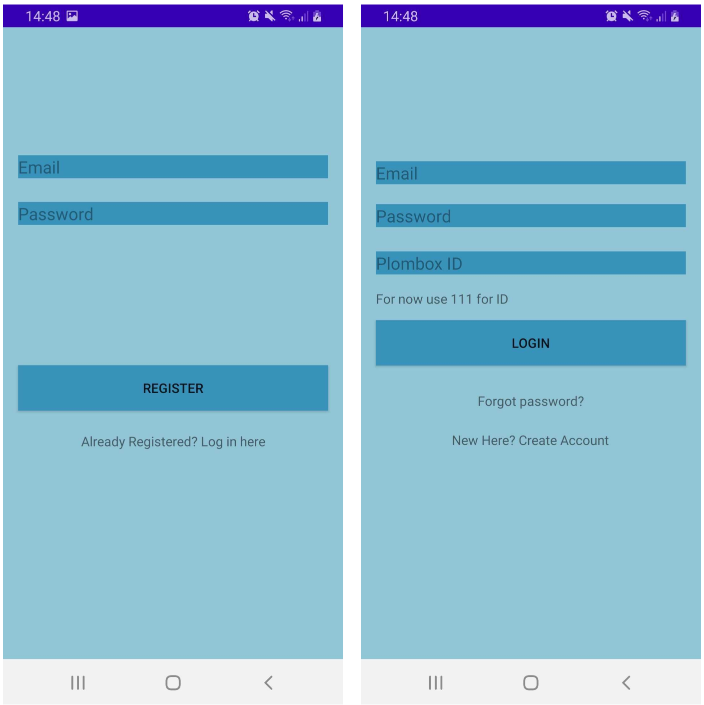

(a) (b)

Figure 5.12: PlomApp activities showing the 5.12a register and 5.12b log in screens. The user can navigate from the register to the log in screen by clicking on the text `"Already Registered? Log in here"`. For the development of the PlomApp, a temporary unique PlomBOX ID of `111` was used.

the users do not need to seek further documentation other than what is presented in the PlomApp. This activity has not been populated with information yet and is being used as a placeholder. The instructions will appear the first time the user opens the PlomApp, but no other times thereafter. They can, however, be accessed via the **Toolbar**, described in Section 5.3.2.4.

5.3.2.3 Languages

The PlomApp can present information in three languages: English, Spanish and Portuguese – Figure 5.14. As there is an intention to launch this project in South America, it was of interest to be inclusive and make the PlomApp practicable for people who may not have mastered English.

In the software related to this activity, three `XML` files were created, one for each language, where all the strings appearing on the activities are stored.

When the user loads the PlomApp, a Language activity will appear where the user can select the desired language. This is registered by the PlomApp and all following activities will use the chosen language.

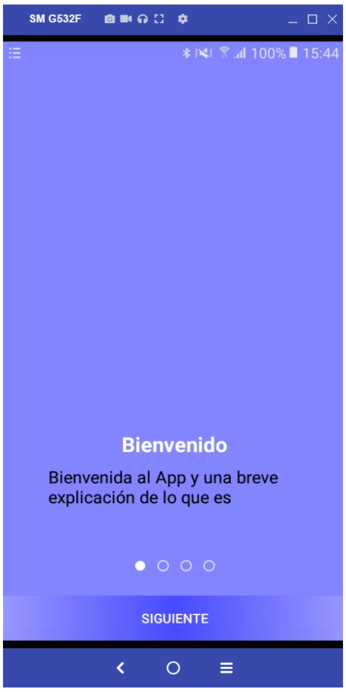

Bienvenido

Bienvenida al App y una breve explicación de lo que es

Figure 5.13: Activity to show user instructions on how to use the PlomApp and the PlomBOX. It is currently being used as a placeholder and does not contain actionable instructions.

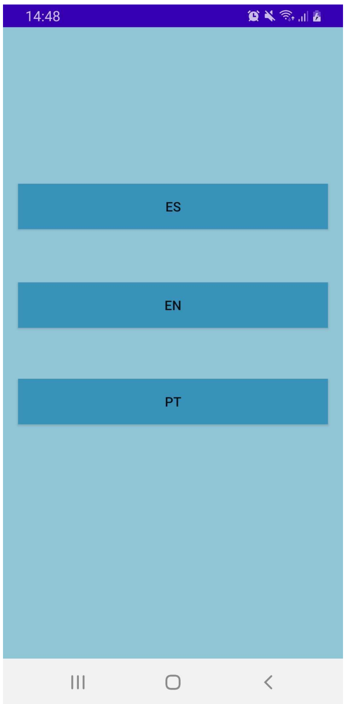

Figure 5.14: Language activity showing three buttons with the languages the user can select to navigate the PlomApp: Spanish, English and Portuguese.

5.3.2.4 Toolbar options

The toolbar contains three buttons for other functions the user can explore (Figure 5.15a): the first button on the left aims to take the user to a website where the results for their measurements are displayed (this has not been implemented yet). The middle button takes the user to the instructions activity, where they can read the instructions again. The button on the right directs the user to further options which includes a button `About us`, which directs the user to the PlomBOX webpage, a button `Survey`, which directs the user to a webpage where they can fill in a survey about conducting a water assay using the PlomBOX, and a button `Logout`, for the user to log out from the PlomApp – Figure 5.15b.

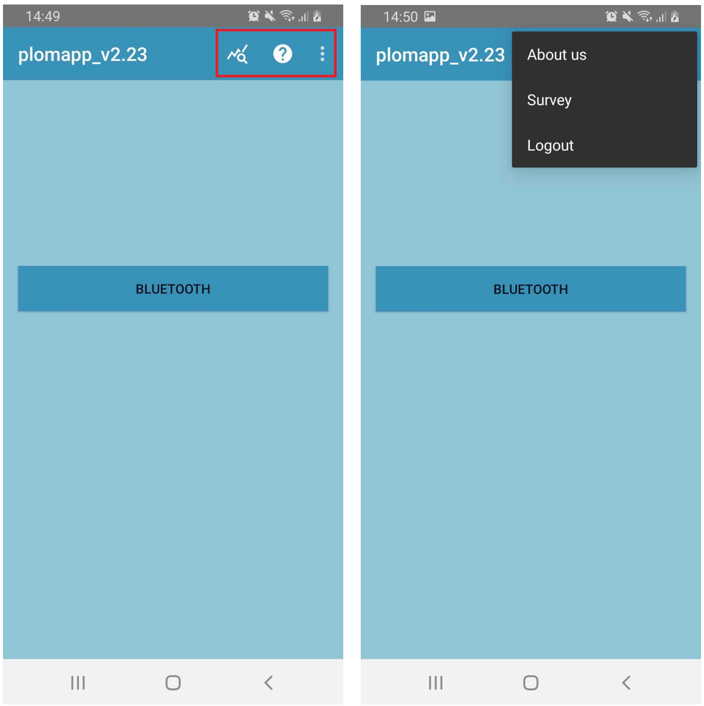

(a) (b)

Figure 5.15: Activity showing toolbar options. Figure 5.15a shows three buttons for the user to look at assay results (left button), view user instructions (middle button) or view further options (right button). This last button takes the user to further options, as seen in Figure 5.15b, for the user to visit the PlomBOX webpage (`About us`), fill in a survey about the assay process with the PlomBOX (`Survey`) and to logout from the PlomApp (`Logout`).

5.3.2.5 Bluetooth connection

The PlomApp contains an activity dedicated to the connection between the PlomApp and the PlomBOX via Bluetooth – Figure 5.16. In this activity there are four buttons with the following options: `Turn on` and `Turn off`, which turn the Bluetooth of the device on and off, respectively; `Make device discoverable` turns Bluetooth on and allows remote devices to see the device when they perform a discovery; `Get paired devices` shows a list of devices the mobile phone is connected to and with which the PlomApp can pair to. This is the option to be chosen for the PlomApp to pair with the PlomBOX.

When the user selects the option to pair with the PlomBOX, another activity appears giving the options to `Take data` or `Get results`, to take or retrieve data from the PlomBOX, respectively – Figure 5.17.

Bluetooth is available

"
Device: "pb-24F7EFC40A24,
24:0A:C4:EF:F7:26

"
Device: "pb-7C3E00C4F5FC, FC:F5:C4:00:3E:
7E

Figure 5.16: Bluetooth activity, with several connection options, including the option to pair with PlomBOX device - `Get paired devices`.

Figure 5.17: Activity where the user can choose to take data with the PlomBOX (`Take data`), or retrieve the images captured by the PlomBOX for a given assay (`Get results`).

5.3.2.6 Taking data

The activity dedicated to data acquisition can be seen in Figure 5.18.

Before data acquisition can begin, the microSD card that is connected to the ESP32-CAM

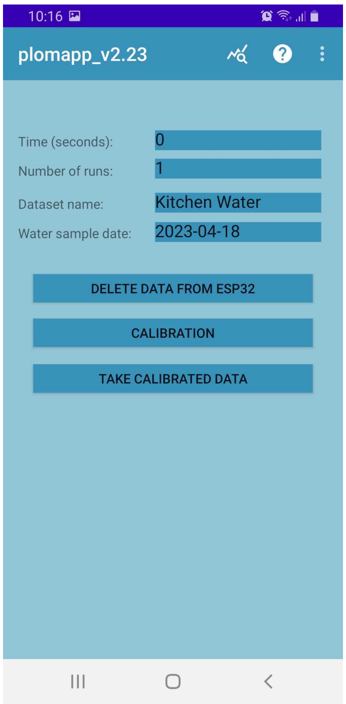

Time (seconds): 0
Number of runs: 1
Dataset name: Kitchen Water
Water sample date: 2023-04-18

Figure 5.18: Activity dedicated to data acquisition. This activity requires user input to determine how many runs should be acquired (`Number of runs`) and what the elapsed time between runs should be (`Time (seconds)`). There are additional inputs for the user to name the dataset (`Dataset name`) and to provide a date for when the water samples were collected (`Water sample date`). The buttons presented in this activity appear in the order these operations should occur. The microSD card connected to the ESP32-CAM needs to be cleared before data acquisition can begin (`Delete data from ESP32`), followed by a calibration run (`Calibration`) and the full calibrated data acquisition (`Take calibrated data`).

needs to be cleared. This is because the current PlomApp software cannot distinguish between different data sets stored in the same SD card and would allocate them to the same measurement ID.

After the SD card is cleared, the user can start data acquisition. This begins with a calibration run to adjust the brightness of the LEDs, which is explained in Section 6.1.2. Once this LED calibration run is acquired, the user can take LED calibrated data with the PlomBOX. The user has the choice of inputting how many images (runs) it wants, and how much time elapses between those runs. For example, a user can request 4 images to be taken 60 seconds apart.

This activity also contains two optional inputs, `Dataset name` and `Water sample date`. These inputs allow the user to name the dataset and to provide a date for when the water samples were collected.

5.3.2.7 Retrieving data

The activity related to this task can retrieve data from the PlomBOX or obtain the final lead concentration results from the server. Both tasks are explained in Sections 5.3.3 and 5.3.4 respectively. The `Request data from camera` button retrieves all the data from the PlomBOX onto the phone – Figure 5.19a. The `Get results from server` button obtains the lead concentration results for the latest set of data associated with the user – Figure 5.19b. The user has the choice of sharing the mobile phone's GPS coordinates, to be associated with the data set. A pop-up window appears the first time the app is run, asking the user for permission to use these. If the user does not consent to it, the JSON strings will appear with GPS coordinates with a latitude and longitude of 0°.

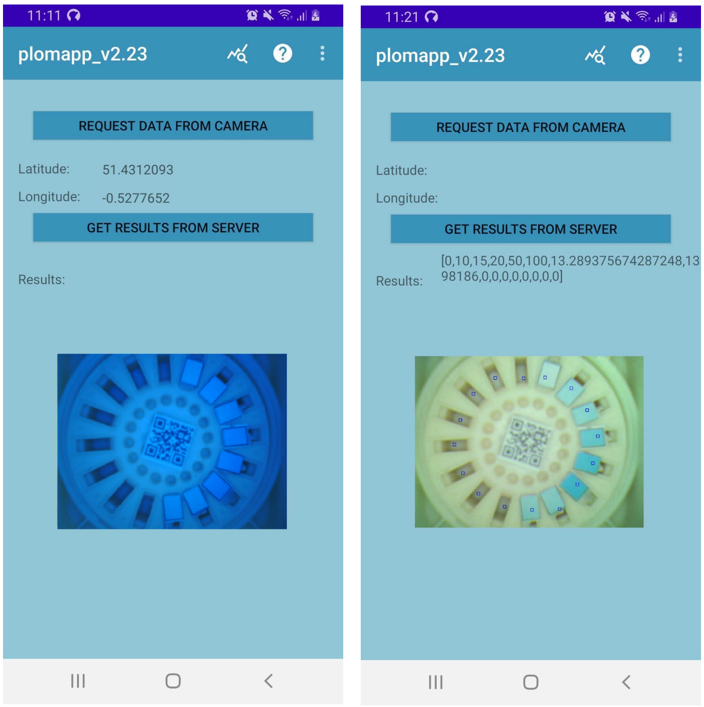

Latitude: 51.4312093
Longitude: -0.5277652
Results:

Latitude:
Longitude:
Results: [0,10,15,20,50,100,13.289375674287248,1398186,0,0,0,0,0,0,0,0]

(a) (b)

Figure 5.19: Activity where user can obtain images from the PlomBOX or retrieve final lead results from the server. 5.19a shows images being received from the PlomBOX before being sent to the server. All the images will appear on the PlomApp one by one. 5.19b shows the same activity as 5.19a but with final lead concentration results. The lead concentration for each well is shown in addition to the analysed image.

5.3.3 Communication between PlomApp and PlomBOX

Two processes take place in the communication between the PlomApp and the PlomBOX: one sends commands to the PlomBOX to begin data acquisition and the other sends commands to receive data taken by the PlomBOX on the PlomApp.

A set of JSON string commands were developed which are sent by the PlomApp via Bluetooth to perform these actions.

As described in Section 5.3.2.6, three tasks occur for the PlomBOX to acquire data: the SD card is emptied, an LED calibration data run, followed by the LED calibrated data run.

For the SD card to be emptied, the PlomApp requires a list of all the JSON files' names stored in it. The PlomApp sends a JSON string to the PlomBOX, shown in Appendix A.2.1. When the PlomApp has the list of files, it will loop through the list and will send a command to delete each file – Appendix A.2.2. When all files have been deleted, the PlomApp sends a command to the PlomBOX to take an LED calibration set of data – Appendix A.2.3. After the LED calibration concludes (explained in Section 6.1.2), the user can begin an LED calibrated data run, using a similar command – Appendix A.2.4. During data acquisition the PlomBOX can be left unattended and the PlomApp can be disconnected from the PlomBOX.

To retrieve data from the PlomBOX, the PlomApp begins by requesting a list of all the files stored in the SD card. Once this list has been received, the PlomApp will loop through the list and request each data file in succession. As the data is being received, the image is extracted from the JSON string, converted into a bitmap and displayed on the activity, as seen on Figure 5.19a. It takes 1 min from the data file request to having the bitmap displayed on the activity. A bitmap is an array of binary data which represents the values of pixels in an image [214]. By displaying the images on the activity as they are being received, the user can confirm that data was acquired and that it is being sent to the server for analysis.

After data is received on the PlomApp and before being sent to the server, the data JSON string is edited. The `"user"`, `"date"`, `"location`, `"measurement":"ID"`, `"measurement":"run"`, `"measurement":"type"` and `"measurement":"dataSetName"` objects are added, with information provided by the PlomApp.

5.3.4 Communication between PlomApp and server

Data files are sent to the server in succession, as they are received on the PlomApp, taking less than 30 sec for data to arrive on the server. Data is sent in JSON string format via Wi-Fi, by publishing it using the MQTT broker, and a topic defined by the UUID. Data is stored on the phone for instances in which Wi-Fi isn't available, but an option to send data straight from the PlomApp to the server has not yet been implemented - it still requires the PlomBOX for data to be sent.

The data is stored on the server but is not analysed until the user requests it. A function to begin analysis automatically still needs to be implemented.

The user can request a lead concentration result on their assay by sending a command similar to the one seen in Appendix A.3. This command specifies a `topic` unique to the user, so only data taken by them is analysed. The latest data run (`runNb`) and image within that run (`dataSampleID`) are found and analysed. A description on how the analysis works is given in Section 6.1.

The server returns the analysed image and the lead concentration for all the wells in this format: `phone test v4 analysis conc': [0, 10, 15, 20, 50, 100, 13.29, 13.38, 0.0,` `0.0, 0.0, 0.0, 0.0, 0.0, 0.0, 0.0]`. This is the lead concentration, in ppb, of each well in the sample holder, with the results presented clockwise, starting at the top of the QR code, as seen in Figure 5.20. The first six values are not calculated from the analysis but are representative of the lead concentrations of the elements of a lead curve used to obtain the concentrations of samples, as described in Section 6.1.

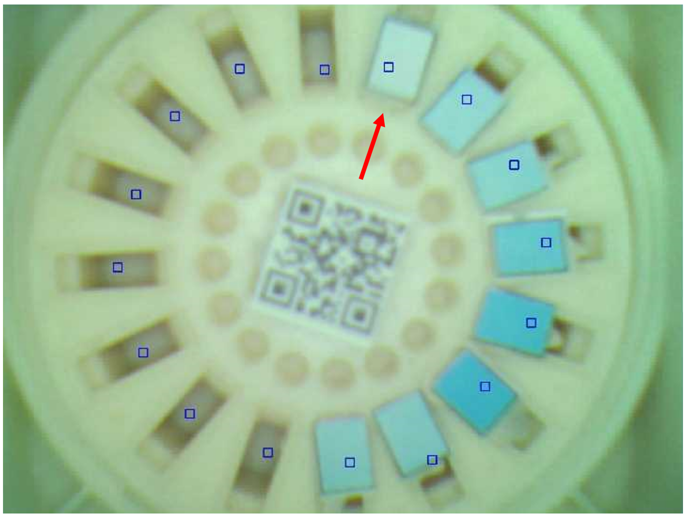

Figure 5.20: Results image obtained from the server, for a given data set. The red arrow shows the first well results are presented for, proceeding clockwise for the rest of the wells.

In Chapter 6 a detailed description of the analysis of assayed water samples will be provided.

Chapter 6

PlomBOX - device evaluation for measurement of lead in water

This chapter evaluates the use of the PlomBOX as a lead detection device.

Section 6.1 will focus on the development of the data analysis package responsible for obtaining a lead concentration in the sample under test from imaging the biosensor. Section 6.2 details studies undertaken to understand the operational imaging conditions required for the PlomBOX to return reliable results. Section 6.3 addresses the *in situ* assays that occurred to test the entire PlomBOX system. The chapter finishes with Section 6.4, which discusses the reliability of the PlomBOX as a lead detection device, based on its capabilities to detect lead at concentrations equal, above or below 10 ppb.

6.1 PlomBOX data analysis

6.1.1 Colour theory in digital imaging

Colour can be represented as a vector in a colour cube model according to three coordinates that describe colour, i.e. the colour primaries red (R), green (G) and blue (B) [215, 216] – Figure 6.1a. In digital image processing, the colour cube model specifies colours for image display, but it is difficult for a user to estimate the quantities of R, G and B necessary to produce a particular colour [215]. The use of HSV is preferred as an alternative representation of the RGB colour model. This is because HSV better represents how human vision perceives colour mixing and it aids artists in digital colour design, analogous to how one would mix paint in a physical palette [216]. For the PlomBOX, variations in lead concentration correspond to various shades of blue, a relationship that is more accurately depicted by measuring saturation as opposed to RGB values.

The HSV model is derived from the RGB colour model as follows [217]:

- The RGB colour cube (Figure 6.1a) is tilted along its main diagonal (the grey axis) from black to white – Figure 6.1b.
- The cube is projected onto a plane perpendicular to the diagonal, creating a hexagonal disk, as seen in Figure 6.1c. Any point inside the hexagonal disk represents colours that would be seen in the RGB colour cube along the grey axis.
- The grey level changes from black (0) to white (1), thus moving from one hexagonal disk to another. The disk at value 0 is a single point, increasing in area the closer it is towards white. This creates the HSV hexcone model – Figure 6.1c. The HSV hexcone disk contains the following colours, starting from red and moving counterclockwise: yellow, green, cyan, blue and magenta. The primary colours, red, green and blue, are equally separated around the hexcone disk, with red at 0°, green at 120° and blue at 240°. The secondary colours, yellow, cyan and magenta are present in-between the primary colours at 60°, 180° and 300° respectively [218].
- To simplify the conversion model formulae, by norm the HSV hexcone model is expanded into cylindrical form [219] – Figure 6.1d.

In the HSV model, Value is defined as the largest component of a colour [216]. Therefore, $V \in [0,1]$:

$$V = \max(R, G, B) \tag{6.1}$$

Hue and saturation specify points in each disk [216]. Hue is the angle around the disk and saturation is the length of a vector centred on the grey point of the disk - Figure 6.2.

Saturation is defined as the colourfulness of a stimulus relative to its own brightness i.e. V [129]. To determine saturation, chroma is required, which is the colourfulness relative to the brightness of a similarly illuminated white [129]. Chroma, C, is calculated by:

$$C = \max(R, G, B) - \min(R, G, B) \tag{6.2}$$

Saturation, $S \in [0,1]$, can be obtained from:

$$S = \begin{cases} 0, & \text{if } V = 0 \\ \frac{C}{V}, & \text{otherwise} \end{cases} \tag{6.3}$$

Hue is defined as the attribute of a stimulus according to which an area appears to be similar to one of the perceived colours: red, green, blue and yellow [129].

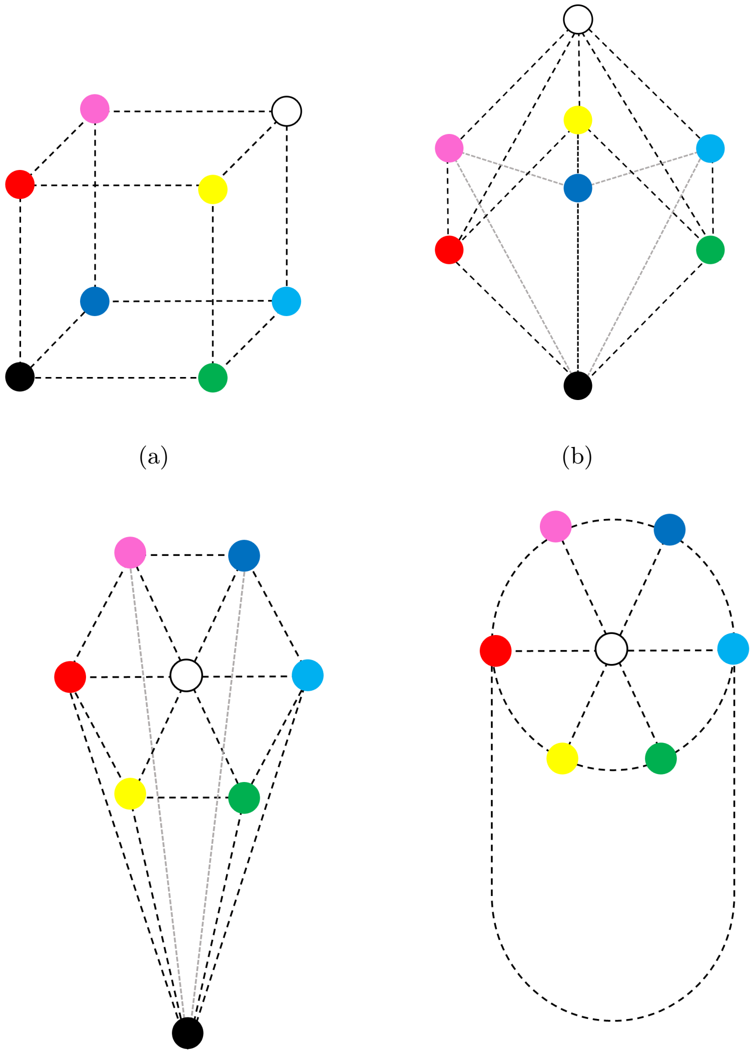

(a) (b) (c) (d)

Figure 6.1: Conversion from the RGB colour cube to the HSV hexcone. 6.1a shows the RGB colour cube, 6.1b shows the result of tilting the cube along its main diagonal (the grey axis), 6.1c shows the resultant HSV hexcone model with the grey level changing from 0 (black) to 1 (white) and 6.1d shows the hexcone model expanded to a cylindrical form, to simplify the conversion model formulae.

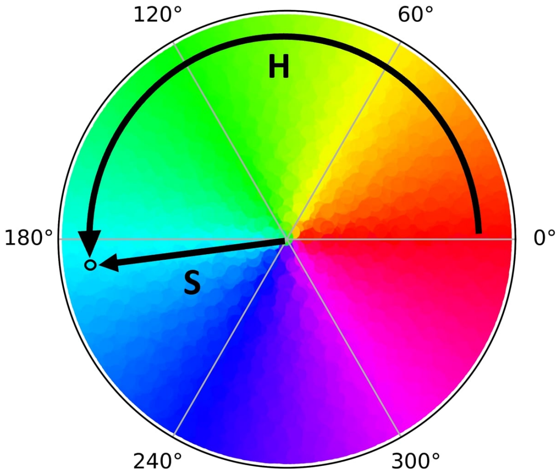

Figure 6.2: HSV disk showing saturation as a vector centred on the grey point of the disk and hue as the angle around the disk for a specific point.

The expression for hue for all cases when V is either R, G or B is presented below, where $H \in [0^{\circ}, 360^{\circ}]$:

$$H = \begin{cases} 60^{\circ} \times \left(\frac{G-B}{C} \text{mod6}\right), & \text{if } V = R \\ 60^{\circ} \times \left(2.0 + \frac{B-R}{C}\right), & \text{if } V = G \\ 60^{\circ} \times \left(4.0 + \frac{R-G}{C}\right), & \text{if } V = B \end{cases} \tag{6.4}$$

The normalisation values of 2 and 4 are in place when either $V = G$ or $V = B$, to indicate which sector the hue will be found on. The modulo operator mod6 is present when $V = R$ to ensure all hue values are positive. For example, a colour with (R,G,B) = (1, 0.42, 0.47) would return a hue of $-5°$ without mod6, as opposed to 355°.

For Figure 6.2, the point of interest has the following (R,G,B) = (0, 0.93, 1). Thus, $V = B$ and hue will be in the sector with a value between 180° and 300°. To determine hue, the two smallest primary colours, R and G, are subtracted and divided by the chroma, B - R. This returns a real number, which is multiplied by 60° to return an angle:

$$H = 60^{\circ} \times \frac{R-G}{C} + 4 = 60^{\circ} \times \frac{0-0.93}{1-0} + 4 = 184.2^{\circ} \tag{6.5}$$

In computing, colours are represented in a scale of 0 to 255, as opposed to a scale of 0 to 1. This representation of colour is commonly referred to as 24 bit colour [220]. This convention has been used on the analysis script of the PlomBOX.

6.1.2 Image analysis

All images taken by the PlomBOX are stored in Joint Photographic Experts Group (JPEG) format. This format was chosen as it prioritises small sized data files, ensuring they can be transmitted via Bluetooth to the PlomApp with ease. JPEG images undergo lossy compression by irreversibly removing data to reduce the file size [221]. This is achieved with chroma subsampling, where colour information has a lower resolution than the brightness information [222]. For example, in a 2×2 block of pixels the 4 chroma values are averaged, so only 1 value is stored for that block. For this project, a balance was struck between file size reduction and loss of colour information when opting for this image format.

Figure 5.20 shows the sample holder, with coloured papers, that is used to illustrate how the analysis script works.

As addressed in Section 5.3.2.6, data acquisition begins with an LED calibration run. This entails acquiring three LED calibration images. Each image has the RGB LED colours set to 255 respectively for red, green and blue, with a white paper on the sample holder – Figure 6.3. These are sent to the PlomApp and subsequently to the server.

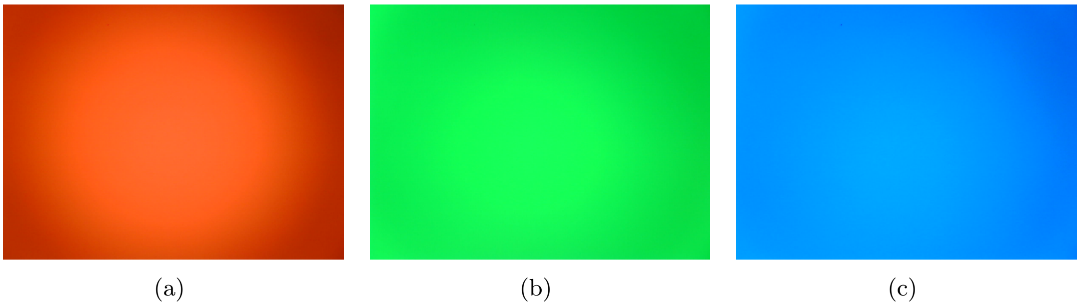
(a) (b) (c)

Figure 6.3: Images of white paper placed on sample holder inside the PlomBOX. This figure shows the 6.3a red 6.3b green and 6.3c blue images taken.

The average colour in the centre of each white paper RGB image ($\overline{RGB}_{\text{meas}}$) is obtained to calibrate the values of the LEDs. This calibration value aims at an average image RGB value, $\overline{RGB}$, of 200 (corresponding to the colour of a piece of white paper), compared to an automatic exposure control (AEC) value of 100. The automatic exposure control sets the aperture and shutter speed of a camera based on the external lighting conditions [223]. An AEC of 100 was assumed for the assays described in Section 6.3 but, in principle, this value can be adjusted to reflect the lighting conditions wherever the PlomBOX is placed for data acquisition.

$$\text{Calibration}(R, G, B) = AEC \times \frac{\overline{RGB}}{\overline{RGB}_{\text{meas}}} = 100 \times \frac{200}{\overline{RGB}_{\text{meas}}} \tag{6.6}$$

This algorithm returns three RGB LED exposure values between 0 and 255, one for each colour, that are returned to the PlomApp.

Following this acquisition, the white paper is removed and data can be acquired for the samples. For each data set, three images, illuminated by red, green and blue LEDs, are acquired – Figure 6.4. These are referred to as LED calibrated images.

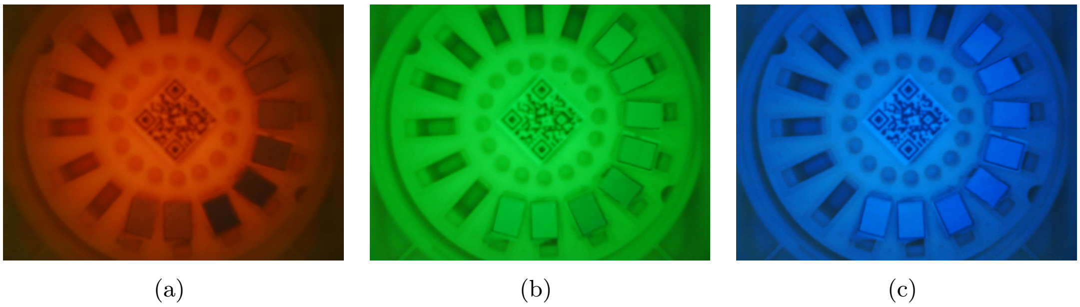
(a) (b) (c)

Figure 6.4: This figure shows the 6.4a red 6.4b green and 6.4c blue images acquired.

6.1.2.1 RGB to HSV conversion

When data acquisition is completed, all LED calibration and LED calibrated images are sent to the server to be analysed. Each set of LED calibration (Figure 6.3) and calibrated (Figure 6.4) images are merged to obtain a single LED calibration image and a single LED calibrated image. This allows for the calibrated image to be flat fielded. For the PlomBOX, flat fielding helps normalise the heterogeneous illumination inside the box. More generally, flat fielding aims to reduce image artifacts caused by dark currents in the CMOS device [224]. This process produces a pixel-by-pixel corrected image following this method [225]:

$$I_{\mathrm{C}} = \frac{(I_{\mathrm{R}} - I_{\mathrm{D}}) \cdot i_{\mathrm{m}}}{(I_{\mathrm{F}} - I_{\mathrm{D}})} \tag{6.7}$$

where I_{C} is the corrected image, I_{R} is the raw (LED calibrated) image, I_{F} is the flat field (LED calibration) image, I_{D} is the dark field image and i_{m} is the image averaged value of (I_{F}-I_{D}). For all data sets $i_{\mathrm{m}} = \overline{RGB} = 200$ corresponding to the colour of a piece of white paper, as mentioned in the previous section. The CMOS sensor does not have a mechanical shutter, therefore dark field images cannot be acquired. The equation above becomes:

$$I_{\mathrm{C}} = \frac{I_{\mathrm{R}} \cdot 200}{I_{\mathrm{F}}} \tag{6.8}$$

The resultant flat fielded image can be seen in Figure 6.5, showing how the heterogeneous illumination of the sample holder has been removed.

After flat fielding, the analysis script uses the QR code seen on the image to find the ROIs where the bacteria samples are placed. The script uses the `opencv-python` PYTHON library to achieve this. After locating the ROIs, the RGB values for each pixel in this region are found –

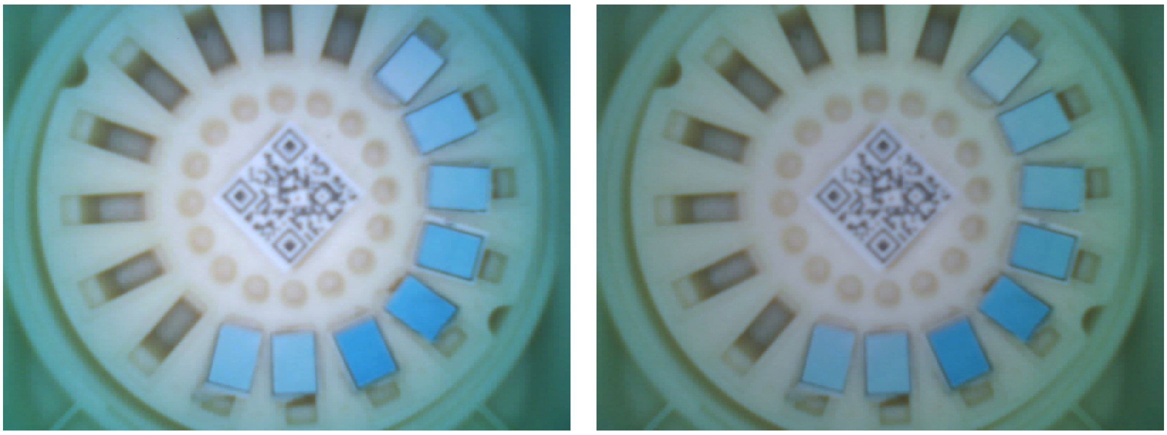
(a) (b)

Figure 6.5: Comparison of sample holder image 6.5a before and 6.5b after flat fielding.

Figure 6.6. All RGB values are averaged for each ROI, so that one ROI has one R, G and B value associated with it.

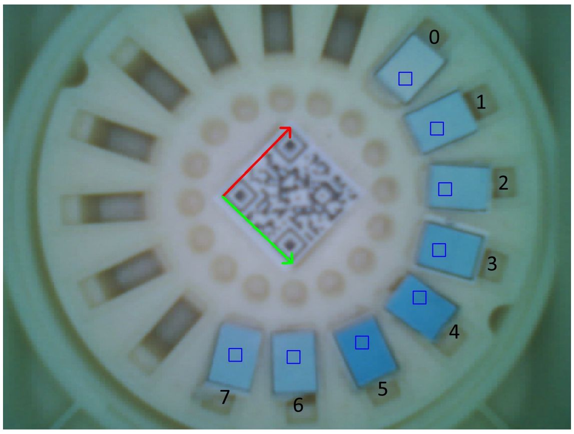

Figure 6.6: ROIs shown on the image as blue squares, labeled from 0 to 7

The HSV values are calculated from the average RGB values of the image using the `pycopy-colorsys` PYTHON library and following the conversion described in Section 6.1.1.

For the example shown above, the RGB, HSV and their uncertainty values, σ_{R}, σ_{G}, σ_{B}, σ_{H}, σ_{S} and σ_{V}, are shown in Table 6.1. The derivation of the uncertainties is shown below. The table illustrates that the package is working as expected: ROI0 has a saturation of 32.7 whereas ROI5 has a saturation of 76.3 and it is clear from Figure 6.6 that ROI5 has a larger saturation than ROI0, since it has a darker shade of blue. The values of S and V are presented in the range of [0, 100] as opposed to [0, 1]. The RGB uncertainties are obtained by calculating the standard error of the mean of R, G and B values, $\sigma_{\bar{i}}$, for all the pixels in each ROI:

$$\sigma_{\bar{i}} = \frac{\sigma_i}{\sqrt{n_{\mathrm{p}}}} \text{ for } i \ \in \ R, G, B \tag{6.9}$$

where σ_{i} is the sample standard deviation for R,G and B and n_{p} is the number of pixels. The chroma, C, and HSV uncertainties are obtained from error propagation:

ROI	R	G	B	σ_{R}	σ_{G}	σ_{B}	H	S	V	σ_{H}	σ_{S}	σ_{V}
0	116.3	159	172.8	0.2	0.2	0.5	194.7	32.7	67.8	0.3	0.3	0.2
1	90.6	151.1	173.9	0.2	0.2	0.2	196.4	47.9	68.2	0.2	0.2	0.1
2	87.8	149.6	174.7	0.1	0.1	0.4	197.3	49.7	68.5	0.2	0.2	0.1
3	66.2	140.2	173	0.2	0.2	0.2	198.4	61.7	67.8	0.1	0.1	0.1
4	45.6	126.9	170	0.3	0.4	0.6	200.8	73.2	66.7	0.2	0.4	0.2
5	40.8	122.3	172.4	0.1	0.1	0.4	202.9	76.3	67.6	0.1	0.3	0.2
6	90.6	143.9	175.7	0.4	0.2	0.3	202.4	48.4	68.9	0.3	0.3	0.1
7	92.8	144.3	176.3	0.3	0.2	0.5	203	47.4	69.2	0.2	0.4	0.2

Table 6.1: RGB, HSV and their uncertainties for each ROI shown in Figure 6.6

$$\sigma_{\mathrm{C}} = \sqrt{\sigma^2_{\mathrm{max(R,G,B)}} + \sigma^2_{\mathrm{min(R,G,B)}}} \tag{6.10}$$

$$\sigma_{\mathrm{H}} = \begin{cases} \sqrt{\left(\frac{\partial H}{\partial G}\right)^2 \cdot \sigma_{\mathrm{g}}^2 + \left(\frac{\partial H}{\partial B}\right)^2 \cdot \sigma_{\mathrm{b}}^2 + \left(\frac{\partial H}{\partial C}\right)^2 \cdot \sigma_{\mathrm{C}}^2} & \text{if } V = R \\ \sqrt{\left(\frac{\partial H}{\partial B}\right)^2 \cdot \sigma_{\mathrm{b}}^2 + \left(\frac{\partial H}{\partial R}\right)^2 \cdot \sigma_{\mathrm{r}}^2 + \left(\frac{\partial H}{\partial C}\right)^2 \cdot \sigma_{\mathrm{C}}^2} & \text{if } V = G \\ \sqrt{\left(\frac{\partial H}{\partial R}\right)^2 \cdot \sigma_{\mathrm{r}}^2 + \left(\frac{\partial H}{\partial G}\right)^2 \cdot \sigma_{\mathrm{g}}^2 + \left(\frac{\partial H}{\partial C}\right)^2 \cdot \sigma_{\mathrm{C}}^2} & \text{if } V = B \end{cases} \tag{6.11}$$

$$\sigma_{\mathrm{S}} = S \cdot \sqrt{\left(\frac{\sigma_{\mathrm{C}}}{C}\right)^2 + \left(\frac{\sigma_{\mathrm{V}}}{V}\right)^2} \tag{6.12}$$

$$\sigma_{\mathrm{V}} = V \cdot \left(\frac{\sigma_{\mathrm{max(R,G,B)}}}{\max(R,G,B)}\right) \tag{6.13}$$

6.1.2.2 Lead curve interpolation and final result

The final step in the analysis is to obtain a value for the lead concentration in the water samples from the saturation value obtained after the RGB to HSV conversion of the pixels' colours in the ROIs.

Each sample holder contains some wells with water samples of known lead concentrations. These constitute a "lead curve" that is used to calibrate the lead values of the samples of unknown concentration. For the test using Figure 6.6 one assumes that the ROIs 0 to 5 represent the lead curve, with concentrations of 0, 10, 15, 20, 50 and 100 ppb respectively. ROIs 6 and 7 represent samples with unknown lead concentrations. The saturations of ROIs 0-5 can be plotted against their lead concentrations. A logarithmic fit can be made on these data points. The saturations for the unknown samples can be placed on this logarithmic fit and interpolated to find their lead concentration – Figure 6.7. For this example, the concentrations would have been 10.2±0.6 and 9.6±0.6 ppb for ROIs 6 and 7 respectively.

The next section will address studies that were undertaken to understand how environmental and temporal effects, as well as the size of ROIs, can change the results obtained by the PlomBOX.

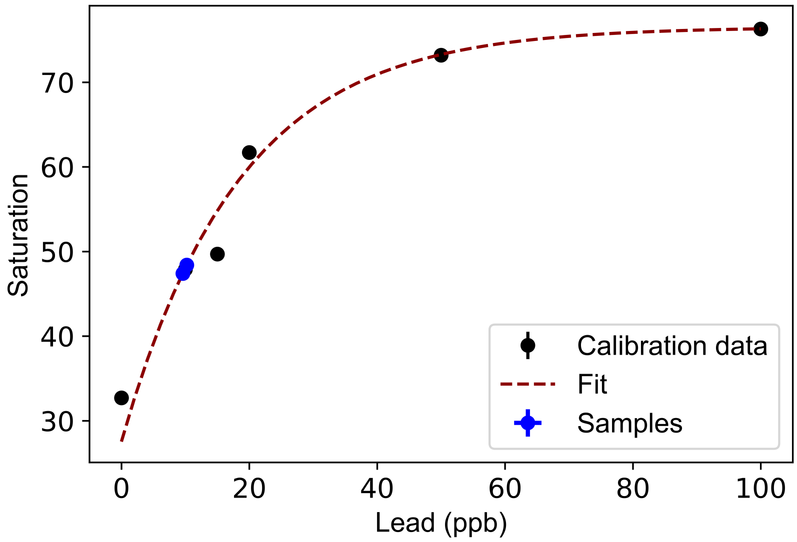

Figure 6.7: Example of how a value for lead concentration can be obtained by using a parallel measurement of calibration samples, i.e. the "lead curve". The figure shows saturation vs lead concentration, in ppb, for lead curve samples from 0 to 100 ppb. The lead curve samples, in black, are fitted with an inversely exponential curve and lead values for the unknown samples, in blue, can be obtained via interpolation of the lead curve.

6.2 PlomBOX operational studies

To conduct these studies, the sample holder depicted in Figure 6.5 and the same coloured papers were used. For brevity, only the results for ROI0 are presented.

6.2.1 Temperature studies

It was important to understand whether the temperature of the PlomBOX device changed the saturation values of data. Two tests were undertaken:

- Compare stability of saturation values when the PlomBOX started taking data immediately after being turned on (0 min), or after being turned on and waiting for a period of 30 min
- Look at fluctuations of temperature over a large timelapse of 18 h and see if similar saturation fluctuations were observed

For the first test, the white PlomBOX was placed inside another box. The outer box was used to reduce the interference of light leaks on the results, i.e. photons which do not originate on the LED ring and come from external light sources.

A total of 10 runs were conducted, with each run occurring 2 min apart. The first iteration was acquired immediately after turning on the PlomBOX, while the second iteration was acquired after leaving the PlomBOX turned on for 30 min before data acquisition. Figure 6.8 illustrates that the PlomBOX's temperature exhibits greater stability during data acquisition when it is powered on 30 min before commencing data collection. Moreover, the second setup shows a reduction in saturation fluctuations. All subsequent assays were carried out with the PlomBOX powered on 30 min prior to data acquisition.

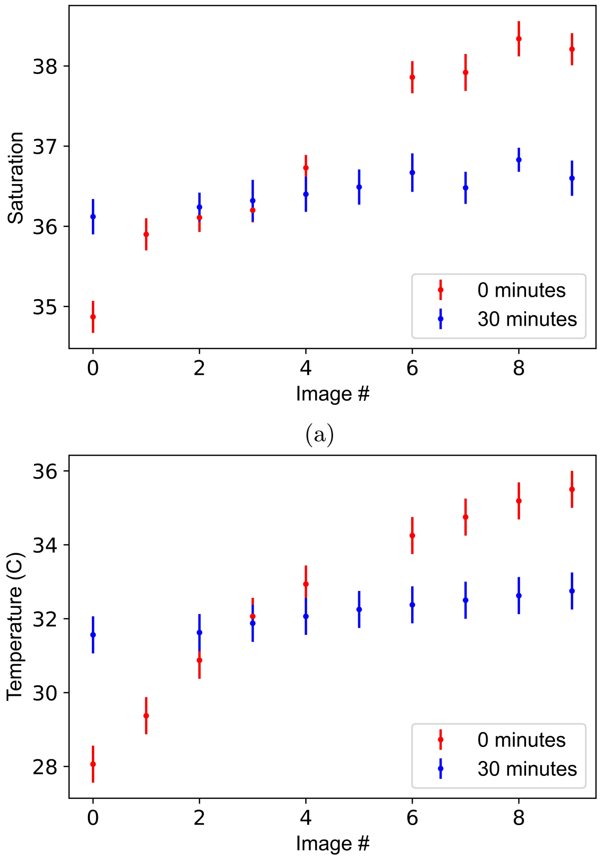

(a)

(b)

Figure 6.8: Comparison of effects of temperature on saturation when the PlomBOX begins data acquisition 0 and 30 min after being turned on, in red and blue respectively. Figure 6.8a compares the saturation values for the images acquired. Figure 6.8b compares the temperature of the PlomBOX, in celsius, for the images acquired.

In the second test, data was taken 30 min apart and the white PlomBOX was subject to the same conditions as in the first test. A digital thermometer was placed inside the external box to measure the external temperature to the PlomBOX. The results are shown in Figure 6.9. Despite the temperature fluctuations observed both in the PlomBOX temperature and external temperature, 80 % of data points are within 1σ band of the average saturation, thus the PlomBOX device can remain stable and acquire data for long periods of time.

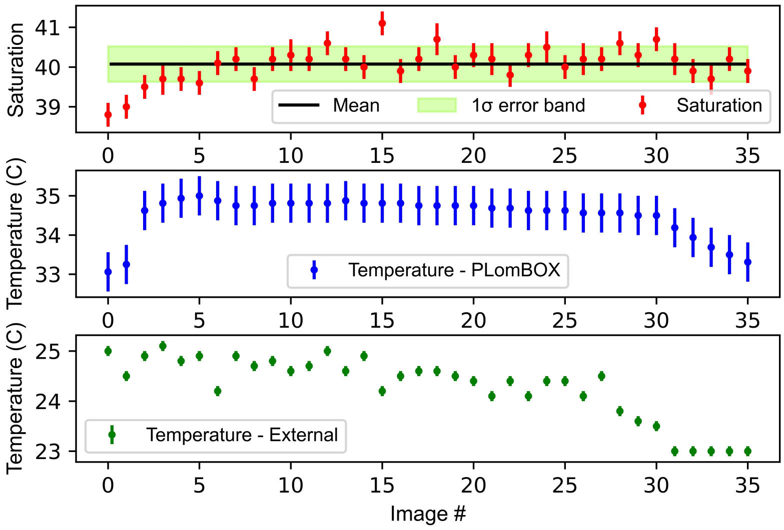

Figure 6.9: Time series data acquisition of the white PlomBOX for ROI0. Data was taken over 18 h, with pictures taken 30 min apart. The top plot shows saturation over time, the middle plot shows the PlomBOX temperature and the bottom plot shows the external temperature over time

6.2.2 Light leak studies

This study checked if the introduction of an external light source to the PlomBOX affected the saturation values. A white and a black PlomBOX were used for this test.

Data was taken with a torch pointing to the top, front, left, right and back of the PlomBOX, and then the saturation values were compared for the different images – Figure 6.10.

Figure 6.10: Example of data acquisition set up for light leak study. A torch was pointed at the PlomBOX from different directions

Figure 6.11 shows the results of data analysed for the dark and white PlomBOXes. Outside light interferes with the saturation values but the dark PlomBOX is more light tight than the white PlomBOX. It is preferable for the PlomBOX to be white inside to maximise light diffusion and illumination of the samples but, when assays are performed, it is preferable to have a dark environment to reduce external light interference. Therefore, subsequent assays to assess PlomBOX performance for lead metrology were conducted with a white PlomBOX in a dark environment.

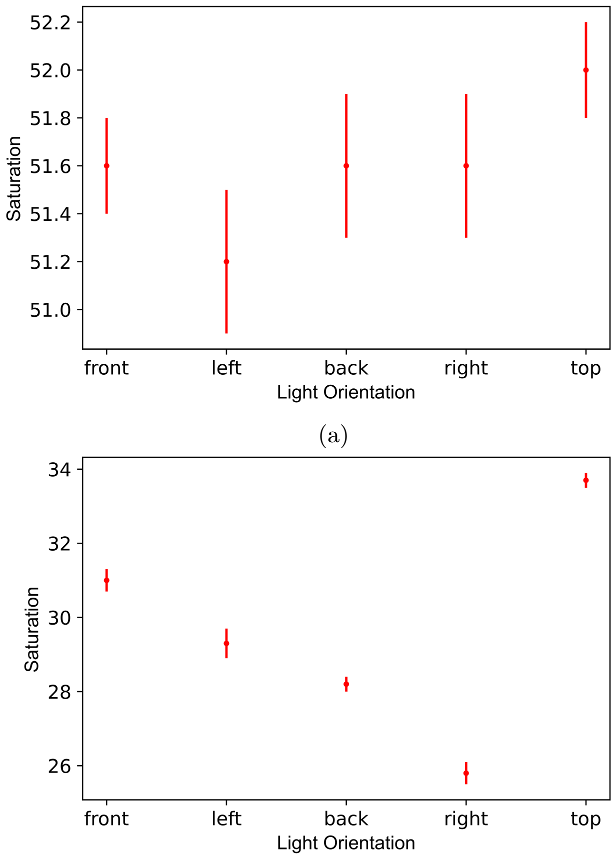

(a)

(b)

Figure 6.11: Comparison of saturation values for ROI 0 for the black (6.11a) and white PlomBOXes (6.11b) in terms of the positioning of the external torch. The black PlomBOX is more stable in terms of saturation values when compared to the white PlomBOX. The absolute saturation values of the dark PlomBOX exceed those of the white PlomBOX due to the box's interior being painted black. The black paint reduces light diffusion, resulting in higher values.

6.2.3 ROI size

A comparison of saturation values was conducted on ROIs of varying sizes within the sample holder wells. The results, presented in Figure 6.12, demonstrate a preference for larger side dimensions in an ROI, as they exhibit lower uncertainty in their saturation values. This reduction in uncertainty arises from the method of calculating RGB uncertainties, as elaborated in Section 6.1.2.1. A larger ROI encompasses more pixels, which results in the standard error of the mean calculation dividing the standard deviation by a larger pixel count than smaller ROIs. ROIs with a radius larger than 0.07 units of length[1] were not investigated because they would exceed the well boundaries, and the analysis focuses solely on the contents within the wells. The analysis of the INA assay shown

---

[1] The size of the ROIs depends on the QR code's dimensions; for instance, a value of 0.07 corresponds to a radius dimension that is 7 % of the QR code's radius.

in Section 6.3 was conducted using ROIs with a radius equal to 0.07.

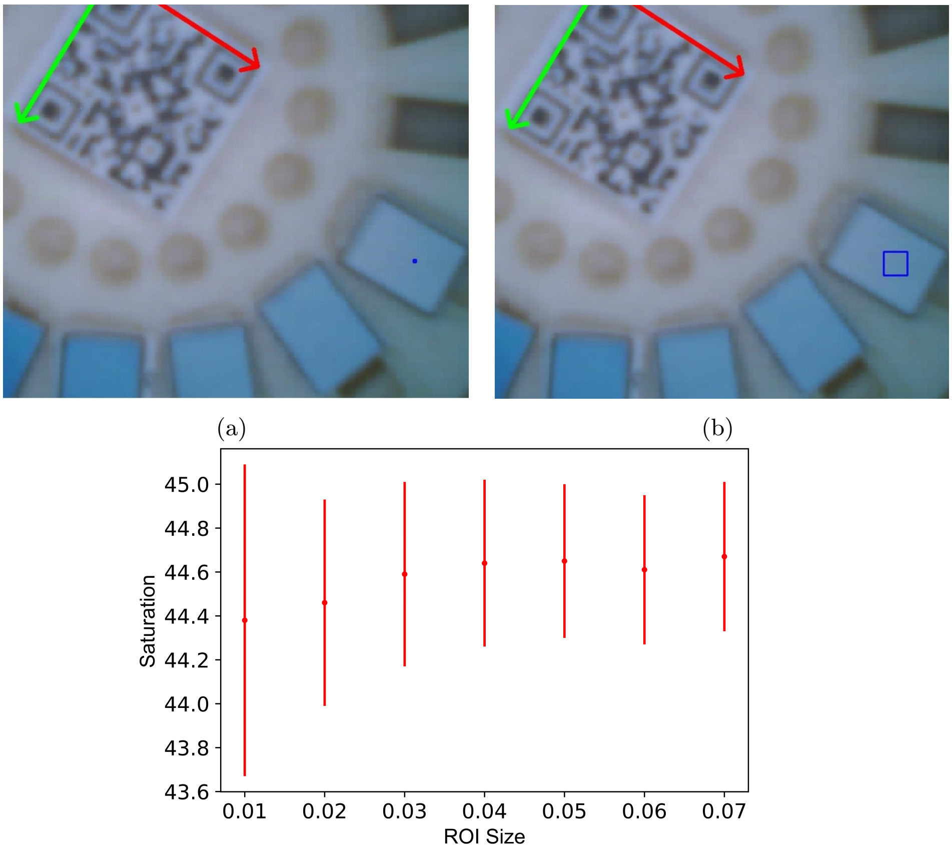

(a) (b)

(c)

Figure 6.12: ROI size comparison. Figures 6.12a and 6.12b show the sample holder analysed with ROIs with a radius of 0.01 and 0.07 units of length respectively. Figure 6.12c compares the saturation values with the ROI side dimensions.

6.2.4 Sample holder material

As addressed in Section 5.2.1, it is recommended to 3D print the sample holder using resin instead of plastic. This choice is informed by the higher resolution of resin printers, which leads to a reduction in leaks between the wells of the sample holder.

In Section 6.3, the initial assays were performed using PLA plastic sample holders, whereas resin sample holders were subsequently introduced and utilised for the remaining assays. Section 6.4.1 empirically demonstrates that the latter sample holder yields superior results, displaying a stronger correlation between the true lead concentration values of the samples and the values reported by the PlomBOX, in contrast to the results obtained from assays involving PLA sample holders.

6.2.5 Dilution of samples with large lead concentrations

Reference [226] details that the growth of *E. coli* can be inhibited when in the presence of media with lead concentrations greater than 3×10^5 ppb. However, it was observed *a posteriori* in PlomBOX assays that *E. coli* growth was inhibited for concentrations lower than 3×10^5 ppb and as low as 100 ppb. Figure 6.13 shows a comparison of saturation and lead values for a test assay of a "lead curve" on tap water, with concentrations of 0, 10, 50, 100 and 500 ppb. It is observed that after 100 ppb, saturation increase begins to plateau as opposed to increasing linearly with lead concentration.

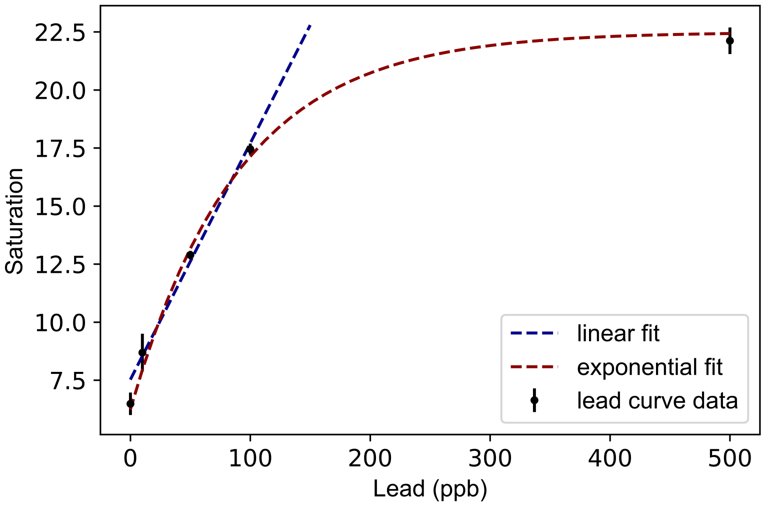

Figure 6.13: Saturation vs lead concentration of a tap water "lead curve". Data between 0 and 500 ppb is fitted with a logarithmic fit and data between 0 and 100 ppb is fitted with a linear fit. After 100 ppb, saturation begins to plateau as opposed to increasing linearly with lead concentration.

It is not possible to know *a priori* if a sample of unknown lead concentration will inhibit the growth of *E. coli*. If an assay returns a value of a sample's lead concentration close to 0 ppb, this sample should be diluted and assayed again. Section 6.4.1 shows that, when this occurs, there is a stronger correlation between the true lead concentration value of the sample and the value reported by the PlomBOX.

6.3 INA assay

In December 2022, the INA in Argentina conducted a study by collecting water samples from selected houses suspected of containing lead plumbing. These samples were analysed by INA following spectrophotometry of atomic absorption to determine their lead content. This is a method similar to ICP-MS in which elements in a liquid sample are detected by applying specific wavelengths from a light source [227]. Distinct elements absorb the wavelengths differently and therefore concentrations of these elements can be found. The samples underwent separate analysis using the

PlomBOX to benchmark its lead metrology performance.

Nine separate assays with the PlomBOX were carried out between November and December 2022 by the team of biologists – Table 6.2. For each of these assays, a lead curve was established, consisting of concentrations of 0, 10, 15, 20, 50, and 100 ppb of lead. These concentrations were placed in different wells, while the remaining wells were filled with the water samples collected by INA. The lead concentrations of these samples were undisclosed until the analysis had been concluded. Some samples underwent multiple assays, and others were diluted in later assays. Certain samples exhibited elevated lead concentrations in the first assays, necessitating their subsequent dilution to achieve lower concentration levels. This is because the growth of *E. coli* can be inhibited when in the presence of media with large lead concentrations, as detailed in Section 6.3.1.6. The procedures described in Section 5.1.3 were followed to mix the bacteria and water samples in the wells.

In the initial three assays, a sample holder made of PLA material was used, while the remaining assays utilised a resin sample holder. Throughout the assays, a timelapse was recorded in which images of the samples holder were captured every 20 min. The PlomBOX was housed inside a light-tight incubator set at a temperature of 24 °C.

Date	Temperature	Time	# of Runs	# of Samples	Sample Holder Type	Dilution
10/11/2022	24 °C	16.3 h	49	9	PLA	
16/11/2022	24 °C	16.3 h	49	9	PLA	
24/11/2022	24 °C	16.6 h	50	9	PLA	
30/11/2022	24 °C	16.6 h	50	9	Resin	
01/12/2022	24 °C	17 h	51	9	Resin	
07/12/2022	24 °C	16.6 h	50	8	Resin	
14/12/2022	24 °C	18.6 h	56	9	Resin	×
15/12/2022	24 °C	19.6 h	59	9	Resin	×
16/12/2022	24 °C	17.3 h	52	8	Resin	×

Table 6.2: Table with list of assays alongside their respective data acquisition conditions. The temperature corresponds to the environment within the incubator housing the PlomBOX, while time pertains to the duration of data acquisition. The count of runs denotes the quantity of images obtained by the PlomBOX during each assay. The number of samples reflects the quantity of specimens subjected to analysis within a given assay. The sample holder type signifies the material employed for 3D printing the sample holder. An × in the Dilution column indicates PlomBOX assays which contained diluted samples.

6.3.1 Analysis procedure

The data is treated as shown in Figure 6.14. The analysis script presented in Section 6.1.2 was expanded to account for aspects specific to these assays. This included data calibration and cuts before the lead curve interpolation occurred, which are detailed in the next sections.

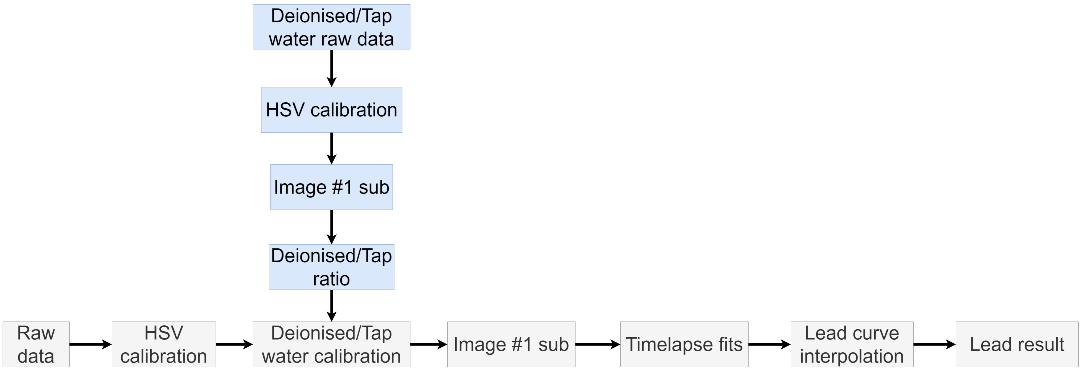

Figure 6.14: Analysis diagram for PlomBOX assays detailing different calibration methods applied to the data.

6.3.1.1 HSV calibration

As shown in Section 6.1.2.1, the analysis script converts RGB colours to HSV. However, the PlomBOX camera captures the colours produced by the biosensor which result from light reflection and are dependant on the LED ring's illumination. The colours produced by the biosensor need to be converted to its corresponding RGB digital values, before analysis can occur.

A wheel of ROIs was coloured digitally with known RGB (and HSV) values. This was printed onto a paper, placed inside the PlomBOX and images were acquired – Figure 6.15. Their saturation values were retrieved and compared with the digital saturation values used to colour the ROIs, as seen in Table 6.3. The digital saturation values were plotted against the measured saturation values. A logarithmic fit was made, $y = a \cdot e^{-b \cdot x} + c$, where y is the measured saturation, x is the digital saturation and a, b and c are the three fit parameters which indicate the intercept with the y-axis, the rate of exponential growth and the y-axis offset, respectively. Assay data was interpolated to determine its digital saturation values – Figure 6.16. These values are used for the remainder of the analysis.

ROI	Measured Saturation	Digital Saturation
0	21.7 ± 0.3	10
1	39.2 ± 0.4	30
2	49.5 ± 0.4	50
3	58.9 ± 0.4	70
4	66.9 ± 0.4	90
5	39.9 ± 0.3	34
6	40.8 ± 0.3	34
7	41.7 ± 0.4	34

Table 6.3: Comparison between digital and measured saturation for colours shown on the sample holder seen in Figure 6.15

The uncertainties were propagated once the value of lead was found for the samples. The fit

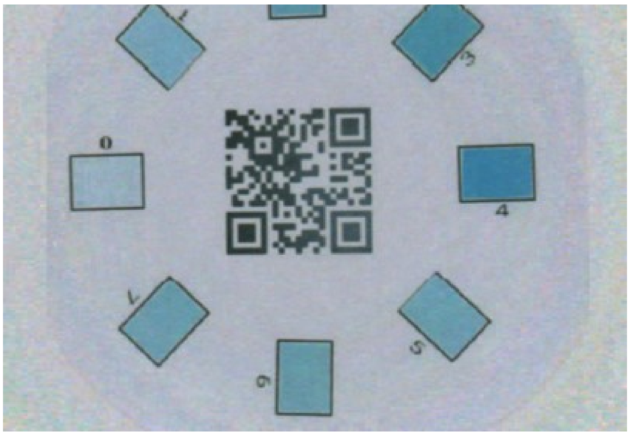

Figure 6.15: Wheel with ROIs coloured digitally with different HSV values, placed on top of the sample holder inside the PlomBOX.

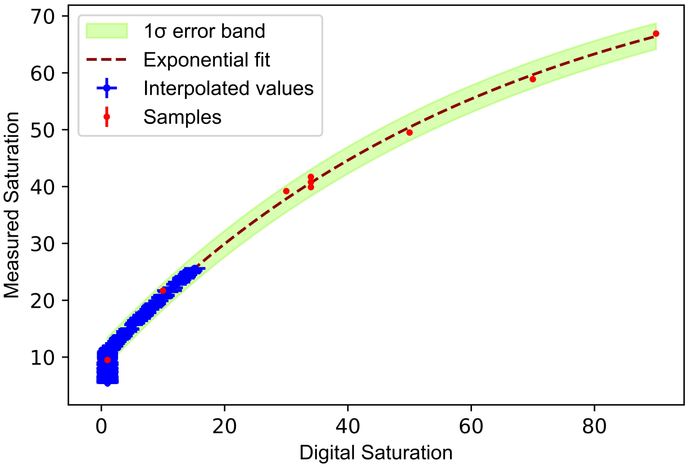

Figure 6.16: Digital saturation vs measured saturation with a logarithmic fit for sample ROIs shown in Figure 6.15, as imaged by the PlomBOX. A logarithmic curve is fitted on the samples, which are seen in red. The measured saturation values, in blue, are interpolated, using the logarithmic fit, to determine their digital saturation values. A 1σ error band is seen in light green.

function was rearranged to find x, and the error propagation formula follows:

$$x = -\frac{\ln\left(\frac{y-c}{a}\right)}{b} \tag{6.14}$$

$$s_{\text{hsv}} = \sqrt{\left(\frac{\partial x}{\partial a}\right)^2 \cdot s_{\text{a}}^2 + \left(\frac{\partial x}{\partial b}\right)^2 \cdot s_{\text{b}}^2 + \left(\frac{\partial x}{\partial c}\right)^2 \cdot s_{\text{c}}^2 + \left(\frac{\partial x}{\partial y}\right)^2 \cdot s_y^2 + \left(\frac{\partial x}{\partial a}\right)\left(\frac{\partial x}{\partial b}\right) \cdot s_{\text{a}} s_{\text{b}} + \left(\frac{\partial x}{\partial a}\right)\left(\frac{\partial x}{\partial c}\right) \cdot s_{\text{a}} s_{\text{c}}}$$
$$\overline{+\left(\frac{\partial x}{\partial b}\right)\left(\frac{\partial x}{\partial c}\right) \cdot s_{\text{b}} s_{\text{c}} + \left(\frac{\partial x}{\partial a}\right)\left(\frac{\partial x}{\partial y}\right) \cdot s_{\text{a}} s_y + \left(\frac{\partial x}{\partial b}\right)\left(\frac{\partial x}{\partial y}\right) \cdot s_{\text{b}} s_y \left(\frac{\partial x}{\partial c}\right)\left(\frac{\partial x}{\partial y}\right) \cdot s_{\text{c}} s_y} \tag{6.15}$$

where

$$\begin{aligned}\frac{\partial x}{\partial a} &= \frac{1}{a \cdot b}\\ \frac{\partial x}{\partial b} &= \frac{\ln\left(\frac{y-c}{a}\right)}{b^2}\\ \frac{\partial x}{\partial c} &= \frac{1}{b \cdot (y-c)}\\ \frac{\partial x}{\partial y} &= \frac{1}{(b \cdot c)-(b \cdot y)}\end{aligned} \tag{6.16}$$

and s_a, s_b, s_c and s_y are the uncertainties for the fit parameters and the saturation respectively. This exercise can be repeated for hue and value but saturation is the relevant quantity to find the lead concentration for any given sample. The HSV calibration was conducted based on the experimental conditions and the PlomBOX unit established by the team of biologists. In principle, this calibration should be tailored to each PlomBOX unit used, as lighting conditions will vary.

6.3.1.2 Tap/deionised water ratio

The assay analyses tap water samples, while the lead curve used in the analysis is established using deionised water (dH20). This choice is driven by the presence of disinfectants in tap water, which can influence the bacterial abundance [228]. Ensuring an uninhibited lead curve is of paramount importance in this context. It is therefore necessary to calibrate the lead curve to saturation values representative of a tap water lead curve.

An assay was conducted with two lead curves, with tap and deionised water – Figure 6.17. To each data set the HSV calibration and first-image-subtraction were applied, as described in Sections 6.3.1.1 and 6.3.1.3. A set of saturation values were obtained for both curves for the lead concentrations of 0, 10, 50, 100, 200 and 500 ppb. Both curves were fitted with a logarithmic fit. These fits were compared and a ratio, ≈ 1.08, was obtained – Figure 6.18. The deionised lead curve saturation values are divided by this ratio to obtain saturation values for a tap water lead curve:

$$\text{Ratio} = \frac{dH_2O}{\text{tap}} \tag{6.17}$$

The uncertainties on the tap water saturation values were calculated as seen below:

$$s_\mathrm{tap} = S_\mathrm{tap} \cdot \frac{s_{\mathrm{dH_2O}}}{S_{\mathrm{dH_2O}}} \tag{6.18}$$

Where S_tap is the tap water saturation value, $s_{\mathrm{dH_2O}}$ is the uncertainty and $S_{\mathrm{dH_2O}}$ the value of saturation for deionised water.

Similar to what was mentioned in Section 6.3.1.1, this correction was conducted for the tap and deionised water utilised by the team of biologists. A user should repeat this exercise for the water they assay, as it will contain different constituents.

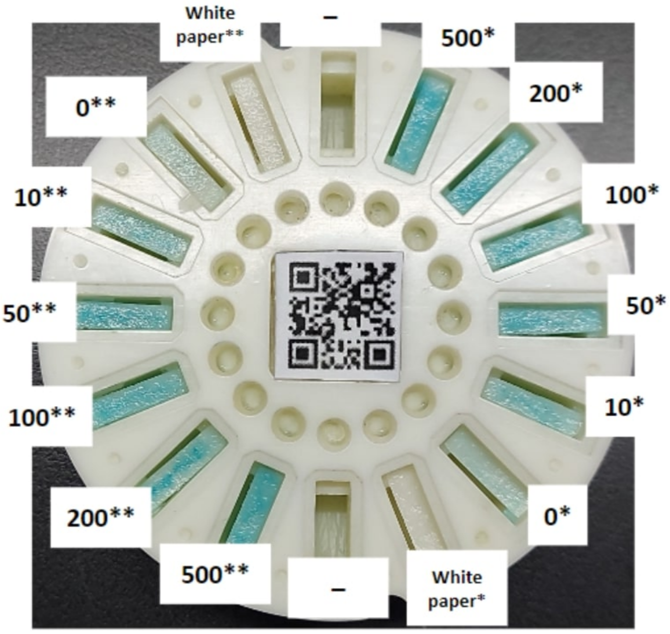

Figure 6.17: Sample holder showing a tap vs deionised water assay. The wells contain bacteria and water doped with different lead concentrations. * denotes deionised water and ** denotes tap water. Labels represent lead concentrations in ppb.

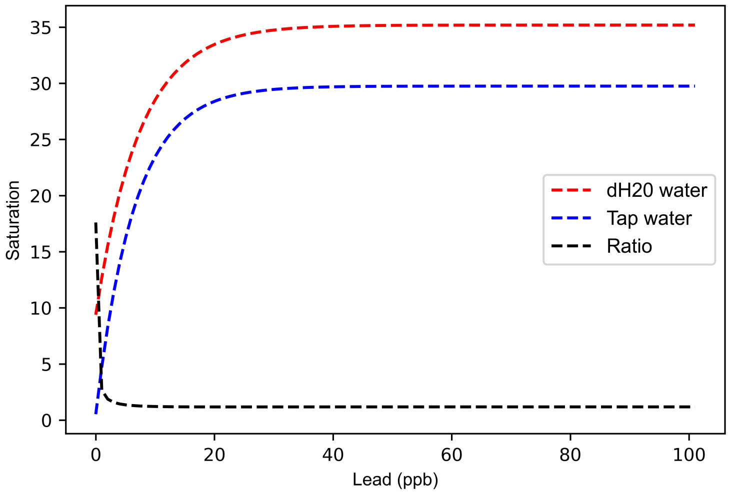

Figure 6.18: Tap vs deionised water ratio. Two lead curves, one of tap water (in blue) and one of deionised water (in red) were assayed and a ratio, ≈ 1.08, was obtained (in black). This ratio is used to calibrate the deionised lead curve.

6.3.1.3 First image subtraction

The sample holder exhibited well staining after subsequent assays, attributed to the production of the blue colour compound in the presence of lead – Figure 6.19.

The staining affected the saturation values obtained for the first images of the timelapse, when the bacteria had not yet started to express blue colour. It also affected wells which had samples with low lead concentrations. In these wells the bacteria response to lead was masked by the staining. All saturation values on the timelapse were therefore subtracted by the saturation value of the initial image – Figure 6.20. The uncertainties on the subtracted saturation values were calculated as seen below:

$$s_{\text{sub}} = \sqrt{s_{\#1}^2 + s_{\#\text{N}}^2} \tag{6.19}$$

Where s_{sub} is the uncertainty of the subtracted saturation, $s_{\#1}$ is the uncertainty of the saturation of the first image on the timelapse and $s_{\#\text{N}}$ is the uncertainty of the saturation of the image being subtracted.

Figure 6.19: Resin sample holder used in assays exhibiting colour staining in some of its wells.

Table 6.4 illustrates the changes the saturation values and uncertainties of a sample undergo following HSV calibration, tap/deionised water correction and first image subtraction. A snapshot is given of the saturation results from the last image acquired on the assay of the 14th December for the 10 ppb element of the "lead curve". The final saturation value shown on the table, 15.2±0.7, is used to create a timelapse that will be fitted later as described in Section 6.3.1.4.

6.3.1.4 Timelapse fits

The timelapses of each sample and each element of the lead curve were considered for the analysis, as opposed to only obtaining results from the final image of the timelapse. The timelapse provides information on how the increase in saturation occurred, from which data cuts can be inferred –

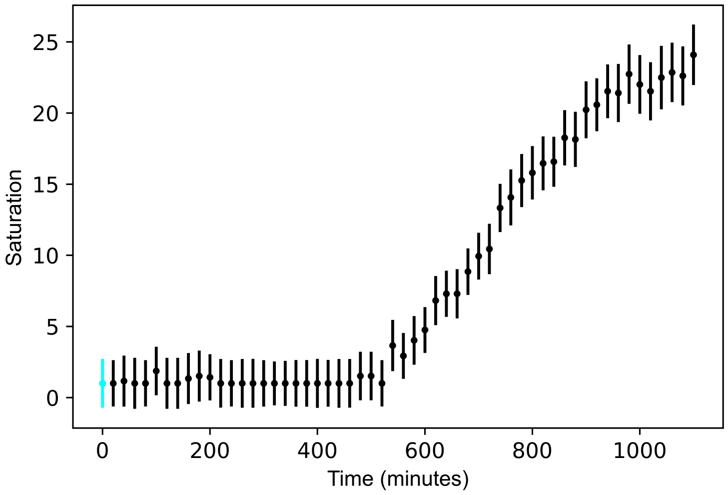

(a)

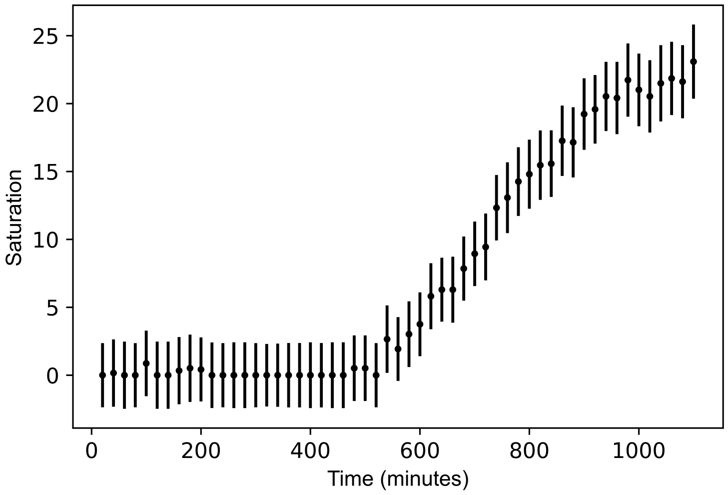

(b)

Figure 6.20: Timelapse data of a given sample before (6.20a) and after (6.20b) first image saturation subtraction, shown in blue.

Procedure	Saturation	$s_{\text{Saturation}}$
RGB to HSV conversion	27.6	0.5
HSV calibration	17.4	1.9
Tap/dH$_2$O correction	16.1	0.5
First image sub	15.2	0.7

Table 6.4: Example of evolution of saturation values ("Saturation") and uncertainties ("$s_{\text{Saturation}}$") for the 10 ppb element of the "lead curve", for the 14th December assay. The initial RGB to HSV conversion values are obtained from the last image acquired on the assay.

detailed in Section 6.3.1.6. A fit on the timelapse will also lower the uncertainties on the final saturation values, contrary to what is observed if only the final image of the timelapse is used.

It was expected that the bacteria response to lead would have the shape of two sigmoid functions (or Monod curves): one to represent the gene expression and one to represent the continuous bacterial growth throughout the assay. The Monod equation models the growth of bacteria populations [229]. It depends on two factors: the growth rate of the bacteria, μ, and the limiting substrate for growth, S. In this context, the LB broth serves as the limiting substrate for the curve representing bacterial growth, while X-Gal serves as the limiting substrate for the curve representing gene expression:

$$\mu = \mu_{\text{max}} \frac{S}{K_{\text{S}} + S} \tag{6.20}$$

Here, μ_{max} is the maximum growth rate for the bacteria and K_{S} is the value of the substrate when $\frac{\mu}{\mu_{\text{max}}} = 0.5$. The Monod curve has five distinct phases [230]: the lag phase at the beginning, which occurs until the bacteria have acclimated to their new environment; the exponential growth phase; the deceleration phase, when the limiting substrate starts to become depleted; the stationary phase, when the net bacteria growth is approximately zero and the death phase when the bacteria are destroyed by lysis, i.e. when the bacteria walls are broken down or destroyed [231]. The first four phases are observed on data acquired for all assays. To represent this curve, the following fit function was used:

$$y = \frac{a}{1 + e^{(-x+b)\cdot\left(\frac{c}{1+e^{-x}}\right)}} \tag{6.21}$$

$\frac{a}{1+e^{(-x+b)}}$ relates to the gene expression, and $(\frac{c}{1+e^{-x}})$ relates to the bacterial growth. The a parameter represents the amplitude of the curve, i.e. the maximum saturation that can be obtained, b is the value of x when y has reached 50 % of its final value and c represents the slope of the curve. x is time, in minutes, and y is saturation. The uncertainty on the final saturation extracted from the fit is propagated, accounting for the uncertainties on the fit parameters s_{a}, s_{b} and s_{c}:

$$s = \sqrt{\left(\frac{\partial y}{\partial a}\right)^2 \cdot s_{\text{a}}^2 + \left(\frac{\partial y}{\partial b}\right)^2 \cdot s_{\text{b}}^2 + \left(\frac{\partial y}{\partial c}\right)^2 \cdot s_{\text{c}}^2 + \left(\frac{\partial y}{\partial a}\right)\left(\frac{\partial y}{\partial b}\right) \cdot s_{\text{a}} s_{\text{b}} + \left(\frac{\partial y}{\partial a}\right)\left(\frac{\partial y}{\partial c}\right) \cdot s_{\text{a}} s_{\text{c}} + \left(\frac{\partial y}{\partial b}\right)\left(\frac{\partial y}{\partial c}\right) \cdot s_{\text{b}} s_{\text{c}}} \tag{6.22}$$

where

$$
\begin{aligned}
\frac{\partial y}{\partial a} &= \frac{1}{1+e^{\frac{c\cdot(b-x)}{1+e^{-x}}}} \\
\frac{\partial y}{\partial b} &= \frac{-a\cdot c\cdot e^{\frac{c\cdot(b-x)}{1+e^{-x}}}}{\left(1+e^{\frac{c\cdot(b-x)}{1+e^{-x}}}\right)^2\cdot(1+e^{-x})} \\
\frac{\partial y}{\partial c} &= -\frac{a\cdot e^{\frac{c\cdot(b-x)}{1+e^{-x}}}\cdot(b-x)}{\left(1+e^{\frac{c\cdot(b-x)}{1+e^{-x}}}\right)^2\cdot(1+e^{-x})}
\end{aligned}
\tag{6.23}
$$

The goodness of the fit was quantified with a reduced chi-square statistic:

$$
\chi^2_{\text{reduced}} = \frac{(\text{Data}-\text{Fit})^2}{s^2_{\text{Data}}\cdot(N_{\text{observations}}-N_{\text{dof}})} \tag{6.24}
$$

Where Data represents the measured values, Fit the calculated values, s^2_{Data} is the variance, $N_{\text{observations}}$ is the number of data points and N_{dof} is the number of fitted parameters.

A 1σ error band was also introduced, with the expectation that 68 % of data points should be within this error band. Figure 6.21 provides an example of a timelapse fit for an analysed INA sample (sample 103 from the assay conducted on the 14th December 2022), exhibiting the sigmoid fits, the 1σ error band and the χ^2_{reduced} value for this fit. The fit returned a saturation value of 21.8 ± 0.4.

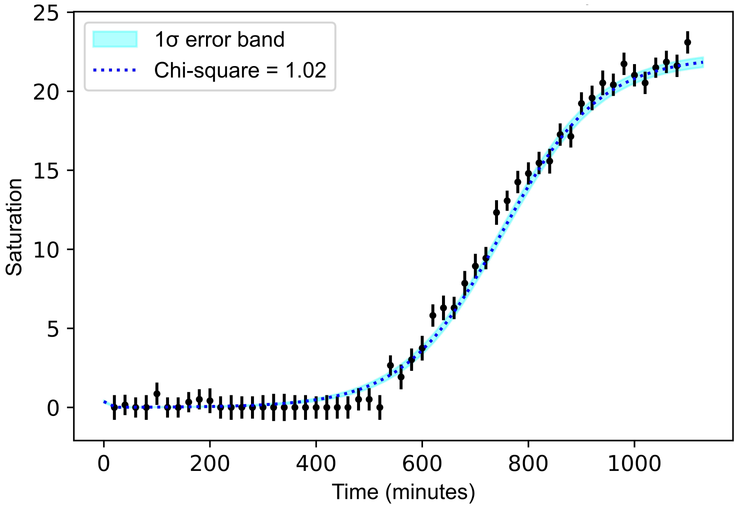

Figure 6.21: Example of timelapse fit, in dark blue, on sample data, in black, with a 1σ error band in light blue. The χ^2_{reduced} statistic for this fit is 1.02 and the fit returned a saturation value of 21.8 ± 0.4.

The saturation values and their uncertainties were extracted from each timelapse fit and were used to estimate the lead content of the sample, as described in Section 6.3.1.5.

6.3.1.5 Lead curve fits

As discussed in Section 6.1, the saturation values of the elements of the lead curve are used to produce a fit, which is used to look up the lead concentration given a measured saturation value of the unknown concentration samples. A first-order polynomial fit was used: $y = ax + b$ where x is lead, in ppb, y is saturation, and a and b are the fit parameters, the slope and the saturation-axis intercept respectively. The saturation values of the samples were linearly interpolated on this fit, returning a value of lead for each of them. The uncertainties were propagated once the value of lead was found for the samples. $y = ax + b$ was rearranged to find x, and the error propagation formula follows:

$$x = \frac{y-b}{a} \tag{6.25}$$

$$s = \sqrt{\left(\frac{\partial x}{\partial a}\right)^2 \cdot s_{\mathrm{a}}^2 + \left(\frac{\partial x}{\partial b}\right)^2 \cdot s_{\mathrm{b}}^2 + \left(\frac{\partial x}{\partial y}\right)^2 \cdot s_y^2 + \left(\frac{\partial x}{\partial a}\right)\left(\frac{\partial x}{\partial b}\right) \cdot s_{\mathrm{a}} s_{\mathrm{b}} + \left(\frac{\partial x}{\partial a}\right)\left(\frac{\partial x}{\partial y}\right) \cdot s_{\mathrm{a}} s_y + \left(\frac{\partial x}{\partial b}\right)\left(\frac{\partial x}{\partial y}\right) \cdot s_{\mathrm{b}} s_y} \tag{6.26}$$

where

$$\begin{aligned} \frac{\partial x}{\partial a} &= \frac{b-y}{a^2} \\ \frac{\partial x}{\partial b} &= \frac{-1}{a} \\ \frac{\partial x}{\partial y} &= \frac{1}{a} \end{aligned} \tag{6.27}$$

and s_{a}, s_{b} and s_y are the uncertainties for the slope, the saturation-axis intercept and the saturation respectively. Figure 6.22 shows the lead curve fit for the 1st December 2022 assay, showing the lead curve data points in black, the interpolated sample data in blue, the fit in red and the 1σ error band in green.

6.3.1.6 Data quality cuts

After analysing all assays, data cuts were applied. The b parameter of the timelapse fit, which represents the time when the saturation reaches 50 % of its final value, was examined for all lead curves. A cut was applied by excluding data points where b parameter > 1000 min.

The majority of the assays have a total time span of ~ 1000 min therefore there is an expectation that b should have a value < 1000 min or less. Observing $b > 1000$ min indicates that the biosensor

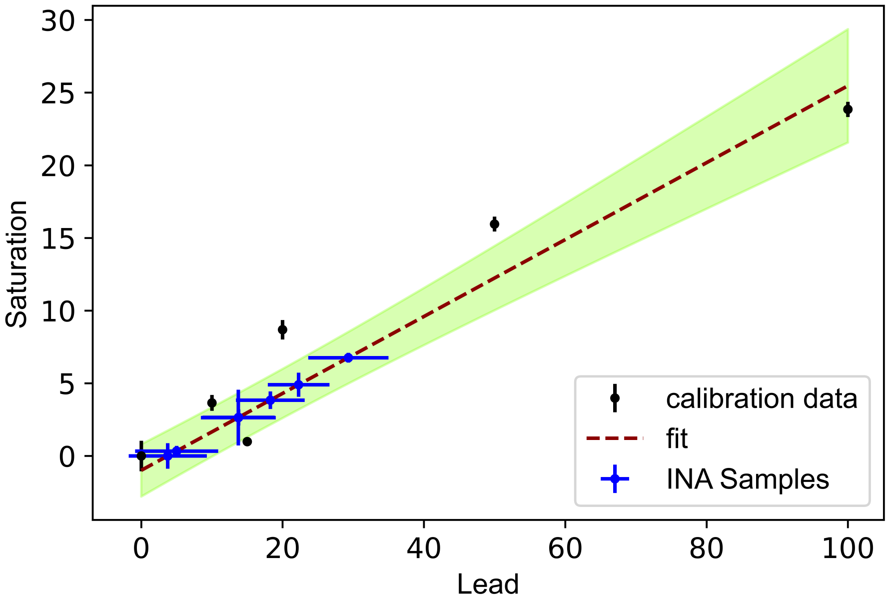

Figure 6.22: Lead curve fit for 1st December 2022 assay. A first-order polynomial fit is produced from the lead curve data, in black. The samples' saturation values are interpolated on this fit to find their lead values in ppb, in blue. The fit is shown in red and the 1σ error band is shown in green.

did not work as expected for that assay and its data should not be considered.

This cut was implemented on all elements of the lead curves and, if more than one element of a lead curve did not meet the cut, the entire assay was disqualified. Conversely, if the cut was met for all elements within a specific lead curve, all samples associated with that assay were deemed compliant with the cut. This approach rested on the assumption that if all elements within a given lead curve passed the cut, then bacterial growth and gene expression occurred as expected.

A further cut was applied to address instances in which the saturation of the 100 ppb element of the lead curve was lower than the saturation corresponding to 50 ppb. As addressed in Section 6.2.5, the growth of *E. coli* can be inhibited when in the presence of media with large lead concentrations. When the saturation for 100 ppb is lower than the saturation for 50 ppb, the 100 ppb is excluded from the lead curve fits.

Table 6.5 shows the assays that passed these cuts. Based on this, the assays of the 16th, 24th November, 1st, 14th and 15th December were used for the analysis discussed in Section 6.4.

6.4 Reliability of the PlomBOX device for lead detection in water

To assess the reliability of the PlomBOX device, multiple factors were taken into account: the correlation between PlomBOX and INA results, an evaluation of the accuracy of the PlomBOX and a measure of the sensitivity and specificity of the device.

Date	No cuts	$b < 1000\,\text{min}$	S (50 ppb) $< S$ (100 ppb)
10/11/2022	×		×
16/11/2022	×	×	
24/11/2022	×	×	
30/11/2022	×		
01/12/2022	×	×	×
07/12/2022	×		×
14/12/2022	×	×	×
15/12/2022	×	×	
16/12/2022	×		×

Table 6.5: INA Assay data cuts. This table shows the assays that passed the data cuts (indicated with a ×) addressed in Section 6.3.1.6. "$b < 1000\,\text{min}$" denotes assays which had no more than one element of the lead curve with $b > 1000\,\text{min}$ on their timelapse fit. "S (50 ppb) $< S$ (100 ppb)" denotes assays which do not have the saturation value of 100 ppb $<$ saturation value of 50 ppb for the lead curve fit.

6.4.1 Correlation between PlomBOX and INA results

The correlation between the PlomBOX and INA results was checked using the Pearson correlation coefficient:

$$r = \frac{\sum(x_i - \overline{x})(y_i - \overline{y})}{\sqrt{\sum(x_i - \overline{x})^2 \sum(y_i - \overline{y})^2}} \tag{6.28}$$

Where r is the correlation coefficient, x_i are the INA lead concentration values, $\overline{x}$ is the mean of INA lead values, y_i are the PlomBOX lead concentration values and $\overline{y}$ is the mean of PlomBOX lead values.

The correlation was calculated for different aspects, such as the use of different sample holders, data above and below 100 ppb, data above and below 10 ppb and diluted and undiluted data. Table 6.6 presents the obtained results. There was no data below 10 ppb acquired using the PLA sample holder. Regarding the results on diluted and undiluted data, a comparison using all PLA and resin data was more apt than considering the sample holders separately. This is because data acquired using the PLA sample holder did not include any diluted samples.

Element	PLA + Resin	PLA	Resin
All data	0.63	-0.24	0.76
Below 100 ppb	0.41	0.53	0.50
Above 100 ppb	0.61	-0.42	0.77
Below 10 ppb	-0.27	-	-0.27
Above 10 ppb	0.63	-0.24	0.77
Undiluted	-0.05	-	-
Diluted	0.78	-	-

Table 6.6: Correlation coefficients for all assays (PLA + Resin) and for assays using only PLA or Resin sample holders.

There is an improvement in the correlation obtained from the resin sample holder data (76 %)

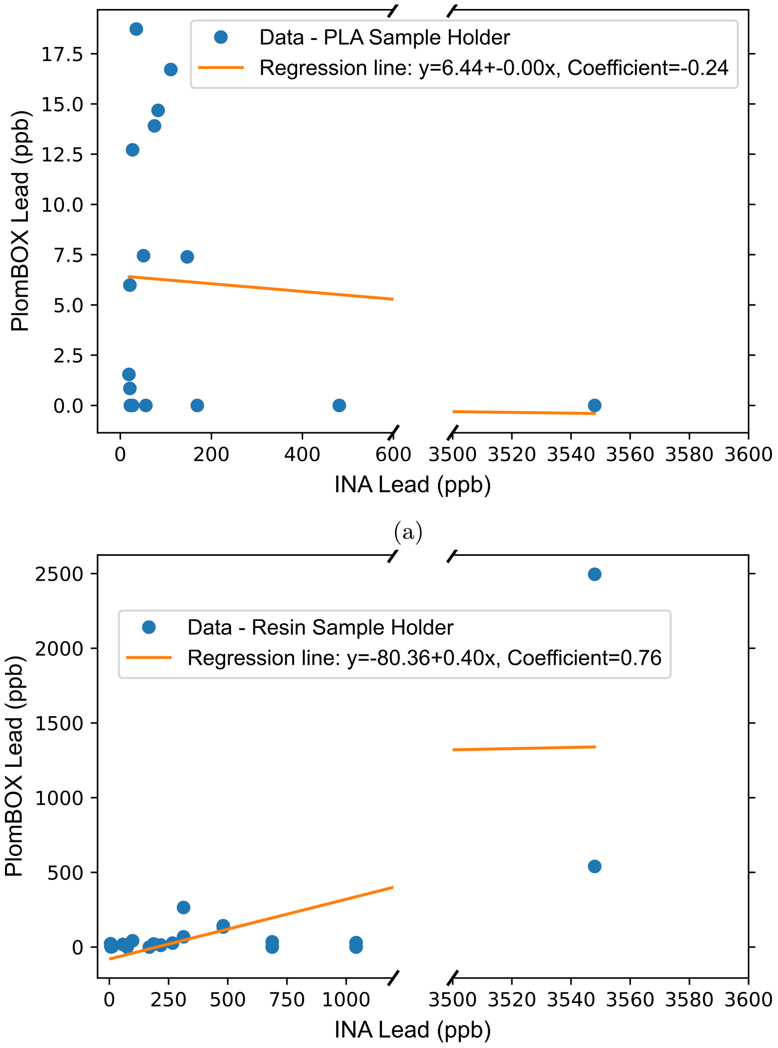

(a)

(b)

Figure 6.23: Correlation between PlomBOX and INA data for PLA (6.23a) and resin (6.23b) sample holders. An axis break was introduced to improve data readability.

when compared to data derived from the PLA sample holder (−24 %) – Figure 6.23. A similar improvement is observed in data obtained from diluted samples (78 %) as opposed to undiluted ones (−5 %) – Figure 6.24. This confirms that, as per what was discussed in Section 6.2.4 and 6.2.5, PlomBOX's results are improved when a resin sample holder is used and when samples with high concentrations of lead are diluted.

6.4.2 PlomBOX accuracy

Accuracy indicates how close a given set of measurements is to their true value. To obtain a value of accuracy for the PlomBOX, a sample was measured in multiple assays. The process involved examining whether the lead concentration confidence interval contained the true value of the sample's lead concentration.

To measure accuracy, the lead curves and the elements of the lead curves were measured as

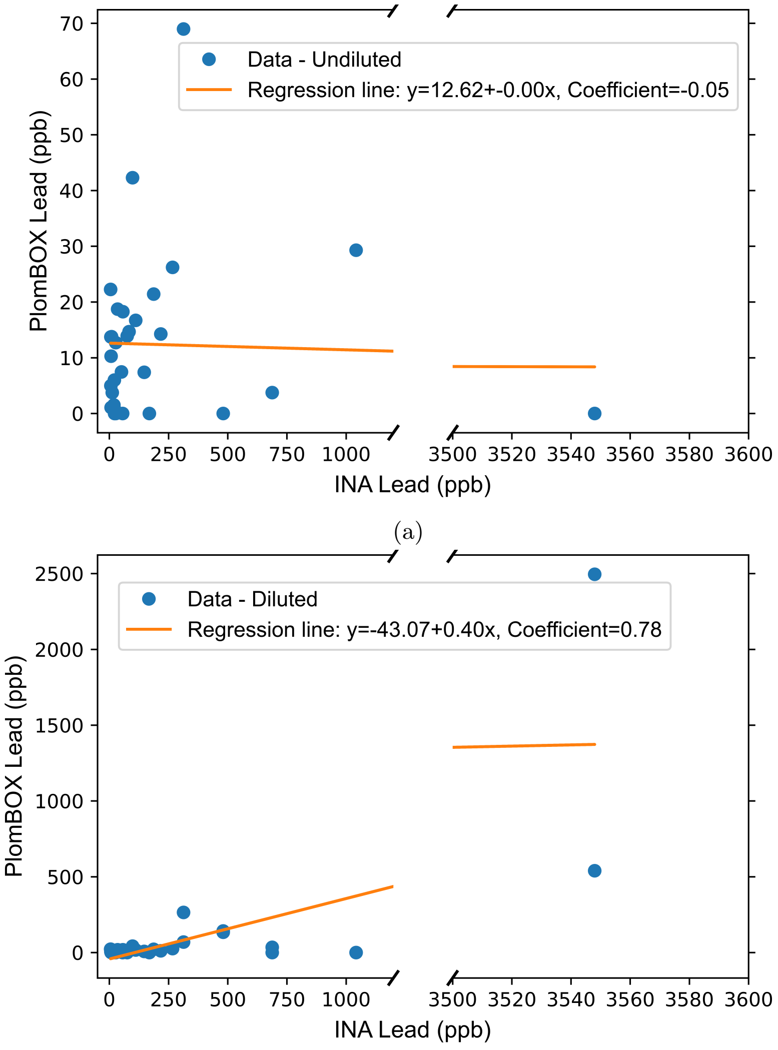

(a)

(b)

Figure 6.24: Correlation between PlomBOX and INA data for undiluted (6.24a) and diluted (6.24b) data sets. An axis break was introduced to improve data readability.

if they were actual samples. This calculation assumed full optimisation of the data, i.e. by only using data taken with the resin sample holder and with diluted samples. The saturation values for all the elements were interpolated on their respective lead curves, and lead values were obtained – Figure 6.25. The $\overline{x}$ of the lead values was used, and CI were obtained for each lead concentration as below:

$$CI = \overline{x} \pm t_{\text{score}} \cdot s_{\overline{x}} \tag{6.29}$$

A $\text{CI} = 95\,\%$ was assumed therefore a $t_{\text{score}} = 2.776$ was used for a two-tailed test. In this case a t_{score} is used over a z_{score} because the sample size is 3, lower than the minimum 30 required for a z-test. Table 6.7 shows the CI and p-values obtained for different lead concentrations. Figure 6.26 compares all the CI.

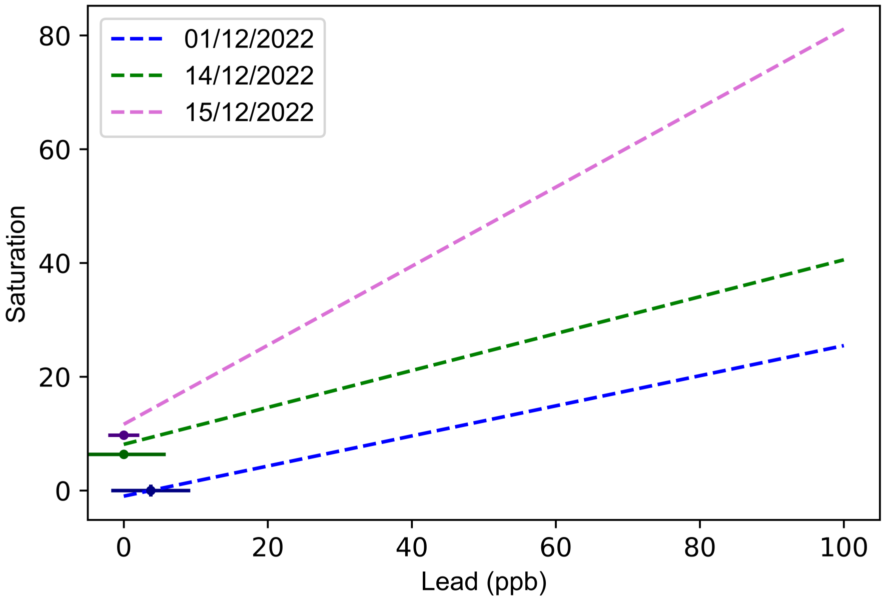

Figure 6.25: Lead curve fits for the assays of the 1st, 14th and 15th December 2022. To obtain the confidence intervals CI (95 %) seen in Figure 6.26, the lead curve fits are used to extract lead values for each element of the lead curve. This plot shows the saturation values for 0 ppb interpolated to obtain its values of lead. The obtained CI (95 %) are shown in Table 6.7 and in Figure 6.26.

Lead (ppb)	$\overline{x}$	$s_{\overline{x}}$	CI (95 %)	p-value
0	1.25	1.25	3.46	0.42
10	15.97	2.33	6.47	0.12
15	18.35	8.25	22.90	0.72
20	34.53	5.63	15.62	0.12
50	52.58	5.75	15.95	0.70
100	69.60	18.80	52.20	0.25

Table 6.7: Table showing accuracy of the PlomBOX by calculating the CI for different concentrations of lead.

Figure 6.26 shows that the 0 and 10 ppb 95 % CI are statistically different and thus there is 95 % confidence that the PlomBOX can distinguish between two samples that have concentrations of 0 and 10 ppb. The 100 ppb point has the widest CI and this is due to the variation of saturation values obtained for this concentration that provide different lead concentrations depending on the assay, as seen in Figure A.1e. This further justifies the cuts requiring the saturation value for 50 ppb be $<$ than that of 100 ppb, mentioned in Section 6.3.1.6.

Some of the CI overlap, however there may be a statistically significant difference between the means of the lead values. To determine whether the overlapping intervals are significantly different, the difference of the means of the two groups should be calculated [232]. A 95 % CI for the difference is obtained and, if it contains the value 0, it indicates there is no significant statistically difference between the groups. If the 95 % CI does not contain 0, then the groups are statistically different.

This was tested for the 10 ppb and 15 ppb CIs. The CI for the difference between these two

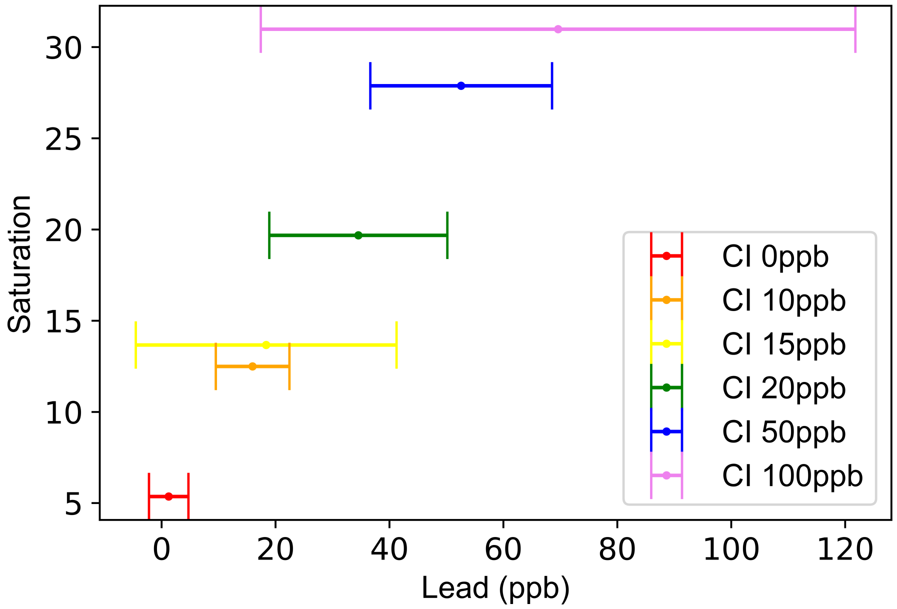

Figure 6.26: Confidence intervals CI (95 %) for different concentrations of lead, 0, 10, 15, 20, 50 and 100 ppb, as shown in Table 6.7.

groups will be:

$$CI_{15-10} = 2.38 \pm (2.776 \cdot 8.57) = 2.38 \pm 23.80 \tag{6.30}$$

In this instance the CI does contain 0, therefore 10 ppb and 15 ppb are not statistically different and the PlomBOX cannot distinguish between 10 ppb and 15 ppb lead concentrations. This was calculated for other groups, as seen in Table 6.8. This test does confirm that 0 ppb and 10 ppb are statistically different, as the 95 % CI of the "10-0" group does not contain the value 0.

Lead difference (ppb)	$\overline{x}$	$s_{\overline{x}}$	CI (95 %)
10-0	8.61	2.64	7.34
15-0	17.10	8.34	23.16
15-10	2.38	8.57	23.80
20-15	16.18	9.99	27.72
50-20	18.05	8.04	22.33
100-50	17.02	19.66	54.58

Table 6.8: Table showing results for overlapping CI

6.4.3 PlomBOX sensitivity and specificity

In medicine, sensitivity quantifies the probability of a population testing positive when a disease is present. It is calculated by determining the number of TP and FN cases [233]:

$$\text{Sensitivity} = \frac{TP}{TP + FN} \tag{6.31}$$

Specificity is a measure of the probability of a population testing negative when a disease is absent. It is calculated by determining the number of TN and FP cases [233]:

$$\text{Specificity} = \frac{TN}{TN + FP} \tag{6.32}$$

Specificity and sensitivity are inversely proportional, meaning that as the number of positive cases increase, the number of negative cases should decrease [233].

This can be applied to the PlomBOX by considering a lead concentration threshold and then measuring the sensitivity and specificity of the PlomBOX based on the lead concentration values returned by the PlomBOX, for a given INA sample.

The LL of the 95 % CIs presented in Section 6.4.2 are considered to calculate the sensitivity and specificity of the PlomBOX. The 27 samples (shown in Table A.1) that met all data quality criteria and were acquired with a resin sample holder are compared against the LL 95 % CIs values. The results are provided in Table 6.9.

Lead (ppb)	Positives	Negatives	FN	TN	FP	TP	Sensitivity	Specifity
0	27	0	0	0	0	27	1.00	0.00
10	21	6	7	2	4	14	0.67	0.33
15	27	0	0	0	0	27	1.00	0.00
20	20	7	9	6	1	11	0.55	0.86
50	20	7	13	7	0	7	0.35	1.00
100	20	7	8	6	1	12	0.60	0.86

Table 6.9: Table detailing sensitivity and specificity results for the PlomBOX, for different lead concentrations, in ppb. For each lead concentration, the total number of positive and negative values are presented, as well as false negatives (FN), true negatives (TN), false positives (FP) and true positives (TP).

The 0 and 15 ppb concentrations have no FN and TN values because their LL 95 % CI values are below 0 ppb, as seen in Figure 6.26. A trend is observed in which the number of FN increases with lead concentration, as seen for concentrations of 10, 20 and 50 ppb. This aligns with the hypothesis stated in Section 6.2.5 and the observations made in Section 6.3.1.6: the growth of *E. coli* appears to be inhibited in the PlomBOX when exposed to media containing high lead concentrations. The only exception is 100 ppb, and this is due to its wide 95 % CI, resulting in a lower than expected LL value (lower than that of 20 and 50 ppb's CIs).

The relation between sensitivity and specificity is confirmed for the PlomBOX: the number of positive values (above threshold) plus the number of negative values (below threshold) total 27 for all measured lead concentrations.

The following conclusion can be made for the 10 ppb concentration: there is a probability of 0.67 that the PlomBOX returns a value $\geq$ 10 ppb for a given sample, when said sample has a true concentration $\geq$ 10 ppb. There is also a probability of 0.33 that the PlomBOX returns a value $<$

10 ppb for a given sample, when said sample has a true concentration < 10 ppb. Therefore, the PlomBOX has a sensitivity of 0.67 and a specificity of 0.33 for a lead concentration value of 10 ppb.

All the work presented in this section, Section 6.4, assumes the INA analysis of the assayed samples to be correct. However, INA reported no uncertainties for their results. In future assays it is recommended that the samples are analysed by at least another independent laboratory, to ensure that the PlomBOX is comparing its results to the true value of lead in a sample.

Chapter 7

Summary and Conclusion

This thesis explored how different detection techniques could be used in the context of environmental monitoring to detect lead in drinking water. The main findings and conclusions are outlined below.

Chapter 3 explored whether CMOS sensors built for optical light detection can perform as decay radiation detectors.

An Neo sCMOS [149] camera was assessed for its effectiveness in detecting photons within the X-ray and low γ-ray energy range. This camera is designed to image photons of optical wavelengths. The analysis (Section 3.3) of camera images identifies clusters (Section 3.3.2) – contiguous pixels with high charge values (unit: ADU) – which are due to energy deposits of radiation impinging on the camera chip. Requiring the cluster size to be larger than 2 pixels allows most of the clusters due to background radiation to be sufficiently rejected. A trend towards larger cluster sizes for increasing photon energy (Section 3.3.2.4) was noted.

The relation of the cluster charge in ADU to eV was measured to be $2.463 \pm 0.007\,\mathrm{eV/ADU}$ or $0.406 \pm 0.001\,\mathrm{ADU/eV}$ (Figure 3.11a, Section 3.4.1.1). This relation is linear without an offset in the energy range from 13.8 keV to 59.5 keV. It reasonably aligns with 2.446 eV/ADU, which is the expected value derived from the supplier's specified gain value of 0.67 electron/ADU and the energy of 3.65 eV needed to create an electron-hole-pair in Si [167].

The energy resolution is slightly better than 2 % (Section 3.4.1.2). It was not possible to measure any peaks below $\sim$10 keV, which is most likely due to the photon absorption in glass for energies $\leq$ 10 keV (Using the information in [162] it can be estimated that in 1 mm (2 mm) of glass almost 97 % (99.04 %) of the photons will be absorbed in the window before they reach the camera.=). With the ^{137}Cs source the CMOS was able to measure photon energies up to 180 keV. The rate of background events detected in the absence of any source was measured to be $20.4 \pm 0.8\,\mathrm{mHz}$ (Section 3.4.2). By increasing the distance between the camera and an ^{241}Am source the activity

incident on the camera chip was reduced. The lowest detectable rate measured 5σ above background was 40 ± 3 mHz, which corresponds to an incident activity of 7 ± 4 Bq. Taking calorimetric information into account and integrating only around the 26.3 keV and 59.5 keV γ-peaks, the minimal detectable rate is 4 ± 1 mHz and 1.5 ± 0.1 mHz, respectively, which corresponds to incident activities of 1.0 ± 0.6 Bq and 57 ± 33 Bq (Section 3.4.2.2) respectively.
By comparing the measured rates with the incident source activity, one can determine the intrinsic efficiency of the Neo sCMOS camera at the two ^{241}Am γ-lines. They are found to be 0.08 ± 0.02 % and 0.0011 ± 0.0002 % for 26.3 keV and the 59.5 keV peaks respectively (Section 3.4.2.3). The efficiency drop from the lower to the higher energy follows the drop of the photon-absorption efficiency in silicon of a few µm thickness as function of energy. The toy MC simulations indicate a thickness in the order of 2 µm to 4 µm for the Neo sCMOS silicon layer. The absolute value of the efficiency for 59.5 keV is lower than expected for a silicon sensor with a few µm thickness when only photo-absorption coefficients are considered (Section 3.4.2.4).

It would be of interest to research if non scientific CMOS devices, such as mobile phone cameras used for optical light detection, could also perform as decay radiation detectors.

Following the findings of Chapter 3, Chapter 4 examined the principles of reducing samples in volume to increase the concentration of heavy metals for measurement. This chapter reported on two volume reduction techniques using enclosed and open system procedures. Each method was tested once with a different water sample.

The enclosed system procedure demonstrated that this technique retains 99 ± 9 % of ^{210}Pb, allowing for an increase of ^{210}Pb concentration from 1.9×10^{-6} ppb to 2.63×10^{-4} ppb, or a factor of 1.4×10^{2}. Given the similarities between ^{210}Pb and stable lead it can be assumed that stable lead is retained with this efficiency.

The open system procedure showed that all samples contained ^{40}K with an energy peak of 1.46 MeV. To establish the retention efficiency in the open boiling method, ^{40}K's concentration was measured across all samples. While some samples showed low variability in activity values, overall the effect of limescale affected these results. It may be of interest to repeat the open water reduction with soft tap water to reduce the interference of limescale on the results. Lead-210 was observed in sample C (which had a reduction factor of 633±4) with a calculated specific activity of 730 ± 150 mBq kg^{-1}. Using a similar calculation as shown in [101], this specific activity is equal to $(2.55 \pm 0.58) \times 10^{-7}$ ppb. To determine the concentration of stable Pb corresponding to the ^{210}Pb concentration of sample C, a ratio of 34 ppb of ^{210}Pb/Pb for rainwater in London was used [47]. This rainwater ratio can be used for the tap water sample as, according to [234], rainwater maintains groundwater levels in the region, which consequently supply water to aquifers and rivers, from where 70 % of drinking water comes. The ratio allowed an estimation that sample C had 7.5 ± 1.7 ppb of stable lead. Taking into consideration the sample's aforementioned reduction factor, the tap water sample, prior to reduction, contained 0.012 ± 0.003 ppb, or $(1.2 \pm 3) \times 10^{-5}\,\mathrm{mg\,kg^{-1}}$ of stable lead, a value well below the WHO limit. This value is compatible with <1 ppb measured by [69] in 2020. When further analysis was done on sample D, ^{131}I and ^{177}Lu were also detected, with calculated specific activities of $2.4 \pm 0.3\,\mathrm{Bq\,kg^{-1}}$ and $3.3 \pm 0.5\,\mathrm{Bq\,kg^{-1}}$ respectively.

Finally, the project combined biology and particle physics assay approaches with the aim of developing a sensor, called PlomBOX, for lead in drinking water.

Chapter 5 reported on the development of the PlomBOX device. The design of the lead sensitive bacterium was presented, with an introduction to the reference biosensor, sensAr, which used genetically modified *E. coli* to produce a colourimetric response to concentrations of arsenic in water samples. An initial fluorescent biosensor was developed using GFP, which produced a green fluorescent response to the presence of lead in water. Due to variability in data sets, a colourimetric biosensor using β-Gal was preferred, which expresses blue colour of higher intensity for higher concentrations of lead. A full analysis of this biosensor's response is shown in Chapter 6.

The design of the hardware devices was described which encompasses a bespoke PCB and a low-cost ESP32-CAM to acquire images of the biosensor. The different designs of the PlomBOX casing were discussed, and an explanation on the final design choices was provided.

The design of the PlomApp was described. This includes the architecture choices, which entailed Android application development using Java, and explaining the communication between the server and the PlomApp (via Wi-Fi) and the communication between the PlomBOX and the PlomApp (via Bluetooth). All data is stored in JSON strings.

Chapter 6 evaluated the use of the PlomBOX as a lead detection device.

A full description of the data analysis package was provided in Section 6.1. PlomBOX images are flat fielded and ROIs are outlined on it. RGB values are obtained for the ROIs and converted to HSV. A "lead curve" is used to calibrate the lead values of the samples of unknown concentration, by plotting lead concentrations vs saturation.

Section 6.3 discusses *in situ* assays obtained to test the PlomBOX system. The analysis package required several calibration and data cut procedures before the final results could be addressed – Section 6.3.1.

From the original nine assays, five assays passed the cuts and were considered for checking the reliability of the PlomBOX as a lead detection device – Section 6.4. This included determining the correlation between PlomBOX and INA results, an evaluation of the accuracy of the PlomBOX and a measure of the percentage of false negative results. After cuts, the PlomBOX data presented a 63 % correlation with INA data. This improved for data points acquired using a resin sample holder (76 %) and for diluted samples (78 %). There is 95 % confidence that the PlomBOX can detect lead with a concentration of 10 ppb with a confidence interval of 15.97 ± 6.47 ppb. The 0 and 10 ppb CI (95 %) are shown to be statistically different. Sensitivity and specificity were calculated for the PlomBOX for lead concentrations of 0, 10, 15, 20, 50 and 100 ppb. The PlomBOX has a sensitivity of 0.67 and a specificity of 0.33 for a lead concentration value of 10 ppb, the WHO's upper limit for lead in drinking water.

It would be of interest to implement another assay campaign with new samples. Our understanding of the accuracy of the PlomBOX would be improved by assaying the same sample more than 3 times, ideally more than 30, as opposed to using the elements of the lead curves as actual samples. In the new assay a resin sample holder should be used, together with the dilution of samples that have lead concentrations greater than 100 ppb. Ideally, each sample should be analysed twice within the same assay: once with dilution and once without, to ascertain whether the lead concentration is inhibiting the bacteria's response. This would avoid having to conduct several assays to reach this conclusion. The assays should begin with the image acquisition of the empty sample holder to aid the first image subtraction described in Section 6.3.1.3. Additionally, the water reduction methods described in Chapter 4 could be used to explore how much the assay of low concentration samples (close to 0 ppb) in the PlomBOX is improved by volume concentration techniques. Different biotransducers, such as the *luciferase* enzyme and the sfGFP, described in Section 2.1.3, could be explored with the goal of improving the PlomBOX's detection capabilities with alternative biosensor designs. Other imaging devices could also be investigated, such as Silicon Photomultipliers (SiPM). The collaboration intends to publish the development and evaluation of the PlomBOX presented in this thesis in the near future.

The PlomBOX, whilst still requiring further research and development, serves as a promising proof of concept for utilising conventional detection methods from physics and biology in unconventional applications, such as the detection of lead in drinking water *in situ*. This thesis has shown that cross-discipline collaborations can successfully develop environmental detection techniques.

Appendix A

Appendix

A.1 PlomBOX JSON string example

```
{
   "phone_test_v1":{
      "version":"v2.14",
      "esp32":{
         "ID":111,
         "firmware":"v1r50"
      },
      "telemetry":{
         "date":"2021-05-01T21:04:16Z",
         "time":1619903056,
         "temp":{
            "C":28.625,
            "F":83.525
         }
      },
      "measurement":{
         "ID":"2",
         "run":"1",
         "fname":"\/7C3E00C4F5FC_21_05_01_21_04_16.jso",
         "image":"...",
         "led":{
            "brightness":255,
```

```
      "R":255,
      "G":255,
      "B":255
   },
   "cam":{
      "brightness":0,
      "contrast":2,
      "saturation":-2,
      "special_effect":0,
      "whitebal":0,
      "awb_gain":0,
      "wb_mode":0,
      "exposure_ctrl":1,
      "aec2":0,
      "ae_level":0,
      "aec_value":400,
      "gain_ctrl":1,
      "agc_gain":0,
      "gainceiling":0,
      "bpc":0,
      "wpc":0,
      "raw_gma":1,
      "lenc":0,
      "hmirror":0,
      "vflip":0,
      "dcw":1,
      "colorbar":0
   },
   "type":"calibration",
   "dataSetName":""
},
"extra":{
   "cmd":"{\"cmd\":\"exp\",\"arg\":\"picTimeLapse\",\"param\":
     {\"picN\":\"2\",\"picT\":\"1000\",\"debug\":\"1\"}}"
},
```

```
      "user":{
         "ID":"XMRwQJ9O3sgCUJK2AOuT3GyKeGA2"
      },
      "date":{
         "plomapp_date":"2021-08-20T17:19:43.275",
         "water_sample_date":""
      },
      "location":{
         "lat":51.4269836,
         "lon":-0.5630935
      }
   }
}
```

A.2 Communication between the PlomApp and the PlomBOX

This section details the commands sent from the PlomApp to the PlomBOX.

A.2.1 List of JSON files' names

```
{
   "cmd":"sd",
   "arg":"ls",
   "param":{
      "comm_port":"0"
   }
}
```

The command `"cmd"` indicates that this is a memory card related function (`"sd"`) to obtain a list of content in the root path of the SD card (`"ls"`). The `"comm_port":"0"` command indicates that this information is to be sent back to the PlomApp via Bluetooth.

A.2.2 Delete JSON files from SD card

```
{
   "cmd":"sd",
   "arg":"rmf",
   "param":{
      "path":"7C3E00C4F5FC_21_05_01_21_09_19.jso",
      "comm_port":"0"
   }
}
```

Here, `"arg":"rmf"` indicates a file removal operation and `"path":"7C3E00C4F5FC_21_05_01_21_09_19.jso"` indicates the file to be deleted.

A.2.3 Take calibration set of data

```
{
   "cmd":"exp",
   "arg":"takeRGB",
   "param":{
```

```
        "path":"\/",
        "picN":"1",
        "picT":"0",
        "r_exposure":100,
        "g_exposure":100,
        "b_exposure":100,
        "type":"whitePaper"
    }
}
```

The `"arg":"takeRGB"` command indicates that the PlomBOX should take three RGB subimages, i.e. one red, one green and one blue, per image. `"picN":"1"` and `"picT":"0"` indicate one picture should be taken with zero seconds between data sets, as there is only one image request. The commands `"r_exposure":100`, `"g_exposure":100` and `"b_exposure":100` indicate that when the data acquisition occurs, the red, green and blue LEDs should turn on for 100 ms.

A.2.4 Take calibrated set of data

```
{
    "cmd":"exp",
    "arg":"takeRGB",
    "param":{
        "path":"\/",
        "picN":"5",
        "picT":"60000",
        "r_exposure":60,
        "g_exposure":60,
        "b_exposure":50,
        "type":"calibrated"
    }
}
```

The RGB exposure commands present calibrated exposure times and `"picN":"5"` and `"picT":"60000"` present the number of data runs and the time elapsed between them that the user requires. In this case, 5 images would be acquired 60 s apart with an LED exposure time of 60 ms, 60 ms and 50 ms for the red, green and blue LEDs respectively.

A.3 Communication between the PlomApp and the server

```
 {
"analysis":"complex",
"database":"plombox",
"topic":"plombox/getData/XMRwQJ9O3sgCUJK2AOuT3GyKeGA2",
"runNb":"40",
"user":"XMRwQJ9O3sgCUJK2AOuT3GyKeGA2",
"prefix":"phone_test_v4",
"dataSampleID":2,
"calibrationSampleID":1
 }
```

A.4 Assay lead curves used to obtain 95 % confidence level (CI)

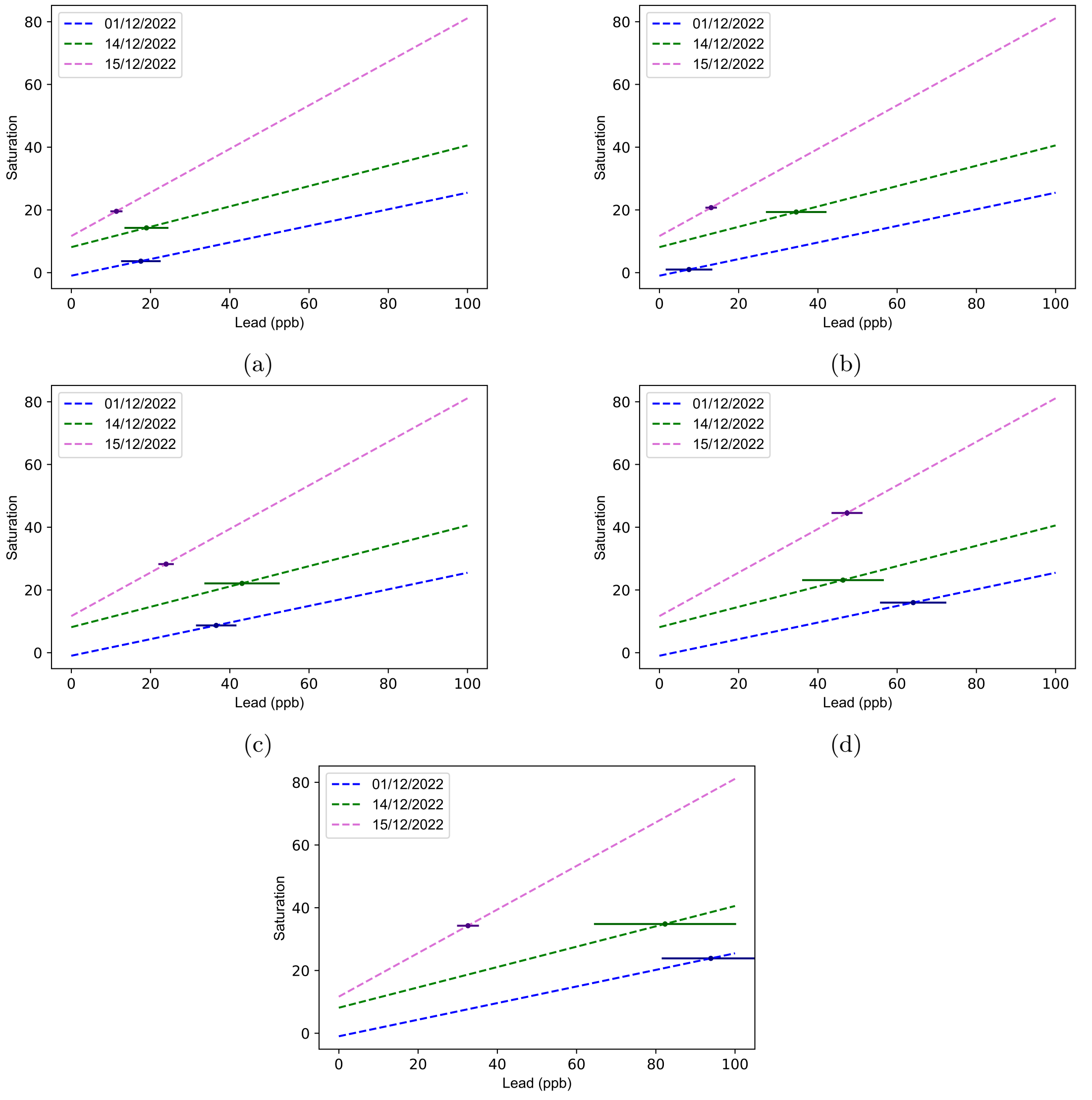

(a)

(b)

(c)

(d)

(e)

Figure A.1: Assay lead curves used to extract lead values for each element of the lead curve. These plots show the saturation values for A.1a 10 ppb, A.1b 15 ppb, A.1c 20 ppb, A.1d 50 ppb and A.1e 100 ppb interpolated to obtain their values of lead. The 100 ppb plot shows a large variation of results, when compared with other lead concentrations.

A.5 Data used to determine PlomBOX's sensitivity and specificity values

Date	Sample #	INA Lead (ppb)	PlomBOX Lead (ppb)
01/12/2022	90	12	3.74
01/12/2022	85	688	3.74
01/12/2022	89	6	4.99
01/12/2022	84	6	13.73
01/12/2022	83	9	13.78
01/12/2022	88	217	14.26
01/12/2022	87	57	18.26
01/12/2022	82	5	22.27
01/12/2022	86	1042	29.29
14/12/2022	71	75	0
14/12/2022	86	1042	0
14/12/2022	101	7	1.08
14/12/2022	102	7	10.29
14/12/2022	85	688	34.90
14/12/2022	103	98	42.31
14/12/2022	65	481	142.59
14/12/2022	67	313	264.99
14/12/2022	62	3548	2495.71
15/12/2022	57	169	0
15/12/2022	85	688	0
15/12/2022	86	1042	0
15/12/2022	88	217	11.41
15/12/2022	68	187	21.43
15/12/2022	100	267	26.21
15/12/2022	67	313	68.98
15/12/2022	65	481	134.06
15/12/2022	62	3548	539.51

Table A.1: Data used to determine PlomBOX's sensitivity and specificity values. The dates of the assays are shown, together with the number of the sample (Sample #) and the lead values, in ppb, obtained by INA and PlomBOX measurements. These samples were checked against the LL of the 95 % CIs presented in Section 6.4.2, to determine the number of TP, TN, FP and FN values. The results are provided in Table 6.9

Bibliography

[1] V. Rich. *The International Lead Trade*. Elsevier Science, 2014. ISBN: 9780857099945.

[2] C. Winder. *The Developmental Neurotoxicity of Lead*. Springer Dordrecht, 1984. ISBN: 978-94-010-8966-1. DOI: `10.1007/978-94-009-5594-3`.

[3] Chapurukha Kusimba. *Making Cents of Currency's Ancient Rise*. 2022. [accessed 3-October-2022]. URL: `https://www.smithsonianmag.com/history/making-cents-currencys-ancient-rise-180963776/`.

[4] L. Yu and H. Yu. *Chinese Coins: Money in History and Society*. Arts of China. Long River Press, 2004. ISBN: 9781592650170.

[5] S. Hong et al. "Greenland Ice Evidence of Hemispheric Lead Pollution Two Millennia Ago by Greek and Roman Civilizations". In: *Science* 265.5180 (1994), pp. 1841–1843. DOI: `10.1126/science.265.5180.1841`.

[6] L Cilliers. "Lead poisoning in ancient Rome". In: *Acta Theologica* 26 (2006), pp. 147–164. DOI: `10.4314/actat.v26i2.52570`.

[7] Kenneth L Barbalace. *Environmental, Chemistry and Hazardous Materials News, Careers and Resources*. 2022. [accessed 30-September-2022]. URL: `https://environmentalchemistry.com/yogi/periodic/Pb.html`.

[8] M. A. Riva et al. "Lead poisoning: historical aspects of a paradigmatic "occupational and environmental disease"". en. In: *Saf Health Work* 3.1 (Mar. 2012), pp. 11–16. DOI: `doi:10.5491/SHAW.2012.3.1.11`.

[9] R. H. Major. *Landmarks in the History of Lead Poisoning*. en. Vol. 3. 2. United States, Mar. 1931, pp. 218–227.

[10] M. Riva, F Sala, and M Sala. "Il male di Saturno, storia e clinica dell'intossicazione da piombo". In: *Doctor Pediatria* 9 (2007), pp. 9–19.

[11] A. Riva. "Les bourses italiennes à l'époque giolittienne (1894-1913): une analyse institutionnaliste de leur organisation". FR. In: *Entreprises et histoire* 48.3 (2007), pp. 9–28. DOI: `10.3917/eh.048.0009`.

[12] J. Eisinger. "Lead and wine. Eberhard Gockel and the colica Pictonum". In: *Medical History* 26.3 (1982), 279–302. DOI: `10.1017/S0025727300041508`.

[13] J. M. S. Pearce. "Burton's Line in Lead Poisoning". In: *European Neurology* 57.2 (2007), pp. 118–119. ISSN: 0014-3022. DOI: `10.1159/000098100`.

[14] K. M. Chow, Z. C. Liu, and C. C. Szeto. "Lead nephropathy: early leads from descriptive studies". In: *Internal Medicine Journal* 36.10 (2006), pp. 678–682. DOI: `10.1111/j.1445-5994.2006.01181.x`.

[15] G. Rosen. *A history of public health*. eng. MD monographs on medical history; no.1. New York: MD, 1958.

[16] J. L. Gibson. "A Plea for Painted Railings and Painted Walls of Rooms as the Source of Lead Poisoning Amongst Queensland Children". In: *Public Health Reports* 120.3 (2005). PMID: 16134572, pp. 301–304. DOI: `10.1177/003335490512000314`.

[17] World Health Organization. *Lead poisoning and health*. 2019. URL: `https://www.who.int/en/news-room/fact-sheets/detail/lead-poisoning-and-health`.

[18] R. Dart, M. Ellenhorn, and E. Caravati. *Medical Toxicology*. MEDICAL TOXICOLOGY. Lippincott, Williams & Wilkins, 2004. ISBN: 9780781728454.

[19] M. A. Flora S J S Mittal Megha. "Heavy metal induced oxidative stress & its possible reversal by chelation therapy". In: *Indian J. Med. Res.* 128.4 (Oct. 2008), pp. 501–523.

[20] B. V. Sanders Talia Liu Yiming and T. P. B. "Neurotoxic effects and biomarkers of lead exposure: a review". In: *Rev Environ Health* 24.1 (Jan. 2009), pp. 15–45. DOI: `10.1515/reveh.2009.24.1.15`.

[21] Geneva: World Health Organization. "Guidelines for drinking-water quality, 4th edition, incorporating the 1st addendum". In: *WHO Library Cataloguing-in-Publication Data* (2017). Licence: CC BY-NC-SA 3.0 IGO.

[22] M. B. Fisher et al. "Occurrence of Lead and Other Toxic Metals Derived from Drinking-Water Systems in Three West African Countries". In: *Environmental Health Perspectives* 129.4 (2021), p. 047012. DOI: `10.1289/EHP7804`.

[23] Centers for Disease Control and Prevention. *CDC National Childhood Blood Lead Surveillance Data*. 2021. [accessed 11-January-2022]. URL: `https://www.cdc.gov/nceh/lead/data/national.htm`.

[24] Public Health England. "Lead Exposure in Children Surveillance System (LEICSS) annual report". In: *Health Protection Report* 15 (5 2021).

[25] Pure Earth. *Fact Sheet: Lead*. 2019. [accessed 04-Feburary-2019]. URL: `http://www.pureearth.org/fact-sheet-lead-2015/`.

[26] *Drinking water and health: a guide for public and environmental health professionals and for those in the water industry in Northern Ireland*. 2020. [accessed 14-April-2020]. URL: `https://www.niwater.com/sitefiles/resources/pdf/reports/2020/guidancedocumentondrinkingwaterandhealth2020.pdf`.

[27] Standing Committee of Analysts. *The Determination of metals in Raw and Drinking waters by Inductively Coupled Plasma Mass Spectrometry (ICP-MS) 2018*. 2022. [accessed 22-September-2022]. URL: `https://secureservercdn.net/160.153.137.128/fkp.e54.myftpupload.com/wp-content/uploads/Blue_Book_Library/262.pdf`.

[28] Labx. *ICP-MS*. 2022. [accessed 07-October-2022]. URL: `https://www.labx.com/product/icp-ms`.

[29] S. J. Cobbina et al. "Comparative Assessment of Heavy Metals in Drinking Water Sources in Two Small-Scale Mining Communities in Northern Ghana". In: *International Journal of Environmental Research and Public Health* 12.9 (2015), pp. 10620–10634. ISSN: 1660-4601. DOI: `10.3390/ijerph120910620`.

[30] B. W. Tukura et al. "Assessment of Heavy Metals in Ground Water from Nasarawa State, Middle Belt, Nigeria". In: *CSIJ* 4.6 (2014), pp. 798–812. DOI: `10.9734/ACSJ/2014/10553`.

[31] V. G. Kanellis. "Sensitivity limits of biosensors used for the detection of metals in drinking water". en. In: *Biophys Rev* 10.5 (Sept. 2018), pp. 1415–1426. DOI: `10.1007/s12551-018-0457-9`.

[32] M. Widorski. "Development of a Detection System to Measure Low Levels of 210Pb using β/γ Coincidence". Master thesis. Egham (UK): Department of Physics, Royal Holloway University of London, 2013.

[33] A. Davidson et al. "Lead". In: *Ullmann's Encyclopedia of Industrial Chemistry*. John Wiley and Sons, Ltd, 2014, pp. 1–55. ISBN: 9783527306732. DOI: `10.1002/14356007.a15_193.pub3`.

[34] C. Langmuir and W. Broecker. *How to Build a Habitable Planet: The Story of Earth from the Big Bang to Humankind*. Princeton University Press, 2012. ISBN: 9780691140063.

[35] USGS - NATIONAL MINERALS INFORMATION CENTER. *Commodity Statistics and Information*. 2022. [accessed 30-September-2022]. URL: `https://www.usgs.gov/centers/national-minerals-information-center/commodity-statistics-and-information`.

[36] International Atomic Energy Agency. *Livechart - Table of Nuclides - Nuclear structure and decay data*. 2022. [accessed 30-September-2022]. URL: `www-nds.iaea.org/relnsd/vcharthtml/VChartHTML.html`.

[37] University of California Nuclear Forensic Search Project. *Nuclear Forensics: A Scientific Search Problem - Decay Chains*. 2022. [accessed 30-September-2022]. URL: `https://metadata.berkeley.edu/nuclear-forensics/`.

[38] Nuclear Power. *Primordial Radionuclides*. 2022. [accessed 24-October-2022]. URL: `https://www.nuclear-power.com/glossary/primordial-matter/primordial-radionuclides/`.

[39] T. Kleine. "Radiogenic Isotopes". In: *Encyclopedia of Astrobiology*. Ed. by R. Amils et al. Berlin, Heidelberg: Springer Berlin Heidelberg, 2014, pp. 1–10. ISBN: 978-3-642-27833-4. DOI: `10.1007/978-3-642-27833-4_1343-2`.

[40] The Editors of Encyclopedia Britannica. *uranium series*. Apr. 2010. URL: `https://www.britannica.com/science/uranium-series`.

[41] The Editors of Encyclopedia Britannica. *actinium series*. Apr. 2010. URL: https://www.britannica.com/science/actinium-series.

[42] The Editors of Encyclopedia Britannica. *thorium series*. Apr. 2010. URL: https://www.britannica.com/science/thorium-series.

[43] The Editors of Encyclopedia Britannica. *neptunium series*. Apr. 2010. URL: https://www.britannica.com/science/neptunium-series.

[44] IAEA Nuclear Data Section. *Live Chart of Nuclides*. 2020. [accessed 03-December-2020]. URL: https://www-nds.iaea.org/relnsd/vcharthtml/VChartHTML.html#dcy1.

[45] J. L. Orrell et al. "Assay methods for ^{238}U, ^{232}Th, and ^{210}Pb in lead and calibration of ^{210}Bi bremsstrahlung emission from lead". In: *J. Radioanal. Nucl. Chem.* 309.3 (2016), pp. 1271–1281. DOI: 10.1007/s10967-016-4732-6.

[46] P. Appleby. "Three decades of dating recent sediments by fallout radionuclides: a review". In: *The Holocene* 18.1 (2008), pp. 83–93. DOI: 10.1177/0959683607085598.

[47] H. Yanga and P. G. Appleby. "Use of lead-210 as a novel tracer for lead (Pb) sources in plants". In: *Scientific reports* 6 (2016), p. 21707. DOI: https://dx.doi.org/10.1038/srep21707.

[48] P.-A. Amaudruz et al. "Design and construction of the DEAP-3600 dark matter detector". In: *Astroparticle Physics* 108 (2019), pp. 1 –23. ISSN: 0927-6505. DOI: 10.1016/j.astropartphys.2018.09.006.

[49] R. M. Eisberg. *Quantum physics of atoms, molecules, solids, nuclei and particles*. eng. New York ; London: Wiley, 1974. ISBN: 0471234648.

[50] A. Beiser. *Concepts of modern physics*. eng. 6th ed. New York: McGraw-Hill, 2003. ISBN: 0-07-115096-X.

[51] G. F. Knoll. *Radiation Detection and Measurement*. John Wiley and Sons, 2000. ISBN: 978-0471073383.

[52] D. Giancoli. *Physics for Scientists and Engineers with Modern Physics*. eng. 4th ed. Harlow, United Kingdom, UNITED KINGDOM: Pearson, 2013. ISBN: 9781292034010.

[53] Australian Radiation Protection and Nuclear Safety Agency (ARPANSA). *Gamma radiation*. [accessed 03-July-2023]. URL: https://www.arpansa.gov.au/understanding-radiation/what-is-radiation/ionising-radiation/gamma-radiation.

[54] D. E. Groom and S. R. Klein. "Passage of particles through matter". In: *The European Physical Journal C - Particles and Fields* 15.1 (Mar. 2000), pp. 163–173. ISSN: 1434-6052. DOI: 10.1007/BF02683419.

[55] NIST. *Stopping-Power and Range Tables for Electrons, Protons, and Helium Ions*. 2019. [accessed 24-October-2022]. URL: https://www.nist.gov/pml/stopping-power-range-tables-electrons-protons-and-helium-ions.

[56] M. J. Berger and S. M. Seltzer. *Tables of energy losses and ranges of electrons and positrons*. National Aeronautics and Space Administration Report NASA-SP-3012, 1964.

[57] R. W. et al. *34. Passage of Particles Through Matter*. 2022. URL: https://pdg.lbl.gov/2022/web/viewer.html?file=../reviews/rpp2022-rev-passage-particles-matter.pdf.

[58] C. Nantais. "Radiopurity measurement of acrylic for the DEAP-3600 dark matter experiment". PhD Thesis. Department of Physics, Engineering Physics and Astronomy, Queen's University, 2014.

[59] X. Hou and P. Roos. "Critical comparison of radiometric and mass spectrometric methods for the determination of radionuclides in environmental, biological and nuclear waste samples". In: *Analytica Chimica Acta* 608.2 (2008), pp. 105–139. ISSN: 0003-2670. DOI: 10.1016/j.aca.2007.12.012.

[60] Y. Y. Ebaid and A. E. M. Khater. "Determination of 210Pb in environmental samples". In: *Journal of Radioanalytical and Nuclear Chemistry* 270.3 (Dec. 2006), pp. 609–619. ISSN: 1588-2780. DOI: 10.1007/s10967-006-0470-5.

[61] A. Nachab and P. Hubert. "210Pb activity by detection of bremsstrahlung in 210Bi β-decay". In: *Nuclear Instruments and Methods in Physics Research Section B: Beam Interactions with Materials and Atoms* 274 (2012), pp. 188–190. ISSN: 0168-583X. DOI: 10.1016/j.nimb.2011.11.020.

[62] S. Yu. "SNO+ background study: polonium on acrylic vessel surface and radon assay". MSc Thesis. Laurentian University, Sudbury, Canada, 2023.

[63] C. M. Nantais, B. T. Cleveland, and M. G. Boulay. "Radiopurity measurement of acrylic for DEAP-3600". In: *AIP Conference Proceedings* 1549.1 (2013), pp. 185–188. DOI: 10.1063/1.4818105.

[64] G. Milton et al. "Ultra trace analysis of acrylic for 232Th and 238U daughters". In: *Applied Radiation and Isotopes* 45.5 (1994), pp. 539–547. ISSN: 0969-8043. DOI: 10.1016/0969-8043(94)90195-3.

[65] D Chauhan and O Chkvorets. "A sensitive assay technique for ^{210}Pb in water". In: *Journal of Physics: Conference Series* 1342.1 (Jan. 2020), p. 012111. DOI: 10.1088/1742-6596/1342/1/012111.

[66] B. Aharmim et al. "High sensitivity measurement of Ra-224 and Ra-226 in water with an improved hydrous titanium oxide technique at the Sudbury Neutrino Observatory". In: *Nucl. Instrum. Meth. A* 604 (2009), pp. 531–535. DOI: 10.1016/j.nima.2009.01.227. arXiv: 0803.4162 [nucl-ex].

[67] Affinity Water Limited Limited. *Water Quality 2018*. 2022. [accessed 22-September-2022]. URL: https://www.affinitywater.co.uk/docs/Water_quality/water-quality-report-2018.pdf.

[68] Affinity Water. *The Laboratory*. 2022. [accessed 22-September-2022]. URL: https://www.affinitywater.co.uk/corporate/scientific-services/laboratory.

[69] Affinity Water Limited Limited. *Water Supply Zone: Bagshot/Sunninghill (AF064)*. URL: https://www.affinitywater.co.uk/docs/water-quality/AF064.pdf.

[70] A. Rodrigues. *Private Communication*. Affinity Water Ltd.

[71] A. Water. *Water Hardness*. 2022. [accessed 07-October-2022]. URL: https://www.affinitywater.co.uk/my-water/water-quality/hardness.

[72] R. A. Gilstrap Jr. “A colloidal nanoparticle form of indium tin oxide: system development and characterization”. PhD Thesis. Georgia Institute of Technology, May 2009.

[73] N. Bhalla et al. “Introduction to biosensors”. en. In: *Essays Biochem* 60.1 (June 2016), pp. 1–8. DOI: `10.1042/EBC20150001`.

[74] H. Kaur and M. Shorie. “Nanomaterial based aptasensors for clinical and environmental diagnostic applications”. In: *Nanoscale Adv.* 1 (6 2019), pp. 2123–2138. DOI: `10.1039/C9NA00153K`.

[75] M. Cremer. *Über die Ursache der elektromotorischen Eigenschaften der Gewebe, zugleich ein Beitrag zur Lehre von den polyphasischen Elektrolytketten*. 1906. URL: `https://books.google.co.uk/books?id=J2j8tgAACAAJ`.

[76] W. R. Heineman and W. B. Jensen. “Leland C. Clark Jr. (1918–2005)”. In: *Biosensors and Bioelectronics* 21.8 (2006), pp. 1403–1404. ISSN: 0956-5663. DOI: `10.1016/j.bios.2005.12.005`.

[77] G. G. Guilbault and J. G. Montalvo. “Urea-specific enzyme electrode”. In: *Journal of the American Chemical Society* 91.8 (1969), pp. 2164–2165. DOI: `10.1021/ja01036a083`.

[78] E.-H. Yoo and S.-Y. Lee. “Glucose Biosensors: An Overview of Use in Clinical Practice”. In: *Sensors* 10.5 (2010), pp. 4558–4576. ISSN: 1424-8220. DOI: `10.3390/s100504558`.

[79] S. Suzuki et al. “Ethanol and Lactic Acid Sensors Using Electrodes Coated with Dehydrogenase—Collagen Membranes”. In: *Bulletin of the Chemical Society of Japan* 48.11 (1975), pp. 3246–3249. DOI: `10.1246/bcsj.48.3246`.

[80] J. Schultz. *Optical sensor of plasma constituents*. 1982. URL: `https://patents.google.com/patent/US4344438A/en`.

[81] M. C. Vestergaard et al. *Nanobiosensors and Nanobioanalyses*. Springer Tokyo, 2015. ISBN: 978-4-431-55189-8. DOI: `10.1007/978-4-431-55190-4`.

[82] C. I. L. Justino, A. C. Duarte, and T. A. P. Rocha-Santos. “Recent Progress in Biosensors for Environmental Monitoring: A Review”. In: *Sensors* 17.12 (2017). ISSN: 1424-8220. DOI: `10.3390/s17122918`.

[83] H. A. Alhadrami. “Biosensors: Classifications, medical applications, and future prospective”. In: *Biotechnology and Applied Biochemistry* 65.3 (2018), pp. 497–508. DOI: `10.1002/bab.1621`.

[84] P. Q. Nguyen et al. “Wearable materials with embedded synthetic biology sensors for biomolecule detection”. In: *Nature Biotechnology* 39.11 (Nov. 2021), pp. 1366–1374. ISSN: 1546-1696. DOI: `10.1038/s41587-021-00950-3`.

[85] R. Svigelj et al. “An Effective Label-Free Electrochemical Aptasensor Based on Gold Nanoparticles for Gluten Detection”. In: *Nanomaterials* 12.6 (2022). ISSN: 2079-4991. DOI: `10.3390/nano12060987`.

[86] S. Atay et al. “Quartz crystal microbalance based biosensors for detecting highly metastatic breast cancer cells via their transferrin receptors”. In: *Anal. Methods* 8 (1 2016), pp. 153–161. DOI: `10.1039/C5AY02898A`.

[87] A. Khanmohammadi et al. “Electrochemical biosensors for the detection of lung cancer biomarkers: A review”. In: *Talanta* 206 (2020), p. 120251. ISSN: 0039-9140. DOI: 10.1016/j.talanta.2019.120251.

[88] V. G. Kanellis. “Sensitivity limits of biosensors used for the detection of metals in drinking water”. en. In: *Biophys Rev* 10.5 (Sept. 2018), pp. 1415–1426. DOI: doi:10.1007/s12551-018-0457-9.

[89] H.-Z. He et al. “Label-free detection of sub-nanomolar lead(II) ions in aqueous solution using a metal-based luminescent switch-on probe”. In: *Biosensors and Bioelectronics* 41 (2013), pp. 871–874. ISSN: 0956-5663. DOI: 10.1016/j.bios.2012.08.060.

[90] H. Sun et al. “A suspending-droplet mode paper-based microfluidic platform for low-cost, rapid, and convenient detection of lead(II) ions in liquid solution”. en. In: *Biosens Bioelectron* 99 (Aug. 2017), pp. 361–367. DOI: 10.1016/j.bios.2017.07.073.

[91] M. Liu et al. “Tailoring porous media for controllable capillary flow”. In: *Journal of Colloid and Interface Science* 539 (2019), pp. 379–387. ISSN: 0021-9797. DOI: 10.1016/j.jcis.2018.12.068.

[92] H. Kuang et al. “Rapid and highly sensitive detection of lead ions in drinking water based on a strip immunosensor”. en. In: *Sensors (Basel)* 13.4 (Mar. 2013), pp. 4214–4224.

[93] P. Estrela, K. Koczula, and A. Gallotta. “Lateral flow assays”. In: *Essays in Biochemistry* 60.1 (June 2016), pp. 111–120. ISSN: 0071-1365. DOI: 10.1042/EBC20150012.

[94] S. M. Tiquia-Arashiro. “Lead absorption mechanisms in bacteria as strategies for lead bioremediation”. In: *Applied Microbiology and Biotechnology* 102.13 (July 2018), pp. 5437–5444. ISSN: 1432-0614. DOI: 10.1007/s00253-018-8969-6.

[95] K. Steward. *Gram Positive vs Gram Negative*. 2022. URL: https://www.technologynetworks.com/immunology/articles/gram-positive-vs-gram-negative-323007.

[96] H.-C. Flemming. “EPS—Then and Now”. In: *Microorganisms* 4.4 (2016). ISSN: 2076-2607. DOI: 10.3390/microorganisms4040041.

[97] H. Salehizadeh and S. Shojaosadati. “Removal of metal ions from aqueous solution by polysaccharide produced from *Bacillus firmus*”. In: *Water Research* 37.17 (2003), pp. 4231–4235. ISSN: 0043-1354. DOI: 10.1016/S0043-1354(03)00418-4.

[98] L. Velásquez and J. Dussan. “Biosorption and bioaccumulation of heavy metals on dead and living biomass of Bacillus sphaericus”. In: *Journal of Hazardous Materials* 167.1 (2009), pp. 713–716. ISSN: 0304-3894. DOI: 10.1016/j.jhazmat.2009.01.044.

[99] N. T. Joutey et al. “Mechanisms of Hexavalent Chromium Resistance and Removal by Microorganisms”. In: *Reviews of Environmental Contamination and Toxicology Volume 233*. Ed. by D. M. Whitacre. Cham: Springer International Publishing, 2015, pp. 45–69. ISBN: 978-3-319-10479-9. DOI: 10.1007/978-3-319-10479-9_2.

[100] H. S. Levinson et al. "Lead resistance and sensitivity in Staphylococcus aureus". In: *FEMS Microbiology Letters* 145.3 (Dec. 1996), pp. 421–425. ISSN: 0378-1097. DOI: `10.1111/j.1574-6968.1996.tb08610.x`.

[101] A. Aguilar-Arevalo et al. "Dosimetry and Calorimetry Performance of a Scientific CMOS Camera for Environmental Monitoring". In: *Sensors* 20.20 (2020). ISSN: 1424-8220. DOI: `10.3390/s20205746`.

[102] A. Aguilar-Arevalo et al. "Volume reduction of water samples to increase sensitivity for radioassay of lead contamination". In: *Applied Water Science* 12.7 (May 2022), p. 151. ISSN: 2190-5495. DOI: `10.1007/s13201-022-01669-5`.

[103] R. Mahr and J. Frunzke. "Transcription factor-based biosensors in biotechnology: current state and future prospects". In: *Applied Microbiology and Biotechnology* 100.1 (Jan. 2016), pp. 79–90. ISSN: 1432-0614. DOI: `10.1007/s00253-015-7090-3`.

[104] J. M. W. Slack et al. *Cell*. Oct. 2022. URL: `https://www.britannica.com/science/cell-biology`.

[105] The Editors of Encyclopedia Britannica. *Cytoplasm*. Dec. 2022. URL: `https://www.britannica.com/science/cytoplasm`.

[106] The Editors of Encyclopedia Britannica. *Eukaryote*. Dec. 2022. URL: `https://www.britannica.com/science/eukaryote`.

[107] The Editors of Encyclopedia Britannica. *Prokaryote*. Sept. 2022. URL: `https://www.britannica.com/science/prokaryote`.

[108] Merriam-Webster. *Definition of Bacteria*. en. Accessed: 2022-12-19. URL: `https://www.merriam-webster.com/dictionary/bacteria`.

[109] D. M. Hillis et al. *Life : The science of biology*. W. H. Freeman & Company, 2020.

[110] C. Books. *A-Level Biology: AQA Year 1 and 2 Complete Revision and Practice with Online Edition (CGP A-Level Biology)*. Coordination Group Publications Ltd (CGP), 2015. ISBN: 9781789080261.

[111] *Definition of RNA polymerase*. en. Accessed: 2022-12-15. URL: `https://www.merriam-webster.com/dictionary/RNA`.

[112] M. M. Mitchler et al. "Transcription factor-based biosensors: a molecular-guided approach for natural product engineering". en. In: *Curr. Opin. Biotechnol.* 69 (June 2021), pp. 172–181. DOI: `10.1016/j.copbio.2021.01.008`.

[113] J. Zhang, M. K. Jensen, and J. D. Keasling. "Development of biosensors and their application in metabolic engineering". In: *Current Opinion in Chemical Biology* 28 (2015). Synthetic biology - Synthetic biomolecules, pp. 1–8. ISSN: 1367-5931. DOI: `10.1016/j.cbpa.2015.05.013`.

[114] M. Debnath, G. B. Prasad, and P. S. Bisen. "Reporter Gene". In: *Molecular Diagnostics: Promises and Possibilities*. Dordrecht: Springer Netherlands, 2010, pp. 71–84. ISBN: 978-90-481-3261-4. DOI: `10.1007/978-90-481-3261-4_5`.

[115] *Definition of BIOLUMINESCENCE*. en. Accessed: 2022-12-16. URL: `https://www.merriam-webster.com/dictionary/bioluminescence`.

[116] Y.-T. Kao, K. L. Gonzalez, and B. Bartel. "Peroxisome Function, Biogenesis, and Dynamics in Plants". en. In: *Plant Physiol* 176.1 (Oct. 2017), pp. 162–177.

[117] The Editors of Encyclopedia Britannica. *Luciferin*. Aug. 2010. URL: `https://www.britannica.com/science/luciferin`.

[118] G. F. Pelentir, V. R. Bevilaqua, and V. R. Viviani. "A highly efficient, thermostable and cadmium selective firefly luciferase suitable for ratiometric metal and pH biosensing and for sensitive ATP assays". In: *Photochemical and Photobiological Sciences* 18.8 (Aug. 2019), pp. 2061–2070. ISSN: 1474-9092. DOI: `10.1039/c9pp00174c`.

[119] F. G. Prendergast and K. G. Mann. "Chemical and physical properties of aequorin and the green fluorescent protein isolated from Aequorea forskalea". In: *Biochemistry* 17.17 (Aug. 1978), pp. 3448–3453.

[120] Stefan Milde, Registry of Standard Biological Parts. *Superfolder GFP coding sequence*. 2008. [accessed 18-July-2023]. URL: `http://parts.igem.org/Part:BBa_I746916`.

[121] R. K. Gary and S. M. Kindell. "Quantitative assay of senescence-associated β-galactosidase activity in mammalian cell extracts". In: *Analytical Biochemistry* 343.2 (2005), pp. 329–334. ISSN: 0003-2697. DOI: `10.1016/j.ab.2005.06.003`.

[122] The Editors of Encyclopedia Britannica. *Hydrolysis*. Apr. 2021. URL: `https://www.britannica.com/science/hydrolysis`.

[123] C. Stylianopoulos. "Carbohydrates: Chemistry and Classification". In: *Encyclopedia of Human Nutrition (Third Edition)*. Ed. by B. Caballero. Third Edition. Waltham: Academic Press, 2013, pp. 265–271. ISBN: 978-0-12-384885-7. DOI: `10.1016/B978-0-12-375083-9.00041-6`.

[124] The Editors of Encyclopedia Britannica. *Galactose*. Mar. 2019. URL: `https://www.britannica.com/science/galactose`.

[125] N. L. of Medicine. *5-bromo-4-chloro-1H-indol-3-ol*. Accessed: 2022-12-16. URL: `https://pubchem.ncbi.nlm.nih.gov/compound/5-bromo-4-chloro-1H-indol-3-ol`.

[126] The Editors of Encyclopedia Britannica. *Indigo*. Dec. 2021. URL: `https://www.britannica.com/technology/indigo-dye`.

[127] J. Zhang, P. Cheng, and K. Pu. "Recent Advances of Molecular Optical Probes in Imaging of β-Galactosidase". In: *Bioconjugate Chemistry* 30.8 (2019), pp. 2089–2101. DOI: `10.1021/acs.bioconjchem.9b00391`.

[128] M. J. Blanco et al. "Tracing Gene Expression Through Detection of β-galactosidase Activity in Whole Mouse Embryos". In: *Journal of visualized experiments : JoVE* 136 (June 2018). ISSN: 1940-087X. DOI: `10.3791/57785`.

[129] M. Fairchild. *Color Appearance Models*. The Wiley-IS&T Series in Imaging Science and Technology. Wiley, 2013. ISBN: 9781119967033.

[130] R. P. Huebener. *Conductors, Semiconductors, Superconductors An Introduction to Solid State Physics*. eng. 2nd ed. 2016. Undergraduate lecture notes in physics. 2016. ISBN: 9783319240107.

[131] K. S. Krane. *Introductory nuclear physics*. eng. New York ; Chichester: Wiley, 1988. ISBN: 0471859141.

[132] M. Avadhanulu. *A Textbook of Engineering Physics*. S Chand & Company, 2008. ISBN: 9788121908177.

[133] M Rizzi, M D'Aloia, and B Castagnolo. "Semiconductor detectors and principles of radiation-matter interaction". In: *Journal of Applied Sciences(Faisalabad)* 10.23 (2010), pp. 3141–3155. DOI: `10.3923/jas.2010.3141.3155`.

[134] H. Kolanoski and N. Wermes. *Particle Detectors: Fundamentals and Applications*. Oxford University Press, 2020. ISBN: 9780198858362.

[135] J. Millman and A. Grabel. *Microelectronics, 2nd Ed.* USA: McGraw-Hill, Inc., 1987. ISBN: 007042330X.

[136] H. Kolanoski and N. Wermes. "Semiconductor detectors". In: *Particle Detectors: Fundamentals and Applications*. Oxford University Press, June 2020. ISBN: 9780198858362. DOI: `10.1093/oso/9780198858362.003.0008`.

[137] D. Bortoletto. "How and why silicon sensors are becoming more and more intelligent?" In: *Journal of Instrumentation* 10.08 (Aug. 2015), p. C08016. DOI: `10.1088/1748-0221/10/08/C08016`.

[138] A. Theuwissen. *Smart Sensor Systems: Emerging Technologies and Applications*. Wiley, 2014. Chap. 7. ISBN: 9780470686003.

[139] H. Wu and P. D. Ye. "Fully Depleted Ge CMOS Devices and Logic Circuits on Si". In: *IEEE Transactions on Electron Devices* 63.8 (2016), pp. 3028–3035.

[140] G. Weckler. "Operation of p-n junction photodetectors in a photon flux integrating mode". In: *IEEE Journal of Solid-State Circuits* (Sept. 1967), P65–P73.

[141] N. Waltham. "CCD and CMOS sensors". In: *Observing Photons in Space: A Guide to Experimental Space Astronomy*. Ed. by M. C. E. Huber et al. New York, NY: Springer New York, 2013, pp. 423–442. ISBN: 978-1-4614-7804-1. DOI: `10.1007/978-1-4614-7804-1_23`.

[142] Teledyne Photometrics. *How Is An Image Made?* 2023. [accessed 21-July-2023]. URL: `https://www.photometrics.com/learn/camera-basics/how-is-an-image-made`.

[143] Y. Ishihara and K. Tanigaki. "A high photosensitive IL-CCD image sensor with monolithic resin lens array". In: *1983 International Electron Devices Meeting*. 1983, pp. 497–500. DOI: `10.1109/IEDM.1983.190552`.

[144] Y. Sano et al. "Solid State Imaging Techniques. On-chip Inner-Layer Lens Technology for an Improvement in Photo-sensitive Characteristics of a CCD Image Sensor." In: *The Journal of The Institute of Image Information and Television Engineers* 50 (1996), pp. 226–233.

[145] H. Watanabe et al. "A 1.4 um front-side illuminated image sensor with novel light guiding structure consisting of stacked lightpipes". In: (Dec. 2011). DOI: `10.1109/IEDM.2011.6131513`.

[146] H. Wakabayashi et al. “A 1/2.3-inch 10.3Mpixel 50frame/s Back-Illuminated CMOS image sensor”. In: *2010 IEEE International Solid-State Circuits Conference - (ISSCC)*. 2010, pp. 410–411. DOI: `10.1109/ISSCC.2010.5433963`.

[147] Teledyne Princeton Instruments. *Quantum Efficiency - Educational Notes*. 2022. [accessed 20-December-2022]. URL: `https://www.princetoninstruments.com/learn/camera-fundamentals/quantum-efficiency`.

[148] B. Vereecke et al. “Quantum efficiency and dark current evaluation of a backside illuminated CMOS image sensor”. In: *Japanese Journal of Applied Physics* 54.4S (Mar. 2015), 04DE09. DOI: `10.7567/JJAP.54.04DE09`.

[149] Oxford instruments. *Neo 5.5 sCMOS Specifications*. 2020. [accessed 18-June-2020]. URL: `https://andor.oxinst.com/products/scmos-camera-series/neo-5-5-scmos`.

[150] L. Kozlowski et al. “Comparison of passive and active pixel schemes for CMOS visible imagers”. In: vol. 3360. Sept. 1998, pp. 101–110. DOI: `10.1117/12.584474`.

[151] M. Pérez et al. “Particle detection and classification using commercial off the shelf CMOS image sensors”. In: *Nuclear Instruments and Methods in Physics Research Section A: Accelerators, Spectrometers, Detectors and Associated Equipment* 827 (2016), pp. 171 –180. ISSN: 0168-9002. DOI: `10.1016/j.nima.2016.04.072`.

[152] L Servoli et al. “Characterization of standard CMOS pixel imagers as ionizing radiation detectors”. In: *Journal of Instrumentation* 5.07 (July 2010), P07003–P07003. DOI: `10.1088/1748-0221/5/07/p07003`.

[153] A. Deisting et al. “Commissioning of a High Pressure Time Projection Chamber with Optical Readout”. In: *Instruments* 5.2 (2021). ISSN: 2410-390X. DOI: `10.3390/instruments5020022`.

[154] Oxford Instruments. *Solis Software*. 2024. [accessed 10-January-2024]. URL: `https://andor.oxinst.com/products/solis-software/`.

[155] LD Didactic GmbH. *Instruction sheet 554 800*. 2020. [accessed 24-April-2020]. URL: `https://www.ld-didactic.de/documents/en-US/GA/GA/5/554/554800e.pdf`.

[156] The FITS Support Office at NASA/GSFC. *Flexible Image Transport System*. 2020. [accessed 20-March-2020]. URL: `https://fits.gsfc.nasa.gov/`.

[157] R. Brun and F. Rademakers. “ROOT: An object oriented data analysis framework”. In: *Nucl. Instrum. Meth. A* 389 (1997). Ed. by M. Werlen and D. Perret-Gallix, pp. 81–86. DOI: `10.1016/S0168-9002(97)00048-X`.

[158] L. Liu and P. Solis. *The Speed and Lifetime of Cosmic Ray Muons*. en. Nov. 2007. URL: `http://web.mit.edu/lululiu/Public/pixx/not-pixx/muons.pdf`.

[159] C. S. Chong et al. “Gamma ray spectrum of Am 241 in a backscattering geometry using a high purity germanium detector”. In: 465 (1997). International Nuclear Conference: a new era in Nuclear Science and Technology - the challenge of the 21st century, pp. 27–28.

[160] D Demir, M Eroğlu, and A Turşucu. "Studying of characteristics of the HPGe detector for radioactivity measurements". In: *Journal of Instrumentation* 8.10 (Oct. 2013), P10027–P10027. DOI: 10.1088/1748-0221/8/10/p10027.

[161] NIST, Physical Measurement Laboratory. *Stopping-Power & Range Tables for Electrons, Protons, and Helium Ions*. 2019. [accessed 20-January-2019]. URL: http://physics.nist.gov/PhysRefData/Star/Text/ASTAR.html.

[162] J. H. Hubbell and S. M. Seltzer. "Tables of X-Ray Mass Attenuation Coefficients and Mass Energy-Absorption Coefficients 1 keV to 20 MeV for Elements Z = 1 to 92 and 48 Additional Substances of Dosimetric Interest". In: *NISTIR 5632* (1995).

[163] M. Berger et al. "XCOM: Photon Cross Sections Database". In: *NIST Standard Reference Database 8 (XGAM)* (2010). DOI: https://dx.doi.org/10.18434/T48G6X.

[164] M. Berger et al. "Stopping-Power & Range Tables for Electrons, Protons, and Helium Ions". In: *NIST Standard Reference Database 124* (2017). DOI: https://dx.doi.org/10.18434/T4NC7P.

[165] D. Zhang et al. *Energy response of GECAM X and gamma-ray detector prototype*. Apr. 2018. URL: https://www.researchgate.net/publication/324492749_Energy_response_of_GECAM_X_and_gamma-ray_detector_prototype.

[166] G. Druit. "Dark Matter Time Projection Chamber (DMTPC) Optical TPC for low energy particle tracking". Egham (UK): Department of Physics, Royal Holloway University of London, 2013.

[167] H. Kolanoski and N. Wermes. *Teilchendetektoren*. Springer, 2016.

[168] NIST. *X-Ray Mass Attenuation Coefficients*. 2020. [accessed 27-January-2021]. URL: https://physics.nist.gov/PhysRefData/XrayMassCoef/ElemTab/z14.html.

[169] S.Y.F. Chu, L.P. Ekström and R.B. Firestone. *WWW Table of Radioactive Isotopes*. 1999. [accessed 26-March-2020]. URL: http://nucleardata.nuclear.lu.se/toi/nuclide.asp?iZA=950241.

[170] G. Milton et al. "Ultra trace analysis of acrylic for 232Th and 238U daughters". In: *Applied Radiation and Isotopes* 45.5 (1994), pp. 539 –547. ISSN: 0969-8043. DOI: 10.1016/0969-8043(94)90195-3.

[171] C. Nantais, B. Cleveland, and M. Boulay. "Radiopurity measurement of acrylic for DEAP-3600". In: *AIP Conf. Proc.* 1549.1 (2013). Ed. by L. Miramonti and L. Pandola, pp. 185–188. DOI: 10.1063/1.4818105.

[172] J. Boger et al. "The Sudbury neutrino observatory". In: *Nucl. Instrum. Meth. A* 449 (2000), pp. 172–207. DOI: 10.1016/S0168-9002(99)01469-2.

[173] B. J. Holland and J. N. Hay. "The kinetics and mechanisms of the thermal degradation of poly(methyl methacrylate) studied by thermal analysis-Fourier transform infrared spectroscopy". In: *Polymer* 42 (2001), pp. 4825–4835.

[174] E. Earle, C. River, and E. Bonvin. *Measurements of Th and U in Acrylic for the Sudbury Neutrino Observatory (SNO)*. AECL (Collection). Neutron and Condensed Matter Science Branch, Chalk River Laboratories, 1993. ISBN: 9780660151984.

[175] C. Cao et al. "A practical approach of high precision U and Th concentration measurement in acrylic". In: *Nuclear Instruments and Methods in Physics Research Section A: Accelerators, Spectrometers, Detectors and Associated Equipment* 1004 (2021), p. 165377. ISSN: 0168-9002. DOI: `10.1016/j.nima.2021.165377`.

[176] Mirion Technologies. *Germanium Detectors*. 2023. [accessed 23-January-2023]. URL: `https://www.mirion.com/products/germanium-detectors`.

[177] K. Vetter. "Recent developments in the fabrication and operation of germanium detectors". In: *Annu. Rev. Nucl. Part. Sci.* 57 (2007), pp. 363–404. DOI: `10.1146/annurev.nucl.56.080805.140525`.

[178] K. Debertin and R. G. Helmer. *Gamma- and X-ray spectrometry with semiconductor detectors*. Netherlands: North-Holland, 1988. ISBN: 0 444 871071.

[179] A. Perez-Andujar and L. Pibida. "Performance of CdTe, HPGe and NaI(Tl) detectors for radioactivity measurements". In: *Applied Radiation and Isotopes* 60.1 (2004), pp. 41–47. ISSN: 0969-8043. DOI: `10.1016/j.apradiso.2003.10.006`.

[180] Eckert & Ziegler. *Single Nuclide Solutions*. 2021. [accessed 07-January-2021]. URL: `https://www.ezag.com/home/products/isotope\_products/isotrak\_calibration\_sources/standardized\_solutions/calibrated_solutions/single\_nuclide\_solutions/#c3903`.

[181] P. Scovell et al. "Low-background gamma spectroscopy at the Boulby Underground Laboratory". In: *Astroparticle Physics* 97 (2018), pp. 160 –173. ISSN: 0927-6505. DOI: `10.1016/j.astropartphys.2017.11.006`.

[182] G. Skinner. "Practical gamma-ray spectrometry: G. Gilmore and J.D. Hemingway, John Wiley, Chichester, UK, 1995, 314 pp. £60.00 ISBN 0-47195-150-1". eng. In: *Spectrochimica Acta Part A: Molecular and Biomolecular Spectroscopy* 52.3 (1996), pp. 379–379. ISSN: 1386-1425.

[183] A. Aguilar-Arevalo et al. "Characterization of germanium detectors for the first underground laboratory in Mexico". In: *Journal of Instrumentation* 15.11 (Nov. 2020), P11014–P11014. DOI: `10.1088/1748-0221/15/11/p11014`.

[184] E. B. Silberstein et al. "The SNMMI Practice Guideline for Therapy of Thyroid Disease with 131I 3.0". In: *Journal of Nuclear Medicine* 53.10 (2012), pp. 1633–1651. ISSN: 0161-5505. DOI: `10.2967/jnumed.112.105148`.

[185] M. P. M. Stokkel et al. "EANM procedure guidelines for therapy of benign thyroid disease". In: *European Journal of Nuclear Medicine and Molecular Imaging* 37.11 (2010), pp. 2218–2228. ISSN: 1619-7089. DOI: `10.1007/s00259-010-1536-8`.

[186] J. Reis. *Environmental Control in Petroleum Engineering*. Elsevier Science, 1996. ISBN: 9780080505756.

[187] European Medicines Agency. *Lumark*. 2021. [accessed 30-April-2021]. URL: `https://www.ema.europa.eu/en/medicines/human/EPAR/lumark`.

[188] J. R. Howe and M. K. Lloyd. “Radio-iodine in thyroid glands of swans, farm animals and humans, also in algae and river water from the Thames Valley, England”. In: *Science of The Total Environment* 48.1 (1986), pp. 13–31. ISSN: 0048-9697. DOI: `10.1016/0048-9697(86)90151-8`.

[189] A. D. Nadra. “SensAr: producto innovador, experiencia excepcional”. Español. In: *Química Viva* (2015). ISSN: 1666-7948.

[190] G. Sezonov, D. Joseleau-Petit, and R. D’Ari. “Escherichia coli physiology in Luria-Bertani broth”. en. In: *J. Bacteriol.* 189.23 (Dec. 2007), pp. 8746–8749. DOI: `10.1128/JB.01368-07`.

[191] F. Barone et al. “Design and evaluation of an incoherent feed-forward loop for an arsenic biosensor based on standard iGEM parts”. In: *Synthetic Biology* 2.1 (Dec. 2017). ISSN: 2397-7000. DOI: `10.1093/synbio/ysx006`.

[192] W. Ng. “Effect of glucose and ammonium chloride supplementation and phosphate buffer on *Escherichia coli* DH5α growth in LB Lennox medium”. In: *PeerJ* (May 2018). DOI: `10.7287/peerj.preprints.26949v1`.

[193] J. Sambrook et al. *Molecular Cloning: A Laboratory Manual*. Molecular Cloning: A Laboratory Manual v. 1. Cold Spring Harbor Laboratory Press, 2001. ISBN: 9780879695774.

[194] Buch Holm. *Chromatography Equipment*. 2024. [accessed 16-February-2024]. URL: `https://www.buch-holm.com/products/chromatography-equipment/chromatography-paper-whatman-grade-1chr-size-9950311`.

[195] Biopack. *PLOMO (II) NITRATO p.a. (A.C.S.)* [accessed 28-August-2023]. 2023. URL: `https://biopack.com.ar/ficha_2000961600_plomo-ii-nitrato-p-a-a-c-s`.

[196] RS. *A Complete Pipette Guide*. 2024. [accessed 16-February-2024]. URL: `https://uk.rs-online.com/web/content/discovery/ideas-and-advice/pipettes-guide`.

[197] A.-T. Technology. *ESP32-CAM camera development board*. Accessed: 2022-08-17. URL: `https://docs.ai-thinker.com/en/esp32-cam`.

[198] Omnivision. *Omnivision OV2640 preliminary datasheet*. Accessed: 2022-08-17. URL: `https://www.uctronics.com/download/cam_module/OV2640DS.pdf`.

[199] S. Alden. *Photo courtesy of Dr. Siobhan Alden*. 2023.

[200] *ELEGOO Mars 3 ULTRA 4K Mono LCD 3D Printer*. Accessed: 2023-04-28. URL: `https://www.elegoo.com/en-gb/products/elegoo-mars-3-lcd-3d-printer?variant=40784027811888`.

[201] *Global mobile OS market share 2022*. en. Accessed: 2023-4-17. URL: `https://www.statista.com/statistics/272698/global-market-share-held-by-mobile-operating-systems-since-2009/`.

[202] Koombea. *How are Android Apps Developed?* Accessed: 2023-04-24. URL: `https://www.koombea.com/blog/how-android-apps-are-developed/`.

[203] The Editors of Encyclopedia Britannica. “Bluetooth”. In: *Encyclopedia Britannica*. Jan. 2023.

[204] The Editors of Encyclopedia Britannica. “Wi-Fi”. In: *Encyclopedia Britannica*. Apr. 2023.

[205] *What is Docker?* Accessed: 2023-05-09. URL: `https://aws.amazon.com/docker/`.

[206] *Getting to know MQTT*. Accessed: 2023-04-24. URL: `https://developer.ibm.com/articles/iot-mqtt-why-good-for-iot/`.

[207] *What is SSL, TLS and HTTPS?* Accessed: 2023-05-10. URL: `https://www.websecurity.digicert.com/en/uk/security-topics/what-is-ssl-tls-https`.

[208] *InfluxDB. It's About Time.* Accessed: 2023-05-09. URL: `https://www.influxdata.com/`.

[209] *Dashboard anything. Observe everything.* Accessed: 2023-05-09. URL: `https://grafana.com/grafana/?plcmt=footer`.

[210] *Introducing JSON*. Accessed: 2023-04-24. URL: `https://www.json.org/json-en.html`.

[211] M. Botta and D. Cavagnino. "A Framework for Reversible Data Embedding into Base45 and Other Non-Base64 Encoded Strings". In: *Applied Sciences* 12.1 (2022). ISSN: 2076-3417. DOI: `10.3390/app12010241`.

[212] *Application fundamentals*. Accessed: 2023-05-10. URL: `https://developer.android.com/guide/components/fundamentals`.

[213] *Google Firebase*. Accessed: 2023-04-24. URL: `https://www.techtarget.com/searchmobilecomputing/definition/Google-Firebase`.

[214] The Editors of Encyclopedia Britannica. "bitmap". In: *Encyclopedia Britannica.* Jan. 2022.

[215] H. Levkowitz and G. T. Herman. "GIHS: A generalized color model and its use for the representation of multiparameter medical images". In: *Mathematics and computer science in medical imaging.* Springer. 1988, pp. 389–399.

[216] A. R. Smith. "Color Gamut Transform Pairs". In: *Proceedings of the 5th Annual Conference on Computer Graphics and Interactive Techniques.* SIGGRAPH '78. New York, NY, USA: Association for Computing Machinery, 1978, 12–19. ISBN: 9781450379083.

[217] A. R. Smith. "Color Gamut Transform Pairs". In: *SIGGRAPH Comput. Graph.* 12.3 (Aug. 1978), 12–19. ISSN: 0097-8930. DOI: `10.1145/965139.807361`.

[218] Prifysgol Bangor University. *Learn Hue Saturation and Brightness (HSB) colour coding*. 2020. [accessed 15-June-2023]. URL: `https://csee.bangor.ac.uk/project-rainbow/learn-hue-saturation-and-brightness-hsb-colour-coding/`.

[219] A. Hanbury and J. Serra. "Colour Image Analysis in 3D-Polar Coordinates". In: *Pattern Recognition.* Ed. by B. Michaelis and G. Krell. Berlin, Heidelberg: Springer Berlin Heidelberg, 2003, pp. 124–131. ISBN: 978-3-540-45243-0.

[220] Computer Science Field Guide (CSFG). *Data Representation - 5.5. Images and Colours*. 2022. [accessed 19-June-2023]. URL: `https://www.csfieldguide.org.nz/en/chapters/data-representation/images-and-colours`.

[221] *JPEG*. en. `https://www.merriam-webster.com/dictionary/JPEG.`. Accessed: 2023-9-7.

[222] flussonic. *Chroma subsampling*. 2023. [accessed 07-September-2023]. URL: https://flussonic.com/glossary/chroma-subsampling/.

[223] Kyle Schurman. *Digital Camera Glossary: Automatic Exposure (AE)*. 2020. [accessed 29-August-2023]. URL: https://www.lifewire.com/automatic-exposure-ae-493263.

[224] M. E. Angelopoulou and M. Petrou. "Uncalibrated flatfielding and illumination vector estimation for photometric stereo face reconstruction: Background Modeling For Foreground Detection in Real-World Dynamic Scenes". eng. In: *Machine vision and applications* 25.5 (2014), pp. 1317–1332. ISSN: 0932-8092.

[225] P. Instruments. *Flat Field Correction*. 2011. [accessed 12-July-2022]. URL: https://web.archive.org/web/20130407013841/http://www.princetoninstruments.com/cms/index.php/ccd-primer/152-flat-field-correction.

[226] M. Kumar and R. K. Upreti. "Impact of Lead Stress and Adaptation in Escherichia coli". In: *Ecotoxicology and Environmental Safety* 47.3 (2000), pp. 246–252. ISSN: 0147-6513. DOI: 10.1006/eesa.2000.1960.

[227] ThermoFisher Scientific. *Atomic Absorption Spectrometry (AAS) Information*. 2023. [accessed 21-August-2023]. URL: https://www.thermofisher.com/uk/en/home/industrial/spectroscopy-elemental-isotope-analysis/spectroscopy-elemental-isotope-analysis-learning-center/trace-elemental-analysis-tea-information/atomic-absorption-aa-information.html.

[228] W. Ng. "Microbes in deionized and tap water: Implications for maintenance of laboratory water production system". In: (Mar. 2018). DOI: 10.7287/peerj.preprints.181v6.

[229] K Kovárová-Kovar and T Egli. "Growth kinetics of suspended microbial cells: from single-substrate-controlled growth to mixed-substrate kinetics". en. In: *Microbiol Mol Biol Rev* 62.3 (Sept. 1998), pp. 646–666. DOI: 10.1128/mmbr.62.3.646-666.1998.

[230] David Moore. *A brief explanatory tutorial about the Monod equation*. World of Fungi. URL: https://www.davidmoore.org.uk/Sec02_02Monod.htm.

[231] M. Shehadul Islam, A. Aryasomayajula, and P. R. Selvaganapathy. "A Review on Macroscale and Microscale Cell Lysis Methods". In: *Micromachines* 8.3 (2017). ISSN: 2072-666X. DOI: 10.3390/mi8030083.

[232] S. H. Tan and S. B. Tan. "The Correct Interpretation of Confidence Intervals". In: *Proceedings of Singapore Healthcare* 19.3 (2010), pp. 276–278. DOI: 10.1177/201010581001900316.

[233] R. Parikh et al. "Understanding and using sensitivity, specificity and predictive values". en. In: *Indian J Ophthalmol* 56.1 (Jan. 2008), pp. 45–50.

[234] Thames Water Utilities Limited. *Reservoir levels and rainfall figures*. 2021. [accessed 24-May-2021]. URL: https://www.thameswater.co.uk/about-us/performance/reservoir-levels-and-rainfall-figures.